A MULTISCALE METHOD FOR MIXED CONVECTIVE SYSTEMS

Coupled calculations with ATHLET and OpenFOAM of the PHENIX NCT

Zur Erlangung des akademischen Grades
Doktor der Ingenieurwissenschaften
der Fakultät für Maschinenbau
Karlsruher Institut für Technologie (KIT)

genehmigte
Dissertation
von

Dipl.-Ing. Klaus Huber

Tag der mündlichen Prüfung:	6. Februar 2017
Hauptreferent:	Prof. Dr.-Ing. Xu Cheng
Korreferent:	Prof. Dr.-Ing Thomas Schulenberg

Abstract

The Generation IV International Forum proposed six innovative reactor concepts as most promising. One of those concepts is the sodium cooled fast reactor (SFR). Its research and development has long history and shows high potential to meet GEN-IV criteria. One of those is the PHENIX reactor build in France. Construction began in 1968 and connected to the grid in 1973. The small-scale prototype reactor was in full operation until 2004 and then mainly used for research on transmutation and accident scenarios.
The final shutdown of the PHENIX reactor was in 2009. Before it was finally shut down, several final tests were planned and performed, including the natural convection test (NCT), which is used in this work for calculations of the primary circuit behavior. The NCT is used as a benchmark excercise for his work, more specifically as a blind test for system code qualification and its validation. These codes use a lumped parameter approach and are used to calculate transient behavior of system thermal-hydraulics (STH) of complete and complex systems like nuclear power plants are. In Germany, the Analysis of thermal-hydraulics of leaks and transients (ATHLET) code is being developed by the Gesellschaft für Anlagen- und Reaktorsicherheit (GRS) gGmbH. As all operating German power plants are cooled by water, ATHLET is used only with material properties of water. One part of the THINS (Thermal-Hydraulics of Innovative Nuclear Systems) project was to qualify light water reactor (LWR) STH codes for GEN-IV purposes. This work shows the extension of the ATHLET code to sodium through a multi-fluid approach. Computational fluid dynamics (CFD) is used in many domains of fluid dynamics' calculations. It provides high quality and high resolution results of the desired domain. Hence the computational effort - and therefore costs - is high and time consuming, a more optimized method is in focus of another part of the THINS project. Combining the effectiveness of a STH code with the high quality of CFD (where needed) is leading to coupled approaches. After an introduction, this work presents the modification of the ATHLET STH code for sodium applications. After that, the feasibility of the implementation is shown with a generated STH model of the PHENIX primary circuit. As far as possible by the NCT the implementations are assessed and discussed. Afterwards, the hot pool of the PHENIX primary circuit is modeled in CFD and calculated with the open source CFD toolbox OpenFOAM. The hot pool has been chosen, as it is one of three large volumes that is considered to have high threedimensional effects that cannot be represented with STH only. The Reynolds Averaged Navier-Stokes (RANS) method is applied with a k-ϵ turbulence model. To merge the two different scales of system thermal-hydraulics and computational fluid dynamics, a coupling methodology is being developed and verified. Its implementation is shown and discussed with the PHENIX NCT. During the transient scenario, the coupled solution shows different behavior in comparison to the STH standalone calculation. This is due to strong three-dimensional effects taking place in the hot pool of the PHENIX primary circuit that cannot be captured with STH standalone. Differences between STH standalone and STH/CFD coupled calculations are discussed in that chapter. Another theoretical scenario is presented, which applies the verified and assessed coupling model and scheme to show the extrapolation capability of the coupling methodology. It can also be observed, when CFD shows uniform flow field behavior at small magnitude in

vertical direction in the hot pool, that results between STH/CFD coupled calculation and STH standalone calculation are very similar.

Kurzfassung

Das Generation IV International Forum schlug sechs Konzepte für Innovative Reaktoren vor, die am vielversprechendsten sind. Eines dieser Konzepte ist der Natrium gekühlte schnelle Reaktor (SFR) mit einer langen Forschungs- und Entwicklungsgeschichte. Dieser Reaktortyp weist ein hohes Potential auf, um die GEN-IV Kriterien zu erfüllen. Dazu gehört der im Jahr 1968 in Frankreich erbaute und 1973 an das Elektrizitätsnetz angeschlossene PHENIX Reaktor. Dieser Prototypreaktor wurde bis 2004 betrieben und anschließend zu Forschungszwecken, wie der Transmutation und der Evaluation von Unfallszenarien weiter verwendet.

Die endgültige Abschaltung des PHENIX Reaktors fand 2009 statt. Zuvor wurden einige finale Tests geplant und durchgeführt, einschließlich eines Tests zur Naturkonvektion (NCT) des Primärkreislaufs. Der Naturkonvektions-Test wird als Benchmark-Test in der vorliegenden Arbeit verwendet und dient Qualifikation und Validierung von System-Rechenprogrammen. Im Rahmen eines EU-Forschungsprojektes wurde der Benchmark-Test als sogenannter Blind-Test durchgeführt. Diese Rechenprogramme verwenden den Ansatz der konzentrierten Parameter und werden zur Berechnung des transienten Verhaltens von thermo-hydraulischen Systemen (STH) angewendet. Mit diesem Ansatz ist es möglich, komplexe Systeme ganzheitlich zu betrachten und zu berechnen. In Deutschland wird das ATHLET Rechenprogramm von der Gesellschaft für Anlagen- und Reaktorsicherheit (GRS) gGmbH entwickelt. Da alle Kernkraftwerke in Deutschland, die zur kommerziellen Stromerzeugung verwendet werden mit Wasser gekühlt sind, wurde ATHLET bislang nur für diese Zwecke entwickelt. Ein Teilprojekt des europäischen THINS Projektes (Thermal-Hydraulics of Innovative Nuclear Systems) ist die Qualifikation von System-Rechenprogrammen, die bisher nur für wassergekühlte Kernkraftwerke entwickelt wurden, für System- und Sicherheitsrechnungen im Rahmen der GEN-IV. Die vorgelegte Arbeit zeigt die Erweiterung des ATHLET Rechenprogramms für Natriumanwendungen mittels eines Multi-Fluid Ansatzes.

Numerische Strömungssimulation (CFD) wird in vielen Gebieten der Strömungsmechanik angewandt. Sie gibt qualitativ hochwertige und hoch aufgelöste Ergebnisse in gewünschten Bereichen. Der Rechenaufwand - und damit die Kosten - sind allerdings durch eine damit verbundene, lange Rechenzeit hoch. Die Entwicklung einer optimierten Methode ist ebenfalls Teil des THINS Projekts, bei der die Effektivität einer Berechnung auf Systemebene mit der hohen Auflösung von CFD kombiniert (gekoppelt) werden.

Nach einem einleitenden Kapitel werden im Rahmen dieser Arbeit Modifikationen des ATHLET Rechenprogramms für Natriumanwendungen erläutert. Anschließend wird an einem System-Modell für den PHENIX Primärkreislauf im Rahmen des NCT eine Machbarkeitsstudie durchgeführt. Soweit möglich, werden Assessments der Implementierungen mit Hilfe des NCT diskutiert. Danach wird das heiße Becken des PHENIX-Primärkreislaufs in CFD modelliert und mit dem quelloffenen Rechenprogramm OpenFOAM berechnet. Das heiße Becken wurde aus einem der drei großen Volumina ausgewählt. Es wird angenommen, dass hier starke dreidimensionale Effekte vorherrschen, welche durch einen System-Ansatz nicht abgebildet werden können. Die Reynolds gemittelte Navier-Stokes Methode mit einem k-ϵ Turbulenzmodell wird hierbei angewandt. Um die zwei unterschiedlichen

Methoden zu kombinieren, wird eine Kopplungsstrategie entwickelt und verifiziert. Die Programmeinbindung wird aufgezeigt und am Beispiel des PHENIX NCT diskutiert. Im Laufe des transienten Szenarios zeigt die gekoppelte Lösungsmethode abweichende Ergebnisse im Vergleich zur alleinigen System-Rechenprogramm Lösung. Dies wird durch starke, dreidimensionale Effekte im heißen Becken des PHENIX Primärkreislaufs hervorgerufen und kann durch das thermo-hydraulische System-Rechenprogramm nicht erfasst werden. Ein weiteres, theoretisches Szenario wird ebenfalls aufgezeigt, um das Potential der verifizierten und diskutierten Kopplungs-Strategie zu veranschaulichen. Hier kann eine Ähnlichkeit zwischen CFD und STH beobachtet werden. Diese tritt auf, wenn die Strömungsrichtung und deren Orientierung in beiden Rechenprogrammen identisch ist. Ebenso müssen die Geschwindigkeitsgrößen sehr klein sein.

Acknowledgements

This thesis was created during my time at the Institute of Fusion and Reactor Technology (IFRT), part of the Karlsruhe Institute of Technology (KIT). I had the honor to be part of an international and very friendly team with its head Prof. Dr.-Ing. Xu Cheng. During my time at IFRT, he guided me with trust, patience, knowledge and creative hints during the whole time. For this, being first reviewer of my work and so many things, I am grateful beyond measure.

I am very grateful to Prof. Dr.-Ing. Thomas Schulenberg, my second reviewer. His practical advices, ideas and encouragement were of great value to me whenever we worked together.

My sincere thanks go to Dr. Ivan Otic for our nice, intense and deep scientific discussions, his advice, point of view and focus. It was a pleasure working together.

Thanks to Prof. Dr.-Ing. Xu Cheng, I also can give my deepest gratitude to Dr. Justin Thomas for being my supervisor during my stay at Argonne National Laboratory (ANL). I also want bring my great gratitude to Dr. Thomas Fanning and Dr. Tyler Sumner, and the whole team I was in touch with for sharing information, fruitful discussions and really awesome lunch breaks.

All my colleagues at IFRT who shared that journey with me, thank you all.

My greatest thanks goes to my family for supporting me in every facet of my studies.

Finally, I want to give my gratitude to Dr. Peter Fritz and his son (Dr.) Michael Fritz, a true friend, who gave me the initial idea to continue my studies at the Institute of Fusion and Reactor Technology (IFRT), part of the Karlsruhe Institute of Technology (KIT).

Contents

List of Tables

List of Figures

Nomenclature

List of abbreviations

Abbrev.	**Description**
AEC	Atomic Energy Commission
API	Application Programming Interface
ATHLET	Analysis of thermal-hydraulics of leaks and transients - thermal-hydraulic system code
BC	Boundary condition
BWR	Boiling water reactor
CEA	Commissariat a l'énergie atomique et aux énergies alternatives
CFD	Computational Fluid Dynamics
ch.	Chapter
CM	Control Mass
CRP	Coordinated Research Project
CSNI	Committee on the Safety of Nuclear Installations
CV	Control Volume
DNS	Direct numerical simulation
DRC	Direct Reactor Cooling
EDF	Électricité de France
EFR	European Fast Reactor
EMWG	Economic Modeling Working Group
Eq.	Equation
FEBE	Forward-Euler and Backward-Euler methods
Fig.	Figure

FP7	7^{th} Framework Programme - European Union's Research and Innovation funding programme for $2007-2013$
FVM	Finite-volume method
GCSM	General control simulation module
GEN-III	Advanced Nuclear Power Reactors
GEN-IV	4^{th} generation of nuclear systems. A new generation of nuclear reactors and related fuel cycles involving different technologies also known as Innovative Nuclear Systems
GFR	Gas-Cooled Fast Reactor System
GIF	Generation IV International Forum
GIT	Version control system that is used for software development and other version control tasks.
GRS	Gesellschaft für Reaktor- und Anlagensicherheit (GRS) gGmbH
GUI	Graphical user interface
HCO	Heat conduction object
HCV	Heat conduction volume
HECU	Heat transfer and heat conduction
Hg	Mercury
HTC	Heat transfer coefficient
htc	Heat transfer correlation
IAEA	International Atomic Energy Agency
IC	Inner core
ICoCo	Interface for Code Coupling
IHX	Intermediate Heat Exchanger
LES	Large eddy simulation
LFR	Lead-Cooled Fast Reactor System
LM	Liquid metal
Lst.	Source code listing
lst.	Listing
LWR	Light Water Reactor
ML	Mixture level

MSR	Molten Salt Reactor System
Na	Sodium
NaK	Sodium potassium
NEA	Nuclear Energy Agency
NEUKIN	Neutron kinetics
NRC	Nuclear Regulatory Commission
NSSS	Nuclear Steam Supply System
OC	Outer core
ODE	Ordinary Differential Equations
OECD	Organization for Economic Co-operation and Development
OpenFOAM	Open Source Field Operation and Manipulation - toolbox for the development of customized numerical solvers
Pb	Lead
PbBi	Lead-Bismuth
PP	Primary Pump
PRPPWG	Proliferation Resistance and Physical Protection Working Group
PVM	Parallel Virtual Machine
PWR	Pressurized Water Reactor
R&D	Research and Development
RANS	Reynolds-average Navier-Stokes
RSWG	Risk and Safety Working Group
RV	Reactor Vessel
SA	Subassembly
SCWR	Supercritical-Water-Cooled Fast Reactor System
SDC	Safety Design Criteria
SFR	Sodium-Cooled Fast Reactor System
SGS	Sub-grid scale
STH	System Thermal-Hydraulics
Tab.	Table

TDJ	Time dependent junction
TFD	Thermo-fluid dynamics
TFO	Thermo-fluid-dynamic object
THINS	Thermal-Hydraulics of Innovative Nuclear Systems
VHTR	Very-High-Temperature Reactor System

List of dimensionless numbers

Symbol	**Description**	**Definition**
Gr	Grashof number	$\mathrm{Gr} \equiv \frac{g\beta(T_{wall}-T_{bulk})L^3}{\nu^2}$
Nu	Nusselt number	$\mathrm{Nu} \equiv \frac{(HTC)\cdot L}{\lambda}$
Pe	Péclet number	$\mathrm{Pe} \equiv \frac{u\cdot L}{\alpha} = Re \cdot Pr$
Pr	Prandtl number	$\mathrm{Pr} \equiv \frac{\nu}{\alpha} = \frac{c_p\cdot\mu}{\lambda}$
Ra	Rayleigh number	$\mathrm{Ra} \equiv \mathrm{Gr}\cdot\mathrm{Pr} = \frac{g\beta}{\nu\alpha}\left(T_w - T_f\right)L^3$
Re	Reynolds number	$\mathrm{Re} \equiv \frac{\rho\cdot u\cdot L}{\mu} = \frac{u\cdot L}{\nu}$

List of Greek symbols

Symbol	**Description**	**SI-Units**
α	thermal diffusivity	$m^2 \cdot s^{-1}$
β	thermal expansion coefficient	K^{-1}
χ	characteristic length scale	m
δ_{ij}	Kronecker delta function	–
ϵ_g	obstruction ratio of cross section by spacer grid	–
ϵ_H	eddy diffusivity of heat	$m^2 \cdot s^{-1}$
ϵ_M	eddy diffusivity of momentum	$m^2 \cdot s^{-1}$
η	Kolmogorov length-scale	m
λ	thermal conductivity coefficient	$kg \cdot m \cdot s^{-3} \cdot K^{-1}$
μ	dynamic viscosity	$kg \cdot m^{-1} \cdot s^{-1}$
ν	kinematic viscosity	$m^2 \cdot s^{-1}$
$\overline{\phi}$	average part of the quantity ϕ	–

ϕ'	fluctuating part of the quantity ϕ	–
Φ	dissipation function (per unit volume)	$kg \cdot m^{-1} \cdot s^{-3}$
ϕ	in CFD the quantity ϕ can represent velocity, density, pressure, enthalpy or temperature	–
Ψ	in eq. (3.22), eq. (3.23), eq. (3.24) and eq. (3.26): ratio of the eddy diffusivity of heat to the diffusivity of momentum	–
Ψ	inter-phase mass transfer rate	$kg \cdot s^{-1}$
ψ	inter-phase mass exchange per unit volume	$kg \cdot m^{-3} \cdot s^{-1}$
ρ	density	$kg \cdot m^{-3}$
ρ_m	mixture density (liquid and vapor)	$kg \cdot m^{-3}$
τ_i	inter-facial shear per unit volume	$kg \cdot m^{-2} \cdot s^{-2}$
τ_{ij}	viscous stress tensor	$kg \cdot m^{-1} \cdot s^{-2}$
υ	linear (parallel to structure) velocity at radial distance r	$m \cdot s^{-1}$
ζ_{Form}	form loss coefficient	–
$\mathbf{\Pi}_{ij}$	Stress tensor	$m^2 \cdot s^{-2}$

List of subscripts

Symbol	**Description**
Ψ	inter-phase mass exchange
i	$i \in \mathbb{N}^+$, used as counter or for classification
in	inlet
j	$j \in \mathbb{N}^+$, used as counter or for classification
l	liquid
m	mixture
out	outlet
v	vapor

List of mathematical expressions

Symbol	**Description**
$\Delta\,()$	discrete value of ( )
$()^T$	transpose of a vector or matrix
∇	Nabla operator
$\nabla \cdot ()$	Divergence of ( )
$\nabla\,()$	Gradient of ( )
$\otimes$	Outer product of two vectors
$\partial\,()$	partial differential of ( )
$d\,()$	differential of ( )
$f\,()$	function of ( )

List of Roman symbols

Symbol	**Description**	**SI-Units**
u, v, w	velocity components (3D flow)	$m \cdot s^{-1}$
A	cross section	m^2
a	steam void fraction	$-$
c_p	specific heat capacity	$m^2 \cdot s^{-2} K^{-1}$
D	Diameter (of a fuel rod in ch. 3.2)	m
d_h	hydraulic diameter	m
E	energy flow	$kg \cdot m^2 \cdot s^{-3}$
e	internal energy per unit mass	$m^2 \cdot s^{-2}$
E_t	total energy per unit mass	$m^2 \cdot s^{-2}$
$\boldsymbol{f}_B$	Body force per unit volume	$m \cdot s^{-2}$
$\boldsymbol{f}_{wall}$	wall friction force per unit volume	$kg \cdot m^{-2} \cdot s^{-2}$
$\boldsymbol{g}$	Gravity vector	$m \cdot s^{-2}$
G	mass flow rate	$kg \cdot s^{-1}$
g	Gravity	$m \cdot s^{-2}$
H	total enthalpy	$kg \cdot m^2 \cdot s^{-2}$

h	enthalpy	$kg \cdot m^2 \cdot s^{-2}$
HTC	Heat transfer coefficient	$kg \cdot s^{-3} \cdot K^{-1}$
$\boldsymbol{I}$	unit tensor	–
L	characteristic length	m
l	length-scale	m
l_0	length-scale of the largest eddies	m
L_f	characteristic length-scale of the flow	m
l_{DI}	demarcation length-scale between the dissipation range and the internal subrange	m
l_{EI}	demarcation length-scale between the energy-containing range of eddies and smaller eddies	m
m	mass	kg
Δp_ρ	pressure loss - density derivative term	$kg \cdot m^{-1} \cdot s^{-2}$
Δp_{fric}	pressure loss - friction and form loss pressure drop	$kg \cdot m^{-1} \cdot s^{-2}$
Δp_{grav}	pressure loss - elevation term	$kg \cdot m^{-1} \cdot s^{-2}$
Δp_I	pressure loss - source term, e.g. pump differential pressure	$kg \cdot m^{-1} \cdot s^{-2}$
Δp_{mf}	pressure loss - momentum flux term	$kg \cdot m^{-1} \cdot s^{-2}$
Δp_r	pressure loss - relative velocity term	$kg \cdot m^{-1} \cdot s^{-2}$
Δp_s	pressure loss between two CVs	$kg \cdot m^{-1} \cdot s^{-2}$
$^P/_D$	Pitch-to-diameter ratio	–
P	Pitch (between two fuel rods in ch. 3.2)	m
p	pressure	$kg \cdot m^{-1} \cdot s^{-2}$
$\dot{q}_i$	heat flow at the phase interface	$kg \cdot m^2 \cdot s^{-3}$
$\dot{q}_s$	heat flow through structures	$kg \cdot m^2 \cdot s^{-3}$
q	heat flux	$kg \cdot s^{-3}$
Q_H	heat source	$kg \cdot m^2 \cdot s^{-2}$

Q_{EH}	interfacial heat exchange	$kg \cdot m^2 \cdot s^{-3}$
R_{ij}	Reynolds stress tensor	$kg \cdot m^{-1} \cdot s^{-2}$
$\boldsymbol{S}_{ij}$	strain rate tensor	s^{-1}
s	length coordingate	m
S_I	Momentum source	$kg \cdot m^{-2} \cdot s^{-2}$
S_W	distance between two opposide sides of a regular hexagon (pitch)	m
T	absolute temperature	K
t	time	s
$\boldsymbol{u}$	velocity vector	$m \cdot s^{-1}$
u	velocity	$m \cdot s^{-1}$
u_r	relative velocity	$m \cdot s^{-1}$
u_{EI}	demarcation velocity-scale between the energy-containing range of eddies and smaller eddies	$m \cdot s^{-1}$
V	volume	m^3
W_f	work of external forces	$kg \cdot m^2 \cdot s^{-2}$
x	quality	–
z_{rod}	number of rods	–

1. Introduction

The expansion to about 11 billion people on our planet by the end of this century [154] comes along with a higher demand of energy and the benefits that it brings: improved standards of living, better health and longer life expectancy, improved literacy and opportunity, and many other benefits. In our days, energy or more specifically electricity is produced mainly by greenhouse-gas-emitting sources like oil, coal or gas. The largest share of non-greenhouse-gas-emitting sources (about 16%) is nuclear energy. Only expanding the distribution of different sources does not help climate change or depleting fossil fuel sources. To continue the benefit of nuclear energy, new systems are required to replace plants as they retire. In the latter part of this century, the environmental benefits of nuclear energy can expand and even extend to other energy products besides electricity [33, p. 1-10].

Besides the challenge of climate change, there is also to mark out nuclear waste disposal [50] as well as non-proliferation [17]. In their roadmap from 2002 the Generation IV International Forum (GIF) made out 8 goals in four broad areas of

- Sustainability [2]
- Economics [19]
- Safety and Reliability [1]
- Proliferation Resistance [17] and Physical Protection

In this process, the GIF evaluated a variety of different reactor types and selected six Generation IV systems which are the most promising. During one decade, significant progress on the development of a next generation of reactor technologies has been done [70]. There are three standing groups set up to assess progress versus goals.

- Risk and Safety Working Group (RSWG)
- Proliferation Resistance and Physical Protection Working Group (PRPPWG)
- Economic Modeling Working Group (EMWG)

Several temporal task forces have also been formed among these work groups. For example, RSWG members play key roles in the SFR Safety Design Criteria (SDC) Task Force. Following the nuclear accident at Fukushima-Daiichi in 2011 ([7], [107]), the Task Force

Generation IV System	Acronym
Gas-Cooled Fast Reactor System	**GFR**
Lead-Cooled Fast Reactor System	**LFR**
Molten Salt Reactor System	**MSR**
Sodium-Cooled Fast Reactor System	**SFR**
Supercritical-Water-Cooled Fast Reactor System	**SCWR**
Very-High-Temperature Reactor System	**VHTR**

Tab. 1.1: GEN-IV systems [33]

ensured that the lessons learned from the event were incorporated into their report, with particular emphasis on external events. GIF expects that the SFR activity will provide an SDC template for the other five reactor systems [70].

The sodium cooled fast reactor (SFR) is the most mature type of fast reactor [82] that has been being investigated. There are different types of SFR around the world which can be classified in pool-type and loop-type reactors. As it is considered to be the most promising reactor type to meet GEN-IV goals, the SFR has been selected for fast reactors by the United States of America, France and Japan [128].

Considering all the results obtained in the various national and international work-programs, French actors CEA, AREVA and EDF have decided to focus their effort on the SFR technology. They consider that it does have potential for improvement, culminating in a GEN-IV design on both safety and economic criteria [128].

Within safety requirements for the fast reactor (FR) system, passive safety plays a major role in GEN-IV systems. Here, research on PHENIX reactor tests are used to qualify tools to advance further [145].

1.1 Motivation

For sodium cooled fast reactors (SFR) of the next generation (GEN-IV), further cost reduction is required, which shall be accomplished by structural simplification and the power increase. To achieve this goal, thermal-hydraulic challenges will be increased progressively, and studies in this field have an important role in the design of SFR. The optimization of thermal-hydraulics directly support the geometrical arrangement at given structural loading constraints and operating conditions. The existence of steep temperature gradients in the primary circuit of SFR gives rise to thermal mixed convection flows or thermally stratified flows. Flow velocities result from pressure gradients and volume forces induced by density gradients. For the design of SFR primary and secondary circuits, comprehensive knowledge about velocities and temperatures is crucial in both, steady state and transient conditions.

One of the advantages of SFR is the possibility of passive decay heat removal based on natural convection effects. Depending on the safety requirements and situation, active and passive decay heat removal systems can be used within present or past SFR applications. During the EFR project [135], [77], the main strategy for decay heat removal had been based on direct reactor cooling (DRC). For that reason, immersed coolers were positioned in the hot plenum. On the primary side of the DRC system, interaction between the immersed coolers and the hot plenum is the major thermal-hydraulic problem to be addressed. When decay heat shall be removed and the primary pumps are still in operation, a mixed convective regime occurs in the hot plenum with sodium, cooled by the DRC system flowing downwards. A direct interaction on the global flow behavior in the hot plenum is observed. The whole transient procedure includes an initial thermal stratification in the hot plenum which will influence the later interaction between the immersed coolers and the hot plenum flow. If the primary pumps are stopped and decay heat shall be removed, a natural circulation occurs and scram is triggered. To demonstrate the reliability of those systems in case of for example a total station black-out, the DRC system operating under natural circulation is a key point [145].

In comparison to water, the thermal conductivity of sodium is about 100 times larger. Consequently, the heat transfer coefficient of sodium is far larger than the one of water. It requires dedicating heat transfer studies for thermal and mechanical behavior of the SFR like thermal-hydraulic applications. In a nominal state, a SFR works at temperatures of about $525°C$ in the hot plenum while the cold plenum has a temperature of about $385°C$. Therefore, thermal studies should focus on temperature differences that can cause thermal fatigue. Thermal stratification depends on a number of parameters, for example pool geometry, operational and thermal-hydraulic conditions [97]. Heat transfer problems due to thermal stratification have to be respected in design and have been studied in previous thermal-hydraulic analysis [24], [145].

To elaborate thermal-hydraulics in nuclear power plant applications, a huge number of data has been gathered since the 1950s [81]. Not only to get a better understanding of thermal-hydraulic behavior of nuclear power plants but also to provide necessary data for modeling, for example through the development of computational codes. Computational codes are being continuously developed and grow in quality with computational power and knowledge in thermal-hydraulics [114]. For accident scenarios, more and more physical phenomena need to be observed, assessed and modeled in thermal-hydraulic computational codes. According to Petruzzi and D'Auria [114], thermal-hydraulic computational codes give a hint of the state of knowledge in thermal-hydraulics. To cover all occurring phenomena in computational simulation methods, scales and approximations are of high influence. As computational power is not unlimited, methods that support the highest resolution for thermal-hydraulic effects cannot be used exclusively to simulate an entire nuclear power plant [127]. To cover such a large field, strengths of individual approaches have to be combined [23]. Hence, different methods still have to be developed, assessed, extended and adapted for GEN-IV reactor types as well as for advanced reactor types. One factor that extends the research field significantly is the large number of different coolants used in reactor types of GEN-III(+) and GEN-IV. Each coolant has its own significant, individual thermal-hydraulic behavior.

Among all the GEN-IV concepts, the SFR has by far the greatest development and deployment history starting from 1950s [127],[128]. Especially in pool-type SFR, the thermal-hydraulic challenges lie in the pools' fluid mechanics. A wide range of different needs and tools is shown in [145]. Beginning with subassembly thermal-hydraulics, scales grow to core, upper and lower plenum or hot and cold plenum, decay heat removal, gas entrainment and piping thermal-hydraulics. To address these phenomena, the International Atomic Energy Agency (IAEA) launched a Coordinated Research Project (CRP) named "Benchmark analyses on the natural circulation test performed during the PHENIX end-of-life experiments" [59] to further study and develop tools for the more accurate prediction of such phenomena with simulation methods. Additionally, in 2010, the large-scale integrated research project THINS (Thermal-Hydraulics of Innovative Nuclear Systems) was launched in the 7th Framework Program FP7 of the European Union [27]. One part of the project is devoted to code coupling of system thermal-hydraulic codes to computational fluid dynamics codes and their qualification with the purpose to improve numerical engineering tools for design analysis of innovative nuclear systems. The focus lies on three-dimensional effects as they appear in pool type reactors and cannot entirely be represented by system thermal-hydraulic codes.

In case of system thermal-hydraulics codes, many reference codes have been developed for light water reactor (LWR) applications. Those codes had to be extended to address needs in focus of GEN-IV applications. One of them is the German system thermal-hydraulics code ATHLET [78]. As the ATHLET code had been developed and validated for LWR applications, one task within the framework of the THINS project is its qualification for sodium applications. A second task within this work is the development of a coupling methodology for the codes ATHLET and OpenFOAM (CFD) and coupled calculations of the CRP "Benchmark analyses on the natural circulation test performed during the PHENIX end-of-life experiments" [59].

1.2 Objective

The "Benchmark analyses on the natural circulation test performed during the PHENIX end-of-life experiments" has also been used during the **THINS** (**T**hermal **H**ydraulics in **I**nnovative **N**uclear **S**ystems) European FP7 project to qualify simulation tools [27]. The objective of this work in the field of development is to receive new multi-scale computational solutions to the PHENIX natural circulation test (PHENIX NCT). A coupled multi-scale solution combines the advantages of different classes of codes (here system thermal-hydraulics (STH) and Computational Fluid Dynamics (CFD)) and provide design tools with feasible efficiency. Qualification of the individual codes, the coupled code methodology and solutions is required here.

PHENIX natural circulation test

The PHENIX NCT [59] is described in two steps. First, the primary circuit is presented to get an idea of the geometrical complexity. Second, the conditions of the natural circulation test are described.

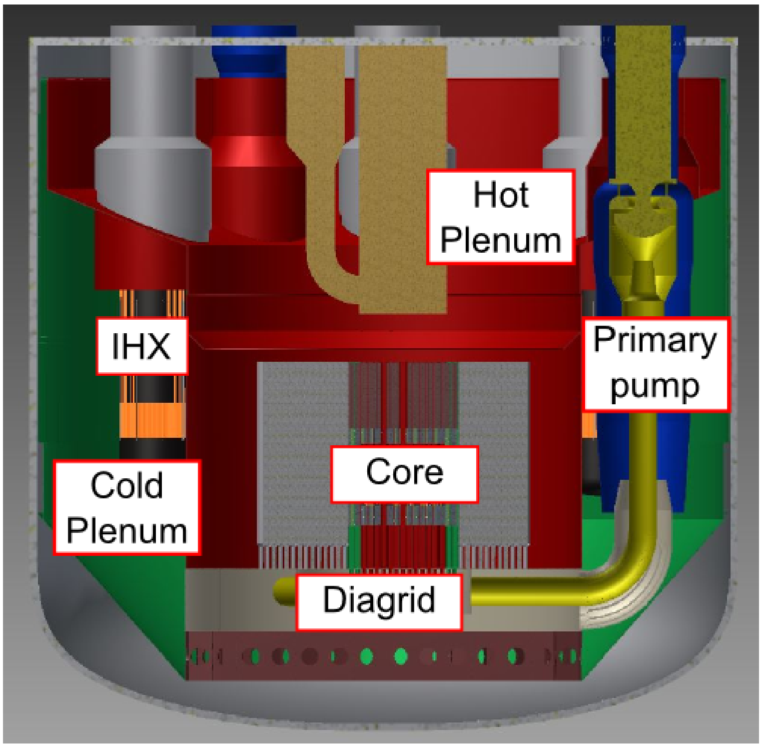

Fig. 1.1: Overview of the PHENIX reactor primary circuit

The PHENIX reactor's primary circuit

The PHENIX reactor is a pool-type liquid metal fast breeder reactor cooled with liquid sodium. The primary pumps (PPs) and intermediate heat exchangers (IHXs) are immersed in the reactor vessel (RV). Fig. 1.1 shows a general overview of the PHENIX reactor, and Fig. 1.2 shows the top view of the RV. The PHENIX power plant consists of the primary circuit with three PPs (PP1, PP2, PP3) and two IHXs next to each PP.

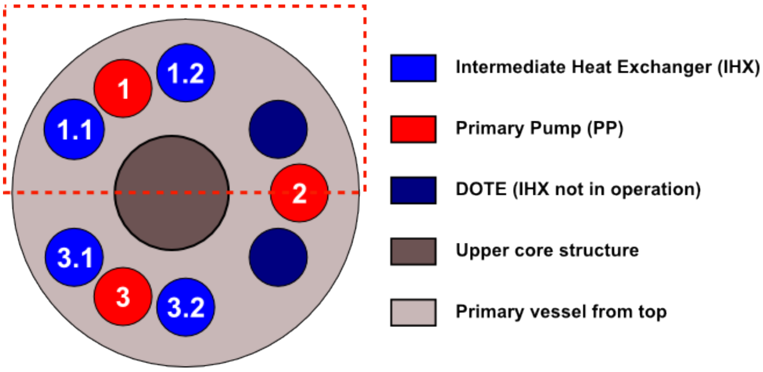

Fig. 1.2: Top view of the PHENIX reactor primary circuit

There are two IHXs connected to each of the intermediate circuits. The RV is composed of a hot plenum (fig. 1.1, red colored) and a cold plenum (fig. 1.1, green colored). The plena are separated by an internal vessel structure. Cold sodium exiting the three PPs enters the diagrid, a large mixing chamber located below the core, and goes vertically upwards through the coolant channels inside the sub-assemblies. The fluid is heated up along the core height, and leaves the core to the hot plenum, where the inlets of the IHXs are located. Hot sodium enters the IHXs and flows vertically downwards to the IHXs' outlet through the primary side. The intermediate side's flow direction is opposite (vertically upwards), so that cold sodium is heated up by the primary side's sodium in counter current flow. The primary side's sodium exits the IHXs to the cold plenum, which is another large volume like the hot plenum. There it enters the PP inlets. The flow circuit is closed by the PPs. Approximately 90% of primary sodium flows through the described circuit while the remaining 10% of sodium mass flow bypasses the core. It flows directly from the diagrid through the vessel cooling system to the cold plenum. The vessel cooling system can be described as covering the outer hull of the cold plenum from geometrical point of view. For the NCT, it should be mentioned, that one intermediate circuit is switched off. The connected IHXs are called DOTE (see fig. 1.2). They are inactive, such that the mass flow of primary sodium does not go through these IHXs.

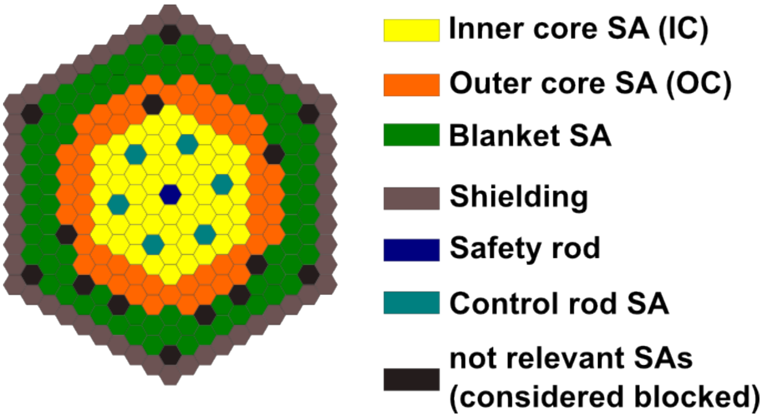

Fig. 1.3: Core configuration of the PHENIX reactor

As shown in fig. 1.3, the PHENIX core consists of several zones. The inner core (IC) in the fissile zone contains 54 fuel subassemblies (SA). The outer core (OC) in the fissile zone contains 56 fuel subassemblies. The fertile zone contains 86 blanket subassemblies. The steel reflector contains 212 subassemblies and there are 6 control rod subassemblies. The total power generated in the core of the PHENIX reactor at nominal operation is $350\mathrm{MW_{th}}$. For the PHENIX NCT[1], the reactor has been operated at a lower power of $120\mathrm{MW_{th}}$. Correspondingly, the core flow rate was reduced to $1280\frac{\mathrm{kg}}{\mathrm{s}}$ from its nominal state of $1988\frac{\mathrm{kg}}{\mathrm{s}}$. Tab.1.2 summarizes the steady state distribution of power and flow rate for different zones in the core at $120\mathrm{MW_{th}}$. In addition to the previously mentioned five zones, an in-containment fuel storage zone with an extra thermal power of 1.7MW is considered a part of the core. $30\frac{\mathrm{kg}}{\mathrm{s}}$ out of the total $1280\frac{\mathrm{kg}}{\mathrm{s}}$ core mass flow is distributed to the fuel storage zone. The position, however, is outside the provided geometry, so for CFD purposes later on, it is considered a part of the Blanket zone. In ATHLET, it is considered as separate part, as parallel geometries, connected to the same previous and following control volumes, which cannot be placed in different horizontal coordinates. For the model, it must be mentioned that the STH model is of half geometrical scale. Mass flow and power are cut half for that case.

Parameter	Power [MW]	Mass flow $[\frac{\mathrm{kg}}{\mathrm{s}}]$
inner core	62.023	554
outer core	49.063	501
fertile zone	8.263	149
steel zone	0.411	41
control rods	0.240	9
in-containment fuel storage zone	1.7	30
total	121.7	1284

Tab. 1.2: Power distribution at initial state of transient ($120\mathrm{MW_{th}}$)

The PHENIX natural circulation test conditions

Time	Action
0s	Dry out of steam generators in intermediate circuit 1 and 3; No change in pumps speed (PPs at 350rpm, intermediate pumps at 390rpm)
458s	Scram; intermediate pumps 1 and 3 rotation speed automatically reduced to 110rpm in 1min
466s	Stop of the three PPs on inertia
4080s	intermediate pumps rotation speed reduced to 100rpm (back-up motors)
10320s	Steam generators in intermediate circuit 1 and 3 cooled by air
24300s	End of test

Tab. 1.3: Schedule of PHENIX NCT [59]

---

[1] As the NCT had been considered a blind test, only very few conditions were given at the beginning of the benchmark exercise. After running the system thermal-hydraulics code ATHLET, more information has been received and will be given here for better understanding.

The test scenario is described in tab. 1.3. Before the start of the transient scenario, the reactor is operating in steady state at a power of 120MW$_{\text{th}}$. The three PPs as well as two of the three intermediate circuits are in operation. The transient is initialized by manual dry out of the steam generators (secondary side), that connected to the two running intermediate circuits (s.a. fig. 1.2, intermediate circuit number 1 and 3). Here, water in the steam generators is evaporated and given to the environment on top of the steam generators, instead of being condensed after driving the turbines. The inlet temperature of the IHXs intermediate side increases consequently as shown in fig. 1.4(a) and following, the temperature difference between the primary and intermediate side of the IHXs decreases. At the time of 458s, the temperature difference at the IHXs inlets decrease to $15°C$, the reactor is manually scrammed (reactor power is as shown in fig. 1.4(c) and (d)). The rotational speeds of the intermediate circuits' (1 and 3) pumps decrease automatically to 110rpm. In this transient scenario, the intermediate pumps rotational speed decreases to 100rpm. In this transient phase, no significant heat sink is present. At 10320s, the steam generator casings are opened on both ends, and the steam generators are cooled by air so an effective heat sink is added. The scenario ends at 24300s. More detailed information about the PHENIX NCT can be derived by [59], [147] and [129].

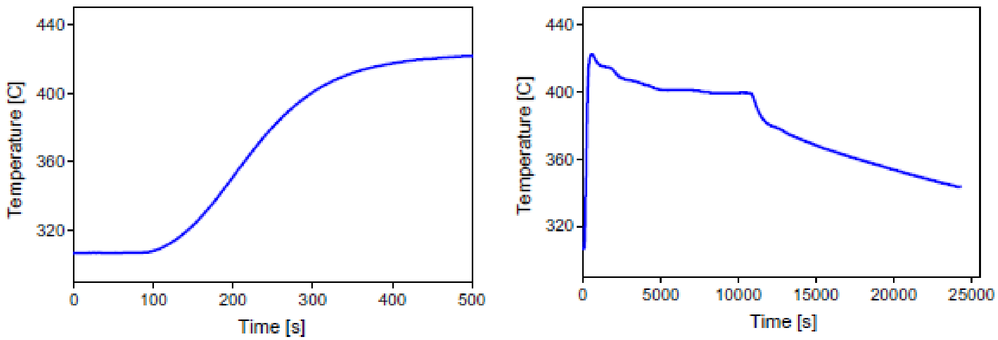

(a) IHX secondary side inlet temperature (short term)

(b) IHX secondary side inlet temperature (long term)

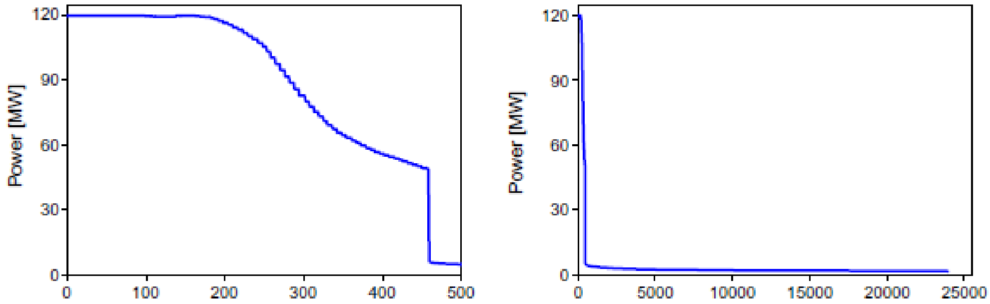

(c) Thermal power (short term)

(d) Thermal power (long term)

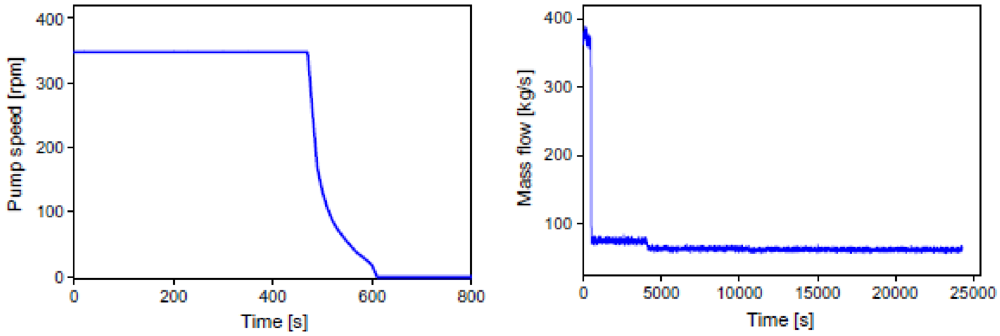

(e) Primary pump speed

(f) IHX secondary mass flow

Fig. 1.4: Boundary conditions of the PHENIX NCT primary circuit (time tables) [59]

1.3 Structure of this thesis

Chapter 1 shows the motivation and objective of this thesis.

Chapter 2 of this thesis provides necessary background information that is required within the following chapters. Theoretical approaches are introduced from literature. The chapter begins with the description of basic field equations that are fundamental in fluid mechanics. Dimensionless numbers are used to compare results between different applications. Forced, mixed and natural convection are states reached in the PHENIX NCT. Basic field equations are used to describe the STH approach and its implementation in the ATHLET code. Afterwards, starting from basic field equations, the CFD approach is introduced and its implementation in the OpenFOAM opensource CFD software package is presented. The last part of this chapter is a summary about different existing approaches of STH/CFD coupling methodologies.

Chapter 3 shows the modification and qualification of the ATHLET code for sodium applications. It is divided in three parts:

- Material properties
- Heat transfer
- Pressure drop

After the implementation of material properties of sodium, the modifications of heat transfer and pressure drop are considered uncorrelated so that each one has its own implementation and verification process. The "ATHLET modification" chapter is concluded by a discussion of the impact on the simulation results of the PHENIX NCT which is used for validation of coupled calculations later on.

Chapter 4 begins with the description of the development process for the hot plenum of the PHENIX primary circuit. Then, steady state conditions are shown and mesh independence is discussed for this individual, specific case. The chapter is concluded by the transient calculation of the PHENIX NCT (standalone), where numerical details (CFD specific) are shown.

Chapter 5 introduces the developed coupling approach beginning with the methodology and concluded with a theoretical verification example.

Chapter 6 shows the coupled solution of the PHENIX NCT with the hot plenum represented in CFD. The impact by only one of the two large volumes on the global solution is shown and discussed.

Chapter 7 provides an application example and its coupled solution.

Chapter 8 & 9 give a conclusion of this thesis and possible future fields of research and development (R&D).

2. Background

Since the 1950s, computational codes are being developed for nuclear applications. The growing importance is discussed in [81]. In general, computational codes can be categorized in different groups, which can be given to:

- Reactor physics codes
- Fuel behavior codes
- Thermal-hydraulic codes, including system codes, sub-channel codes and computational fluid dynamics codes
- Containment analysis codes
- Atmospheric dispersion dose codes
- Structural codes

According to [58], each category contains highly sophisticated codes, the combination of codes from different categories would consequently reduce uncertainty or errors associated with the transfer of interface data and improve the accuracy of calculation results. One way to combine two or more codes is their integration. In general, an integrated code means a new code, in which two or more codes are merged and a new structure is created [58]. This method may lead to good functionality and highly optimized code systems but on the other hand also blocks development or integration of further codes to the system as the recent code structure has to be re-assessed or even rewritten completely. Coupled codes on the other hand interconnect existing codes with clear code boundaries, points of data exchange and with separation of input/output as well as restart parts and data files [58]. Coupling of codes is usually done by coupling of a thermal-hydraulic code and other disciplines according to the objective of the coupling. After [58], they can be categorized into three broad groups:

- 3D neutron kinetics/thermal-hydraulics
- System behavior and local behavior
  - System thermal-hydraulics / core thermal-hydraulics (sub-channel)
  - Thermal-hydraulics / fuel behavior
  - STH/CFD

- Thermal-hydraulics / mechanical behavior

The approach of this present work is to couple STH and CFD. As the objective is the modeling and simulation of the PHENIX NCT (s.a. chapter 1.2), preliminary steps have to be fulfilled. The ATHLET code has initially been developed for water application but not for other coolants. Consequently, the STH code must be qualified for sodium applications. Additionally, water applications like pressurized water reactors (PWR) lack in their description of large volumes as they appear in pool-type sodium-cooled fast reactors (SFR). As STH codes generally use a 1D approach, some difficulties may appear when 3D phenomena occur due to non-symmetrical situations or important buoyancy effects and thermal stratification as discussed in [127]. In the framework of this approach the PHENIX hot plenum is considered as such.

2.1 Basic Field Equations

In thermal-hydraulics, physics are modeled in approaches of different magnitude and severity. A brief overview of fundamental physics that build the basics for the used codes in this framework, is given here, based on different literature sources. All approaches follow the conservation equations for continuum media:

- Conservation of mass
- Conservation of momentum
- Conservation of energy

Conservation of Mass

The conservation of mass, also known as continuity is fundamental in fluid-dynamic behavior of a continuum. More generally, the change of mass inside the continuum, dependent on time, must equal the sum of mass streaming in and streaming out the continuum. More fundamentally it means, no mass can be created or lost, hence it can be mathematically described as

$$\frac{dm}{dt} = \int\limits_{\Delta V} \frac{\partial \rho}{\partial t} dV, \tag{2.1}$$

where t is time, m is mass, ΔV is a fixed volume, and ρ stands for the density. A continuum can be assumed to be a volume in time. This assumption leads to the consequence that mass can only be transported into or out of the volume at each face of ΔV through the normal component $\rho \boldsymbol{u} \cdot \boldsymbol{n}$ multiplied by the corresponding surface area (A). Following the Gauss' theorem, this results in

$$\int\limits_{\partial V} \rho \boldsymbol{u} \cdot \boldsymbol{n} dA = \int\limits_{\Delta V} \nabla \cdot (\rho \boldsymbol{u}) dV, \tag{2.2}$$

where $\boldsymbol{n}$ is the unit vector orthogonal to each face of ΔV and $\boldsymbol{u}$ is the velocity vector. For an infinitesimal volume ΔV, eq.(2.1) and eq.(2.2) can be expressed as

$$\frac{\partial \rho}{\partial t} + \nabla \cdot (\rho \boldsymbol{u}) = 0 \tag{2.3}$$

Conservation of Momentum

Newton's second law of motion is used here to derive the momentum conservation equation. There are different ways to derive the momentum conservation equation, e.g. [121], [103].

If Newton's second law of motion is applied to a fluid passing through a volume that is infinitesimal and fixed (unit volume), the equation can be written as

$$\frac{\partial(\rho \boldsymbol{u})}{\partial t} + \nabla \cdot (\rho \boldsymbol{u} \otimes \boldsymbol{u}) = \boldsymbol{f}_B + \nabla \cdot \boldsymbol{\Pi}_{ij} \tag{2.4}$$

$\otimes$ is the outer product of two vectors (in eq.(2.4), the velocity $\boldsymbol{u}$). The first term describes the increase of momentum per unit volume. The second term describes the rate of momentum transferred through the surface by convection per unit volume. $\boldsymbol{f}_B$ can mainly be represented by body forces like gravity. The second term on the right-hand side represents surface forces per unit volume, which basically include pressure as well as normal and shear stresses, represented by the stress tensor $\boldsymbol{\Pi}_{ij}$. Eq. (2.4) gives a very general description of the momentum equation. If shear stress is applied to *Newtonian fluids*, stress at a point is linearly dependent on the raise of strain (deformation) of the fluid. The assumption of *Newtonian fluids* gives the possibility to derive a general deformation law that relates the stress tensor to the pressure and velocity components.

$$\boldsymbol{\Pi}_{ij} = -p\delta_{ij} + \boldsymbol{\tau}_{ij} \tag{2.5}$$

The expression δ_{ij} in eq.(2.5) is the Kronecker delta function. δ_{ij} is equal 1 in case of $i = j$ and it is equal to 0 in case of $i \neq j$. τ_{ij} represents the *viscous* stress tensor. With the previous assumption of *Newtonian fluids*, the *viscous* stress tensor can also be written as

$$\boldsymbol{\tau}_{ij} = 2\mu \boldsymbol{S}_{ij} - \left(\frac{2}{3}\mu \nabla \cdot \boldsymbol{u}\right) \boldsymbol{I}, \tag{2.6}$$

where I is the unit tensor and $\boldsymbol{S}_{ij}$ the strain rate (deformation) tensor.

$$\boldsymbol{S}_{ij} = \frac{1}{2}\left(\nabla \boldsymbol{u} + (\nabla \boldsymbol{u})^T\right) \tag{2.7}$$

If cartesian coordinates are used with index notation, the viscous stress tensor can be written as

$$\boldsymbol{\tau}_{ij} = -\frac{2}{3}\mu \frac{\partial u_j}{\partial x_j}\delta_{ij} + \mu \left(\frac{\partial u_i}{\partial x_j} + \frac{\partial u_j}{\partial x_i}\right). \tag{2.8}$$

Substitution of eq.(2.8) and eq.(2.5) into eq.(2.4), the *Navier-Stokes equation* is obtained in coordinate-free form

$$\frac{\partial(\rho \boldsymbol{u})}{\partial t} + \nabla \cdot (\rho \boldsymbol{u} \otimes \boldsymbol{u}) = -\nabla \cdot p\boldsymbol{I} + \nabla \cdot \boldsymbol{\tau}_{ij} + \rho \boldsymbol{g} \tag{2.9}$$

Conservation of Energy

The third conservation law is derived from the first law of thermodynamics. It can be described as the change of energy in a system to be equal to the heat transferred to and the work done on that system. If this law is applied to a fluid passing through an infinitely small and fixed control volume (CV), the equation can be written in coordinate-free conservative form as

$$\frac{\partial}{\partial t}(\rho E_t) + \nabla \cdot (\rho \boldsymbol{u} E_t) = \nabla \cdot (\lambda \nabla T) + \nabla \cdot (\boldsymbol{\Pi}_{ij} \cdot \boldsymbol{u}) + W_f + Q_H \tag{2.10}$$

where E_t is the total energy per unit mass. E_t can further be described as the sum of internal energy e and kinetic energy per unit mass.

$$E_t = e + \frac{\boldsymbol{u}^2}{2} \tag{2.11}$$

The first term on the left-hand side of eq.(2.10) describes the rate of change of E_t in a control volume. The second term on the left-hand side of eq.(2.10) characterizes the rate of total energy transported by convection through the control volume's surface. The right-hand side of eq.(2.10) starts with the term describing diffusion of heat in a material due to molecular thermal conduction based on Fourier's law of heat conduction $-\lambda \nabla T$. T is considered the absolute temperature and λ the thermal conductivity coefficient. The second term on the right-hand side describes work done on the fluid due to internal stresses acting on the surface of the control volume. The last two terms are W_f, work of external forces and Q_H, a given heat source. The external force W_f is given by

$$W_f = (\rho \boldsymbol{g} + \boldsymbol{F}_B) \cdot \boldsymbol{u} \tag{2.12}$$

With the total enthalpy H

$$H = e + \frac{p}{\rho} + \frac{\boldsymbol{u}^2}{2} = h + \frac{\boldsymbol{u}^2}{2} = E_t + \frac{p}{\rho} \tag{2.13}$$

where h is the enthalpy of the fluid. Clarifying the term $\nabla \cdot (\boldsymbol{\Pi}_{ij} \cdot \boldsymbol{u})$, the energy conservation equation eq.(2.10) can be described as

$$\frac{\partial}{\partial t}(\rho H) + \nabla \cdot (\rho \boldsymbol{u} H) = \frac{\partial p}{\partial t} + \nabla \cdot (\lambda \nabla T) + \nabla \cdot (\boldsymbol{\tau}_{ij} \cdot \boldsymbol{u}) + W_f + Q_H \tag{2.14}$$

2.2 Dimensionless numbers in fluid mechanics

For the description of flow behavior, information of velocities, temperatures and pressure are necessary. However, for a given experiment or calculation those quantities are dependent on the volume and time schedule of a given transient. If the experiment was reproduced with half the fluid volume but same shape, it may be hard to directly compare the results as they depend on dimension. For that reason, it is of high benefit, if experimental results and simulation results can be presented in non-dimensional form and additionally some dimensional dependent results are given. Dimensionless numbers are often received by ratio of values of the same dimension. These are described by the *similarity theory*, as given in [36], [130].

Reynolds number

[159] describes the Reynolds number to be the ratio of internal forces to diffusive forces.

$$\mathrm{Re} \equiv \frac{\rho \cdot u \cdot L}{\mu} = \frac{u \cdot L}{\nu} \tag{2.15}$$

In eq.(2.15) L represents the characteristic length, ρ the fluid density, u the velocity, μ the dynamic viscosity and ν the kinematic viscosity. If the term on the right hand side of eq.(2.15) is multiplied by $\frac{\rho \cdot u \cdot L}{\rho \cdot u \cdot L}$, the ratio of inertial forces to viscous forces is presented directly [8]. Reynolds numbers < 2300 indicate laminar flow, while Reynolds numbers > 4000 indicate turbulent flow. The range $2300 < Re < 4000$ is called transition flow. For further information, please refer to [130].

Grashof number

The Grashof number describes the ratio between buoyancy and viscous forces. In thermal-hydraulics, the Grashof number (Gr) is used instead of the Reynolds number for the description of flow at natural convection.

$$\mathrm{Gr} \equiv \frac{g \beta \left(T_{wall} - T_{bulk}\right) L^3}{\nu^2} \tag{2.16}$$

On the right hand side of eq.(2.16), g represents the gravity vector, β is the volumetric thermal expansion coefficient, T_{wall} is the fluid surface temperature at the (heated) wall, T_{bulk} is the bulk temperature and ν the kinematic viscosity. More detailed information about the Grashof number is given in [159].

Prandtl number

The Prandtl number describes the ratio of momentum diffusivity (kinematic viscosity) to thermal diffusivity

$$\mathrm{Pr} \equiv \frac{\nu}{\alpha} = \frac{c_p \cdot \mu}{\lambda} \tag{2.17}$$

where α is the thermal diffusivity

$$\alpha = \frac{\lambda}{\rho c_p} \tag{2.18}$$

In comparison to the Reynolds (Re) and Grashof (Gr) number, the Prandtl (Pr) number only depends on the material properties of the fluid and its state, but not on geometry. For more detailed information about the Prandtl number, please refer to [159].

Péclet number

In case of thermal-hydraulics, the Péclet number describes the ratio of advective transport rate to diffusive transport rate

$$\mathrm{Pe} \equiv \frac{u \cdot L}{\alpha} = Re \cdot Pr \tag{2.19}$$

It can also be received as the product of Reynolds (Re) number and Prandtl (Pr) number. It is often used as basis for the description and presentation of heat transfer phenomena. More detailed information about the Péclet number is given in [113].

Nusselt number

The Nusselt number is defined as the ratio of convective heat transfer to conductive heat transfer,

$$\mathrm{Nu} \equiv \frac{(HTC) \cdot L}{\lambda} \tag{2.20}$$

where HTC is the convective heat transfer coefficient, L the characteristic length and λ the thermal conductivity. The Nusselt (Nu) number is used to describe heat transfer across a fluid's boundary (surface). More fundamental information about the Nusselt number can be received from [67]. A further discussion is given in chapter 3.2.

Rayleigh number

The Rayleigh number is associated with buoyancy driven flow (natural convection). It is defined as the product of the Grashof number (see ch.2.2) and the Prandtl number (see ch.2.2). For natural convection near a vertical wall, the definition is

$$\mathrm{Ra} \equiv \mathrm{Gr} \cdot \mathrm{Pr} = \frac{g\beta}{\nu\alpha} \left(T_{wall} - T_{bulk}\right) L^3 \tag{2.21}$$

where T_{wall} represents the temperature at the wall, T_{bulk} the fluid temperature distant to the wall, L the characteristic length (here, distance from the leading edge), β the thermal expansion coefficient, g gravity, ν the kinematic viscosity and α the thermal diffusivity. If the Rayleigh number at a given position L is below a fluid specific critical value, heat transfer primarily occurs in form of conduction. If the critical value is exceeded, convective heat transfer is dominant.

2.3 Types of convection

In thermal-hydraulics heat is transferred in different modes: Conduction, Radiation and Convection. Rohsenow et al. [124] show all of those modes and explain them in detail. Heat transfer by conduction is a diffusive mechanism where heat is transferred on an atomic scale. Convection is the transport of heat by a (moving) fluid through diffusion or advection or a combination of both. Dependent on the fluid flow, it can be classified in forced and natural (or free) convection. Forced convection appears for example when pumps drive the fluid [124]. This can also be interpreted as mechanical force driving the fluid through a circuit. The ratio $\frac{Gr}{Re^2} \ll 1$ indicates forced convection. As soon as the pumps are switched off but heat source and heat sink still keep operational, the fluid is driven by density differences [124]. The ratio can then be given by $\frac{Gr}{Re^2} \gg 1$ and indicates natural convection. In technical applications, forced and natural convection superimpose which leads to mixed convection [103]. Density can be seen as a function of temperature and pressure. In the framework of this thesis, temperature is considered to have the greatest impact. Consequently, the influence of pressure to the (liquid) fluid properties is negligible [45].

2.4 System thermal-hydraulics (STH)

Approximately half a century ago, system thermal hydraulic code development for the analysis of steady state and transient behavior of nuclear applications began. This discipline can be seen as one of the constitutive disciplines in the development of technology for nuclear safety and design. Since the 1960s, its development was forced by the US NRC (Nuclear Regulatory Commission), previously AEC (Atomic Energy Commission) to face nuclear safety needs [34]. ”The word ’system’ became of common use following the OECD/NEA/CSNI (Organization for Economic Co-operation and Development, Nuclear Energy Agency, Committee on the Safety of Nuclear Installations) Conference held in Aix-En-Provence in 1992” according to D’Auria and Galassi [34]. A time scale of development approaches in STH codes and CFD codes is presented in fig. 2.1. It also shows the benefit of increasing computational power so that the number of numerical operations (number of CVs times involved equations per CV) for one problem can be increased to receive a better representation, higher accuracy and more detailed information.

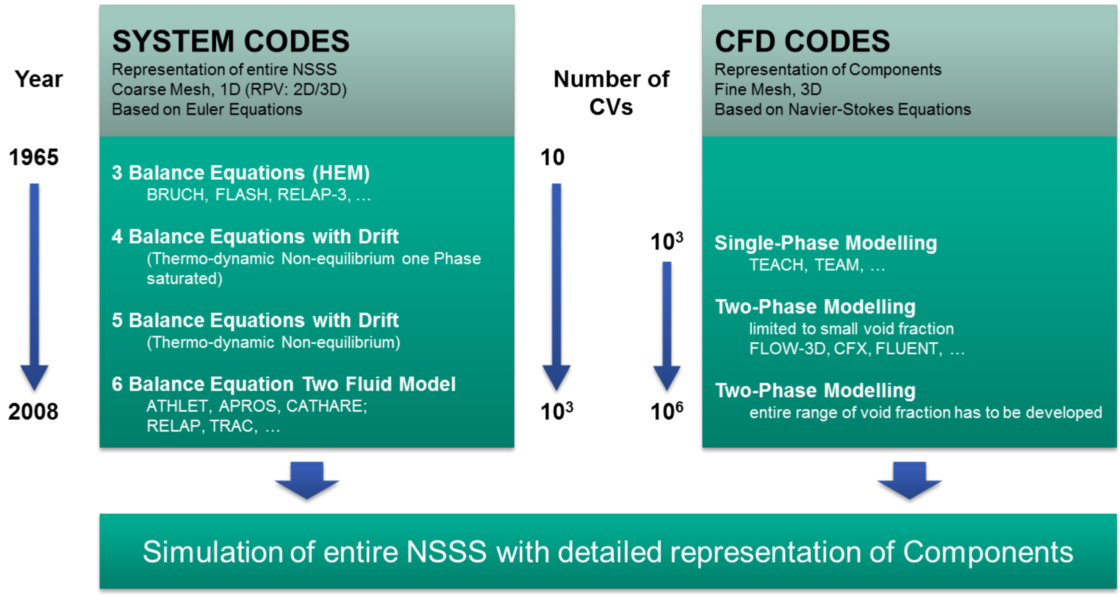

Fig. 2.1: Thermal-hydraulic Codes - Code Development Activities [161]

STH analyses involve the solution of transport equations of mass, momentum and energy. Depending on the necessary level of resolution, this can be achieved through the solution of general equations in space and time as well as the nature of involved media's properties, and numerical accuracy required for the analysis. The medium can be considered a continuum which can be divided in smaller (discrete) volumes. These volumes must be large enough to permit macroscopic scale [76], so average values are still representative at each point of the system. Temperature, velocity, density and pressure can thus be given by scalars.
Two approaches are commonly used for the development of transport equations (see tab. 2.1). A system of specific region or mass can be described with the *integral* approach. If the system is more complex, a chain of compartments can be built using a *lumped parameter integral* approach. To obtain the integral equations, spacial distributions of the field variables and transport parameters within each compartment are ignored. On the other hand, for the *distributed parameter integral* approach, spacial dependence of the variables within the continuum is taken into consideration to obtain the equations. In contrast to the *integral* approach, the *differential* approach is exclusively a distributed parameter approach with balance equations for each point instead of an entire region. When the *integral* approach is used in combination with distributed parameters, its differential equations must be integrated over a volume. More information about the numerical approaches can be obtained from Todreas and Kazimi [152].

Integral approach	Differential approach
Lumped parameter	
• Control mass (CM) • Control volume (CV)	
Distributed parameter	
• Control mass (CM) • Control volume (CV)	• Lagrangian equations • Eulerian equations

Tab. 2.1: Classification of transport equations [152]

Those approaches are used in system thermal-hydraulics (STH) computational codes like

- ATHLET (GRS) [80]
- CATHARE (CEA, EDF, FRAMATOME-ANP and IRSN) [146]
- RELAP (U.S. NRC) [149]
- SAS4A/SASSYS-1 (ANL) [42]
- TRAC/TRACE (U.S. NRC) [104], [105], [106]

STH codes have a modular structure. By this means, flow regions like primary and secondary circuits can be assembled. Those codes are of high quality and have been validated during at least the last 30 years. To extend the reliability, performance and range of applications of STH codes, validation benchmark tests are still being conducted. The intension to develop such STH codes was, to replace evaluation model approaches [11] and widen the range of applications for safety and design purposes. Examples of applications are given by Bestion [11]:

- Safety analysis
- Quantification of the conservative analyses margin
- Investigation of Plant Operating Procedures and Accident Management
- Definition and verification of Emergency Operating Procedures
- Investigations for new types of fuel management
- Preparation and interpretation of experimental programs
- Licensing when used together with a methodology to evaluate uncertainties on the code predictions
- Design of new reactors and systems including passive features for the 3$^{\text{rd}}$ and 4$^{\text{th}}$ generations of nuclear power plants (NPPs)
- System code application has often been extended to the field of severe accidents. For this purpose they are coupled with other codes, which model core degradation and fission product release.
- Implementation in Full Scope Plant Simulator: simplified versions were first used to obtain real time simulations and later, thanks to the increasing computer performance, the standard versions were used.

Additionally, Jaeger et al. [63] summarize the capabilities of STH against subchannel and CFD codes. However, the ATHLET code is in focus of this work.

The ATHLET code

The ATHLET code is being developed by the “Gesellschaft für Reaktor- und Anlagensicherheit (GRS) gGmbH”. The following sub-chapters are based on [78], [5] and [79] to give a brief inside. The code provides the analysis of nuclear safety issues like leaks and transients in LWR and is being developed for the analysis of transient plant behavior. The design basis for the ATHLET code are modules for the calculation of different phenomena:

- Thermo-fluid dynamics (TFD)
- Heat transfer and heat conduction (HECU)
- Neutron kinetics (NEUKIN)
- General control simulation module (GCSM)

Temporal integration of the TFD is performed by a general purpose ordinary differential equation (ODE) solver using Forward-Euler and Backward-Euler (FEBE) methods. Solutions of a general non-linear system of differential equations of first order can thus be solved. Generally, the full-implicit option is used. For the linearization of implicit systems, a Jacobian matrix is used.

ATHLET uses the finite-volume method (FVM) for the spatial integration of the conservation equations (see ch. 2.1). The modular network technique used to represent a thermal-hydraulic system is made by assembling basic fluid-dynamic elements, the so-called thermo-fluid-dynamic objects (TFOs). Those TFOs can be classified into three basic categories:

- Pipe objects (simulation of one-dimensional fluid flow)
- Branch objects (simulation of major branchings or mass and energy capabilities, where no dominant flow direction exists)

- Special objects (simulation of components requiring a dedicated model or a macro network configuration)

TFOs are composed by two primitives: CVs and junctions. CVs are interconnected by junctions (see fig. 2.2). Junctions are defined between the centers of adjacent control volumes. This way, a grid is created, where the junction centers are displaced by half a CV length from the CV centers.

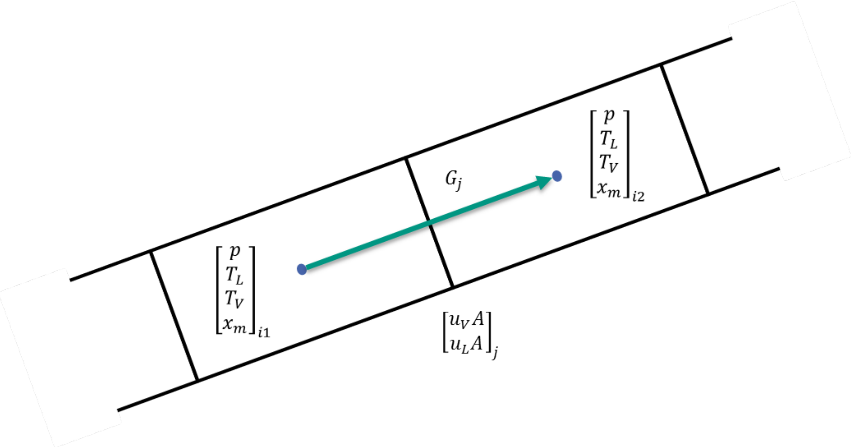

Fig. 2.2: Control Volumes (CVs) and Junctions

The conservation equations given in ch. 2.1 are distributed on the two primitives. For the spacial integration of the mass and energy conservation equations, CVs are used as integration domain. The momentum conservation equation's domain for integration is the junction. Quantities are spatially averaged and are time dependent. CVs are further divided in two different types. The homogeneous CVs, in which the fluid is assumed to be homogeneous and isotropic and mixture level CVs. Mixture level (ML) consist of two homogeneous sub-CVs which are separated by a horizontal mixture level. The mixture level CV can only be used in conjunction with the 5-equation (described after the 6-equation model later on).

The 6-Equation Model

The ATHLET code is one of the state-of-the-art 6-equation codes [127]. With the 6-equation model, two phases can be handled which is prerequisite for LWR applications. The solution variables for pressure p, temperature T_l and T_v (liquid and vapor), mass quality x_m and phase velocities multiplied by total flow area u_lA and u_vA (liquid and vapor) are derived by differential equations.

Conservation of mass in ATHLET 6-equation model

For the conservation of mass (eq. (2.3)) in ATHLET, the 6-equation model has two equations. One equation for liquid and one for vapor with an interconnecting term for the inter-phase mass exchange per unit volume (ψ in eq. (2.22) and eq. (2.23)). The FVM can be applied with some simplifications due to CV topology. If the Gaussian integral law is applied, integration over a CV gives the mass conservation equations for liquid and vapor as

$$\int\limits_{V_i} \frac{\partial\left((1-a)\rho_l\right)}{\partial t} dV + \int\limits_{A_i} (1-a)\rho_l \boldsymbol{u}_l d\boldsymbol{A} = -\int\limits_{V_i} \psi dV \tag{2.22}$$

$$\int\limits_{V_i} \frac{\partial(a\rho_v)}{\partial t} dV + \int\limits_{A_i} a\rho_v \boldsymbol{u}_v d\boldsymbol{A} = \int\limits_{V_i} \psi dV \tag{2.23}$$

After performing the integration, the following (simplified) equations can be used. All vectors disappear and averaged (scalar) values over the CV are used. Through this, the computational effort is simplified significantly. The steam void fraction a used in eq. (2.22) and eq. (2.23) is defined by

$$a = \frac{V_v}{V} = \frac{m_v \rho_v^{-1}}{m_v \rho_v^{-1} + m_l \rho_l^{-1}} \tag{2.24}$$

This way, the mass balance for a given CV can be described as

$$\begin{aligned} \frac{dm_l}{dt} &= \sum_{in} G_l - \sum_{out} G_l - \Psi \\ \frac{dm_v}{dt} &= \sum_{in} G_v - \sum_{out} G_v + \Psi \end{aligned} \tag{2.25}$$

where G_l is the liquid mass flow rate, G_v the vapor mass flow rate and Ψ the inter-phase mass transfer rate. In both equations for the mass flow rate, a is derived from eq. (2.24). Further information can be obtained by Austregesilo et al. [5].

Conservation of Momentum in ATHLET 6-equation model

Like the mass conservation equation, the momentum conservation equation (eq. (2.9)) also has one liquid and one vapor part in ATHLET. For the liquid phase, it is

$$\begin{aligned} &\frac{\partial\left(\left(1-a\right)\rho_l \boldsymbol{u}_l\right)}{\partial t} + \nabla\left(\left(1-a\right)\rho_l \boldsymbol{u}_l \boldsymbol{u}_l\right) + \nabla\left(\left(1-a\right)p\right) = \\ &+\boldsymbol{\tau}_i - \left(1-a\right)\boldsymbol{f}_{wall} - \psi \boldsymbol{u}_\Psi - \left(1-a\right)\rho_l \boldsymbol{g} + a\left(1-a\right)\left(\rho_l - \rho_v\right)\boldsymbol{g} d_h \nabla a \\ &+a\left(1-a\right)\rho_m \left(\frac{\partial \boldsymbol{u}_r}{\partial t} + \nabla \boldsymbol{u}_r\right) + S_{I,l} \end{aligned} \tag{2.26}$$

where $S_{I,l}$ is the momentum source for the liquid phase and $S_{I,l}$ the momentum source for the vapor phase. ψ is the inter-facial mass exchange per unit volume and u_Ψ as the velocity of the interface. The mixture density ρ_m is defined as

$$\rho_m = a\rho_v + (1-a)\rho_l \tag{2.27}$$

where the index m stands for mixture. The relative velocity u_r is defined by $u_r = u_v - u_l$. τ_i is the inter-facial shear per unit volume and f_{wall} is the wall shear stress.

$$\begin{aligned} &\frac{\partial\left(a\rho_v \boldsymbol{u}_v\right)}{\partial t} + \nabla\left(a\rho_v \boldsymbol{u}_v \boldsymbol{u}_v\right) + \nabla\left(ap\right) = \\ &-\boldsymbol{\tau}_i - a\boldsymbol{f}_{wall} + \psi \boldsymbol{u}_\Psi - a\rho_v \boldsymbol{g} - a\left(1-a\right)\left(\rho_l - \rho_v\right)\boldsymbol{g} d_h \nabla a \\ &-a\left(1-a\right)\rho_m \left(\frac{\partial \boldsymbol{u}_r}{\partial t} + \nabla \boldsymbol{u}_r\right) + S_{I,v} \end{aligned} \tag{2.28}$$

These momentum equations (eq. (2.26) and eq. (2.28)) can be expressed one-dimensionally as a function of the defined solution variables u_l and u_v. By subtraction of mass balances and division of the momentum equations by flow area and void fraction for liquid or vapor, Austregesilo et al. [5] derive following equation for the liquid phase, where s is the scalar for the distance between boundaries of a CV (see fig. 2.3)

$$\begin{aligned} &\frac{\rho_l}{A}\left(\frac{\partial(u_l A)}{\partial t} - u_l \frac{\partial A}{\partial t} + \frac{A}{2}\frac{\partial(u_l u_l)}{\partial s}\right) + \frac{\partial p}{\partial s} = \\ &a\rho_m \left(\frac{\partial u_v}{\partial t} - \frac{\partial u_l}{\partial t} + \frac{1}{2}\frac{\partial(u_v^2 - u_l^2)}{\partial s}\right) \\ &+a(\rho_l - \rho_v) g sin(\gamma) d_h \frac{\partial a}{\partial s} + \frac{\tau_i}{1-a} - \frac{\psi u_\Psi}{1-a} + \frac{\psi u_l}{1-a} - \rho_l g sin(\gamma) - f_{wall} + \frac{S_{I,l}}{1-a} \end{aligned} \tag{2.29}$$

where A is the cross section of the CV. γ is the inclination angle of the CV and is shown in fig. 2.3. Accordingly the vapor phase

$$\begin{aligned}\frac{\rho_v}{A}\left(\frac{\partial(u_vA)}{\partial t} - u_v\frac{\partial A}{\partial t} + \frac{A}{2}\frac{\partial(u_vu_v)}{\partial s}\right) + \frac{\partial p}{\partial s} &= \\ -(1-a)\rho_m\left(\frac{\partial u_v}{\partial t} - \frac{\partial u_l}{\partial t} + \frac{1}{2}\frac{\partial(u_v^2-u_l^2)}{\partial s}\right)& \\ -(1-a)(\rho_l-\rho_v)gsin(\gamma)d_h\frac{\partial a}{\partial s} - \frac{\tau_i}{a} + \frac{\psi u_\Psi}{a} - \frac{\psi u_v}{a} - \rho_v gsin(\gamma) - f_{wall} + \frac{S_{I,v}}{a}&\end{aligned} \tag{2.30}$$

The integration of the momentum equations is performed over a junction connecting the centers of two adjacent control volumes, "left CV" and "right CV" (fig. 2.3). The positive flow direction is defined from left CV to right CV.

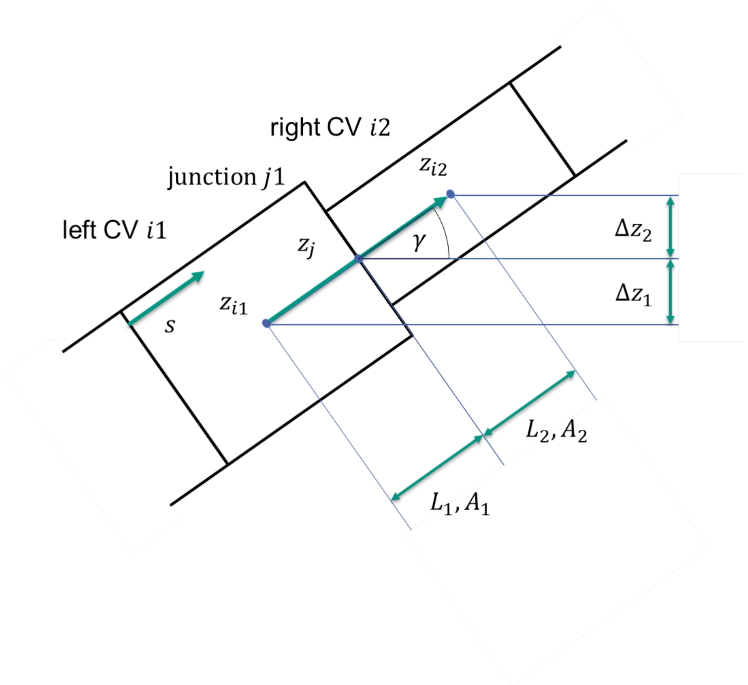

Fig. 2.3: Junction connection of two adjacent CVs

Assumed, that volumetric flow along a junction j_i is constant and flow areas are constant in time, the differential equations can be developed, so that all forces on the phases can be expressed as pressure differences. Pressure drops due to wall friction and inter-facial shear are calculated with constitutive equations as well as the calculations for pump pressure in case of the 6-equation model. Further information about individual equations and calculation handling, please refer to Austregesilo et al. [5].

Conservation of Energy in ATHLET 6-equation model

The energy equation given in eq. (2.14) needs to be adapted for the 6-equation model in ATHLET. Additional terms for phase interaction and phase change need to be applied as well as the one-dimensional approach that is used in ATHLET. Austregesilo et al. [5] give the differential equation for the conservation of liquid energy

$$\begin{aligned}\frac{\partial\left(\left(1-a\right)\rho_l\left(h_l+\frac{1}{2}\boldsymbol{u}_l\boldsymbol{u}_l-\frac{p}{\rho_l}\right)\right)}{\partial t}+\nabla\left(\left(1-a\right)\rho_l\boldsymbol{u}_l\left(h_l+\frac{1}{2}\boldsymbol{u}_l\boldsymbol{u}_l\right)\right)=\\ -p\frac{\partial\left(1-a\right)}{\partial t}+\boldsymbol{\tau}_i\boldsymbol{u}_l+\left(1-a\right)\boldsymbol{\tau}_i\left(\boldsymbol{u}_v-\boldsymbol{u}_l\right)+\left(1-a\right)\rho_l\boldsymbol{g}\boldsymbol{u}_l\\ +\dot{q}_{s,l}+\dot{q}_{i,l}+\psi\left(h_{\psi,l}+\frac{1}{2}\boldsymbol{u}_l\boldsymbol{u}_l\right)+Q_{H,l}\end{aligned} \tag{2.31}$$

and for the conservation of vapor energy

$$\begin{aligned}\frac{\partial\left(a\rho_v\left(h_v+\frac{1}{2}\boldsymbol{u}_v\boldsymbol{u}_v-\frac{p}{\rho_v}\right)\right)}{\partial t}+\nabla\left(a\rho_v\boldsymbol{u}_v\left(h_v+\frac{1}{2}\boldsymbol{u}_v\boldsymbol{u}_v\right)\right)=\\ -p\frac{\partial a}{\partial t}+\boldsymbol{\tau}_i\boldsymbol{u}_v+a\boldsymbol{\tau}_i\left(\boldsymbol{u}_v-\boldsymbol{u}_l\right)+a\rho_v\boldsymbol{g}\boldsymbol{u}_v\\ +\dot{q}_{s,v}+\dot{q}_{i,v}+\psi\left(h_{\psi,v}+\frac{1}{2}\boldsymbol{u}_v\boldsymbol{u}_v\right)+Q_{H,v}\end{aligned} \tag{2.32}$$

In eq. 2.31 and eq. 2.32, h stands for enthalpy, so h_l is the liquid enthalpy and h_v is the vapor enthalpy. The last term on the right hand side of each of the equations is a given internal volumetric heat source per volume $Q_{H,l}$ and $Q_{H,v}$ of the individual CV. There are two more heat sources to each of the equations. $\dot{q}_{s,l}$ is the wall heat flow to the liquid phase per volume of the CV and $\dot{q}_{s,v}$ to the vapor phase respectively. More information about wall heat transfer is given by eq. 2.36 and eq. 2.37 and its description later on. $\dot{q}_{i,l}$ and $\dot{q}_{i,v}$ are the inter-facial heat flow per volume of the CV. Detailed information about the inter-facial heat flow can be found in Austregesilo et al. [5]. By integrating eq. (2.31) and eq. (2.32) over a given CV with volume V_i the ODEs for phase temperatures are obtained.

The 5-Equation Model

The 5-equation approach is based on the 6-equation approach described previously in this chapter. The goal of the 5-equation approach is, to reduce the number of calculations during each time step. This way, calculation time is saved significantly. Instead of six equations, the 5-equation system solves the mass and energy equations in the CVs separately for the liquid and vapor phases. The momentum equation at the junctions is solved for a mixture of liquid and vapor phases. Solution variables of the derived system of differential equations are mass quality, temperature (liquid and vapor) and pressure within the CVs and the mixture mass flow rate G at the junctions. The differential equation for the mixture flow rate is obtained by integration of the global momentum equation (eq. (2.26) and (2.28)) over a junction j connecting two control volumes i_1 and i_2.

$$\frac{dG}{dt}=\frac{1}{\int\frac{1}{A}ds}\left[\Delta p_s+\Delta p_{mf}+\Delta p_r+\Delta p_{grav}+\Delta p_{fric}+\Delta p_\rho+\Delta p_I\right] \tag{2.33}$$

The pressure losses in eq. (2.33) on the right hand side are given in tab. 2.2. The main feature of the 5-eq. model is the consideration of the relative velocity between phases by means of a drift-flux formulation. The phase velocities are calculated by

$$u_l=\frac{G}{A\rho_m}-\frac{a\rho_v u_r}{\rho_m} \tag{2.34}$$

$$u_v=\frac{G}{A\rho_m}+\frac{(1-a)\rho_l u_r}{\rho_m} \tag{2.35}$$

The constitutive equations for the determination of the relative velocity u_r are described by the drift-flux theory [5]. Drift-flux theory provides a one-dimensional description of relative velocity between the liquid and vapor phase of a fluid. The calculation of friction and form losses are described in [5].

Δp_s	$=$	$-\int \frac{\partial p}{\partial x}dx = p(i_2) - p(i_1)$	pressure loss between two CVs
Δp_{mf}	$=$	$-\int \rho_m \vec{u}_m \frac{\partial \vec{u}_m}{\partial x}dx$	momentum flux term
Δp_r	$=$	$-\int \frac{\partial\left(a(1-a)\frac{\rho_l\rho_v}{\rho_m}\vec{u}_r\vec{u}_r\right)}{\partial x}dx$	relative velocity term
Δp_{grav}	$=$	$\int \rho_m \vec{g} dx$	elevation term
Δp_{fric}	$=$	$\int f_{W,m} dx$	friction and form loss pressure drop
Δp_ρ	$=$	$\int \vec{u}_m \frac{\partial \rho_m}{\partial t}dx$	density derivative term
Δp_I	$=$	$\int S_{I,m} dx$	source term, e.g. pump differential pressure

Tab. 2.2: Description of pressure losses in eq. (2.33)

Conjugate Heat Transfer in ATHLET

Heat sources in ATHLET can be given by direct implementation of energy to a CV or by a heat conductor. Heat conductors are modeled one-dimensional in ATHLET. The model characteristics are given by [5] and are determined by energy conservation laws in a CV as given in eq. (2.36).

$$\underbrace{\int_V W \cdot dV}_{\text{Rate of heat generation}} = \underbrace{c_p \cdot \rho \cdot \int_V \frac{\delta T}{\delta t} \cdot dV}_{\text{sensible heat}} + \underbrace{\int_S \boldsymbol{q} \cdot d\boldsymbol{A}}_{\text{heat flow crossing the boundary}} \tag{2.36}$$

If the Gaussian rule for heat flow is applied and substituted in eq. (2.36), the well known Fourier equation can be given in differential form.

$$\frac{\partial T}{\partial t} = \frac{\lambda}{c_p \cdot \rho}\nabla^2 T + \frac{1}{c_p \cdot \rho} \cdot W \tag{2.37}$$

Energy balance is applied to a heat conductor layer as illustrated in fig. 2.4.

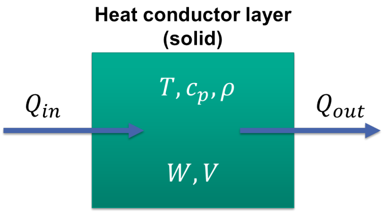

Fig. 2.4: Energy balance for a heat conductor layer [5]

The equation for a simple single layer simulation of a heat conductor can be seen as a basis for more complex calculations of heat transfer in ATHLET. With eq. (2.36), a heat conductor with volume V can be described.

$$\underbrace{Q_{in}}_{\text{Rate of heat flow into the layer}} + \underbrace{W \cdot V}_{\text{Rate of heat generation in the layer}} = \underbrace{Q_{out}}_{\text{Rate of heat flow out of the layer}} + \underbrace{\rho \cdot c_p \cdot V \cdot \frac{dT}{dt}}_{\text{Rate of change of internal energy in the layer}} \tag{2.38}$$

If it is further assumed the distribution of heat generation in the heat conduction volume (HCV) layer to be uniform as well as the temperature T and properties like density, specific heat capacity and specific heat conductivity, eq. (2.38) can be rearranged. Then the time derivative of the temperature in the CV can be written as

$$\frac{dT}{dt} = \frac{1}{\rho \cdot c_p \cdot V} \cdot (Q_{in} + W \cdot V - Q_{out}) \tag{2.39}$$

Different basic geometrical shapes like cylinder, plate and sphere are taken into account. Specific equations can be found in [5]. As an example, an annulus heat conductor geometry is shown in fig. 2.5. The equations can be written as

$$Q_{in} = \frac{2 \cdot \pi \cdot L \cdot (T_{left} - T)}{\frac{1}{htc_{left} \cdot r_{left}} + \frac{1}{\lambda} \cdot ln \frac{r}{r_{left}}} \tag{2.40}$$

for Q_{in} and Q_{out}

$$Q_{out} = \frac{2 \cdot \pi \cdot L \cdot (T - T_{right})}{\frac{1}{htc_{right} \cdot r_{right}} + \frac{1}{\lambda} \cdot ln \frac{r_{right}}{r}} \tag{2.41}$$

The expression htc stands for Heat-Transfer-Coefficient. htcs are obtained experimentally for heat transfer between material and material (solid/solid) as well as material and fluid (solid/fluid). In case of sodium as work-fluid, a group of heat transfer coefficients are being implemented in the ATHLET code within this framework for the PHENIX application (see ch. 3.2).

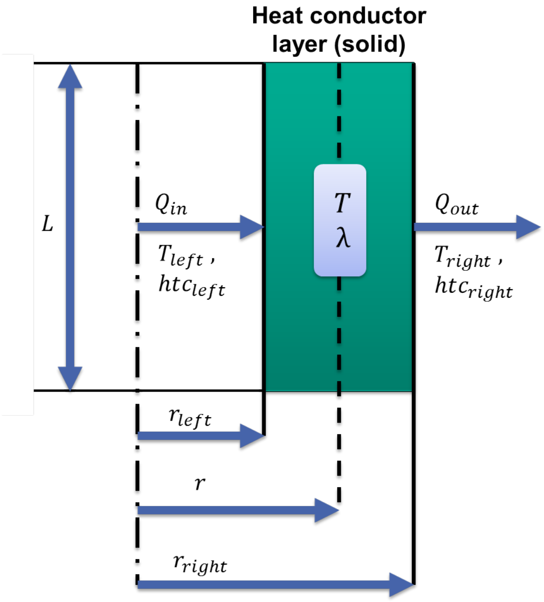

Fig. 2.5: Modeling of a hollow cylinder with one heat conduction layer [5]

2.5 Computational Fluid Dynamics (CFD)

With the increase of computational power during the last half century, also computational fluid dynamics evolved. STH codes as they are described in ch. 2.4 are being developed with large scale CVs. The boundaries of such CVs can be based on the example of a pipe; an inlet, outlet and the pipe's wall. During the last decades, knowledge in fluid dynamics had been gathered and physical effects have been recorded during measurements that could not be described in such large scale STH code applications. With the development of

CAE (Computer-Aided-Engineering) tools that support three-dimensional representation of geometries, the industrial production process is subjected to an accelerated evolution toward the computerization of the whole production cycle, using various software tools [54]. Geometries are no longer split along a given length coordinate, but is filled with CVs that can exchange fluid flow through more than two surfaces. Again, with increase in computational capabilities, the number of CVs can be increased significantly as shown in fig. 2.1.

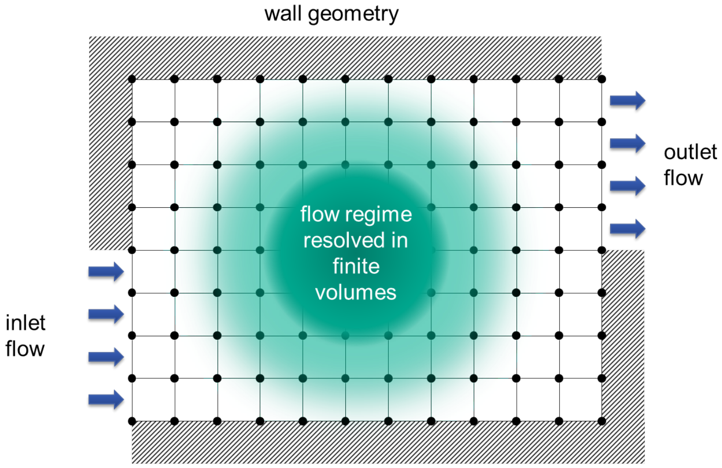

Fig. 2.6: Example of a grid layout in CFD [113]

CFD follows the approach to resolve a given domain in finite volumes (discretization). The domain volume and shape are discretized in small finite volumes (e.g. fig. 2.6). Dependent on the methodology of grid generation, the CVs inside the mesh have specific shapes. This can be cubic, hexahedral or even polyhedral, dependent on the approach used. When a geometry is three-dimensional resolved, the common approach is based on Cartesian coordinates. However, there is no limit so that for example pieces of the geometry can be defined making use of symmetries like rotation or axis. This way, the number of CVs can be reduced significantly which leads to (as of today significantly) smaller calculation time. Shapes of CVs are discussed in [76], [113], [118], [44] and [99] as well as the Finite-Volume-Method (FVM) which is used for such approaches.

With smaller geometrical scales, also time scales shrink. Taking this in consideration, and observing flows at small time scales and small geometrical scales, flows appear not only to be less smooth but even chaotic. A completely smooth flow can be described as laminar. With increase of flow velocity chaotic behavior within the fluid domain grows and can be observed. This behavior is described as turbulent. Turbulence can be described as a state of motion of a fluid. During laminar flow condition, flows can be observed as continuous stream line pattern. However, this state is likely to be instable during all states of flow. Fluid flow motion tends to be instable especially with increase of flow velocity. A small rotation in flow can develop turbulence and can be set in motion aided by a slight disturbance. It can then be observed as a spontaneous vortex motion - probably inside the fluid regime and not near any geometrical boundary. The tendency of fluids to have turbulent behavior can be described with the Reynolds number Re (eq. (2.15)). E.g. in pipe flow, the critical Reynolds number is at about $Re = 2300$ when flows begin to have turbulent behavior. The velocity distribution of turbulent flows is significantly uniform inside the flow regime. Near wall, the velocity profile is reduced sharply in comparison to laminar flow. This behavior is a result of the chaotic turbulent behavior of flow where flow mixing and cross-flows appear. Diffusive effects are increased because of turbulent behavior. After Richardson's notion [123], large eddies are unstable and transfer their

energy to smaller eddies. This process is also known as energy cascade in which energy is transferred successively to smaller eddies until the Reynolds number is sufficiently small. Then, the eddy motion can be considered stable and molecular viscosity is effective in dissipating kinetic energy. This theory gives a good notion of turbulent motion but needs further investigation about the size of the smallest eddies that are responsible for the dissipation of energy. Kolmogorov advanced the theory of turbulence by developing hypothesis. The first hypothesis is about isotropy of small-scale motions where Kolmogorov [71] states that at sufficiently high Reynolds numbers, the small scale turbulent motions ($l \ll l_0$) are statistically isotropic (s.a. fig. 2.7). Kolmogorov gives a length-scale l_{EI} as demarcation between anisotropic large eddies and isotropic small eddies. Further, Kolmogorov's second similarity hypothesis states, that every turbulent flow at sufficiently high Reynolds numbers, the statistics of the motions of scale l in range of $l_0 \gg l \gg l_{mu}$ have a universal form that is uniquely determined by ϵ and independent of ν [119] (see fig. 2.7).
In CFD different methods are being developed to describe turbulent flow. Dependent on computational resources and need for accuracy, three different methods can be used

- Direct Numerical Simulation (DNS)
- Large Eddy Simulation (LES)
- Reynolds Averaged Navier-Stokes (RANS)

Although there are a lot more approaches available, these three may built a framework for classification. DNS [96] is the approach of the smallest scale in time and space. The resolution of flow motion must be small enough to resolve even smallest turbulent occurrences. Very high resolution requires a very small mesh. Therefore, computational efforts are very high and often only applicable at low Reynolds numbers [52].

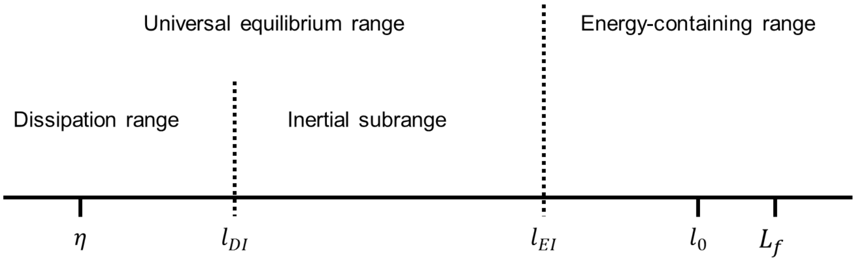

Fig. 2.7: Eddy sizes l (on a logarithmic scale) at very high Reynolds number, showing the various length-scales and ranges [119]

More coarse structure models like LES ([126], [117], [162]) are more applicable for higher Reynolds numbers than DNS is. Kolmogorov [71] states small turbulent structures to be isotropic and homogeneous. The LES approach requires mesh sizes to resolve turbulence until such small turbulent scales are reached. Models can then be used to represent isotropic behavior of such small turbulent occurrences within the grid and are therefore called sub-grid scale (SGS) models. This approach yields small mesh sizes but not as small as DNS. With increase in calculation power, LES does become more and more applicable for more complex geometries besides channel or pipe flow [117].
In RANS simulations, Navier-Stokes equations are solved to receive a time independent mean flow field. Turbulence must be modeled, not fully resolved like in DNS or partially in LES. In the case of transient applications, the Navier-Stokes equations must be of sufficient large scale so everything in scale of turbulence is filtered and time averaging can be ensured [87]. RANS is widely used in engineering applications. Therefore, it is used in this work (see ch. 4). Engineering applications are of more complex geometrical nature. As consequence, calculation efforts for RANS are considerably smaller than they are for

LES or DNS. An overview of the RANS approach is given in ch. 2.5. In this work, it is assumed, that the influence of pressure to material properties of a liquid flow regime is negligible. Consequently, material properties like density will be treated only as temperature dependent later on (ch. 3.1 and ch. 4.1).

Reynolds-averaged Navier-Stokes equations (RANS)

Recalling the notion of randomly appearing turbulent structures, a time-dependent flow quantity ϕ can be assumed to be the sum of its average quantity $\overline{\phi}$ and a fluctuating quantity ϕ'.

$$\phi = \overline{\phi} + \phi' \tag{2.42}$$

In the case of fluid motion, the quantity ϕ can represent velocity, density, pressure, enthalpy or temperature. This leads to following equations to be considered

$u = \overline{u} + u'$	$v = \overline{v} + v'$	$w = \overline{w} + w'$
$\rho = \overline{\rho} + \rho'$		
$p = \overline{p} + p'$		
$h = \overline{h} + h'$	$T = \overline{T} + T'$	$H = \overline{H} + H'$

Tab. 2.3: RANS - quantites with fluctuation

The total enthalpy H is here defined as $H = h + \frac{u_i u_i}{2}$. Other fluid properties are given as functions of temperature later on.

Continuity equation (RANS)

The Navier-Stokes equations built the fundamental basis of fluid dynamics. If incompressible flow and Cartesian coordinates are assumed, the continuity equation (eq. (2.3)) can be written as

$$\frac{\partial \overline{\rho}}{\partial t} + \frac{\partial}{\partial x_j}\left(\overline{\rho}\,\overline{u}_j + \overline{\rho' u_j'}\right) \;=\; 0 \tag{2.43}$$

where x_i $(i = 1, 2, 3)$ are the Cartesian coordinates, u_i are the Cartesian components of the velocity, t is the time, p the pressure, ρ the density and ν the kinematic viscosity. Whenever the same index appears twice in any term, summation over the range of that index is assumed to be implied. In the Reynolds-averaged Navier-Stokes (RANS) approach, unsteadiness in flow disappears by averaging and is considered as part of the turbulence. The discrete time-step Δt is the interval over which is averaged. It must be large compared to the typical time scale of velocity fluctuations u_i'. With mass-averaging (described in [118]), the Reynolds-averaged continuity equation in Reynolds form for incompressible fluids is

$$\frac{\partial \overline{u}_j}{\partial x_j} \;=\; 0 \tag{2.44}$$

Momentum equation (RANS)

The Reynolds form of the momentum equation (eq. (2.9)) written in conservation-law form can be further developed with the idea of turbulence as an average and a fluctuation parts (see eq. (2.42)). Linear fluctuating terms become zero when time averaging is applied. This way, the Reynolds momentum equations can be written as

$$\frac{\partial}{\partial t}\left(\overline{\rho}\,\overline{u}_i + \overline{\rho' u_i'}\right) + \frac{\partial}{\partial x_j}\left(\overline{\rho}\,\overline{u}_i \overline{u}_j + \overline{u}_i \overline{\rho' u_j'}\right) = -\frac{\partial \overline{p}}{\partial x_i} + \frac{\partial}{\partial x_j}\left(\overline{\tau_{ij}} - \overline{u_j}\,\overline{\rho' u_i'} - \overline{\rho}\,\overline{u_i' u_j'} - \overline{\rho' u_i' u_j'}\right) \tag{2.45}$$

where τ_{ij} is defined as

$$\overline{\tau_{ij}} = \mu\left(\frac{\partial \overline{u}_i}{\partial x_j} + \frac{\partial \overline{u}_j}{\partial x_i}\right) - \frac{2}{3}\delta_{ij}\frac{\overline{u}_k}{x_k} \tag{2.46}$$

If the fluid is assumed to be incompressible, the momentum equation can be simplified to

$$\frac{\partial}{\partial t}\left(\rho\overline{u}_i\right) + \frac{\partial}{\partial x_j}\left(\rho\overline{u}_i\overline{u}_j\right) = -\frac{\partial\overline{p}}{\partial x_i} + \frac{\partial}{\partial x_j}\left(\overline{\tau}_{ij} - \rho\overline{u'}_i\overline{u'}_j\right) \tag{2.47}$$

Energy equation (RANS)

Starting with eq. (2.14), a general form of the energy equation, the energy equation can be developed to obtain the Reynolds energy equation. The relation between H, h and T must be defined as they are all related. If total energy is assumed to be only composed of internal energy and kinetic energy, the general form of the energy equation can be written in Cartesian coordinates as

$$\frac{\partial}{\partial t}\left(\rho H\right) + \frac{\partial}{\partial x_j}\left(\rho u_j H + q_j - u_i\tau_{ij}\right) = \frac{\partial p}{\partial t} \tag{2.48}$$

If in eq. (2.48) all fluctuating quantities ϕ are replaced by $\overline{\phi} + \phi'$, time-averaged and $H = c_p T$, the equation can be written in conservative form as

$$\frac{\partial}{\partial t}\left(\rho c_p T\right) + \frac{\partial}{\partial x_j}\left(\rho c_p u_j T - \lambda\frac{\partial T}{\partial x_j}\right) = \frac{\partial p}{\partial t} + u_j\frac{\partial p}{\partial x_j} + \Phi \tag{2.49}$$

where the dissipation Φ can be expressed as

$$\Phi = \tau_{ij}\frac{\partial u_i}{\partial x_j} = \mu\left[-\frac{2}{3}\left(\frac{\partial u_k}{\partial x_k}\right)^2 + \frac{1}{2}\left(\frac{\partial u_j}{\partial x_i} + \frac{\partial u_i}{\partial x_j}\right)^2\right] \tag{2.50}$$

Further information about RANS energy equation details can be received from [118]. The terms of eq. (2.49) for incompressible flow at a given temperature can be written as

$$\frac{\partial}{\partial t}\left(\rho c_p\overline{T}\right) + \frac{\partial}{\partial x_j}\left(\rho c_p\overline{T}\overline{u}_j\right) = \frac{\partial\overline{p}}{\partial t} + \overline{u}_j\frac{\partial\overline{p}}{\partial x_j} + \overline{u'_j\frac{\partial p'}{\partial x_j}} + \frac{\partial}{\partial x_j}\left(\lambda\frac{\partial T}{\partial x_j} - \rho c_p\overline{T'u'_j}\right) + \overline{\Phi} \tag{2.51}$$

where $\overline{\Phi}$ is reduced slightly in complexity owing to the vanishing of the volumetric dilatation term in $\overline{\tau}_{ij}$ for incompressible flow [118].

Closure problem

With the recent definition of the Reynolds-averaged Navier Stokes equations, the number of variables exceeds the number of equations because of the non-linear term $-\rho\overline{u'_i u'_j}$ in the momentum equation (eq. (2.47)). To find a solution, the Reynolds stress tensor

$$R_{ij} = -\rho\overline{u'_i u'_j} \tag{2.52}$$

can be modeled. The function of turbulence modeling is to devise approximations for the unknown correlations in terms of flow properties that are known so that a sufficient number of equations exists [160].

Boussinesq eddy viscosity

The eddy viscosity hypothesis was introduced by Boussinesq [16]. According to the hypothesis the relationship is

$$\overline{u_i' u_j'} \;=\; -\nu_T \left(\frac{\partial \overline{u}_i}{\partial x_j} + \frac{\partial \overline{u}_j}{\partial x_i} \right) + \frac{2}{3} k \delta_{ij} \tag{2.53}$$

where the positive scalar field $\nu_T = \nu_T(x_i, t)$ is the turbulent viscosity. The turbulent-viscosity hypothesis substituted into eq. (2.47) is

$$\frac{\partial \overline{u}_i}{\partial t} + \overline{u}_j \frac{\partial \overline{u}_i}{\partial x_j} \;=\; \frac{\partial}{\partial x_j} \left[\nu_{\text{eff}} \left(\frac{\partial \overline{u}_i}{\partial x_j} + \frac{\partial \overline{u}_j}{\partial x_i} \right) \right] - \frac{1}{\rho} \frac{\partial}{\partial x_i} \left(\overline{p} + \frac{2}{3} \rho k \right) \tag{2.54}$$

where

$$\nu_{\text{eff}}(x_i, t) \;=\; \nu + \nu_T(x_i, t) \tag{2.55}$$

is the effective viscosity. Eq. (2.54) has the same appearance as the incompressible Navier-Stokes equation with $\overline{u}_i$ and ν_{eff} in place of u_i and ν and with $\overline{p} + \frac{2}{3}\rho k$ modifying the pressure. The advantage of this model is its simplicity. For many flows the accuracy of the model is poor [131]. However, for simple shear flows, where the mean velocity gradients and turbulence characteristics develop slowly, the hypothesis is reasonable.

Turbulence kinetic energy

The most popular method for the characteristic turbulent velocity scale is to solve it proportional to the square root of the specific kinetic energy of turbulent fluctuations. The Turbulence kinetic energy (k) uses this relation similarly as Reynolds stresses relates τ_{ij} to u_{EI} and l_{EI}. The Reynolds averaged kinetic energy of turbulent eddies can be written per unit mass as

$$k = \frac{1}{2} \left(\overline{u_i' u_j'} \right) \tag{2.56}$$

As k is defined in eq. (2.56) to be one half of the sum of the Reynolds stresses, the full form of the turbulence kinetic energy can be noted as

$$\begin{aligned} \underbrace{\frac{\partial k}{\partial t}}_{\substack{\text{Local}\\\text{derivative}}} + \underbrace{\overline{u}_j \frac{\partial k}{\partial x_j}}_{\text{Advection}} = \\ - \underbrace{\frac{1}{\rho_0} \frac{\partial \overline{u_i' p'}}{\partial x_i}}_{\substack{\text{Pressure}\\\text{diffusion}}} - \underbrace{\frac{1}{2} \frac{\overline{u_j' u_j' u_i'}}{\partial x_i}}_{\substack{\text{Turbulent}\\\text{transport}\\\mathcal{T}}} + \underbrace{\nu \frac{\partial^2 k}{\partial x_J^2}}_{\substack{\text{Molecular}\\\text{viscous}\\\text{transport}}} - \underbrace{\overline{u_i' u_j'} \frac{\partial \overline{u_i'}}{\partial x_j}}_{\substack{\text{Production}\\\mathcal{P}}} - \underbrace{\nu \overline{\frac{\partial u_i'}{\partial x_j} \frac{\partial u_i'}{\partial x_j}}}_{\substack{\text{Dissipation}\\\epsilon_k}} - \underbrace{\frac{g}{\rho_0} \overline{\rho' u_i'} \delta_{ij}}_{\substack{\text{Buoyancy flux}\\\lfloor}} \end{aligned} \tag{2.57}$$

The explicit derivation of this term can be derived from e.g. [119] or [160]. At this point, there are still more unknown quantities than equations to solve the system of equations. Higher order correlations of fluctuating quantities produce more unknowns than equations. As a result, the closure problem (see ch. 2.5) is not solved yet. One way to solve that problem is its specification in light of physical reasoning and experimental evidence. That way, the k-equation can be solved and correlations for the Reynolds stresses, dissipation, turbulent diffusion, and pressure diffusion can be found.

The k-ϵ turbulence model

The standard two-equation turbulence model is the k-ϵ turbulence model [75], [3]. The k-equation is combined with a transport equation for ϵ, so one more turbulent quantity can be solved. This way, the need for a specific turbulent length scale $l(x_i)$ can be eliminated. The exact equation for ϵ can be derived in a similar manner as the k-equation [160].

$$\frac{\partial \epsilon}{\partial t} + \overline{u}_j \frac{\partial \epsilon}{\partial x_j} = \frac{\partial}{\partial x_j}\left(\frac{\nu_T}{\sigma_\epsilon}\frac{\partial \epsilon}{\partial x_j}\right) + C_{\epsilon 1}\frac{\epsilon}{k}\left[\nu_T\left(\frac{\partial \overline{u}_i}{\partial x_j} + \frac{\partial \overline{u}_j}{\partial x_i}\right) - \frac{2}{3}k\delta_{ij}\right]\frac{\partial \overline{u}_i}{\partial x_j} - C_{\epsilon 2}\frac{\epsilon^2}{k} \tag{2.58}$$

The turbulent viscosity can be written as

$$\nu_T = \frac{C_\mu k^2}{\epsilon} \tag{2.59}$$

and $l(x_i)$ is obtained from k and ϵ. Here C_μ is a model constant. The equation for k and ϵ together with the specification of ν_T, form the k-ϵ turbulence model. This model is considered to be more complete since it does not require specifications such as the turbulent length scale $l(x_i)$.

Two model equations are solved for k and ϵ. The turbulent viscosity is defined by $\nu_T = \frac{C_\mu k^2}{\epsilon}$. The Reynolds stresses are found from the turbulent-viscosity hypothesis and the Reynolds equations are solved for $\overline{u}_i$ and $\overline{p}$. Standard values of the model constants (closure coefficients) of the k-ϵ turbulence model used in the model equations are

$$C_\mu = 0.09\,,\, C_{\epsilon 1} = 1.44\,,\, C_{\epsilon 2} = 1.92\,,\, \sigma_k = 1.0\,,\, \sigma_\epsilon = 1.3 \tag{2.60}$$

Near wall flows

Flow in a wall contained volume, additionally needs to be investigated near the bounding walls. [156] shows the possibility of a continuous velocity and shear distribution for turbulent flow near a smooth wall. In following, some basics will be given for further understanding of flow near walls. Detailed information can be received from [119], [160] or [44].

Close to the wall, no slip is assumed for any kind of flow ($u_i(x_i,t) = 0$). All wall shear stress (shear stress directly at the wall boundary) is due to the viscous contribution. At free flow condition, shear stresses are negligible small compared to Reynolds stresses. However, at the wall boundary, this contribution of shear stress must be taken into account which leads to the two parameters for viscosity ν and wall shear stress τ_ω. These two parameters are the basis for viscous scales which define the appropriate velocity and length scales in the so-called 'near wall region'; friction velocity

$$u_\tau \equiv \sqrt{\frac{\tau_\omega}{\rho}} \tag{2.61}$$

and viscous length-scale

$$\delta_\nu \equiv \nu\sqrt{\frac{\rho}{\tau_\omega}} = \frac{\nu}{u_\tau} \tag{2.62}$$

The distance from the wall measured in viscous length or wall units is defined as

$$y^+ \equiv \frac{x_2}{\delta_\nu} = \frac{u_\tau x_2}{\nu} \tag{2.63}$$

y^+ defines the regions with flow near the wall boundary (near-wall flow). The viscous region near the wall is defined for $y^+ < 50$, where viscosity contributes to the shear stress. For $y^+ > 50$, the effect of the viscosity is negligible. The viscous sublayer is defined for $y^+ < 5$. Here, the Reynolds shear stresses are negligible compared to viscous stresses.

[157] describes this group of regions with the law of the wall. To fully describe the law of the wall, one dimensionless velocity u^+ must be defined in addition. It describes the velocity u parallel to the wall as a function of the distance y from the wall divided by the friction velocity u_τ.

$$u^+ \equiv \frac{\overline{u}}{u_\tau} \tag{2.64}$$

The law of the wall is defined by the integral of $\frac{du^+}{dy^+}$ (see [119] for details). When y^+ is large the viscosity has little effect. u^+ can be written in explicit form as

$$u^+ = \frac{1}{\kappa} lny^+ + \mathrm{C} \tag{2.65}$$

where C is a constant (see fig. 2.8). This relationship is known as the log law and κ is the von Kármán constant.

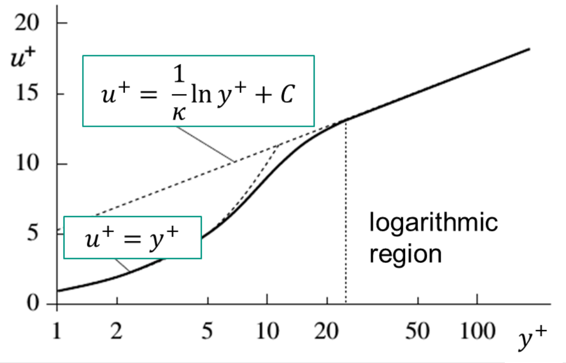

Fig. 2.8: The turbulent boundary layer [44]

The OpenFOAM CFD code

The Open source Field Operation and Manipulation CFD Toolbox (OpenFOAM) is an open source software package. It contains a variety of solvers for specific CFD problems and utilities for data manipulation. The entire software package is written in the C++ programming language, providing libraries that e.g. represent the equation

$$\frac{\partial(\rho u)}{\partial t} + \nabla \cdot \phi u - \nabla \cdot \mu \nabla u = -\nabla p$$

in the form

```
solve
(
fvm::ddt(rho, U)
+ fvm::div(phi, U)
- fvm::laplacian(mu,U)
==
- fvc::grad(p)
);
```

This way, the user is able to modify existing physical models for the purpose of a given application in case there is physical evidence that requires modification. The code structure of OpenFOAM is divided in three different parts (see fig. 2.9): Pre-processing, Solving and Post-processing.

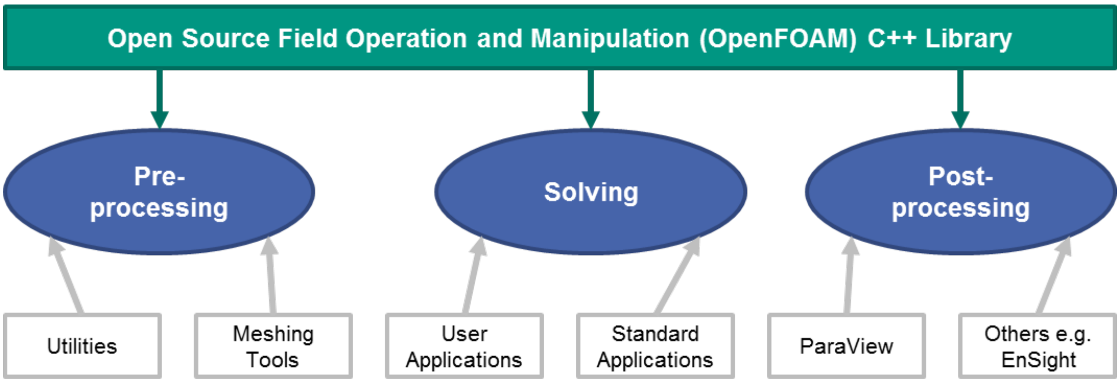

Fig. 2.9: OpenFOAM structure [108]

There is no graphical user interface (GUI) directly provided in OpenFOAM. For that reason, all case definitions and computation results are file based. For accessibility of case definition files like fluid definition or boundary conditions' specifications, so-called case-file directories are required that are standardized. Information about geometry, fluid properties and turbulence models are contained in the sub-folder 'constant'. The solver setup files are in the sub-folder 'system'. Boundary conditions and initial conditions together with initial field information are given in the sub-folder '0'. Specific information about case definitions are given in [89].

Visualization of results is part of the post-processing. OpenFOAM converts result data so that the open source application ParaView can represent results conveniently. The used version of OpenFOAM in this work is "2.3.x" which has been downloaded from GIT[1] repositories and compiled in April 2014.

Solvers

OpenFOAM contains many groups of solvers to serve different specialized purpose. According to the physics needed, an adequate solver must be chosen. If sufficiently sophisticated, the solver can be used as is. As the OpenFOAM CFD toolbox is open source, research and development of higher sophisticated solvers can start at this point. In the framework of the presented work later on, it is not necessary to enhance the chosen buoyantPimpleFoam solver as it provides enough possibilities and quality for the recent purpose. A brief description of the used solver is given further on. For simplicity reason, a more simple solver is given first which is part of the buoyantPimpleFoam solver, the simpleFoam solver. The PIMPLE algorithm which is used during this work, has been created as a merge of the SIMPLE algorithm which is used for steady state calculations and the PISO algorithm which is used for transient calculations [108]. This way, it is possible to enlarge time steps and save computation time. Specifics about the SIMPLE and PISO algorithm from a mathematical point of view will not be presented here, but can be read in [119], [99], [113] or [118].

simpleFoam

One of the very basic solver in OpenFOAM is the simpleFoam solver. It is a solver for incompressible turbulent flow in steady state condition. With the incompressible restriction, the fluid is considered to have constant density and viscosity. For that reason, temperature can be neglected as it does not have any influence, neither is accounted in the equations of the solver. As density is considered constant, gravitational effects like buoyancy are not

---

[1] GIT is a distributed version control system, https://git-scm.com/

present. The continuity equation (eq. (2.44)) keeps the same. However, the momentum equation (eq. (2.47)) shrinks to

$$\frac{\partial}{\partial x_j}\left(\rho\overline{u}_i\overline{u}_j\right) - \frac{\partial}{\partial x_j}\left(\tau_{ij} - \rho\overline{u'}_i\overline{u'}_j\right) = -\frac{\partial\overline{p}}{\partial x_j} \tag{2.66}$$

As the solution is considered steady state, the time derivative on the left hand side of eq. (2.47) vanishes. With the simpleFoam solver, velocity fields without gravitational influence can be predicted very quickly, as only a small number of equations per CV need to be solved within one iteration. This not only leads to quick results but also the solver is considered to be very robust against mesh inconsistencies. Fig. 2.10 shows a flow chart of the run process of the SIMPLE algorithm.

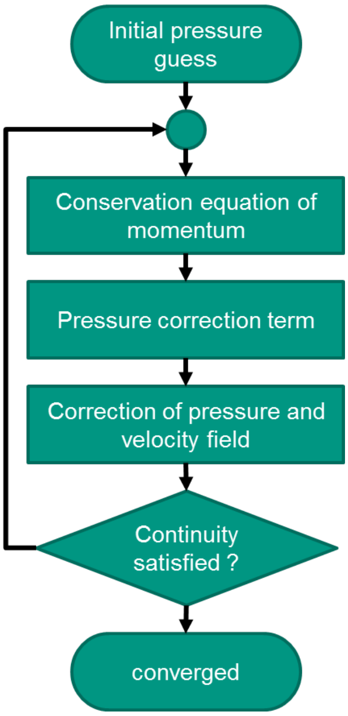

Fig. 2.10: The SIMPLE Algorithm [108]

```
    // Momentum predictor

    tmp<fvVectorMatrix> UEqn
    (
        fvm::div(phi, U)
      + turbulence->divDevReff(U)
     ==
        fvOptions(U)
    );

    UEqn().relax();

    fvOptions.constrain(UEqn());

    solve(UEqn() == -fvc::grad(p));

    fvOptions.correct(U);
```

Lst. 2.1: Implementation of the momentum equation (simpleFoam)

In OpenFOAM, all solvers that contain the name simple use the SIMPLE algorithm [99] to solve the Navier-Stokes equations. The implementation of `UEqn.H` and `pEqn.H` which

are part of the simpleFoam solver are listed below (see lst. 2.1 and lst. 2.2).
In the momentum equation, the discretization of the convective term leads to a non-linear system of equations. The flux ϕ is introduced to avoid complex non-linear solvers. This supports the linearization of the convective term. This way, the newly approximated velocity field can be computed. Line 6 in lst. 2.1 shows the implementation of the turbulence model. As the simpleFoam algorithm is used for incompressible flow, the pressure equation is derived from the incompressible equation of momentum in a semi discretized manner.

$$a_p U_p = H(U) - \nabla p \tag{2.67}$$

```
{
    volScalarField rAU(1.0/UEqn().A());
    volVectorField HbyA("HbyA", U);
    HbyA = rAU*UEqn().H();
    UEqn.clear();

    surfaceScalarField phiHbyA("phiHbyA", fvc::interpolate(HbyA) & mesh.Sf());
    adjustPhi(phiHbyA, U, p);

    fvOptions.relativeFlux(phiHbyA);

    // Non-orthogonal pressure corrector loop
    while (simple.correctNonOrthogonal())
    {
        fvScalarMatrix pEqn
        (
            fvm::laplacian(rAU, p) == fvc::div(phiHbyA)
        );

        pEqn.setReference(pRefCell, pRefValue);

        pEqn.solve();

        if (simple.finalNonOrthogonalIter())
        {
            phi = phiHbyA - pEqn.flux();
        }
    }

    #include "continuityErrs.H"

    // Explicitly relax pressure for momentum corrector
    p.relax();

    // Momentum corrector
    U = HbyA - rAU*fvc::grad(p);
    U.correctBoundaryConditions();
    fvOptions.correct(U);
}
```

Lst. 2.2: pressure correction - simpleFOAM

$H(U)$ contains the matrix coefficients of the neighbor cells and all source terms [64]. First the coefficient a_p and then the velocity U is calculated. The flux ϕ can be received by interpolation of U from the cell center to the faces and multiplied with its' surface normals S_j. The pressure equation is solved repeatedly according to the number of non-orthogonal correctors previously specified by the user.

buoyantPimpleFoam

In this work, the buoyantPimpleFoam solver is used. The solver covers transient fluid behavior with buoyancy effects. Additionally, different turbulence models (RANS and LES) can be chosen. Originally, the solver treats incompressible flow, but density can be used as a function of temperature which is crucial for buoyancy effects. The used algorithm, PIMPLE is the merge of the `PISO` and `SIMPLE` algorithms. Conservation equations (eq. (2.3), eq. (2.9), eq. (2.14)) are not simplified. To reduce the number of calculations in every cell and time step, the artificial pressure p_{rgh} is introduced.

$$p \; = \; p_{rgh} + \rho g h \tag{2.68}$$

The convergence behavior of the solver is more sensitive with the buoyantPimpleFoam in comparison to the simpleFoam as more equations need to be solved. The contribution of errors from meshing cannot be treated as it is with the simpleFoam solver. When unstructured meshing is applied, the number of `nNonOrthogonalCorrectors` must be increased to compensate non-orthogonal vectors. To support a smooth solution and keep computational time in acceptable range, other so-called correctors like `nCorrectors` or `nOuterCorrectors` must be treated with caution. For more information about the buoyantPimpleFoam, please refer to [108].

Wall function implementation

In OpenFOAM, wall functions are only applied to the nearest cell to the boundary wall. For the calculation, the effective viscosity is used instead of only the turbulent viscosity ($\nu_{\text{eff}} \; = \; \nu + \nu_t$).
For all other cells, the standard turbulence model is used. To check the cell quality near the wall, y^+ (see ch. 2.5) can be computed with the `yPlusRAS` function after finishing the transient calculation. This way, the mesh can be improved by iterating procedures (a-posteriori only). Especially when heat is transferred from wall to fluid, the range of $30 \leq y^+ \leq 500$ can be considered as valid according to [87] for the application of the standard $k - \epsilon$ turbulence model. Other turbulence models may have different ranges of validity [87].

2.6 Approaches for STH/CFD coupling

During the last decade, several STH codes have been coupled with CFD codes. An overview about coupling is given in following. Because coupling of STH and CFD codes does not have a large history, there is no standardized nomenclature or vocabulary yet. On the other hand, it is crucial to have a global wording for similar procedures or methodologies for comparison reason. To start such, it is necessary, to look at different coupling procedures and the individual codes used. Coupling is done in time and space. Coupling in time can be sequential or iterative. When a system is coupled sequentially, time steps can be given to the coupled system explicitly or semi-implicitly. An implicit coupling would require the reconfiguration of existing solvers, which requires extensive programming and is therefore not practical (solvers have to be merged). Additionally, implicit coupling is only valid for one single solution type. Semi-implicit time step management uses an estimation of the time step based on error levels of the previous time step (prediction). The time step size is reduced, when error levels increase and is enlarged when error levels are small enough. All time steps are global and therefore matching time steps. It is possible, that STH and CFD codes use smaller internal time steps but must meet at the given global time steps for data exchange. Parallel coupling indicates, that both codes perform the same time step at once. To do so, either fully implicit coupling is required or one code must be driven by estimated boundary conditions (BCs). Coupling in space is possible with redundant regions, partially redundant regions or non-redundant regions. Accordingly, the methodology can be called overlapping when regions exist in STH and CFD domain (redundant), partial overlapping or distributed. When redundant regions are used, parameters are exchanged which overwrite calculated values of the respective other code. Dependent on the implementation of the coupling interface, the coupled system can be seen as a typical master-slave system where either the STH code or the CFD code are governing or the coupling interface is used as supervisor for both codes. As an overview and to classify different coupling approaches, tab. A.1 gives an overview of assumed possible options. In following subchapters, a group of different coupling approaches is presented.

GRS - ATHLET & CFX

At GRS, the ATHLET code is not only being developed but also extended for the purpose of coupled calculations [111]. Coupling of STH and CFD codes requires the exchange of directly dependent hydraulic parameters like fluid velocity, energy flow and pressure to solve continuity, momentum and energy equations in each code. The coupled calculation diverges, if mass, momentum and energy are not conserved. The coupling scheme shown in [112] provides two different solutions to the coupling problem. Either an explicit time step is provided statically or a semi-implicit time step is used, where the executed time step is recalculated until convergence criteria is reached.

Regions (flow continua in space) are strictly separated so that redundancies are not present. The coupling methodology with explicit time step can be classified as master-slave sequential explicit distributed coupling according to the scheme given in fig. A.1. Accordingly, the coupling methodology with semi-implicit time step can be classified as master-slave sequential semi-implicit distributed coupling (see fig. A.2). To support master-slave execution control for the ATHLET/CFX coupling methodology, the ATHLET code is executed as subroutine by CFX. This way, ANSYS CFX can call ATHLET when needed. In addition, a key variable is implemented to define the starting point within the ATHLET code. Different coupling options in both codes are implemented for stability reason. Different hydraulic parameters like pressure, velocity and mass flow rate can be specified at different locations as boundary conditions. The STH code provides the scalar variables pressure, fluid temperature, mass flow rate and quality. At the same time, the CFD code provides vector variables like mass flow or velocity and related temperature and pressure at the coupling boundary [111].

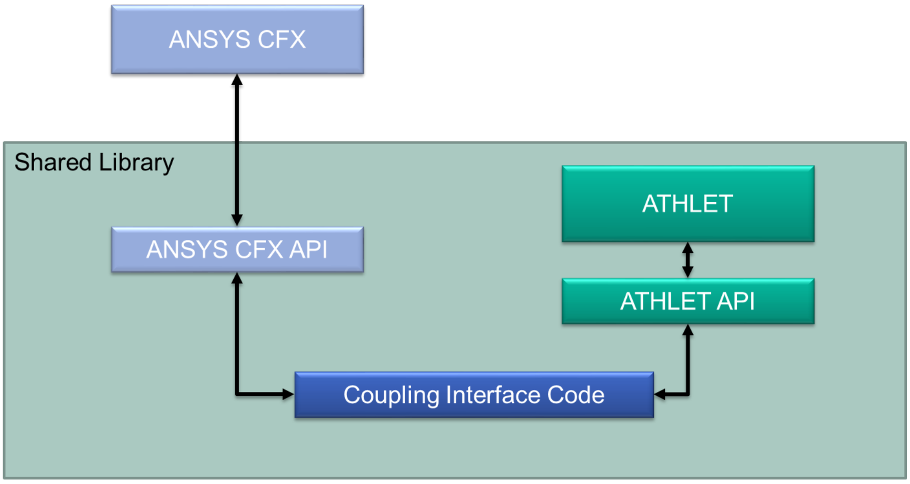

Fig. 2.11: ATHLET/ANSYS-CFX: Shared Library scheme (GRS) [110]

The CFD coupling is based on a more general framework. It has already been established by ANSYS CFX for coupling purposes with other 1D codes (fig. 2.11). CFX uses an extension of its input deck definitions and the utilization of a shared library which contains the coupling interface and the STH code, as well as modifications to the calling sequence used within ATHLET [110].

CEA - CATHARE & TRIO_U

The coupling architecture is based on a common application programming interface (API), called 'Interface for Code Coupling' (ICoCo) given in fig. 2.12 and will be available soon in the SALOME platform[2] [21]. The intension to create a common API is the capability for multi-physics coupled calculations beyond STH/CFD. SALOME acts here as a supervisor and performs standardized actions like individual code calls [10].

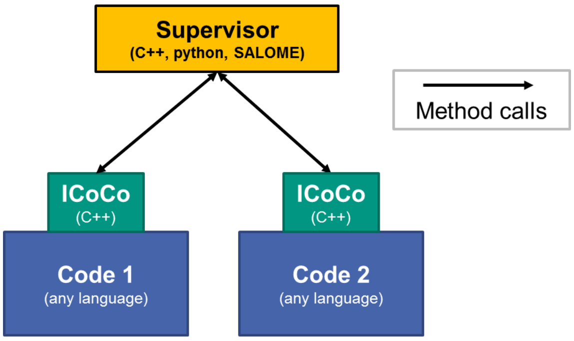

Fig. 2.12: CATHARE/TRIO_U: Scheme of coupling architecture [10]

The STH/CFD coupling methodology here can be described as supervised sequential explicit overlapping coupling. The SALOME platform executes all coupled codes when needed with information about the time step, type and destination of information propagation. Boundary conditions (BC) can be transferred directly between the codes [10]. During the THINS project [27], the PHENIX NCT [148] was performed with this coupling methodology, the CATHARE (STH) code and TRIO_U (CFD) code [9]. Fig. 2.13 gives an example of an abstract reactor scheme with a possible arrangement of CFD and STH domains for a coupled calculation with overlapping domains. In this example, the CFD domain (overlapping domain) is restricted to the core whereas the system code domain include both the core and the loops with their components [10].

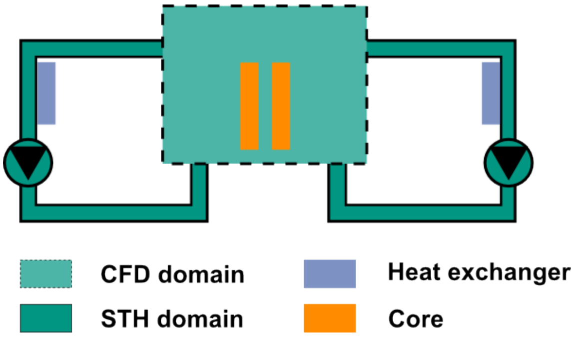

Fig. 2.13: CATHARE/TRIO_U: Code domains for a coupled calculation – overlapping method [10]

For stability reasons, the hydraulic boundary conditions are not defined by mass flow rate at the inlets and pressure at the outlets, as usual. After experiencing hydraulic

---

[2] http://www.salome-platform.org/

instabilities, mass flow rates were imposed at all hydraulic boundaries of the CFD domain [10]. The velocity profile used as BC at the CFD boundaries is flat (rectangular profile). For energy feedback, the CATHARE code is modified to equalize energy transfer through the boundaries of the CFD domain between the two codes [9]. For momentum feedback, reference points are used

$$\Delta p(O_i) = \sum_{\Delta \mathrm{t}} [p(O_{ref}) - p(O_i)]_{\mathrm{STH}} - [p(O_{ref}) - p(O_i)]_{\mathrm{CFD}} \quad \text{with} \quad i = 1, .., N \tag{2.69}$$

where O_{ref} marks a reference point at a boundary O_i. To apply a momentum balance between STH and CFD, the source term given in eq. (2.69) is used to minimize the pressure difference between STH and CFD [10]. Dependent on the applied turbulence model, corresponding BCs are given at the same positions as velocities are. In the case of the PHENIX NCT, a laminar description of the flow field is used in CFD [10]. A general description of the coupling at interfaces between the two codes is shown in [9].

KTH - RELAP5 & STAR-CCM+

The coupling strategy presented by [65] can be described as supervised parallel explicit overlapping coupling. Both codes first need to establish steady state condition in standalone mode. After steady state is reached, the coupled calculation starts (see fig. 2.14). CFD performs one time step (transient). STH is then iterated until coupling parameters reach sufficient accordance with CFD results. For the next time step, STH parameters are given to CFD as BCs (mass flow rate and temperature at the inlet). In case of flow reversal, BCs at the inlet and outlet are switched. The data exchange is illustrated in fig. 2.15.

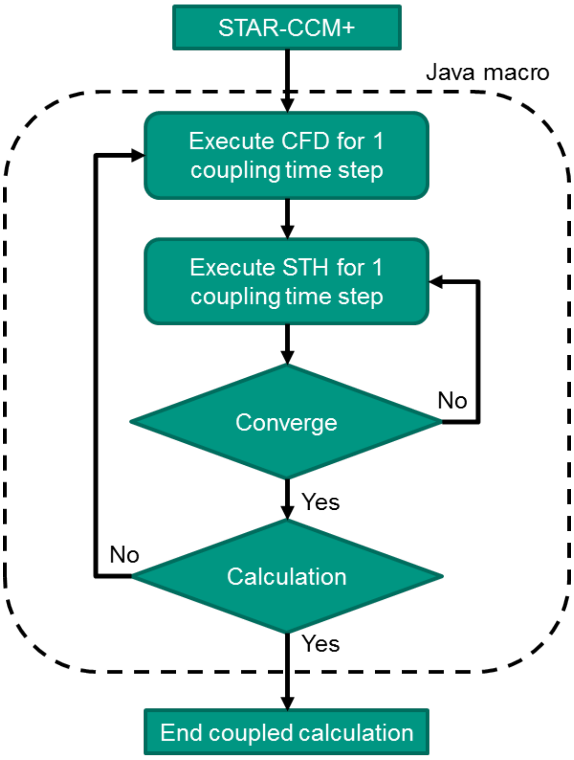

Fig. 2.14: RELAP5/STAR-CCM+: Explicit coupling scheme between STH and CFD via Java interface [65]

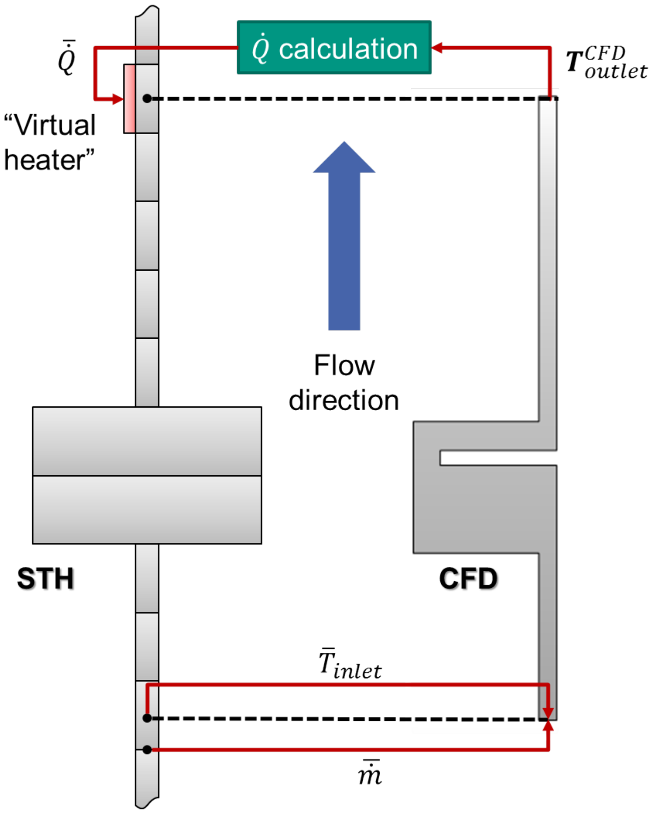

Fig. 2.15: RELAP5/STAR-CCM+: Variables exchanged during the coupling procedure. same applied at reversed flow conditions. [65]

$\overline{T}_{inlet}$ and $\overline{\dot{m}}$ are extrapolated parameters, dependent on the two latest STH time steps. The virtual heater is used to adjust the temperature in STH at the elevation of the CFD outlet. It can also be negative to remove heat from the STH domain. Coupling time step is set to be equal to CFD time step and its size is kept small. This is to ensure that the difference between extrapolated and converged STH solution is fairly small in case that CFD is not iterated [65].

ANL - SAS4A/SASSYS-1 & STAR-CCM+

Coupling between SAS4A/SASSYS-1 (STH) and STAR-CCM+ (CFD) started with [41], where instead of STAR-CCM+, STAR-CD was used as CFD code. The module PRIMAR-4 of SAS4A/SASSYS-1 is used to calculate STH loops. Details about the code can be taken from [42]. In PRIMAR-4 two different types of models are used to create the thermal hydraulic loop, control volumes (CV) and segments. The coupled approach can be described as supervised sequential overlapping explicit coupling. Communication between SAS4A/SASSYS-1 (STH) and STAR-CCM+ (CFD) occurs at the flow boundaries of the CFD region. CFD can only be used for the substitution of a STH CV, so flow boundary conditions (BC) are given to the connecting segments directly. The parameters exchanged at the BCs are mass flow/velocity and enthalpy/temperature to the referring CFD surface. At a specified elevation within the SAS4A/SASSYS-1 CV, the momentum equation

$$p_{in} = p_r + \int_{z_{in}}^{z_r} \rho(T)dz \tag{2.70}$$

is substituted by

$$p_{in} = p_r + \Delta p_{CFD} \tag{2.71}$$

where Δp_{CFD} is the pressure difference in three-dimensional space calculated by CFD between the inlet and the reference locations. With the above modifications, liquid flow rates and reference pressures for all connected compressible volumes and liquid flow segments are solved simultaneously. Once updated flow rates are known, the CFD calculation updates the flow and temperature distributions within each compressible volume for which a high-fidelity treatment option has been selected [41].

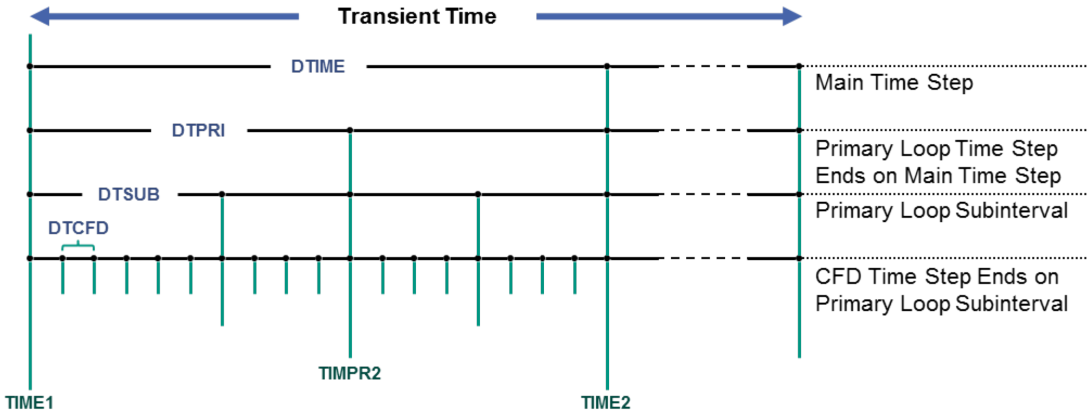

Fig. 2.16: SAS4A/SASSYS-1 / STAR-CCM+: Time step management

Data exchange between STH and CFD takes place in every PRIMAR-4 subinterval (`DTSUB` in fig. 2.16). A multilevel adaptive time step approach that resolves power and reactivity, heat transfer, core flow and whole system responses at appropriate scales is required. The coupled system is synchronized with “main” time steps (`DTIME` in fig. 2.16). Further information about the coupling and application examples can be seen in [150] and [56].

INL - RELAP5-3D & ANSYS Fluent

Aumiller et al. [4] and Weaver et al. [158] show coupling methodologies between RELAP5-3D [120] and different thermal hydraulic codes. Schultz et al. [133] show the coupling between RELAP5-3D (STH) and Fluent (CFD) using the same methodologies which are described briefly in following. In a first step, a master-slave sequential explicit distributed coupling methodology is introduced. As a successor a supervised sequential semi-implicit distributed coupling methodology is developed because of numerical instabilities when using explicit time step management. The explicit time step management follows a master-slave approach with RELAP5-3D as master. The semi-implicit time step management uses an executive program based on Parallel Virtual Machine (PVM) for time step management and data transfer [133]. Although in literature the semi-implicit scheme is described as master-slave, it was decided in this work to adapt naming to the existing classification as given in tab. A.1.

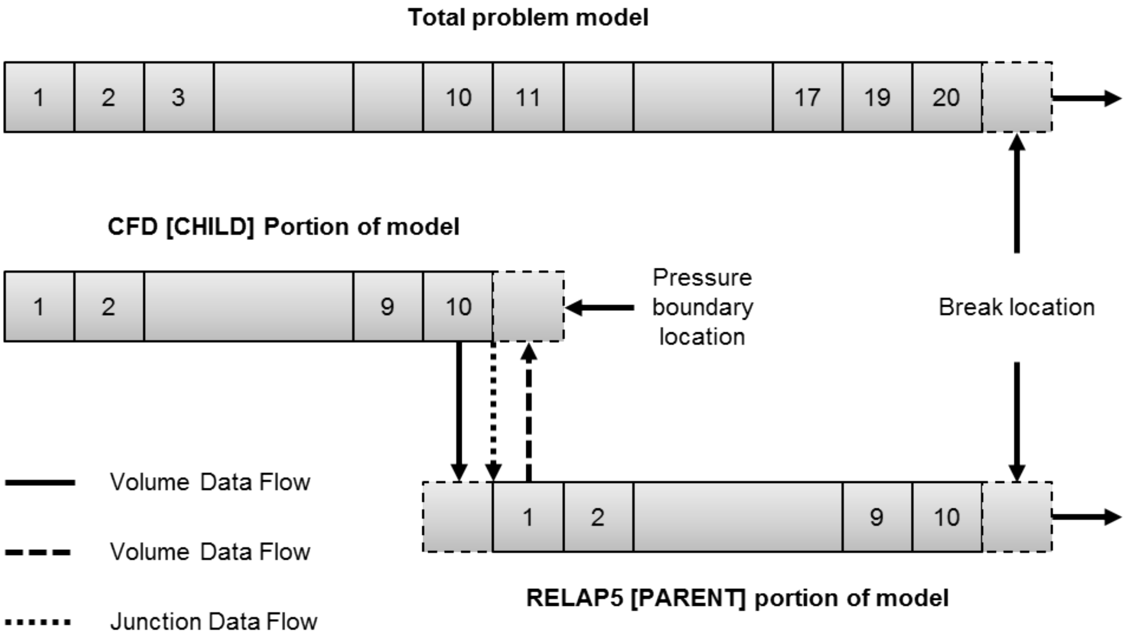

Fig. 2.17: Nodalization for full and coupled analysis [4] (graph modified)

RELAP5-3D → CFD	CFD → RELAP5-3D
Pressure (p)	Pressure (p)
Liquid density (ρ_f)	Liquid internal energy (u_f)
Gas density (ρ_g)	Gas internal energy (u_g)
Liquid temperature (T_f)	Void fraction (ϕ_g)
Gas temperature (T_g)	Liquid mass flow rate ($\dot{m}_f$)
Void fraction (ϕ_g)	Gas mass flow rate ($\dot{m}_g$)

Tab. 2.4: List of transmitted data

As can be seen in fig. 2.17, the coupling is performed by using artificial boundary conditions in each code. RELAP5-3D has a time dependent volume (TDV) and a time dependent junction (TDJ). The conditions in the TDV are only used for determining the quantities and are provided by the appropriate node in the CFD portion. The mass flow rates for the TDJ are calculated in the CFD portion of the code. Tab. 2.4 identifies the variables that are transmitted between the codes.

Summary

Five different coupling schemes have been shown. Tab. 2.5 classifies the shown approaches based on tab. A.1.

Organization, Codes	code architecture	information propagation	time-step management	geometry handling
GRS, ATHLET / CFX	master-slave	sequential	explicit, semi-implicit	distributed
CEA, CATHARE / TRIO_U	supervised	sequential	explicit	overlapping
KTH, RELAP5 / STAR-CCM+	supervised	parallel	explicit	overlapping
ANL, SAS4A/SASSYS-1 / STAR-CCM+	supervised	sequential	explicit	overlapping
INL, RELAP5-3D / Fluent	supervised	sequential	explicit, semi-implicit	distributed

Tab. 2.5: Overview of assumed possible coupling methodologies

3. ATHLET modification

The STH code ATHLET is being developed by GRS. It provides the analysis of nuclear safety issues like leaks and transients in pressurized water reactors (PWR) as well as boiling water reactors (BWR) in the whole spectrum of design transients and accidental transients. It is the STH code to the challenge of the Phénix natural convection test scenario (NCT) described later on.

The thermal-hydraulic system code ATHLET (**A**nalysis of **TH**ermal-hydraulics of **LE**aks and Transients) is being developed for the analysis of anticipated and abnormal plant transients, small and intermediate leaks as well as large breaks in light water reactors (LWR). ATHLET takes into account the whole spectrum of design transients and accidental transients (without core degradation) for PWRs and BWRs. The time integration of the thermo-fluid dynamics (TFD) is performed with the general purpose ODE-Solver called FEBE (Forward Euler, Backward Euler). This solver provides the solution of a general non-linear system of first order differential equations. The system is split into two subsystems: the first beginning integrated explicitly, the second implicitly. Generally, the fully implicit option is used in ATHLET. The linearization is done numerically for the implicit system by calculation of the Jacobian matrix.

The ATHLET code can be run under different operating systems. The modular structure allows the coupling of models of different physical formulation with different spatial discretization techniques. Because of this modularity, ATHLET is used as STH code for innovative systems of the Gen-IV studies for this work. In addition, ATHLET is one of the two major codes developed in Europe for nuclear safety analysis.

As the ATHLET code provides a modular network approach for the representation of a thermal-hydraulic system, different types of TFOs can be used. The different types of TFOs are:

- Pipe objects
- Branch objects
- Special objects

Because TFOs are not fully capable to represent heat transfer like heat conduction in structures, fuel rods or heaters of different type, the HECU model is used. It gives the possibility to assign heat conduction objects (HCOs) to all TFOs of a given network [78].

3.1 Material properties

To extend the ATHLET code's application range to SFRs, a property package to calculate sodium thermo-physical and transport properties is implemented into the code. The properties include enthalpy, heat capacity, latent heat of vaporization, density, thermal expansion, compressibility, speed of sound, and surface tension [151] [45]. Transport properties include viscosity and thermal conductivity [151] [45]. The temperature range of the property package is from 371K to 2503.7K. The sodium property package is an independent module, and is connected to the ATHLET program through a general interface [163]. Fig. 3.1 shows the schematic of the interface. The interface acts as a platform for information exchange between ATHLET and external physical modules. It includes the transmission of thermal-hydraulic parameters to describe fluid conditions and states from ATHLET to the modules. The modules then provide physical quantities like heat transfer coefficients to the ATHLET code for multi fluid application ([163], [164]).

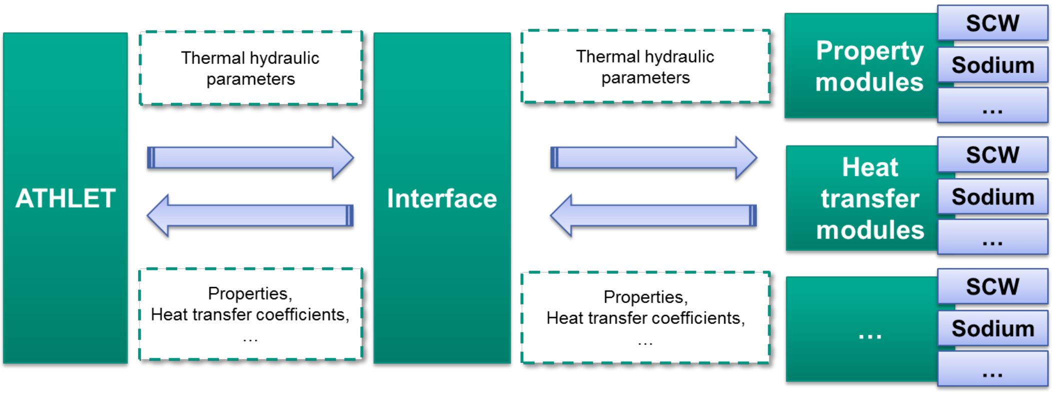

Fig. 3.1: ATHLET: Schematic of interface to the ATHLET code

3.2 Heat transfer

Heat transfer characteristics of LM significantly differ from heat transfer characteristics of water. The Prandtl number, ratio of momentum diffusivity to thermal diffusivity, of the two fluids differ significantly. LMs have a very low Prandtl number. In the temperature region between 200°C to 800°C, the Prandtl number of sodium changes from 0.01 to 0.005, while for water from 10 to 1 in corresponding liquid temperature range. Consequently, the contribution to the total heat transfer by conduction towards the thermal convection in LMs is much higher than in water. In ch. 2.4 the implemented heat transfer calculation methodology in the ATHLET code has been explained. The heat conduction and heat transfer module HECU of the ATHLET code describe the HTC to be expressed in the form

$$\begin{aligned} HTC &= f\left(\lambda, L, \mathrm{Nu}\right) \\ \lambda &= f(T) \\ Nu &= \begin{cases} f\left(\mathrm{Re}, \mathrm{Pr}\right) \\ f\left(\mathrm{Re}, {}^{\mathrm{P}}\!/\!_{\mathrm{D}}, \mathrm{Pr}\right) \\ f\left(\mathrm{Gr}, \mathrm{Pr}\right) \\ f\left(\mathrm{Gr}, {}^{\mathrm{P}}\!/\!_{\mathrm{D}}, \mathrm{Pr}\right) \end{cases} \end{aligned} \tag{3.1}$$

where λ is the thermal conductivity of the fluid, L is the characteristic length and Nu the Nusselt number. The thermal conductivity is considered a material property and is thereby given as a function only dependent on temperature. For example characteristic length L in bundle geometries, with flow direction parallel to the bundles, is the hydraulic diameter d_h. Generally, the Nusselt number can be described as the ratio of convective heat transfer to conductive heat transfer. For the direct calculation of heat transfer, correlations must be used, which are empirical and are received from experiments. In ATHLET, Nusselt correlations are called htc [5]. Examples for the implementation of htc are given in eq. (2.40) and eq. (2.41). If $T_{wall} > T_{fluid}$, the fluid is heated by the wall; if $T_{fluid} > T_{wall}$, the fluid is cooled by the wall. In the open literature, numerous correlations for the Nusselt number of LMs are available. Most of them are based on the expression

$$Nu \;=\; a + b \cdot \mathrm{Pe}^{c} \tag{3.2}$$

where a, b and c are constants and Pe is the Péclet number. It has been found through extensive experimental researches that the constant c is close to 0.8, while a and b depend on the geometry (e.g. circular tube, tube bundle) of the flow channels ([73], [95]).
For the heat transfer prediction of sodium, suitable correlations must be added to the ATHLET code. In the past decades a considerable number of Nusselt correlations for the LM heat transfer coefficient using the previously form differ from each other ([26], [115]). Here, six widely used correlations, including three for circular tube and three for tube bundle are implemented to the sodium heat transfer module for a preliminary evaluation.

- Lyon [86]
- Skupinski et al. [138]
- Sleicher et al. [139]
- Gräber and Rieger [49]
- Ushakov et al. [155]
- Mikityuk [95]

The Lyon [86] correlation is considered here as the first semi-empirical equation for heat transfer calculations of LM at constant heat flux. It is also selected as the default heat transfer model for LM in other system codes, like TRACE, SIMMER-III and SAS4A/SASSYS-1. Based on experimental heat transfer data in NaK flows, the correlation by Skupinski et al. [138] gave the best agreement with test data. The correlation by Sleicher et al. [139] was suggested for uniform heat flux conditions based on experimental investigation of local heat transfer coefficients in NaK flows in a pipe at different boundary conditions. These three correlations were developed for circular tube geometries. In case of tube bundles, Mikityuk [95] reviewed and assessed a number of correlations recommended for LM heat transfer with test data for LM flow in a lattice of circular rods from four independent experimental studies. The Mikityuk [95] correlation, as well as the correlation by Ushakov et al. [155] and the correlation by Gräber and Rieger [49] had the highest quality among the correlations considered in predicting the results of the experiments over the whole region of pitch-to-diameter (P/D) ratio from 1.1 to 1.95, and Péclet number from 30 to 5000.

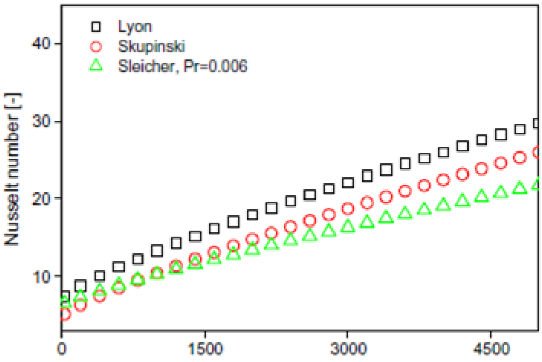

(a) Correlations for circular tube

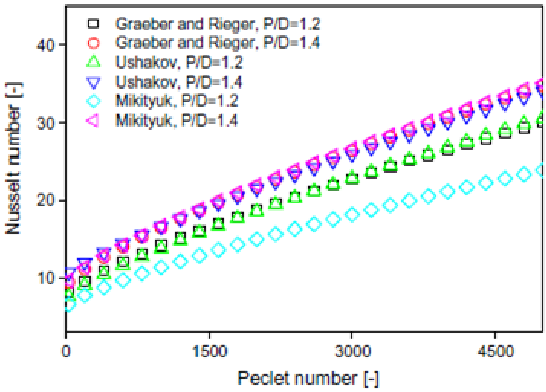

(b) Correlations for tube bundle

Fig. 3.2: ATHLET: Calculated Nusselt number according to different correlations [164]

To compare the difference of the selected correlations, the Nusselt number is calculated using these correlations. Fig. 3.2 shows the comparison of calculated individual Nusselt numbers. Considering the application of the modified ATHLET code to the PHENIX NCT, the Prandtl number of 0.006 is used in the correlation by Sleicher et al. [139]. For the PHENIX NCT, the pitch-to-diameter (P/D) ratio of the rod bundles in the fissile subassemblies is 1.187, in the fertile subassemblies 1.081 and in the IHXs' tube bundles 1.429. Two P/D values (1.2 & 1.4) are used for the comparison of the three correlations for the tube bundle geometry. For the circular tube correlations, the Lyon [86] correlation gives the highest prediction of Nusselt number, while the Sleicher et al. [139] correlation gives the lowest values. On the other hand, for the tube bundle correlations with P/D of 1.2, the Gräber and Rieger [49] correlation and the Ushakov et al. [155] correlation show good agreement. In comparison, the Mikityuk [95] correlation gives a lower Nusselt number. For the P/D of 1.4, these three correlations show very close results. However, heat transfer is also dependent on the flow regime (forced or natural convection) and the geometry. In the following, a classification of Nusselt correlations, dependent on geometry is shown. For each geometry key, correlations for forced and natural circulation have been found.

Nusselt correlations for plane surfaces

Churchill and Chu [29] described the Nusselt number for natural convection along a vertical surface to be

$$\mathrm{Nu}_{\mathrm{nat}} = \left[0.825 + 0.387 \left(\mathrm{Ra} \cdot f_1(\mathrm{Pr})^{\frac{1}{6}}\right)\right]^2 \tag{3.3}$$

With the function

$$f_1(\mathrm{Pr}) \;=\; \left[1+\left(\frac{0.492}{\mathrm{Pr}}\right)^{\frac{9}{16}}\right]^{-\frac{16}{9}} \tag{3.4}$$

it can be used for laminar and turbulent flow in the range of $0.1 \leq \mathrm{Ra} \leq 10^{12}$. According to Churchill and Usagi [31], the validity of the function $f_1(\mathrm{Pr})$ is given in a range of $0.001 \leq \mathrm{Pr} \leq \infty$. In the transition between laminar and turbulent flow ($10^8 \leq \mathrm{Ra} \leq 10^9$), the correlation can be used when discrepancies of 4% are acceptable [29]. Eq. (3.3) is based on water, but can be used for liquid metals as long as the Ra number is in the valid range. For liquid metals, Gregg and Sparrow [51] developed a heat transfer correlation for vertical surfaces. Chang et al. [22] extended that correlation for low Prandtl numbers $\mathrm{Pr} \leq 0.01$.

$$\mathrm{Nu} \;=\; 0.563 \cdot \mathrm{Pr}^{0.46}\,\mathrm{Gr}^{\frac{1}{4}} \tag{3.5}$$

This correlation can be used in range of $0.01 \leq \mathrm{Pr} \leq 0.05$. The wall temperature is assumed to be constant. For more specified correlations which can be used for flat surfaces and natural convection, especially for liquid sodium, please refer to Sheriff and Davies [136].
For forced convection, a theoretical based correlation for liquid metals is given by Holman [55].

$$\mathrm{Nu} \;=\; 0.530 \cdot \mathrm{Pe}^{\frac{1}{2}} \tag{3.6}$$

The range of validity according to Holman [55] is $\mathrm{Pr} \approx 0.01$ with the restriction of isothermal plate.
Another theoretical based correlation is given by Çengel et al. [20, p.402].

$$\mathrm{Nu} \;=\; 0.565 \cdot \mathrm{Pe}^{\frac{1}{2}} \tag{3.7}$$

It differs only marginally from eq. (3.6) and has a defined validity of $\mathrm{Pr} \leq 0.05$ [20].
To receive a single correlation that can be applied to all fluids, Churchill and Ozoe [30] curve-fitted existing data points from experiments and proposed a correlation which is valid for all Prandtl numbers.

$$\mathrm{Nu} \;=\; \frac{0.3387 \cdot \mathrm{Pr}^{\frac{1}{3}} \cdot \mathrm{Re}^{\frac{1}{2}}}{\left[1+\left(\frac{0.0468}{\mathrm{Pr}}\right)^{\frac{2}{3}}\right]^{\frac{1}{4}}} \tag{3.8}$$

The values computed by Churchill and Ozoe [30] and the values computed by Gregg and Sparrow [51] are in good agreement and are correlated within 1% for all Prandtl numbers.
For forced convection along flat surfaces, all correlations shown are restricted to conditions of uniform heating. All surfaces are assumed to be smooth so the free-stream is considered turbulence free [30].

Nusselt correlations for tubes

Jackson [62] studied turbulent mixed convection in smooth vertical tubes with the fluid liquid sodium. A derived (empirical) correlation for natural convection is divided in a laminar and a turbulent flow regime. The correlation for laminar flow is

$$\mathrm{Nu} \;=\; 0.675 \cdot \left(\mathrm{Gr} \cdot \mathrm{Pr}^2\right)^{0.25} \tag{3.9}$$

and for turbulent flow

$$\mathrm{Nu} \;=\; 5 + 0.4 \cdot \left(\mathrm{Gr} \cdot \mathrm{Pr}^2\right)^{0.3} \tag{3.10}$$

The correlation given in eq. (3.9) is valid in a range of $\mathrm{Gr} \cdot \mathrm{Pr}^2 \leq 3 \cdot 10^5$. The correlation given in eq. (3.10) is valid in a range of $\mathrm{Gr} \cdot \mathrm{Pr}^2 \geq 3 \cdot 10^5$. [62] gives the transition zone between laminar and turbulent flow at $\mathrm{Gr}\cdot\mathrm{Pr}^2 \approx 3\cdot10^5$ where neither of the correlations are fully valid. Because correlations for Nusselt numbers at natural convection for horizontal or inclined tubes are very rare, [62] can be used with caution.

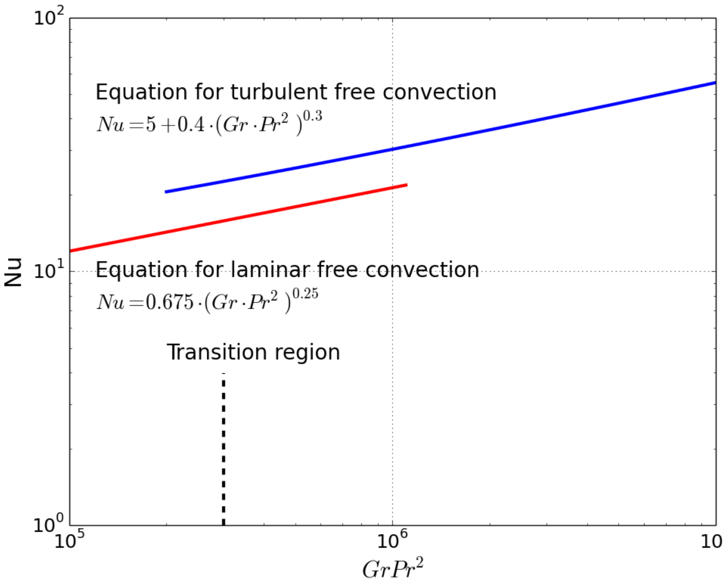

Fig. 3.3: Natural convection in a vertical tube $\mathrm{Nu} \sim \mathrm{GrPr}^2$ [62]

Lyon [85] gives a correlation for forced convection in tubes at low Prandtl numbers. The function of the correlation is based on

$$\mathrm{Nu} = a + b\cdot\mathrm{Pe}^c \tag{3.11}$$

where a, b and c are parameters dependent on material properties of the fluid and geometry of the flow region. It is valid for liquid metals in circular tubes with smooth surface.

$$\mathrm{Nu} = 7.0 + 0.025\cdot\mathrm{Pe}^{0.8} \tag{3.12}$$

According to Rust [125], restrictions to the correlation are uniform heat-flux and Reynolds numbers $Re \geq 10^4$.
Seban and Shimazaki [134] published a correlation for turbulent tube flow with constant wall temperature. The same correlation was found by Subbotin et al. [144] for sodium flow in a circular tube.

$$\mathrm{Nu} = 5.0 + 0.025\cdot\mathrm{Pe}^{0.8} \tag{3.13}$$

The range of validity for this correlation is given by $40 \leq \mathrm{Pe} \leq 1150$ [144]. Additionally, Kutateladze et al. [73] developed two equations which are also suitable for calculations of heat transfer coefficients in standard tubes.

$$\mathrm{Nu} = 3.3 + 0.014\cdot\mathrm{Pe}^{0.8} \tag{3.14}$$

and

$$\mathrm{Nu} = 5.0 + 0.0021\cdot\mathrm{Pe} \tag{3.15}$$

These correlations are valid in a range of $300 \leq \mathrm{Pe} \leq 15000$ and $\mathrm{Re} \geq 10^4$ [73]. For Péclet numbers in range of $20 \leq \mathrm{Pe} \leq 300$, equation

$$Nu = 0.7\cdot Pe^{\frac{1}{3}} \tag{3.16}$$

can be used, according to Kutateladze et al. [73]. Eq. (3.13), eq. (3.14), eq. (3.15) and eq. (3.16) fluids with low Prandtl numbers in range of 0.01 to 0.05 were used. For sodium, where Prandtl numbers are ≤ 0.006

$$\mathrm{Nu} = 5.9 + 0.015 \cdot \mathrm{Pe}^{0.8} \tag{3.17}$$

is more applicable. Validity of eq. (3.17) is given between $100 \leq \mathrm{Pe} \leq 1400$ and turbulent flows [73].
Borishanskii et al. [13] developed an empirical function for clean sodium flowing in a smooth tube to

$$\mathrm{Nu} = 4.36 + 0.016 \cdot \mathrm{Pe} \tag{3.18}$$

with constant heat flux. According to Borishanskii et al. [13], eq. (3.18) is valid for $30 \leq \mathrm{Pe} \leq 300$ and $\mathrm{Re} \geq 3 \cdot 10^3$.
Cheng and Tak [26] analyzed different correlations and found for NaK, mercury and LBE a best fitting correlation (eq. (3.19)).

$$\begin{aligned} \mathrm{Nu} &= A + 0.018 \cdot \mathrm{Pe}^{0.8} \\ A &= \begin{cases} 4.5 & Pe \leq 1000 \\ 5.4 - 0.0009 \cdot \mathrm{Pe} & 1000 \leq \mathrm{Pe} \leq 2000 \\ 3.6 & Pe \geq 2000 \end{cases} \end{aligned} \tag{3.19}$$

During the last half century, a huge amount of different correlations were found for different low Prandtl number fluids. In tab. B.2 most of the correlations found until 1959 are collected by Kutateladze et al. [73].

Nusselt correlations for triangular and square fuel pin arrangements

According to Pfrang and Struwe [115], heat transfer correlations used for fuel pins with triangular or square pattern can also be used for tube banks. At natural convection condition, due to Foust [46], the same correlations used for flat plates are also applicable for fuel pin arrangements and tube banks. However, the outer diameter has to be larger than 50mm. For laminar boundary flow and uniform wall temperature, Eckert [38] developed the correlation

$$\mathrm{Nu} = 0.508 \left[\frac{\mathrm{Gr}\mathrm{Pr}^2}{0.952 + \mathrm{Pr}} \right]^{\frac{1}{4}} \tag{3.20}$$

which is valid in the range of all Prandtl numbers, laminar boundary flow ($\mathrm{Re} \leq 2300$) and $\mathrm{Gr} \leq 10^8$.
The best fitting correlation for laminar flow and uniform heat flux is given by Chang et al. [22]. It is valid in the range of $0.01 \leq \mathrm{Pr} \leq 0.05$.

$$\mathrm{Nu} = 0.563 \mathrm{Pr}^{0.46} \mathrm{Gr}^{\frac{1}{4}} \tag{3.21}$$

Several Nusselt correlations are given for turbulent flow, but similar to cases with flat surfaces, these correlations are doubtful to be applicable to liquid metals [46].
At forced convection flow condition and triangular arrangements, Dwyer and Tu [37] derived the equation

$$\mathrm{Nu} = 0.93 + 10.81 \cdot (P/D) - 2.01 \cdot (P/D)^2 + 0.0252 \cdot (P/D)^{0.273} \cdot (\Psi \mathrm{Pe})^{0.8} \tag{3.22}$$

Accordingly Friedland and Bonilla [47]

$$\mathrm{Nu} = 7.0 + 3.8 \cdot (P/D)^{1.52} - 0.027 \cdot (P/D)^{0.27} (\Psi \mathrm{Pe})^{0.8} \tag{3.23}$$

derived two correlations which describe the heat transfer of liquid metal flowing through triangular bundle of circular rods. In eq. (3.22) and eq. (3.23), Ψ is the ratio of eddy diffusivity of heat (ϵ_H) to the diffusivity of momentum (ϵ_M). An empirical equation for Ψ can be described as

$$\Psi \;=\; 1 - \frac{1.82}{\mathrm{Pr} \cdot \left(\frac{\epsilon_M}{\upsilon}\right)^{1.4}_{\max}} \tag{3.24}$$

For calculation applicability, the approximation

$$\lg\left(\frac{\epsilon_M}{\upsilon}\right) \;\approx\; 0.864 \cdot \lg(\mathrm{Re}) - 0.24 \cdot (P/D) - 2.12 \tag{3.25}$$

can be used for the ratio of eddy diffusivity to the diffusivity of momentum. The major difference between eq. (3.22) and eq. (3.23) are assumptions in the velocity profile. This gives different ranges for validity, where eq. (3.22) is recommended at $70 \leq \mathrm{Pe} \leq 10^4$ and $1.375 \leq P/D \leq 2.2$ and eq. (3.23) is recommended at $0 \leq \mathrm{Pe} \leq 10^5$ and $1.3 \leq P/D \leq 10$. Both experiments were performed with mercury as fluid [37], [47].

Maresca and Dwyer [88] used mercury in a 13 pin bundle and NaK in a 19 pin bundle. In both cases, the Pitch-to-Diameter ratio was 1.75. The derived correlation

$$\mathrm{Nu} \;=\; 6.6 + 3.126 \cdot (P/D) - 1.184 \cdot (P/D)^2 + 0.0155\,(\Psi \mathrm{Pe})^{0.86} \tag{3.26}$$

is valid in the range of $70 \leq \mathrm{Pe} \leq 10^4$.

Subbotin et al. [144] derived a correlation for the Pitch-to-Diameter ratio of $1.1 \leq P/D \leq 1.5$ and Péclet numbers between $80 \leq \mathrm{Pe} \leq 4000$.

$$\mathrm{Nu} \;=\; 0.58 \left(\frac{2\sqrt{3}}{\pi} \cdot (P/D)^2 - 1\right)^{0.55} \cdot \mathrm{Pe}^{0.45} \tag{3.27}$$

Borishanskii et al. [14] show results gained in 7 pin arrangements with $1.1 \leq P/D \leq 1.5$ by using different liquid metal coolants like sodium and mercury. The correlation was extended by measurements obtained by the IPPE ([95], [115]).

$$\begin{aligned} \mathrm{Nu} \;&=\; 24.15 \log\left(-8.12 + 12.76 \cdot (P/D) - 3.65 \cdot (P/D)^2\right) + 0.0174\left(1 - e^{-6(\cdot(P/D)-1)}\right) \cdot \mathrm{B} \\ B \;&=\; \begin{cases} 0 & 60 \leq Pe \leq 200 \\ (\mathrm{Pe} - 200)^{0.9} & 200 \leq Pe \leq 2200 \end{cases} \end{aligned} \tag{3.28}$$

Derived by three sets of measurements of the fluid NaK and Pitch-to-Diameter ratios of 1.25, 1.6 and 1.95, Gräber and Rieger [49] give a correlation as

$$\mathrm{Nu} \;=\; 0.25 + 6.2 \cdot (P/D) + (-0.007 + 0.032 \cdot (P/D)) \cdot \mathrm{Pe}^{0.8 - 0.024 \cdot (P/D)} \tag{3.29}$$

The fluid temperature varied from 100°C to 425°C. Accordingly, the Prandtl number varied from 0.011 to 0.024. The correlation is valid in the range of $1.2 \leq P/D \leq 2$ and $150 \leq \mathrm{Pe} \leq 4000$.

The correlation given by Ushakov et al. [155] slightly depends on the geometry of the pin arrangements. Due to Mikityuk [95], the correlation can therefore be simplified to

$$\mathrm{Nu} \;=\; 7.55 \cdot (P/D) - \frac{20}{(P/D)^{13}} + \frac{0.041}{(P/D)^2} \mathrm{Pe}^{0.56 + 0.19 \cdot (P/D)} \tag{3.30}$$

Kazimi and Carelli [69] developed a correlation which is valid for $10 \leq \mathrm{Pe} \leq 5000$ and $1.1 \leq P/D \leq 1.4$. Different experimental campaigns were performed with Na, Hg and NaK.

$$\mathrm{Nu} \;=\; 4 + 0.16 \cdot (P/D)^5 + 0.33 \cdot (P/D)^{3.8} \left(\frac{\mathrm{Pe}}{100}\right)^{0.86} \tag{3.31}$$

The latest correlation was developed by Mikityuk [95] using more than 600 different data points, which had been collected from different sets of test data. The used data has been the result of many experimental campaigns used for the development of previous correlations. Measurements from the BREST lead-cooled reactor project [166] have been used additionally. Because the BREST lead-cooled reactor project applied square lattice fuel assemblies, this correlation can be used for both, triangular and square lattice.

$$\mathrm{Nu} \;=\; 0.047 \left(1 - e^{-3.8\cdot((P/D)-1)}\right) \left(\mathrm{Pe}^{0.77} + 250\right) \tag{3.32}$$

This correlation is valid in a range of $30 \leq \mathrm{Pe} \leq 5000$ and $1.1 \leq P/D \leq 1.95$. According to Mikityuk [95], the correlation is also valid for very low Prandtl numbers.

It is possible to transfer correlations for triangular arrays to square array application. The dependency can be described with

$$(P/D)_{triangular} \;=\; 1.075\,(P/D)_{square} \tag{3.33}$$

Heat transfer correlations derived for triangular pin arrangements can be applied to square lattice [115]. As this transfer function is not verified yet, Pfrang and Struwe [115] and Foust [46] suggest to verify calculation results before application.

Ushakov et al. [155] performed an experimental study with mercury and NaK. The fluid was electrical heated by cylindrical rods in square lattice. However, the uncertainty of the derived correlation is given at a range of 20% at a Pitch-to-Diameter ratio of 1 [46].

$$\mathrm{Nu} \;=\; 0.48 + 0.0133 \cdot \mathrm{Pe}^{0.7} \tag{3.34}$$

Mikityuk [95] used measurements gained by the BREST Report [166], which also provides its own correlation for square arranged rod bundles. Pfrang and Struwe [115] suggest the correlation given in eq. (3.35) is assumed to be valid in range of $1.28 \leq P/D \leq 1.46$ and $100 \leq \mathrm{Pe} \leq 1600$.

$$\mathrm{Nu} \;=\; 7.55 \cdot (P/D) - 20 \cdot (P/D)^{-5} + \frac{0.0354}{(P/D)^2} \cdot \mathrm{Pe}^{0.56+0.204\cdot(P/D)} \tag{3.35}$$

A NaK experiment with a 25-pin rod bundle was performed by Zhukov et al. [165]. In the more detailed report, Zhukov et al. [166] suggests a correlation

$$\begin{aligned} \mathrm{Nu} \;&=\; 7.55 \cdot (P/D) - 14 \cdot (P/D)^{-5} + \mathrm{A} \cdot \mathrm{Pe}^{0.64+0.264\cdot(P/D)} \\ A \;&=\; \begin{cases} 0.007 & \text{for smooth rods} \\ 0.009 & \text{for spacer } \epsilon_g = 10\% \\ 0.010 & \text{for spacer } \epsilon_g = 20\% \end{cases} \end{aligned} \tag{3.36}$$

where the influence of a spacer grid had been investigated as well. Spacer grids were used with the spacer grid (ϵ_g) obstructing 10% and 20% of the cross section. The range of validity for A = 0.007 is given by $1.2 \leq P/D \leq 1.5$ and $10 \leq \mathrm{Pe} \leq 2500$ although the experimentally covered range is only $1.25 \leq P/D \leq 1.46$ and $60 \leq \mathrm{Pe} \leq 2000$.

Implementation

The previously shown Nusselt correlations are selected to contribute to the heat transfer package in ATHLET for sodium applications. The previously developed methodology for the qualification of material properties of sodium in ATHLET (see fig. 3.1) is applied here. However, the methodology cannot be applied directly but needs to be modified slightly. The reason is that opposing sodium as single fluid, there exists a rather large amount of possible Nusselt correlations with different validity ranges to model heat transfer. Therefore, it should be possible to let the user select the best fitting correlation for a given HCO in ATHLET. Additionally, it must be ensured that older ATHLET input decks are still compatible. This divides the ATHLET implementation procedure in following steps:

- Library for Nusselt correlations for sodium applications
    - Create library in ATHLET
- Input deck
    - Compatibility
    - Selectable Nusselt correlations per HCO
- Calculation process
    - Extension of heat transfer package for sodium
    - Preserve original calculation process for non-sodium applications

The library for Nusselt correlations for sodium applications in ATHLET was implemented as a first step. It directly uses calculation results (e.g. temperature, dimensionless numbers, geometrical values) from ATHLET and provides the Nusselt number to the selected HCO. This far, however, the library is not called yet by ATHLET. Therefore, the input deck is modified in the next step.

Input deck modification

In ATHLET, conjugate heat transfer (see lst. 3.1) is modeled by HCOs. Heat structures are defined in the HEATCOND section of the input deck. An example is given in lst. 3.1. It can be seen, that two sides are connected by one HCO. Each side can be a TFO or more abstract, a defined signal. The HCO then needs to be described further. It is possible to use predefined models for heat transfer objects like a heater rod or a steam generator. Afterwards, the structure of the HCO needs to be described further in detail. For example a fuel rod's HCO would consist of the fuel, a gap and the surrounding cladding. A simple example of such a cylinder shaped geometry is shown in fig. 2.5. More information about the shape of a HCO can be found in [79].

```
K---- H-coreFI
@      AOLH           SBOLH        SEOLH          AORH       SBORH     SEORH
      'ADIABAT'          0.0          0.0       'coreFI'      1.078     1.928
@
@      NIHC0    N10    N20    N30    IGEO0    ICOMP0   ACOMP0    ICHF0  IPRIPLO
           1      4      2      0        2         1  'RODFI'        1        0
@
----- GEOMETRY
@      FPARH          TL0
      5859.0    7.773D-03
@
@        SG0         Z0     DI0       DS10      GAP10       DS20   GAP20    DS30
      0.000     -5.162     0.0   2.71D-03   1.15D-04   0.45D-03     0.0     0.0
      0.850     -4.312     0.0   2.71D-03   1.15D-04   0.45D-03     0.0     0.0
@
----- HTCDEF
@      AIAL(1...4)                                                 XHTC
      'DUMMY'        'HTCCALC'        'HTCCALC'       'DUMMY'        1
@
@        SH0       HTCL0(1...4)                          QTHRU0
      0.000        0.0      1.0D+4      1.0D+4     0.0       0.0
      0.850        0.0      1.0D+4      1.0D+4     0.0       0.0
@
----- MATPROP
@      AMATL(1...3)
      'MOX'       'AUST-STEEL'      'DUMMY'
@
```

Lst. 3.1: Example of a HCO in the input deck

After the definition of the geometry in section ‘GEOMETRY’, each material is defined by HTCDEF, the heat transfer coefficient definition section within HEADCOND. Here, the user can choose if the corresponding HTC is derived by a given input value or with a correlation for the Nusselt number. To use the implemented library for Nusselt correlations for sodium applications, a new parameter XHTC of type Integer is implemented in HTCDEF. If it is set to 1, the ATHLET code will run without contacting the library. This is necessary, to make sure, older input decks are still compatible with the modified ATHLET code. If the parameter XHTC is defined according to tab. 3.1, it specifies the Nusselt correlation. However, if a static heat transfer coefficient is chosen by the user, none of the correlations will be taken into reference.

Correlation	**XHTC**	**Range of validity, comments**
Nusselt correlations for plane surfaces		
eq. (3.3)	10	$0.1 \leq \mathrm{Ra} \leq 10^{12}$, $0.001 \leq \mathrm{Pr} \leq \infty$ with eq. (3.4)
eq. (3.5)	11	$0.005 \leq \mathrm{Pr} \leq 0.01$, isothermal plate
eq. (3.6)	12	$\mathrm{Pr} \sim 0.1$, isothermal plate
eq. (3.7)	13	$\mathrm{Pr} \leq 0.05$, isothermal plate
eq. (3.8)	14	$0 \leq \mathrm{Pr} \leq \infty$, isothermal plate
Nusselt correlations for tubes		
eq. (3.9)	20	$\mathrm{Pr} \ll 1$, $\mathrm{Gr} \cdot \mathrm{Pr}^2 \leq 3 \cdot 10^5$
eq. (3.10)	21	$\mathrm{Pr} \ll 1$, $\mathrm{Gr} \cdot \mathrm{Pr}^2 \geq 3 \cdot 10^5$
eq. (3.12)	22	$0.01 \leq \mathrm{Pr} \leq 0.05$, $\mathrm{Re} \geq 10^4$, constant heat flux
eq. (3.13)	23	$\mathrm{Pr} \ll 1$, $\mathrm{Re} \geq 10^4$, $40 \leq \mathrm{Pe} \leq 1150$, constant wall temperature
eq. (3.14)	24	$0.01 \leq \mathrm{Pr} \leq 0.05$, $\mathrm{Re} \geq 10^4$, $300 \leq \mathrm{Pe} \leq 15000$
eq. (3.15)	25	$0.01 \leq \mathrm{Pr} \leq 0.05$, $\mathrm{Re} \geq 10^4$, $300 \leq \mathrm{Pe} \leq 15000$
eq. (3.16)	26	$0.01 \leq \mathrm{Pr} \leq 0.05$, $20 \leq \mathrm{Pe} \leq 300$
eq. (3.17)	27	$\mathrm{Pr} \leq 0.006$, $100 \leq \mathrm{Pe} \leq 1400$
eq. (3.18)	28	$\mathrm{Pr} \leq 0.01$, $\mathrm{Re} \geq 3000$, $30 \leq \mathrm{Pe} \leq 300$, constant heat flux
eq. (3.19)	29	$0.01 \leq \mathrm{Pr} \leq 0.1$
Nusselt correlations for triangular and square fuel pin arrangements		
eq. (3.20)	30	$\mathrm{Re} \leq 2300$, $\mathrm{Gr} \leq 10^8$, constant wall temperature
eq. (3.21)	31	$0.01 \leq \mathrm{Pr} \leq 0.05$, $\mathrm{Re} \leq 2300$, $\mathrm{Gr} \leq 10^8$, constant heat flux
eq. (3.32)	48	$\mathrm{Pr} \ll 1$, $1.1 \leq P/D \leq 1.95$, $30 \leq \mathrm{Pe} \leq 5000$
Nusselt correlations for square fuel pin arrangements		
eq. (3.34)	32	$\mathrm{Pr} \ll 1$, $P/D = 1$
eq. (3.35)	33	$\mathrm{Pr} \ll 1$, $P/D = 1.46$ and 1.28, $100 \leq \mathrm{Pe} \leq 1600$
eq. (3.36)	34	$\mathrm{Pr} \ll 1$, $1.2 \leq P/D \leq 1.5$, $10 \leq \mathrm{Pe} \leq 2500$
Nusselt correlations for triangular fuel pin arrangements		
eq. (3.22)	40	$\mathrm{Pr} \ll 1$, $1.375 \leq P/D \leq 2.2$, $70 \leq \mathrm{Pe} \leq 10^4$, with (3.25)
eq. (3.23)	41	$\mathrm{Pr} \ll 1$, $1.3 \leq P/D \leq 10$, $0 \leq \mathrm{Pe} \leq 10^5$, with (3.25)
eq. (3.26)	42	$\mathrm{Pr} \ll 1$, $1.3 \leq P/D \leq 3$, $70 \leq \mathrm{Pe} \leq 10^4$
eq. (3.27)	43	$\mathrm{Pr} \ll 1$, $1.1 \leq P/D \leq 1.5$, $80 \leq \mathrm{Pe} \leq 4000$

Correlation	XHTC	Range of validity, comments
eq. (3.28)	44	$\mathrm{Pr} \ll 1$, $1.1 \leq P/D \leq 1.5$, $60 \leq \mathrm{Pe} \leq 2200$
eq. (3.29)	45	$\mathrm{Pr} \ll 1$, $1.2 \leq P/D \leq 2.0$, $150 \leq \mathrm{Pe} \leq 4000$
eq. (3.30)	46	$\mathrm{Pr} \ll 1$, $1.3 \leq P/D \leq 2.0$, $0 \leq \mathrm{Pe} \leq 4000$
eq. (3.31)	47	$\mathrm{Pr} \ll 1$, $1.1 \leq P/D \leq 1.4$, $10 \leq \mathrm{Pe} \leq 5000$

Tab. 3.1: Implemented Nusselt correlations for sodium with range of validity

Code modification

A lot of different subroutines are involved during an ATHLET calculation run. In fig. 3.4 only a small part of the ATHLET calculation process is shown in a flow chart. It illustrates the read-in and calculation process for conjugate heat transfer. In ATHLET all TFOs are created first and then heat structures are added to the simulation. The reason is the dependency of heat volumes on fluid volumes [5].
To account for the above-defined modification in the input, some subroutines had to be modified in ATHLET (blue color in fig. 3.4):

- HINPUT
- HCINP
- HOBJ
- MHTCN
- MHTCN1
- MHTCN2

Mainly, the modification is for the creation of interfaces to the newly developed Nusselt correlation library for sodium applications. On the other hand, it was made sure to maintain a smooth running process with the claim of compatibility to older input decks. However, the calculation of Nusselt numbers as well as their storage in memory had to be newly created. Those subroutines or modules are (green color in fig. 3.4):

- MNUCORR
- ALLOCHTC
- CHTC

Fig. 3.4 illustrates the handling of HCOs in ATHLET. During the read-in process of the input deck, heat structures are generated according to the user input. TFOs are generated before HCOs, because HCOs depend on attached TFOs. The formation of HCVs in ATHLET is geared to the CVs of the flow regime previously formed. For reasons of readability, the calculation process of ATHLET is not shown entirely in fig. 3.4. For full information about the ATHLET programming structure, please refer to Lerchl et al. [80]. During each time step in ATHLET, e.g., material properties of the fluid are calculated dependent on calculation results, i.e., temperature, velocity, pressure and steam void fraction. The subroutines responsible for these calculations are not shown in fig. 3.4.

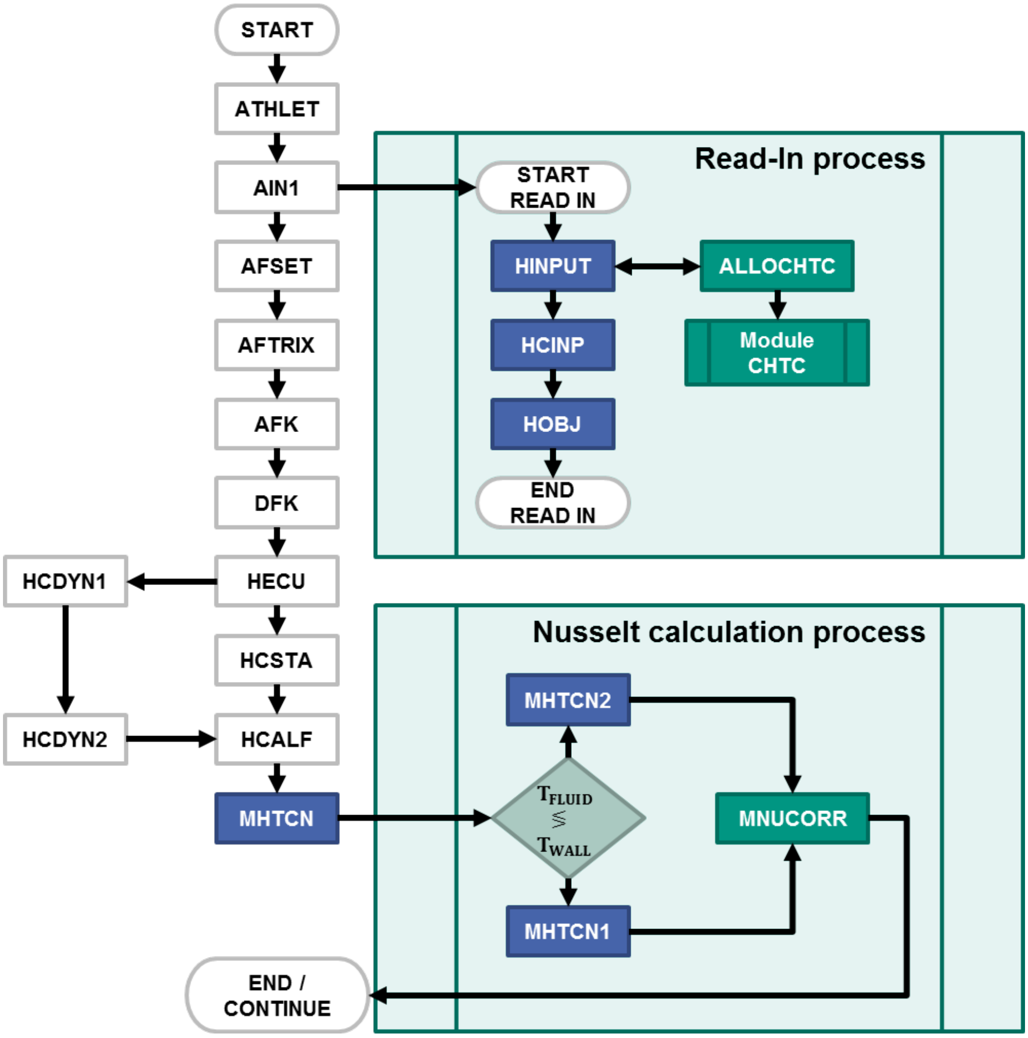

Fig. 3.4: HCO handling and calculation of Nusselt numbers

As one of the first steps after an ATHLET calculation is executed, AIN1 starts reading the input deck, which is defined by the user and contains, e.g., model information, boundary conditions and initial conditions. Different parts of the input deck are handled by different subroutines in the code. HINPUT reads all defined HCOs that are specified and activated in the input deck. Then subroutines to allocate modules are called to save these definitions out of the input text file. In the end of the HINPUT run, HINPUT calls HCINP which derives data about HCV geometry and model data. Elementary checks of the input are performed as well. In case of incorrect specifications by the user, the subroutine stops the simulation run and returns information about the error. If all plausibility checks by HCINP have succeeded, HCOBJ reads parts of the HCO definition that is specified in the input deck. One task of this subroutine is to read HTC data from the input deck. At this position, the new identifier XHTC is specified. This parameter is then stored in the new module CHTC to be accessible at every time step during the calculation run in combination with the referring HCO. The newly created subroutine ALLOCHTC defines (allocates) the dimension of the module CHTC.
Following the simulation process of ATHLET (white boxes in fig. 3.4), it can be seen, no further changes are yet necessary. As soon as the HECU subroutine is called during the simulation run, conjugate heat transfer calculations are run. HECU is used for steady state and transient calculation. MHTCN is used to determine the direction of heat transfer.

Austregesilo et al. [5] show the necessity of this separation between heating and cooling for nucleate boiling, transition boiling and film boiling. The code structure has been developed by GRS accordingly. However, there is no observable difference between heating and cooling a liquid, as long as boiling is not present. For the modification, MHTCN is used to distinguish the direction of heat transfer ($T_{wall} > T_{fluid}$ or $T_{wall} < T_{fluid}$) and therefore if the work fluid is heated or cooled. If the fluid is cooled by its bounding wall, MHTCN1 is executed and if the fluid is heated by its bounding wall, MHTCN2 is executed. Both subroutines are modified to calculate the Nusselt number with the previously specified correlation. For this process, the subroutine MNUCORR is called, if sodium is used as work fluid and the library for Nusselt number correlations is activated (see fig. 3.4).
After the Nusselt number is calculated by MNUCORR, the result is saved to the module CHTC. It should be noted here, that each HCV has its own Nusselt number. From there, it can be retrieved by the simulation when needed. CHTC is a global module and can be accessed from anywhere in the code. The input deck is only read once, also are the subordinated subroutines. All other subroutines used for the computation of heat transfer coefficients are run at every time step during the ATHLET calculation. For more detailed information about the specific code modification, please refer to [132].

Verification

A verification process has been worked out, to ensure the ATHLET calculation of the Nusselt number is accurate. Each Nusselt correlation given in tab. 3.1 is tested by that process and evaluated later on. As previously described, the ATHLET code is extended for liquid metal heat transfer calculations with focus on sodium applications. A direct comparison of Nusselt numbers is chosen for the verification process. Eq.3.1 describes the HTC calculated by ATHLET. The correlation for the Nusselt number is a function of specific input parameters. To keep the uncertainty at a minimum level, the Nusselt numbers calculated by ATHLET are compared to Nusselt numbers calculated by a Python program. The Python program has been created especially for the verification process to handle large amounts of calculation tasks. A WRITE command line in the ATHLET code is added to each correlation. If switched on (not commented in source code), ATHLET prints calculation results and needed correlation input parameters which can be recorded. This way, a csv-file is created for verification purposes.
After the ATHLET code modification, the PHENIX NCT transient is used to calculate Nusselt numbers. Exactly one position in the modeled PHENIX primary circuit is specified to calculate the Nusselt number via correlation with the modified calculation routines. The reason why only one position is chosen is to avoid mixtures of different flow regimes. The position is the inner core HCO (H-coreFI) of the PHENIX core. It is considered the most sensitive and important position in the core. This way, the implementation itself can be verified. If there was no output by ATHLET, the correlation would not be used. This can be seen as a global function check procedure for each correlation. As a second and more important benefit of this process, the Nusselt correlation results can be checked for accuracy. Dependent on the input parameters accuracy, the Nusselt correlation results can have an error in the order of 10^{-6} to 10^{-4} (conservative estimate in percentage $\approx 0.005\%$). This numerical error is considered to be larger than the ATHLET internal numerical error of the calculation because of the restriction of decimal places in the created csv-file.
The csv-file is used as input to the Python program. The Python program uses input parameters to recalculate the Nusselt correlation. In a next step, the two groups of calculated Nusselt numbers are plotted. The whole process is illustrated in a flow chart given in fig. 3.5.

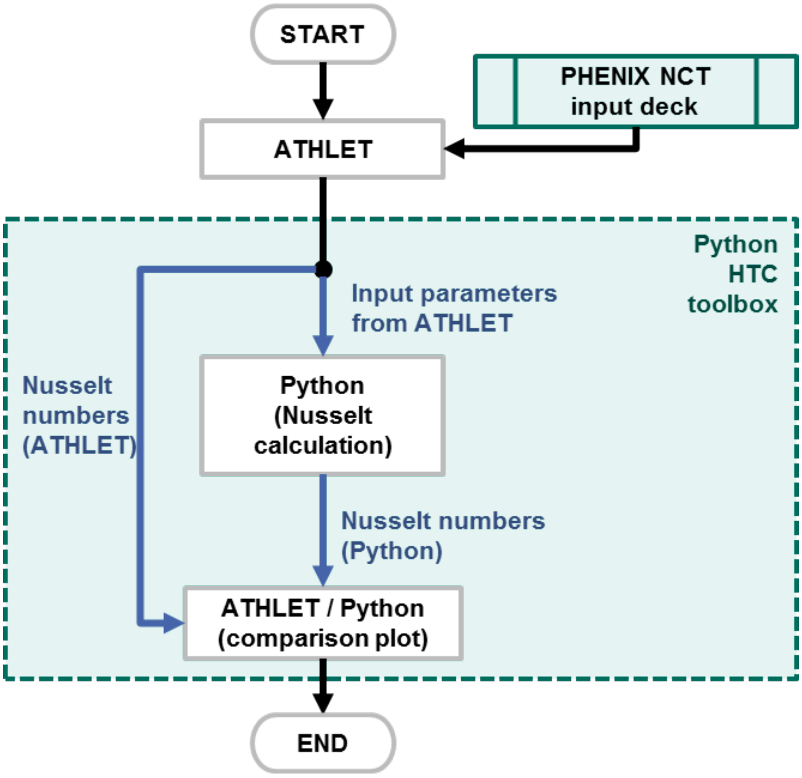

Fig. 3.5: Nusselt correlation verification process with the Python-HTC-toolbox

Following this methodology, the collected data points can then be visualized within one diagram. The Python results (Nusselt numbers) are used as abscissa values and ATHLET results (Nusselt numbers) are used as ordinate values. Additionally, a dashed line is plotted where Python results are used as abscissa and ordinate value. Fig. 3.6 illustrates the process result for the Nusselt correlation described by eq.3.32.

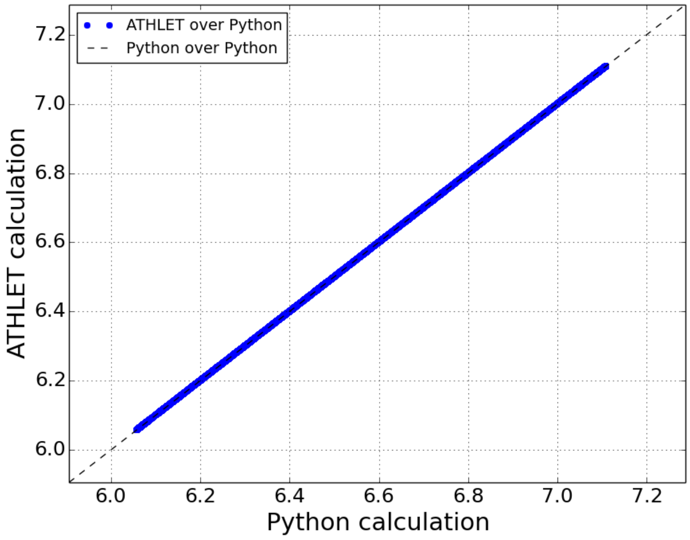

Fig. 3.6: Verification of Mikityuk [95] (eq.3.32, XHTC 48)

The verification process only checks the accuracy of the calculation results. This way, all correlations can be checked at the same position. However, it does not make sense, if a correlation for plate heat transfer is used in a rod bundle geometry. This will be discussed in the next chapter. Verification results for all correlations are given in Appendix B.

Assessment

Most of the Nusselt correlations found in the open literature are based on experiments. The range of conducted experiments for correlations is of restricting factor for the range of validity. It was also found that theoretically derived Nusselt correlations have a limited range of validity. For a full validation of all Nusselt correlations for the PHENIX NCT, detailed measurements at all regions of conjugate heat transfer are necessary. For the PHENIX NCT, the PHENIX reactor had not been applied with measuring devices in such detail, because other effects were in focus of that test. As a result, the most promising implemented Nusselt correlations for the PHENIX NCT are discussed, based on the range of validity specified in the literature.
The previously mentioned *Python-HTC-toolbox* was not exclusively created to serve the purpose of verification. It is also used to gather information about the valid ranges of each implemented Nusselt correlation during the PHENIX NCT. The assessment process used in the Python-HTC-toolbox is shown in fig. 3.7 to give a better understanding. The output is shown in the following paragraphs, where results from the *Python-HTC-toolbox* are illustrated and discussed. Detailed data of all Nusselt correlation assessment data is provided in Appendix B.

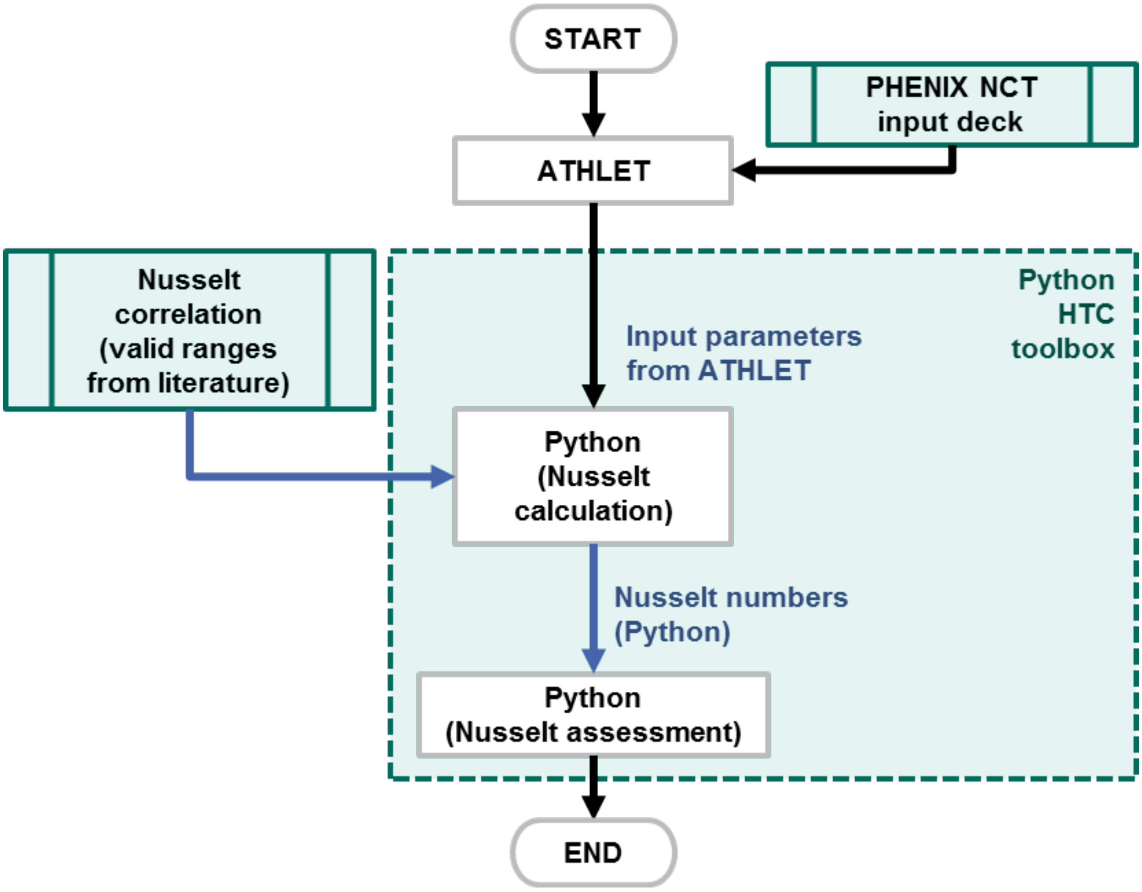

Fig. 3.7: Assessment of Nusselt correlations with the Python-HTC-toolbox

Eckert [38] correlation

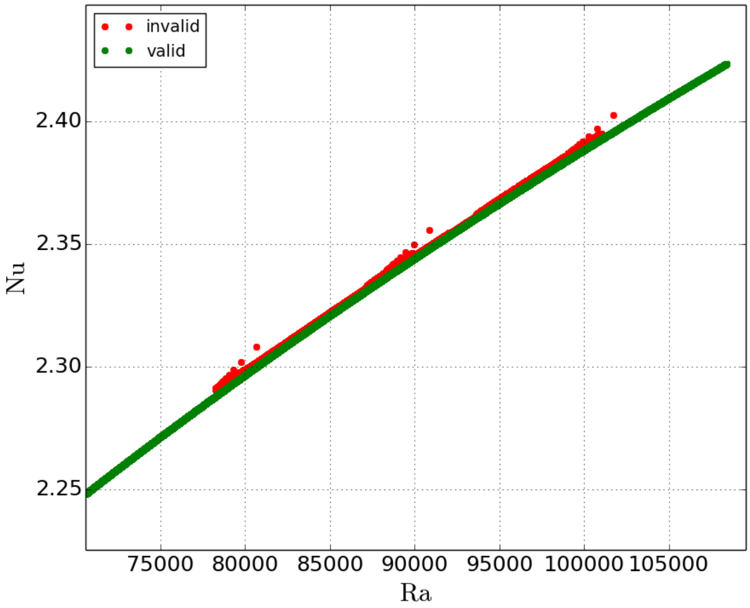

Fig. 3.8: Nusselt numbers in NCT with Eckert [38] correlation

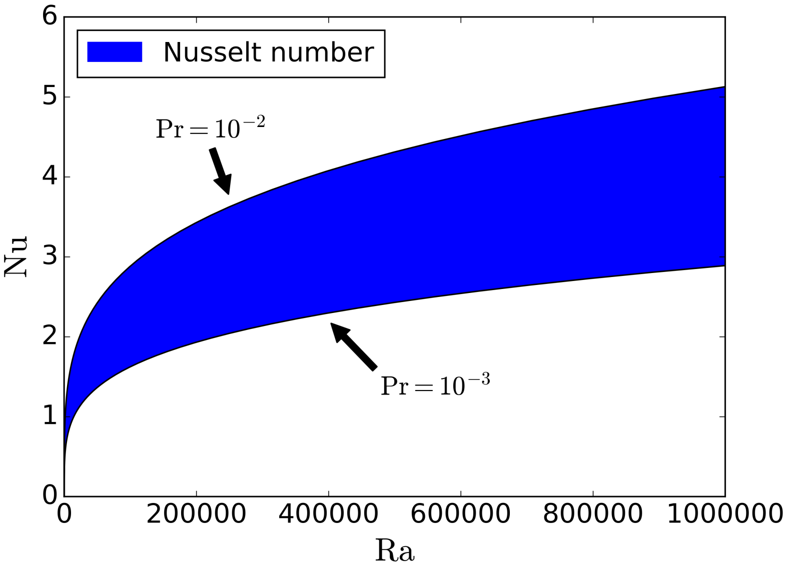

Fig. 3.9: Range of valid Nusselt numbers according to Eckert [38]

The Eckert [38] correlation generally shows good applicability over the whole range of the PHENIX NCT case scenario. In fig. 3.8 all results of Nusselt numbers are printed. With the given range of validity provided by Eckert [38], all valid Nusselt numbers are printed in green. Results derived outside the valid range are printed in red. Nusselt numbers are plotted here over Rayleigh numbers, because the correlation is a function of Prandtl

number and Grashof number. The invalid Nusselt numbers are because of the transition to turbulent flow. As previously described, the correlation is only valid for laminar flow. It can be seen, there are multiple possible Nusselt numbers for a given Rayleigh number. This is due to different combinations of Prandtl numbers and Grashof numbers. However, those higher Nusselt numbers appear to be in a not valid range, according to the boundaries given by the authors. The range of valid Nusselt numbers covers a huge field of Prandtl numbers. In fig. 3.9 the correlation is printed for a range of Prandtl numbers from $10^{-3} \leq \mathrm{Pr} \leq 10^{-2}$.
Some restrictions to the correlations given in the literature cannot be represented with the Python-HTC-toolbox. A closer look at eq. (3.20) shows, only natural circulation considered. Additionally, the experiments have been conducted with uniform wall temperature. Fuel subassemblies show a different temperature distribution over vertical length. Eckert [38] also notes, the correlation to be in valid range only at laminar boundary flow condition. Those reasons lead to the conclusion, to not consider the Eckert [38] correlation for the PHENIX NCT case scenario.

Kazimi and Carelli [69] correlation

Kazimi and Carelli [69] derived a Nusselt correlation by combining several experiments with the coolants Na, Hg and NaK. The PHENIX NCT is applied, to check the valid range of this correlation (fig. 3.10). With the given range of validity provided by Kazimi and Carelli [69], all valid Nusselt numbers are printed in green. Results derived outside the valid range are printed in red. Nusselt numbers are plotted here over Péclet numbers, as the correlation is a function of the pitch-to-diameter ratio number and the Péclet number, which itself is defined as the product of Reynolds and Prandtl number (see eq. (3.31)).

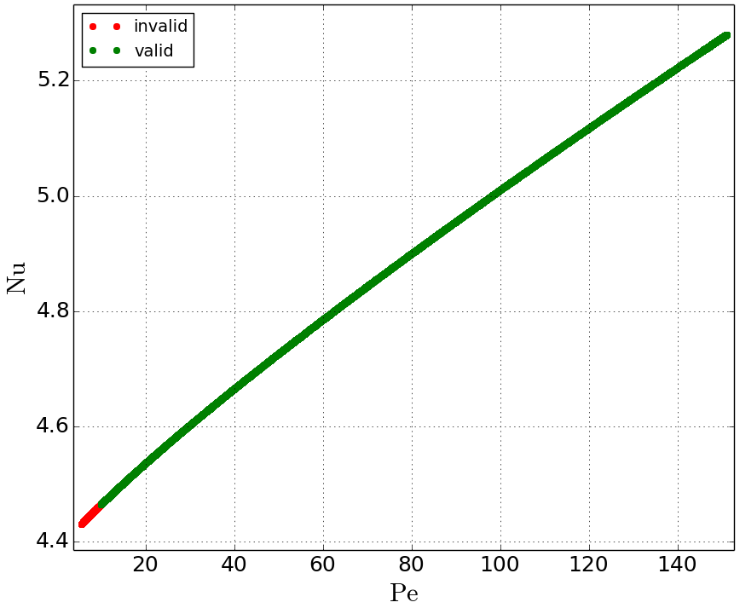

Fig. 3.10: Nusselt numbers in NCT with Kazimi and Carelli [69] correlation

The Kazimi and Carelli [69] correlation shows very good agreement. A very large range of Nusselt numbers is in valid range. However, in comparison to other valid Nusselt numbers generated by other correlations, this specific correlation shows slightly smaller values as result. This can lead to an under-prediction of the cladding temperature. For the theoretical result it means the structure material doesn't heat up that much, whenever the correlation is applied. To have a more conservative computation of accident scenarios, it does make sense to use a correlation, that is more conservative.

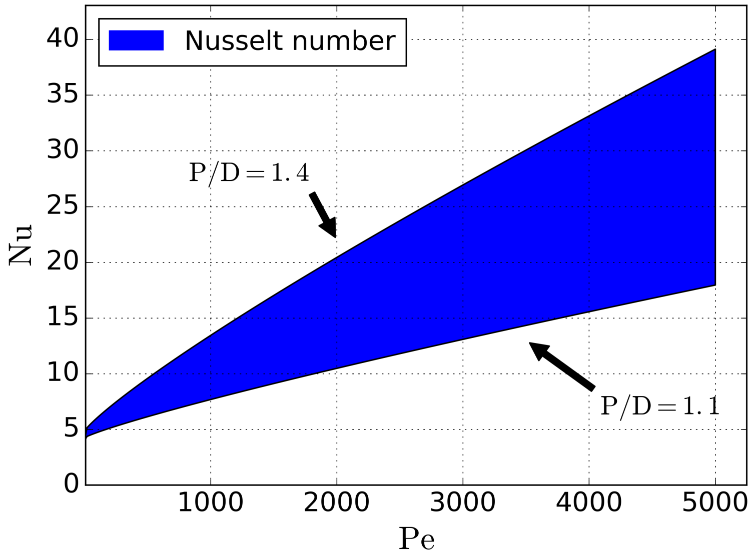

Fig. 3.11: Range of valid Nusselt numbers according to Kazimi and Carelli [69]

In fig. 3.11, the range of valid Nusselt numbers is shown. It can be seen, the higher the Péclet number, the higher the range of possible Nusselt numbers. At a low range of Péclet numbers, the pitch-to-diameter is dominant. The heat capacity of liquid sodium is approximately half the heat capacity of water. Additionally, it should be mentioned that the heat conductivity of sodium is approximately 160 times higher than the heat conductivity of water. Based on these observations, heat transfer to sodium can be assumed to be of diffusive character, especially at low flow velocities (low Péclet numbers). Accordingly, the range of Nusselt numbers at a given (constant) Péclet number can be argued with the range of pitch-to-diameter ratios that are given as valid for $1.1 \leq \mathrm{Pe} \leq 1.4$. The first two terms on the right hand side of eq. (3.31) are also independent from flow characteristics. It can be considered as conductive part of the Nusselt number.

Mikityuk [95] correlation

Mikityuk [95] developed the latest Nusselt correlation for liquid metals in bundle geometries. It must be mentioned here, that the correlation uses data points from experiments of different geometrical shape: triangular arranged bundles and square arranged bundles. The experiments have been taken from literature. With the given range of validity provided by Mikityuk [95], all valid Nusselt numbers are printed in green (fig. 3.12). Results derived outside the valid range are printed in red. Nusselt numbers are plotted here over Péclet numbers, because the correlation is a function of the pitch-to-diameter ratio number and the Péclet number, which itself is defined as the product of Reynolds and Prandtl number (see eq. (3.35)).

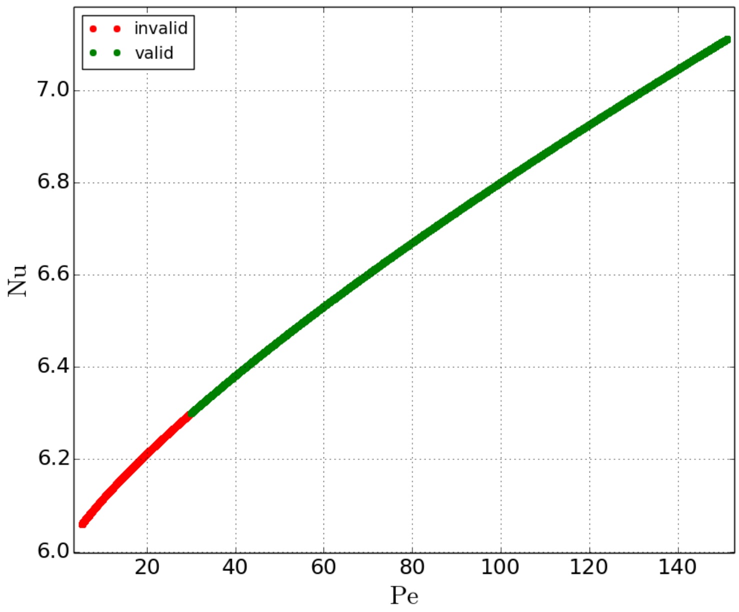

Fig. 3.12: Nusselt numbers in NCT with Mikityuk [95] correlation

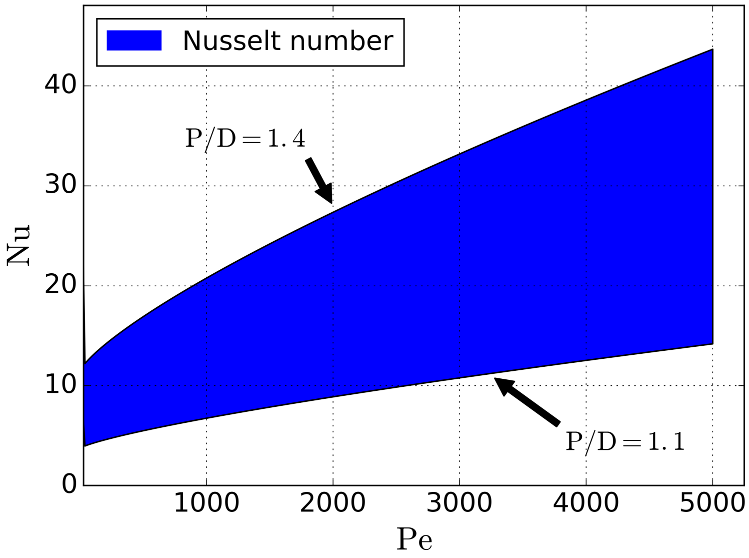

Fig. 3.13: Range of valid Nusselt numbers according to Mikityuk [95]

The Mikityuk [95] correlation shows very good agreement. A large range of Nusselt numbers is in valid range. The correlation is based on a high number of data points. However, the correlation is not only based on sodium experiments. In comparison to other valid Nusselt numbers generated by other correlations (different from Kazimi and Carelli [69], see fig. 3.2), the correlation by Mikityuk [95] shows very similar quantities. The maximum Nusselt number derived by Mikityuk [95] is about 45 and can be seen in fig. 3.13. It can be argued that the range of validity given by Mikityuk [95] is smaller than results given by Kazimi and Carelli [69]. On the other hand, the derived Nusselt numbers are considered to be more realistic even in non-valid range, if compared with other correlations. Additionally, the Mikityuk [95] correlation uses more experimental data points.

Summary

The extension of the ATHLET heat transfer model for liquid metal applications, especially sodium applications, is presented in ch. 3.2. The literature review shows a large group of correlations for liquid metal applications. Not only sodium but also other metals like lead, lead-bismuth in different compositions, sodium-potassium and mercury are used to develop correlations. For compatibility reasons, the implementation of the extension of the ATHLET code was designed to be selectable. It can be selected through the input deck when needed. If the extension is not selected, a previous version engineered by the first preliminary evaluation, as shown in the beginning of this chapter, is used. The verification shows the implementation to provide correct computation of Nusselt numbers. However, while comparing results with the PHENIX NCT, one can observe during the phases of natural circulation that the Nusselt number gets very small due to a considerable reduction of mass flow. The influence to the heat transfer can be observed and assumed to be of conductive nature. For reasons of coupling ATHLET and OpenFOAM (shown later on), it was decided, to create HCOs only in regions where boundary conditions are provided. Those are the core regions and the IHXs (heat transfer from primary to secondary side). Additionally, for reason of heat capacity of steel, the pump geometry is also designed with one HCO. Because the volume of sodium does get close to the volume of steel in that region, it was decided to take the heat capacity in reference. E.g. if the structure is heated up over time and then, by switching off the heat source, the coolant is considerably colder, the steel structure could function as a short-time heat source due to its different heat capacity.

In case of the PHENIX NCT, all HCOs use the correlation engineered by Mikityuk [95]. In literature, it appears to be based on the largest amount of data points. Because it is a hybrid correlation for triangular and square arrangements, it is also used for the IHX structure. The range of valid Nusselt numbers as well as the range of validity itself has been shown and discussed. The ATHLET model, designed for the PHENIX NCT, serves the purpose of code qualification and the development of a coupling methodology between ATHLET and OpenFOAM. For that reason, the PHENIX NCT input deck is designed to be rather simple. For more detailed system analysis of the PHENIX NCT with ATHLET, it is recommended to extend the input and include conjugate heat transfer. Corresponding principles have been elaborated in this chapter and can now be applied.

In addition to this chapter, the reader can also find the verification of all implemented Nusselt correlations (see tab. B.2) in Appendix B as well as the range of valid Nusselt numbers derived form literature and their application to the PHENIX NCT.

3.3 Pressure drop

In the presented work, the ATHLET code is applied using the 5-equations model. It is described in ch. 2.4 and gives the differential equation for mixture flow with eq. (2.33) and the sum of pressure losses in tab. 2.2. It appears in the ATHLET code, that pressure losses are well formulated and are applicable for liquid metal (LM). This chapter shows improvement to the ATHLET code for LM applications as the fuel subassemblies of the core are wire-wrapped and no spacer grids are used. The ATHLET code as been developed only for LWR applications. Wire-wrapped subassemblies have not been considered yet. Wires are helically wrapped around a fuel rod to keep the rod pitch constant (see fig. 3.14). Their helical form disturbs the coolant flow parallel to the rod and is the cause of an enhanced pressure drop. The description and model idea of the ATHLET code is given in ch. 2.4. With focus on flow behavior represented by fluid traveling through a pipe object, eq. (2.33) needs to be explained closer than given in ch. 2.4. Two-phase (sodium in liquid and vapor state) flow had not been observed during the PHENIX NCT (see ch. 1.2). Hence, the focus here is on pressure loss of liquid flow exclusively. In tab. 2.2 different pressure losses are defined and listed separately from each other. If more information is required, please refer to Austregesilo et al. [5]. The pressure loss component Δp_{fric} is essential, as it handles friction and form losses within the momentum equation. In [98] the expression Δp_{Wall} is used to express frictional pressure loss and Δp_{Form} is pressure loss due to geometry and flow direction with

$$\begin{aligned} \Delta p_{Wall} &= f_D \frac{L}{d_h} \frac{\rho u^2}{2} \\ &= f_D \frac{L}{d_h A^2} \frac{\dot{m}^2}{2\rho} \end{aligned} \tag{3.37}$$

as the Darcy-Weisbach equation which describes the relation between pressure loss and shear stress and fluid viscosity at the wall. In eq. (3.37), f_D is the friction factor, d_h is the hydraulic diameter and L is the distance in the pipe between two center points of a CV. To avoid confusion, the Darcy-Weisbach friction factor will be written as f_D and the Fanning friction coefficient as f_F. The relation is

$$f_F = 4 \cdot f_D \tag{3.38}$$

The friction factor f can be derived through correlations. The geometrical form loss can be expressed as

$$\begin{aligned} \Delta p_{Form} &= \zeta_{Form} \frac{\rho u^2}{2} \\ &= \frac{\zeta_{Form}}{A^2} \frac{\dot{m}^2}{2\rho} \end{aligned} \tag{3.39}$$

where Δp_{Form} is the pressure loss due to geometry and flow direction such as in diameter changes or bent pipes. To describe the geometry of a flow region in ATHLET, the hydraulic diameter, cross-section area, length and nodalization are the minimum to be specified. Considering the complex flow region of the core, this appears to be a coarse specification of a flow regime.

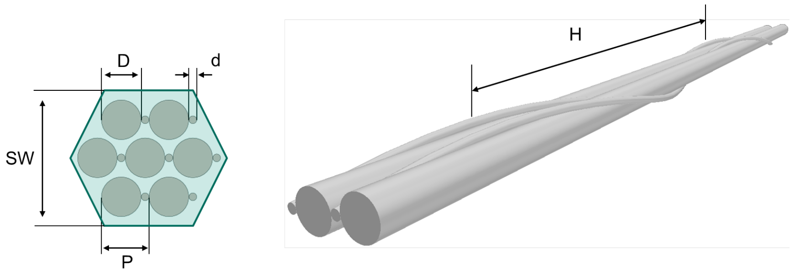

Fig. 3.14: Geometry parameters of a wire-wrapped fuel sub-assembly

The geometry of a wire-wrapped rod bundle is illustrated in fig. 3.14. On the right hand side, the influence of the wire-wrap to the P/D ratio is shown. Geometrical parameters are given in tab. 3.2.

Parameter	Description	Comment
D_{rod}	Rod diameter	D in fig. 3.14
D_{wire}	Wire diameter	d in fig. 3.14
P_t	Rod pitch	distance between two rod centers in cross section, P in fig. 3.14
H	Axial pitch of helical wire	
Z	Number of rods in subassembly	
SW	width of subassembly	important to derive external perimeter and flow cross section

Tab. 3.2: Description of geometrical parameters in fig. 3.14

In STH a given subassembly consists of different parts [18]: inlet, outlet, orifices and a main part with rods and spacers. The estimation of pressure drop across a complete fuel subassembly can be given accordingly to

$$\Delta p_{FSA} = \Delta p_{Inlet} + \Delta p_{Outlet} + \Delta p_{Orf} + \Delta p_{friction} + \Delta p_{spacers} \tag{3.40}$$

where $\Delta p_{friction}$ represents the pressure drop (due to friction) at the inner circumference of the sub-assembly and is usually determined by eq. (3.37) and eq. (3.41). Pressure losses at fuel subassemblies' inlet, outlet and orifices are based on form loss as given in eq. (3.39).

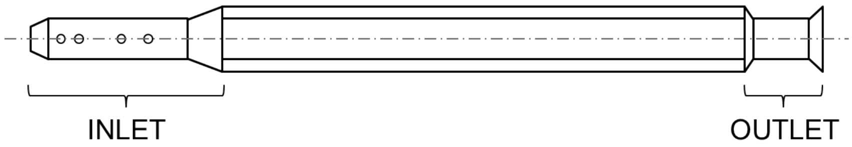

Fig. 3.15: Schematic of a fuel subassembly

Pressure drop correlations

The friction factor f_D (given in eq. (3.37)) is a dimensionless factor, assumed to be dependent on geometry and flow characteristics. Many experiments were conducted to elaborate correlations. For the evaluation of the friction factor, the Blasius correlation is adapted to pipe flow with Re $\geq$ 2000. It is given as

$$f_D = 0.3164\, Re^{-\frac{1}{4}} \tag{3.41}$$

Churchill [28] gives a more complex description that is applicable for more geometries and flow conditions.

$$\begin{aligned} f_D &= 8\left[\left(\frac{C_1}{Re}\right)^{12} + \frac{1}{(A+B)^{3/2}}\right]^{\frac{1}{12}} \\ A &= \left(\frac{1}{\sqrt{C_t}} \cdot \ln\left[\frac{1}{\left(\frac{7}{Re}\right)^{0.9} + 0.27\frac{\epsilon}{D_h}}\right]\right)^{16} \\ B &= \left(\frac{37530}{Re}\right)^{16} \end{aligned} \tag{3.42}$$

C_1 and C_t are constant parameters dependent on geometry. For tubular flow, they can be given as $C_1 = 8$ and $C_2 = \frac{1}{2.457}$.
At laminar flow condition ($Re < 2000$), the Hagen-Poiseuille correlation (eq. (3.43)) can be used.

$$f_D = \frac{64}{Re} \tag{3.43}$$

At turbulent flow condition in a circular pipe ($Re > 3000$), modelling of the flow type gets more challenging. Therefore, more correlations are available. Colebrook and White [32] provide a combination of experimental results that was used to derive the implicit equation

$$\frac{1}{\sqrt{f_D}} = -2\log_{10}\left(\frac{2,51}{Re\sqrt{f_D}} + \frac{\epsilon}{3,7D}\right) \tag{3.44}$$

where roughness is given by the parameter ϵ which depends on material of the pipe and its manufacturing process. For the usability in STH codes, an explicit form of the equation is given as

$$\frac{1}{\sqrt{f_D}} = -2\log_{10}\left(\frac{\epsilon}{3,7D_h} + \left(\frac{6.81}{Re}\right)^{0.9}\right) \tag{3.45}$$

The well known Moody-diagram (see [137, p.218]) illustrates an overview on the variation of the friction factor dependent on the Reynolds number and relative pipe roughness. The friction loss correlations (eq. (3.41), eq. (3.42), eq. (3.43), eq. (3.45)) are implemented and used in ATHLET. In following, a group of correlations is gathered that are developed for SFR purposes, where wire-wrapped fuel bundles are most relevant to be represented.
Rehme [122] proposed following model for the estimation of friction factors

$$\begin{aligned} f &= \left(\tfrac{64}{Re}F^{0.5} + \tfrac{0.0816}{Re^{0.133}}F^{0.9335}\right)\tfrac{P_{bundle}}{P_{bundle}+P_{wall}} \\ F &= \sqrt{P_t/D_{rod}} + \left[7.6\frac{D_{rod}+D_{wire}}{H}\left(\frac{P_t}{H}\right)^2\right]^{2.16} \end{aligned} \tag{3.46}$$

where F is a geometrical parameter, Z_{rod} is the number of fuel rods and P_{bundle} can be determined by

$$P_{bundle} = Z_{rod} \cdot \pi \cdot (D_{rod} + D_{wire})$$

The range of validity for this correlation was given by Rehme [122] to $1.125 \leq P_t/D_{rod} \leq 1.147$, $6 \leq H/D_{wire} \leq 45$ and $7 \leq Z_{rod} \leq 61$.
For his first correlation, Engel et al. [39] measured pressure drops in four 61-pin bundle arrangements cooled by water and sodium.

$$\begin{aligned} &f_L = \tfrac{99}{Re} && Re < 400 \\ &f_T = \tfrac{0.48}{Re^{0.25}} && Re > 5000 \\ &f_{Tt} = f_T\sqrt{\psi} + f_L\sqrt{1-\psi}, \text{with } \psi = \tfrac{Re-400}{4600} && 400 < Re < 5000 \end{aligned} \tag{3.47}$$

After review and analysis of the friction factor in wire-wrapped bundles, Bubelis and Schikorr [18] recommended a modification to Engel et al. [39] in 2008 with following modified constant parameters

$$\begin{aligned} &f_L = \tfrac{110}{Re} && Re < 400 \\ &f_T = \tfrac{0.37}{Re^{0.25}} && Re > 5000 \\ &f_{Tt} = f_T\sqrt{\psi} + f_L\sqrt{1-\psi}, \text{with } \psi = \tfrac{Re-400}{4600} && 400 < Re < 5000 \end{aligned} \tag{3.48}$$

The friction factor calculated by the correlation of Novendstern [101] takes the bulk temperature T_B and the wall temperature T_w into account. T_w corresponds to the boundary temperature between rod and coolant. The correlation is defined stepwise [43] to

$$\begin{aligned}
&f_L = \left(\frac{K}{Re}\right)\left(\frac{T_w}{T_B}\right), K = \frac{80}{\sqrt{H}}\left(\frac{P_t}{D_{rod}}\right)^{1.5} && \text{Laminar flow: } Re < 400 \\
&f_{Tt} = f_T\sqrt{\psi} + f_L\sqrt{1-\psi} && \text{Transition flow: } 400 \leq Re \leq 5000 \\
&f_T = \frac{0.316M}{Re^{0.25}} && \text{Turbulent flow: } Re > 5000
\end{aligned} \tag{3.49}$$

where H needs to be given in **cm** ($10^{-2}m$) and

$$\begin{aligned}
\psi &= \tfrac{Re-400}{4600} \\
M &= \left[\frac{1.034}{\left(\frac{P_t}{D_{rod}}\right)^{0.124}} + \frac{29.7\left(\frac{P_t}{D_{rod}}\right)^{6.9}}{\left(\frac{H}{D_{rod}+D_{wire}}\right)^{2.239}} Re^{0.086}\right]^{0.885}
\end{aligned}$$

No and Kazimi [100] recommended a combination of Markley and Engel [90] and Novendstern [101] (eq. (3.50)).

$$\begin{aligned}
&f_L = \tfrac{32}{\sqrt{H}}\left(\tfrac{P_t}{D_{rod}}\right)^{1.5}\tfrac{1}{Re} && Re < 400 \\
&f_T = \tfrac{0.316\,M}{Re^{0.25}}; \text{where } M \text{ refers to (3.49)} && Re > 2600 \\
&f_{Tt} = f_T\sqrt{\psi} + f_L\sqrt{1-\psi}, \text{with } \psi = \frac{Re-400}{2200} && 400 < Re < 2600
\end{aligned} \tag{3.50}$$

Eq. (3.50) and eq. (3.49) are based on Novendstern [101] for turbulent flow, which has a given range of validity of

- $19 \leq Z_{rod} \leq 217$
- $4.9mm \leq D_{rod} \leq 11.8mm$
- $1.06 \leq \frac{P_t}{D_{rod}} \leq 1.42$
- $8 \leq \frac{H}{D} \leq 96$
- $2600 \leq Re \leq 200000$

Sobolev [140] developed a correlation for friction factors in wire-wrapped bundle flow as

$$f = \left(1 + 600\left(\frac{D_{rod}}{H}\right)^2\left(\frac{P_t}{D_{rod}} - 1\right)\right)\left(\frac{0.210}{Re^{0.25}}\left(1 + \left(\frac{P_t}{D_{rod}} - 1\right)^{0.32}\right)\right) \tag{3.51}$$

Once the wall friction factor is determined, the pressure drop due to wall friction can be estimated through eq. (3.37). Tab. 3.3 shows an overview of the discussed pressure drop components with parameters needed to be determined.

Term	Needed variables	Observations
Δp_s	$p(i_1)$; $p(i_2)$	Pressure of previous and following control-volumes
Δp_{MF}	$A(i_{1/2})$; $\rho_m(i_{1/2})$; $G(j)$	The mass flow is one of the variable hence the differential equation, the cross-section areas and the densities define also ranges of application where specific formulas are used
Δp_{WR}	u_R; $A(i_{1/2})$; $\alpha(i_{1/2})$; $\rho_L(i_{1/2})$; $\rho_V(i_{1/2})$; $\rho_m(i_{1/2})$	Relative velocity u_R assumed known and calculated in a subroutine which will not be modified, densities and void-fraction
Δp_{Grav}	$\rho_m(i_1)$; $\rho_m(i_2)$; $\Delta z(i_1)$; $\Delta z(i_2)$	Mixture density and and elevation difference to the center of the common junction
Δp_{Fric}	$G(j)$; $k(i_{1/2})$; $\rho_m(i_{1/2})$; $\xi_{Form}(i_{1/2})$	The friction K-value is calculated as a function of the Darcy friction factor and also depends on the friction model chosen by the user, the form loss coefficients are given in input deck
Δp_ρ	-	Not taken into account in current code version
Δp_I		Depends on the specific model used (pump or turbine)

Tab. 3.3: Pressure drop components in ATHLET with required parameters, [15]

Implementation

The correlations for wire-wrapped bundles to be implemented are given in tab. 3.5. The implementation follows a similar methodology as the HTC modification which was explained in ch. 3.2. The input deck must be extended to give the user the possibility to further specify the friction that occurs at given positions. Those parameters are required by ATHLET for the calculation via correlation, which were previously described. In detail, those modifications take place in the following parts of the ATHLET calculation. A proper implementation must be guaranteed. For that reason the verification is crucial.

Input deck modification

The input deck is extended in card `OBJECT`. After the common `FRICTION` input, a new section is inserted, called `FRICBNDL` (e.g. lst. 3.2). Wire-wrapped bundle parameters that are additionally required can now be specified.

```
------ FRICBNDL
@     BDLT
    %BDLT%
@   SP0        PT0     HL0     DROD0     DW0     ZROD0     PWAL0     FR10
    0.000      %PT%    %HL%    %DROD%    %DW%    %ZROD%    %PWAL%    0.0
    %SPEND%    %PT%    %HL%    %DROD%    %DW%    %ZROD%    %PWAL%    0.0
```

Lst. 3.2: New layout for bundle parameters

Tab. 3.4 gives an overview of input parameters required in the newly implemented input `FRICBNDL` (lst. 3.2) together with a small description.

Input deck	Geometry	Unit	Description
BDLT	–	–	Bundle type (= 1 for wire-wrapped bundles)
SP0	–	m	Length coordinate in TFO where the parameters are intended to be specified
PT0	P_t	m	Rod pitch, distance between the centers of two consecutive rods
HL0	H	m	Axial pitch of the helix formed by the wire
DROD0	D_{rod}	m	Rod diameter
DW0	D_{wire}	m	Wire diameter
ZROD0	Z	–	Number of rods (note that it is defined as a real number allowing more flexibility)
PWAL0	P_{wall}	m^2	Wall perimeter, corresponds to the perimeter of the external shape only
FR10	–	–	Further geometrical bundle related parameter (not used yet)

Tab. 3.4: Pressure drop components in ATHLET with required parameters, [15]

Code modification

To save the additional input during the simulation, a new module (`CBUNDLE`) and a referring subroutine `ALLOCBUNDLE` for allocation is implemented to the ATHLET code. Full information about the parameters type and dimension can be seen in [15, p. 46 ff.]. A flow diagram of the extended ATHLET routines for reading the input deck can be seen in fig. 3.16. With focus on wire-wrapped bundles and the calculation of the required friction factor, the `DPDROP` subroutine for the 5-equation model in ATHLET (see ch. 2.4) needs to be modified. To maintain downwards compatibility with input decks written for previous (original) ATHLET calculations, the parameter `ITMPO` used in `FRICTION` of the original input deck is used as a trigger. Tab. 3.5 gives an overview of selectable correlations for the modified ATHLET version.

ITMPO	Description
61	Blasius correlation - eq. (3.41)
62	Churchill model - eq. (3.42)
63	Rehme model - eq. (3.46)
64	Original Engel model - eq. (3.47)
65	Modified Engel model - eq. (3.48)
66	No-Kazimi model - eq. (3.50)
67	Sobolev model - eq. (3.51)
68	Baxi and Dalle-Donne model - eq. (3.49)

Tab. 3.5: Identifier (ITMPO) and correlation, [15, p. 51]

If `ITPMO` is specified with one of the numbers given in tab. 3.5, pressure drop calculation will be bypassed in ATHLET and the subroutine `MFFRICWW` will be called. An illustration can be seen in fig. 3.16 where the index L stands for liquid, G for vapor. For the purpose of liquid sodium, only the friction factor for liquid phase will be calculated. The two-phase multiplier is assumed to be equal to 1.

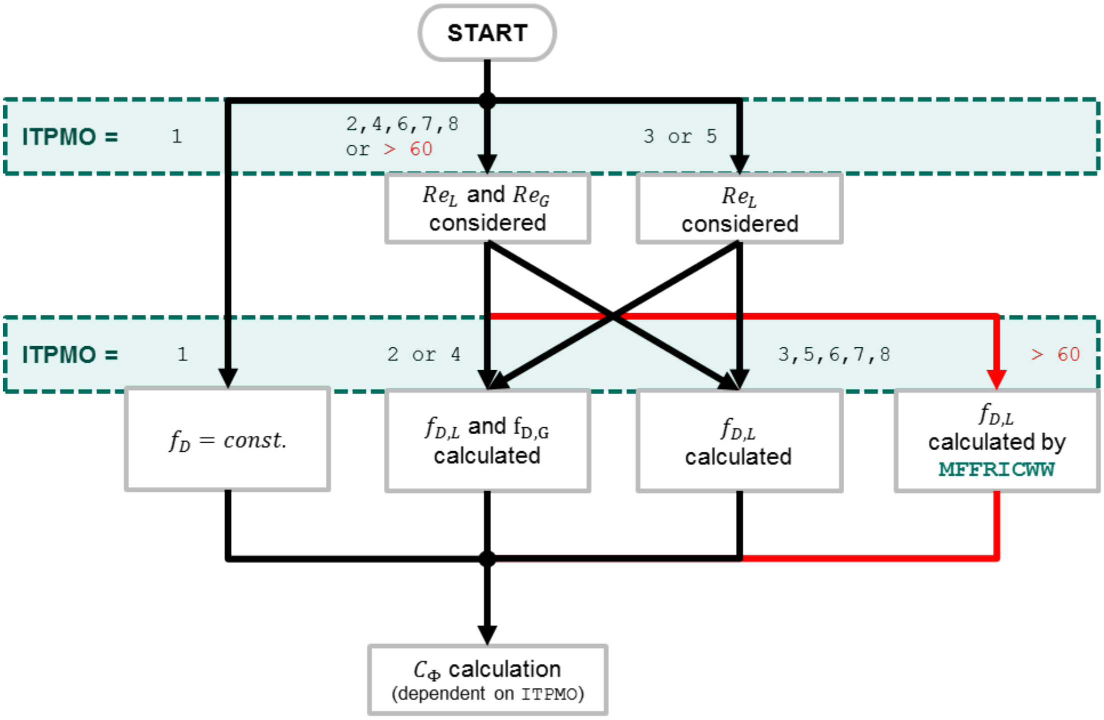

Fig. 3.16: Flow diagram for the calculation of the Darcy friction factor f_D in the modified version of ATHLET

Verification

To check the implementation, a verification process similar to the heat transfer correlation verification process is applied. Necessary input parameters are retrieved from ATHLET and used as input for a python program. Result data from Python is plotted over result data from ATHLET. Additionally, the Python results are plotted over themselves. This way, two lines are received which can be plotted. If the two lines fully cover each other, the numerical error can be assumed to be of no relevance. According to Marten et al. [91], the verification is only realized for one geometry type, namely ‘Geometry type A10’. The verification is only realized for one geometry type[1]. It is assumed by the author, that the code modification can be considered as verified, as soon as one example is computed and the results (ATHLET computation) meet the specifications (Python computation). Because of their assumed different behavior, the verification process for friction correlations is run separately for each correlation. In each case, the friction factor is calculated with ATHLET and a Python script at the same Reynolds number. Then, for each plot (left hand side in fig. B.32 and fig. B.33) the abscissa obtains ATHLET results and the ordinate obtains Python results. The line $y = x$ marks 0 error level. For the numerical value plotted in fig. B.32 and fig. B.33, the Pearson’s correlation coefficient R^2 is calculated (eq. (3.52)).

$$R^2 = \frac{\sum_{i=1}^{N}(x_i - \bar{x}) \cdot (y_i - \bar{y})}{\sqrt{\sum_{i=1}^{N}(x_i - \bar{x})^2} \cdot \sqrt{\sum_{i=1}^{N}(y_i - \bar{y})^2}} \tag{3.52}$$

---

[1] Marten et al. [91], Geometry type A10

Fig. 3.17 (a) and fig. 3.17 (b) show the two described curves. The left hand side illustrates the friction factor comparison. The right hand side shows the friction factors over Reynolds numbers for both, ATHLET and Python results.

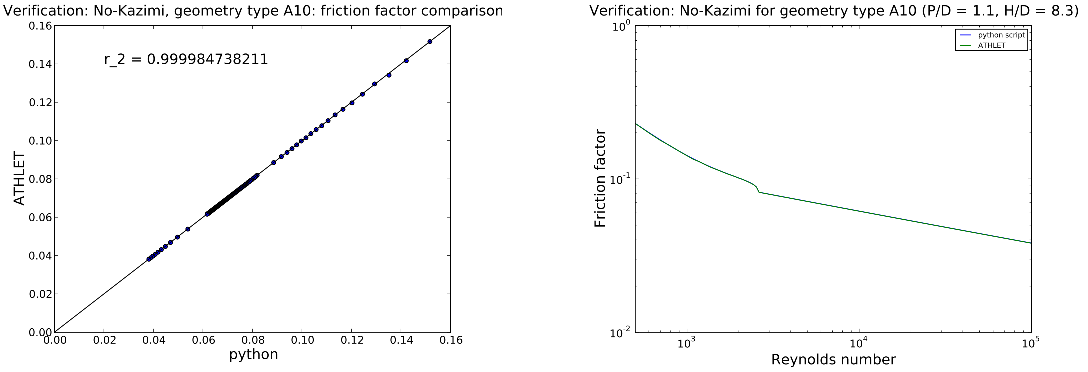

(a) ATHLET over Python (eq. (3.50))

(b) Friction factor over Reynolds number (eq. (3.50))

Fig. 3.17: Verification result for No and Kazimi [100] with test case Marten et al. [91], Geometry type A10

The Blasius correlation (eq. (3.41)) and the Baxi Dalle-Donne correlation (eq. (3.49)) seem incomplete but in fact the friction factor does not exceed 0.1 for these models as shown on in the diagrams on the right hand side. At low mass flow rates, numerical instabilities in ATHLET and difficulties in the determination of fluid properties occure which can lead to slight discrepancies when plotting friction factor over Reynolds number. The correlation given by Churchill (eq. (3.42)) describes a transition flow for Re values between 1000 and 2000. Due to inherent and discontinuous definition of Engels formulas eq. (3.48) and (3.47), No-Kazimi eq. (3.50) and Baxi Dalle-Donne eq. (3.49) models, the border between transition and turbulent flow can be easily noticed at $Re = 5000$ or 2600 by the curves' shapes which are very different from a model to another. The friction models are developed on the basis of different experiments and with different form of equations. The trend of the Baxi Dalle-Donne correlation (eq. (3.49)) is quite different from all other correlations. It shows a considerable lower friction factor at low Reynolds numbers, where no wall and bulk temperatures are considered and their ratio is set to 1. The given procedure shows that the implementation of pressure drops referencing wire-wrapped bundles is verified. It can be noted in addition, no numerical error is observed.

Assessment

Similar to the heat transfer package, the correlations for wire-wrapped bundles found in literature are given with their individual range of validity. The developer has to choose which correlation best corresponds to the present application. In case of the PHENIX NCT, there is a lack of information concerning pressure drops. For that reason, the experiments presented by Marten et al. [91] were used for an assessment. The experiments were carried out on a set of test pipes. Each of the pipes has its individual geometry, depending on the parameter study. The outer shell is of hexagonal shape. It is parametrized by the distance between two opposite sides of the regular hexagon S_W. The number of rods is given by z_{rod} and is constant. The rod diameter D_{rod}, wire diameter D_{wire}, rod pitch P_t and axial pitch H differ between test sections. An overview of the parameter variations is given in tab. 3.6.

Type (−)	D_{rod} (mm)	D_{wire} (mm)	d_h (mm)	A (mm^2)	P_t/D_{rod} (−)	H/D_{rod} (−)	z_{rod} (−)
A01	16.21	0.35	2.73	1557.17	1.02	8.3	37
A02	16.21	0.35	2.73	1557.17	1.02	12.5	37
A03	16.21	0.35	2.73	1557.17	1.02	16.7	37
A04	16.21	0.35	1.527	914.	1.04	8.3	37
A05	16.21	0.35	1.527	914.	1.04	12.5	37
A06	16.21	0.35	1.527	914.	1.04	17.	37
A07	15.35	1.1	4.08	2314.3	1.07	8.3	37
A08	15.35	1.1	4.08	2314.3	1.07	12.5	37
A09	15.35	1.1	4.08	2314.3	1.07	16.7	37
A10	14.87	1.5	4.789	2705.6	1.1	8.3	37
A11	14.87	1.5	4.789	2705.6	1.1	12.5	37
A12	14.87	1.5	4.789	2705.6	1.1	16.7	37

Tab. 3.6: Table of experiments for Nusselt correlations [73]

The assessment gives an overview, which correlations may fit best to the test case scenario. Marten et al. [91] is also used by Borsenberger [15] for validation. However, the range of validity of each correlation doesn't necessarily fit the full PHENIX NCT scenario. In following, an example (fig. 3.19) is discussed which is geometrically considered very close to the fissile region given in the PHENIX NCT. For more detailed information, please refer to Borsenberger [15].

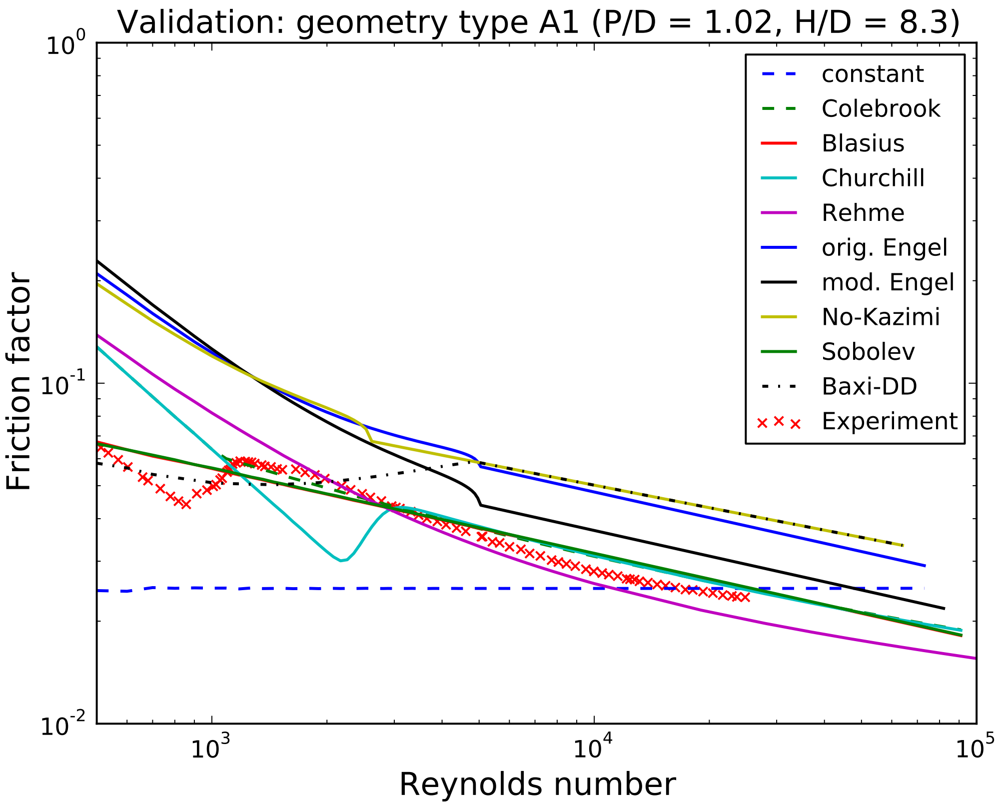

Fig. 3.18: Validation: Geometry type A1 [15]

In all cases (e.g. fig. 3.18 and fig. 3.19), measurements are plotted with red crosses. Those examples have been chosen to be presented here directly and are discussed. For more test cases, please refer to Appendix B or [15].

To receive all results that are plotted in fig. 3.18 and fig. 3.19, many points were generated. Each point of each curve is the steady state result of one simulation, similar to the points received in the referring experiments. In the experiments with geometry type A1, a rise of the friction factor can be observed in fig. 3.18. It is expected that the friction factor drops with rising Reynolds number. However, the experiment starts at very low Reynolds numbers. Then in the range of $800 \leq \mathrm{Re} \leq 1030$, the friction factor rises. It is assumed to be caused by the transition from laminar to turbulent flow.

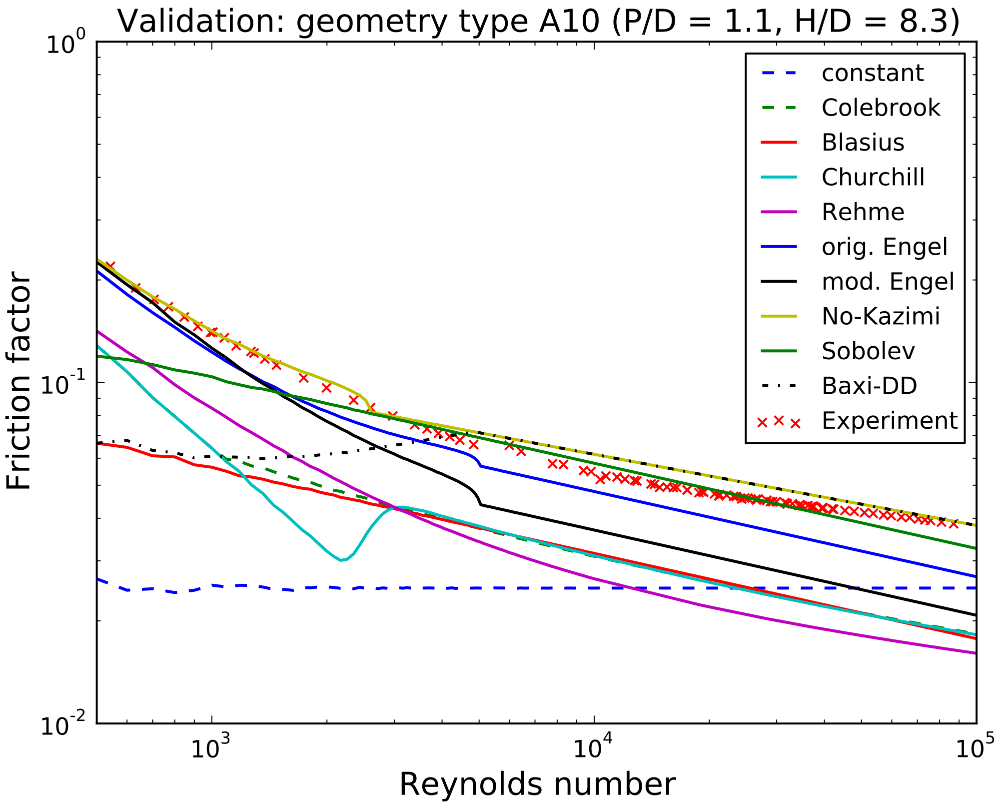

Fig. 3.19: Validation: Geometry type A10 [15]

In [15], all experiments are assessed, which are relevant to the PHENIX NCT because of geometrical similarities. A peak can be observed for pitch-to-diameter ratios ($^P/_D$) at 1.02 and 1.04 which is assumed to appear because of the perturbation of fluid flow at low mass flow rates and low cross-section area. The axial pitch-to-diameter ratio $^H/_D$ did not show significant influence on the Darcy friction factor f_D. Because of their design limits, eq. (3.45), eq. (3.41), eq. (3.51) and eq. (3.49) do not describe a large increase of the friction factor at laminar flow (low Reynolds number) condition. Over the total range of the experiments, eq. (3.50) shows most satisfactory results with only one restriction at low $\frac{P}{D}$ ratio (1.02), where eq. (3.50) over-predicts the friction factor over the whole range of the experiment.

For the turbulent flow, eq. (3.51) gives satisfying results over the whole range of the experiment which is $1.02 \leq {}^P/_D \leq 1.1$ and even for laminar flow and low pitch to diameter ratio (1.02).

Eq. (3.47), eq. (3.48), eq. (3.41) and eq. (3.42) are only dependent on the Reynolds number. This can be observed in their results' similarity over all geometries in the experiments. The influence of the bundle geometry used in eq. (3.46) does not show significant impact on the range of the experiment. For further explanations and details about the validation, please refer to [15].

Summary

Ch. 3.3 has shown the importance of pressure drop correlations in STH. However, at this step it is decided, to continue with the ATHLET code without this extension. The field of experiments for liquid sodium turned out to be very small, so not all required cases for full scale application could be covered. Far more important is, the implementation cannot be validated with the PHENIX NCT directly because of insufficient measurements of pressure drops in subassemblies.

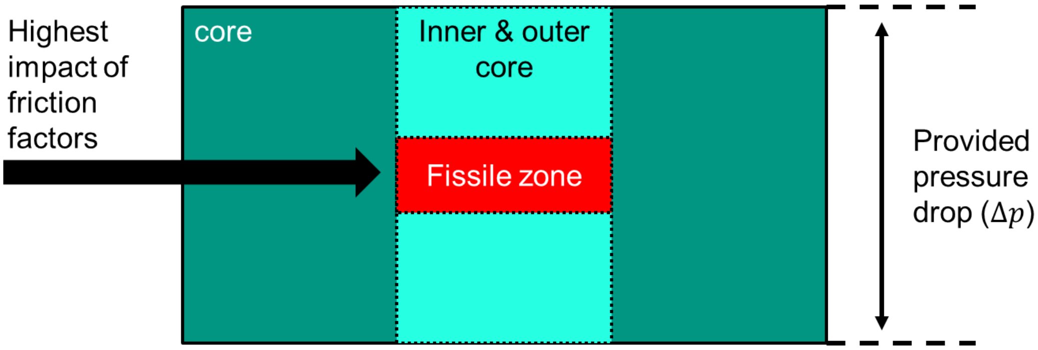

Fig. 3.20: Given pressure drop results and impact of friction factor

Information about pressure drop in the PHENIX primary circuit, that is given for adjustments, is not detailed enough. Especially pressure drops within subassemblies over the whole transient would be of interest for the validation. It is assumed, that the highest impact by the modification takes place in the fissile zone of the core (see fig. 3.20). The provided pressure for steady state condition at nominal power is shown in fig. 3.20. Provided pressure drops of the PHENIX [59] are given for nominal condition at full power which is not part of the PHENIX NCT. It has been decided to take these pressure drop informations into consideration for the PHENIX primary circuit modeling in ATHLET and therefore use a more coarse approach supported by the ATHLET code without extension.

4. OpenFOAM case adaption

As previously described in ch. 2.5, the buoyantPimpleFoam Solver is used for CFD applications in the following cases (s.a. ch. 6 and ch. 7). The CFD domain supports the results of the STH solution. Therefore, it is necessary to replace STH regions. As regions, the large pools in the PHENIX reactor make sense to be represented in CFD. Flows are strongly three-dimensional, not only in steady state but especially in transient cases. In this work, the hot plenum has been decided to be represented in CFD.

4.1 Discretization

For numerical analysis of a given steady state or transient case, both geometry and temporal behavior must be discretized to benefit from computational aid. The work-flow shown in tab. 4.1 provides the steps of discretization used in this work.

Discretization type	Corresponding step
Geometrical	1. CAD - Geometry
Geometrical	2. Meshing (automated)
Geometrical	3. Boundary conditions (placement)
Temporal	3. Boundary conditions (time table)
Temporal	4. Solver specific adjustments

Tab. 4.1: Workflow for OpenFOAM case setup

Step 1. and 2. (see tab. 4.1 right hand side) are performed with the CFD package STAR-CCM+.

Geometrical discretization

As a first step (in present case this is followed), one can create a CAD model of the needed flow region. STAR-CCM+ provides a capable CAD modeler, similar to common CAD software packages. Geometries can be created with the help of common CAD features like

- Sketches
- Extrusions

- Rotation
- Faces and Edges
- Patterns
- Fillets and Chamfers
- Design Parameters
- Volume Extraction

The CFD region in focus of this work is the hot plenum of the PHENIX reactor. It has been successfully modeled in STAR-CCM+.

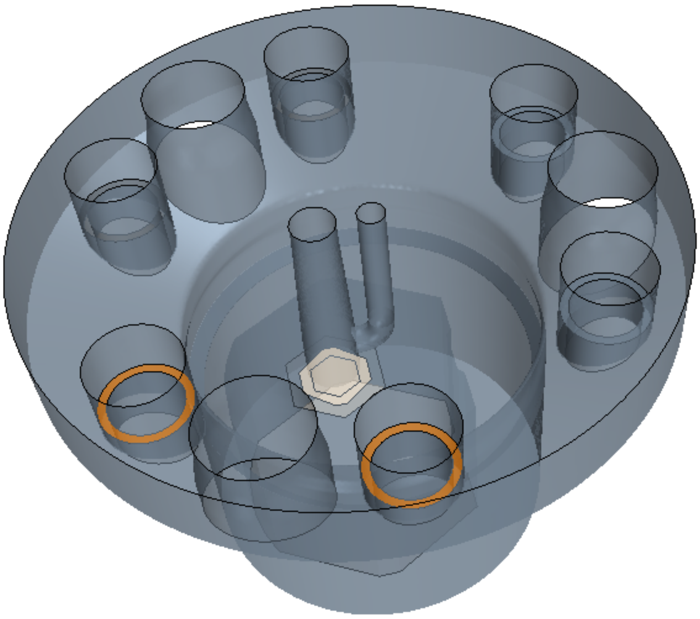

Fig. 4.1: Hot pool geometry

Polyhedral Mesher

The geometry is complex for flow and temperature fields development as it is for transients, too. The three dimensional shape gives a flavor about the flow that is to be calculated later on. After the creation of the geometries, the meshes' construction follows. Here, non-structural meshing is used to master the given complex geometries. In STAR-CCM+ the geometries are assigned to parts. Those parts are further assigned to regions which are used by the mesh continuum for region based meshing.
As main meshing tool, polyhedral meshes are used. Those can be used mainly for complex geometries when structured meshing is considered too time consuming as the case is here. Polyhedral meshes do not require more surface preparation than the equivalent tetrahedral meshes. Additionally, polyhedral meshes contain approximately five times fewer cells than a tetrahedral mesh for a given starting surface. In STAR-CCM+, a special dualization scheme is used to create the polyhedral mesh from an underlying tetrahedral mesh, which is automatically created as part of the process. The polyhedral cells that are created typically have an average of 14 cell faces. For mesh improvement, a "Run Optimizer" can be run several times. It performs additional optimization of vertices during the dualization process, resulting in higher-quality meshes. It needs additional CPU time, but is also used here for optimization.

Prism Layer Mesher

For wall treatment, the prism layer mesh model is used to generate orthogonal prismatic cells next to wall surfaces or wall boundaries (if not specified differently). A prism layer is defined in terms of:

- Thickness
- Number of cell layers within
- Size distribution of the layers

These general properties are defined globally within the mesh continuum. Local properties like regions, boundaries or volumetric controls are not used in the presented meshes here.

Surface Remesher

In order to improve the overall quality of an existing surface and optimize it for the volume mesh models, the surface remesher can be used to retriangulate the surface. The remeshing is primarily based on a given target edge length and can also include feature refinement that is based on curvature and surface proximity. The surface remesher is typically used for remeshing surfaces that are output from the surface wrapper and STL type data. As well as improving the surface for the volume meshers it also aids the subsurface generator when the prism mesher option is selected. The properties of the surface remesher model can be changed to provide additional meshing control during the meshing process. The input values used for the surface remesher can be set on four different levels:

- Global level
- Part surface or boundary level
- Feature curve level
- Interface level (not used here)

Import mesh to OpenFOAM

Derived meshes in STAR-CCM+ are exported in .ccm format. This format is supported by the routine ccm26ToFoam in OpenFOAM. Information about cells, faces and patches (inlets and outlets) are transferred to OpenFOAM format. The geometry can now be treated further in OpenFOAM.

Temporal discretization

To avoid time consuming CFD calculations, two options are possible. One way would be to reduce the number of calculations in each cell of the mesh. This leads to a more and more coarse representation of turbulence and may lead to stability problems during the calculation. The other way is to reduce the number of cells in one mesh. The procedure of reducing the number of cells in one mesh is not trivial. As each cell represents one point of a grid, it is necessary to place cells where needed. Normally, structured meshing is used for this purpose. Here, with STAR-CCM+ a lot of different options can be used to derive an adequate mesh with a minimal number of cells. This in mind, the calculation here is carried out with a solver that takes material properties into account. The fluid can be specified with temperature dependent polynomial functions - as it is done in the STH code ATHLET. The solver uses an algorithm that is based on a coupled PISO and SIMPLE algorithm. It is called PIMPLE. The SIMPLE algorithm is well known by steady state or time independent solution methods while the PISO algorithm performs time dependent solution. The PIMPLE algorithm uses an ordinary PISO core but time steps can be repeated with an outer time independent SIMPLE loop. This combination is used for stability purpose or to keep time steps large [61]. Additional information about the buoyantPimpleFoam solver can be received from ch. 2.5.

Material properties

To take buoyancy effects into account in CFD, additional terms are added to describe thermo-physical properties more accurately than constant. The parameters are dependent on temperature. The dynamic viscosity of sodium μ_{Na} can be described in a range between 317K and 2400K and atmospheric pressure [57].

$$\ln\mu_{Na}(T) = \frac{556.835}{T} - 0.3958 \cdot \ln(T) - 6.4406 \ [\mathrm{Pa \cdot s}] \tag{4.1}$$

For an explicit formulation, the logarithmic scheme has been approximated through the following polynomial function:

$$\begin{aligned} \mu_{Na}(T) = 1.39837319 \cdot 10^{-2} - 1.22580805 \cdot 10^{-4} \cdot T \\ +4.95037362 \cdot 10^{-7} \cdot T^2 - 1.14071673 \cdot 10^{-9} \cdot T^3 \\ +1.59523376 \cdot 10^{-12} \cdot T^4 - 1.34358355 \cdot 10^{-15} \cdot T^5 \\ +6.28347029 \cdot 10^{-19} \cdot T^6 - 1.25544876 \cdot 10^{-22} \cdot T^7 \end{aligned} \tag{4.2}$$

For the density ρ_{Na}, the heat capacity $c_{p_{Na}}$ and the heat conductivity λ_{Na} following correlations have been adopted [57], [75], [74].

$$\rho_{Na}(T) = 1011 - 0.244 \cdot T \ [\frac{kg}{m^3}] \tag{4.3}$$

$$c_{p_{Na}}(T) = 1608 - 0.7481 \cdot T + 3.929 \cdot 10^{-4} \cdot T^2 \ [\frac{J}{kg \cdot K}] \tag{4.4}$$

$$\lambda_{Na}(T) = 99.5 - 0.0391 \cdot T \ [\frac{W}{m^2 \cdot K}] \tag{4.5}$$

The OpenFOAM calculation strongly depends on calculation results of the ATHLET code. The values at the inlet that serve as boundary conditions are mass flow and temperature; at the outlet pressure must be given. Those boundary conditions in OpenFOAM are constant over the determined surface (patch). Plots of these material properties are given in Appendix C.

4.2 Steady state conditions

To receive steady state, normally the Simple algorithm is used. Here to have consistency between solvers, it is assumed that the transient PIMPLE algorithm can reach quasi steady state condition, too. The transient setup is run with constant boundary conditions, derived from the first time step of the transient ATHLET calculation, as measurements are taken in places different from CFD boundaries. As it is an optimization problem to receive a small mesh size and have high accuracy together, the steady state calculations are all simulated with transient solvers before starting the transient test case. An additional refinement study can help here through the comparison of calculated boundary conditions such as mass flows, temperature and pressure. If discrepancies are small enough, one can assume the meshes to provide results independent from mesh size, so a sufficient mesh size is achieved. When running constant boundary conditions in a large and complex three-dimensional geometry, there may appear fluctuations among flow streams and jets. As long as those fluctuations do not impact the needed result, meshes are assumed to be sufficient for the transient calculation but must be well regarded concerning transient results. Those meshes may lead to false results with rather chaotic flow patterns. This in mind, the following geometries are being meshed with the commercial software STAR-CCM+, always with the goal of minimal cell size but sufficient accuracy within the CFD region for later research. As soon as fluctuations and mesh sizes have reached the requirements defined, flow fields, temperature fields, pressure distribution, etc. have to be developed for CFD in steady state. For this reason, the transient solver is run for a minimum time of 1000s of physical time.

Mesh sensitivity

In case of the reliability of the calculation, the influence on the mesh and its structure must be negligible. Therefore, a mesh sensitivity study is carried out. The smaller the number of cells, the smaller the number of numerical operations during one time step. I.e., the quickest results are received through the smallest number of cells possible, that is able to perform accurate results. The wording for the number of cells during this work is also given as so-called mesh size. A large mesh is equivalent to a high number of cells in that mesh and vice versa. In case of the hot plenum, one has to deal with a complex geometry and large scales in all dimensions. Hence, as the OpenFOAM calculation of this specific case behaves very sensitively concerning unstructured meshes with complex geometries, the starting mesh size should be as small as possible. As soon as steady state conditions can be considered as converged (changes on calculated boundaries), the developed field can be mapped to larger mesh sizes. To check the flow fields for higher mesh sizes, existing, previously calculated results received by smaller mesh sizes are used. Fields are mapped and interpolated to the larger mesh size and additionally, the transient simulation is run 1000s of physical time with constant boundary conditions. The final calculation results can then be compared. It is not necessary to compare small details, but the results which are crucial for coupling later on. In tab. 4.2 mass flows are shown. Mass flows are given by tables at the inlets (innerCore, outerCore, Blanket) as boundary conditions and calculated by OpenFOAM at the outlets (IHX11, IHX12, IHX31, IHX32). Same is done for temperatures shown in tab. 4.3 at the end of this paragraph. Afterwards, the flow field at time 1000s is mapped to time 0s (starting point).

mesh	innerCore	outerCore	Blanket	IHX11	IHX12	IHX31	IHX32
140k	561.317	495.735	218.647	317.1	320.84	321.415	317.692
271k	561.320	495.72	218.642	317.166	324.24	323.047	311.898
550k	561.322	495.74	218.642	317.76	319.671	315.642	323.376
1080k	561.322	495.74	218.642	321.554	322.98	324.248	307.722
2088k	561.322	495.74	218.642	309.642	320.086	317.47	329.222

Tab. 4.2: Steady state results - Hot pool - mass flow (kg/s)

mesh	innerCore	outerCore	Blanket	IHX11	IHX12	IHX31	IHX32
140k	718.677	709.261	662.796	701.45	701.266	701.57	701.052
271k	718.35	709.00	662.795	702.873	703.465	703.333	702.925
550k	719.093	709.69	662.804	703.293	703.309	703.924	703.305
1080k	719.093	709.69	662.804	703.354	703.272	703.314	703.244
2088k	719.093	709.69	662.804	703.539	703.552	703.76	703.367

Tab. 4.3: Steady state results - Hot pool - temperature (Kelvin)

As the calculations are carried out with the buoyantPimpleFoam solver which is a transient solver, fluctuations in mass flow are observable. Averaging over time may show the mean values at each outlet being close to each other. The temperature fields behave similarly. Through mass flow fluctuations, also the temperature field fluctuates while the average keeps constant (s.a. tab. 4.3). Overall, the boundary conditions for mass flow and temperature are fixed in the innerCore, outerCore and Blanket. As pressure boundary condition, p_{rgh} is given. For incompressible fluids, this boundary condition is of minor influence. Further discussion on how this boundary condition is received from ATHLET will be given in ch. 5. Minor differences here may occur from the ATHLET calculation that is needed to provide all boundary conditions for the CFD calculation. From steady state conditions, it can be observed, that a mesh size starting from 271000 cells is feasible for coupling purposes. However, it must be noticed there is no conjugate heat transfer inside the CFD region which would require a more detailed discussion about the mesh sensitivity. The fluid volume size is large and although the geometry is complex, the used coarse approach is feasible and does not show significant impact on the coupling interfaces (s.a. tab. 4.2 and tab. 4.3).

4.3 Transient conditions

Starting from steady state, boundary conditions are given as time tables. As it supports stability, quasi steady conditions of about 1000s are added at the beginning of the transient. This time is used to adjust slight changes at the starting point and receive fully developed flow at the beginning of the transient. It may not be necessary for a standalone CFD calculation as it is described here, but crucial for stability purposes later on.
The boundary conditions (see tab. 1.2 and Appendix C) for the transient calculation are mass flow and temperature (in Kelvin) at each inlet and static pressure without hydrostatic influence ($p_{rgh} = p_{stat} - \rho g h$, with g as gravity and h as elevation). In fig. 4.2, outlets of the hot plenum region are marked in orange while inlets are colored in beige.

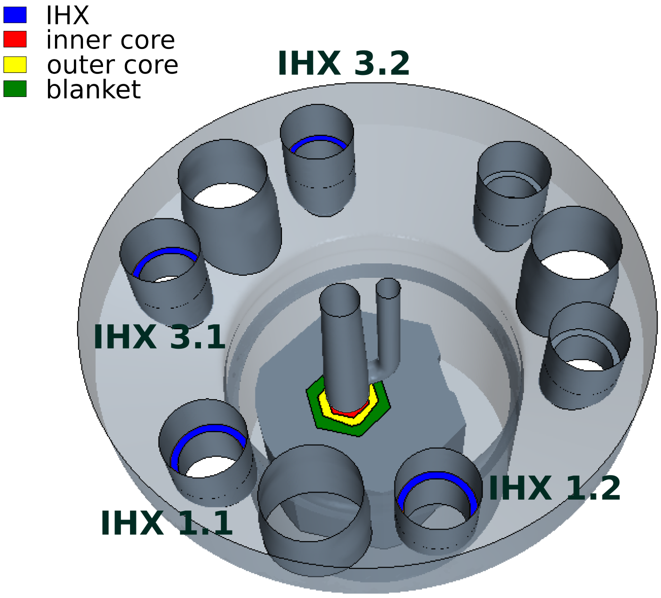

Fig. 4.2: Hot pool geometry

Inlet BC	
OpenFOAM	**ATHLET**
inner core	inner core, control rods, safety rod
outer core	outer core
blanket	blanket, shielding, fuel storage
Outlet BC	
OpenFOAM	**ATHLET**
IHX11, IHX31	IHX1
IHX12, IHX32	IHX2

Tab. 4.4: BCs: CFD/STH

All transient boundary conditions are received from ATHLET STH calculation. Outlet of the core region is mass flow and temperature boundary for the CFD calculation. As there are 7 different core regions defined with partly small mass flow rates, some are gathered for the CFD calculation. In case of mass flow rates, STH results can be simply gathered as sum. For temperatures, individual values are weight averaged with their corresponding mass flow rates.

$$T = \frac{\sum_i T_i \cdot \dot{m}_i}{\sum_i \dot{m}_i}$$

In case of the blanket boundary condition during the pump trip, mass flow drops below zero. Flow recovers from reversal during the natural circulation part of the transient. As the temperature for this boundary condition is weight averaged (see equation above), singularities occur in case of mass flow rates at zero (division by zero). Because even such small mass flow rates differ highly between the averaged STH regions, temperature cannot be arithmetically averaged. Spikes in the temperature boundary condition may lead to errors, even divergence of the CFD calculation. For that the use of a filter function was considered, that smoothens high frequencies - as it is the case for the received spikes in the temperature time table. As a result, the profile of the blanket temperature boundary condition stays the same but spikes are taken out. Graphs of all boundary conditions to the hot plenum can be seen in ch. C. The ATHLET STH calculation provides the pressure boundary condition for CFD as well. OpenFOAM calculations with the buoyantPimpleFoam solver are processed with p_{rgh}, the ATHLET pressure can not be used directly as it may lead to incorrect total pressure values. For this reason, ρ is averaged and the term $\rho \cdot g \cdot h$ is subtracted from the static pressure with reference elevation at the bottom of the OpenFOAM geometry taken into account.

Transient results

In the case of the NCT transient case, the hot plenum regime does not provide steady results for y^+ (see ch. 2.5) but transient ones. All bounding walls of the hot plenum region are either of type inlet, outlet or wall. For reasons of better classification and mesh generation, the wall type boundaries are grouped in patches. There is a number of different patches that are defined as walls with wall functions. To give a flavor, one patch is picked out and shown here. More plots of y^+ for the transient results can be found in Appendix C.

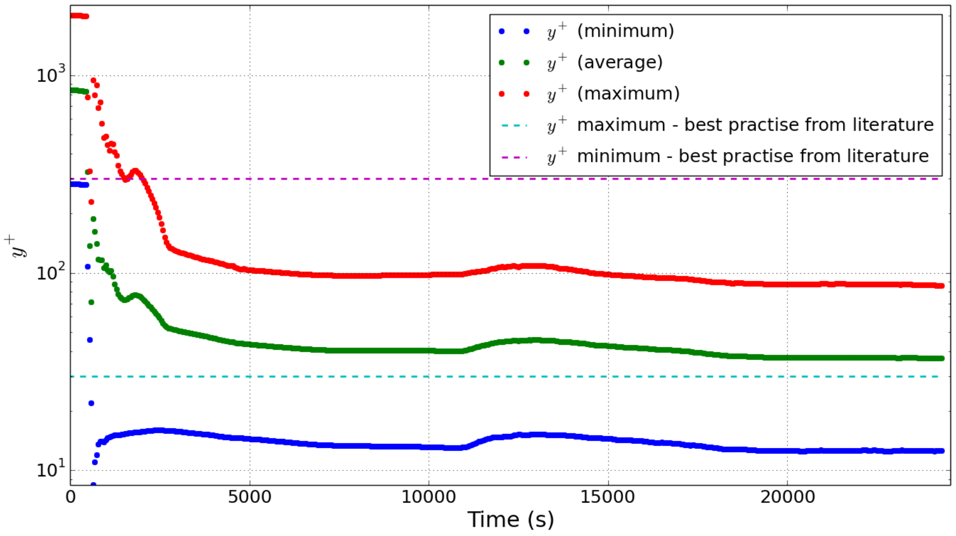

Fig. 4.3: y^+ at Cover Plug Bottom

Some results are shown in fig. 4.3. More are given in Appendix (ch. C). It is well observable, that the y^+ values change as much as the boundary mass flow rates do. In fig. 4.3 y^+ at the structure directly above the core outlet is shown. One can see that in steady state condition, the results are not within the limits given by best practice guidelines [87]. As it only appears in the beginning of the transient (about 2% of the whole transient)

and disappears with the reduction of mass flow at the inlet, the mesh configuration is considered suitable for this transient case. This compromise had to be made because of high deviation of the mass flow rate during the PHENIX NCT case scenario, which is shown in following.
The velocity field is one of the most significant differences between a ATHLET STH simulation and OpenFOAM CFD simulation. As the hot plenum had been picked out because of its large volume and is assumed to contain strong three dimensional behavior in steady state condition as well as in the given transient case, extensive research on exactly this behavior begins with investigation in velocity fields. During the transient with steady state boundary conditions, fluctuations between the outlets of the hot plenum (IHXs inlets) are observed.

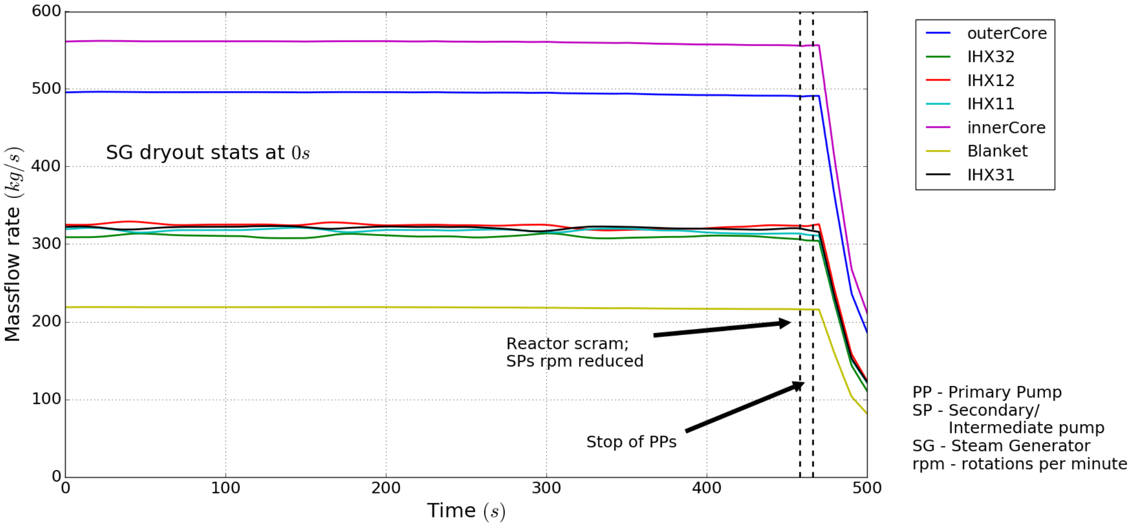

Fig. 4.4: CFD - mass flow - steady state

Even with very high cell resolution (see ch. 4.2) this behavior is observable and does not simply occur through numerics. Fig. 4.4 can be explained with three dimensional fluctuations which cannot be represented in STH. At the beginning ($0s \rightarrow 468s$), the primary pumps are in full operation and are stopped afterwards. A look at the transient case may help to better understand the necessity of CFD in the hot plenum region. To have a better understanding of the strong three dimensional behavior, some time steps of the given transient (NCT) were picked out and velocities along one line plotted as illustrated in fig. 4.5. For larger graphs one may refer to Appendix C (fig. C.46) where the dimensionless vertical component (u_z) is illustrated with referring vertical cross-section of the hot plenum (flow field).

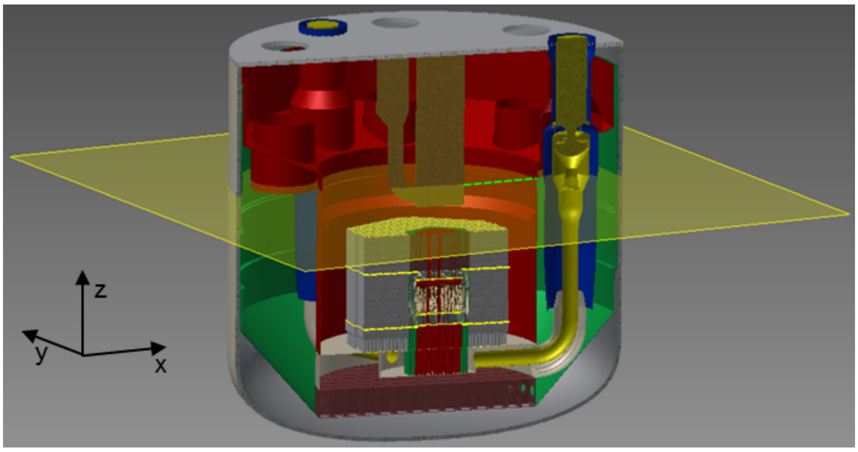

Fig. 4.5: Position of velocity probes (green dashed line) along x-axis

Velocity probes are placed along a line in positive (horizontal) x direction. This way, velocities can be illustrated in each cartesian direction. Parts that are not within the fluid region are left out so it can be considered as a horizontal line through the fluid region along the x axis at the elevation of $-1.25m$. Considering the graphs in fig. fig.4.5, fig.4.6, fig.4.7 and fig.4.8 (or Appendix C, page 163), three dimensional behavior of flow during the whole transient can be observed. In case of U_z, a jet during steady state coming from core outlet flowing towards the IHX inlet can be observed. It first shrinks and then, during the transient when the primary pumps are shut down but residual heat is still high, this jet flips to a straight vertical direction (at $4000s$) before it collapses (between $10300s$ and $24250s$). This behavior is supported by U_x component while the U_y is rather chaotic and therefore represents the three dimensional flow behavior through the whole hot plenum with fluctuating jets at steady state condition that also shrink.

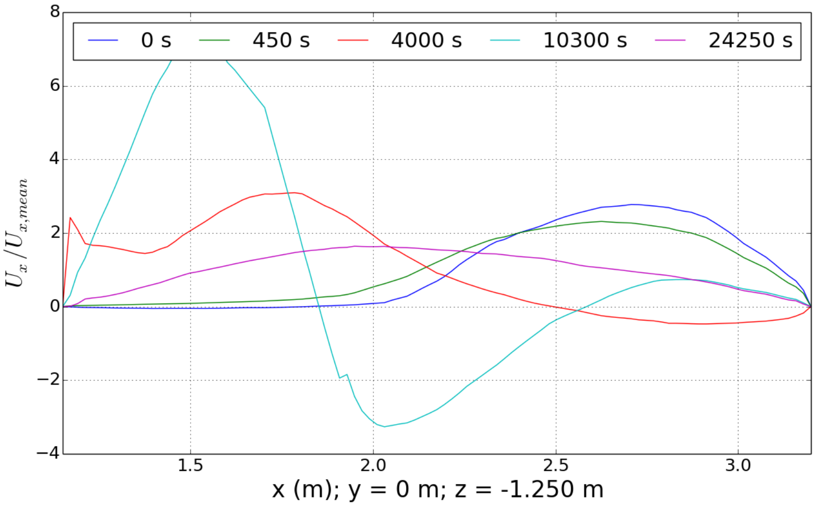

Fig. 4.6: $U_x/U_{x,mean}$ along x coordinate

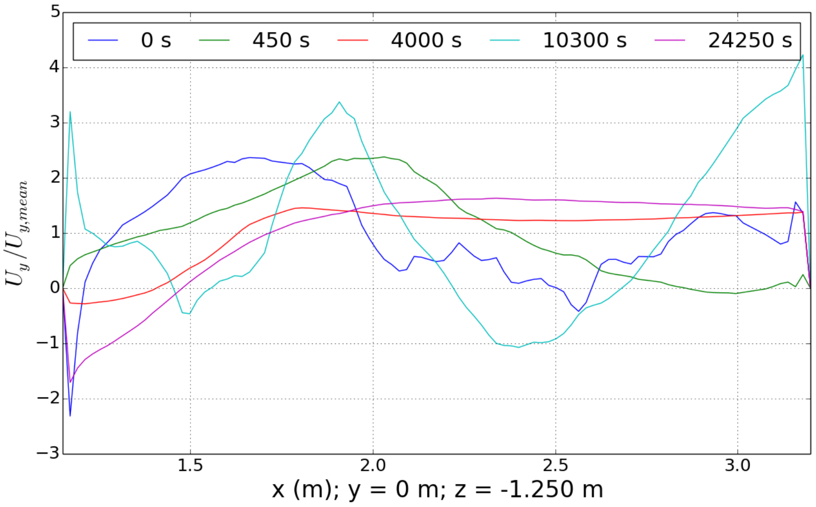

Fig. 4.7: $U_y/U_{y,mean}$ along x coordinate

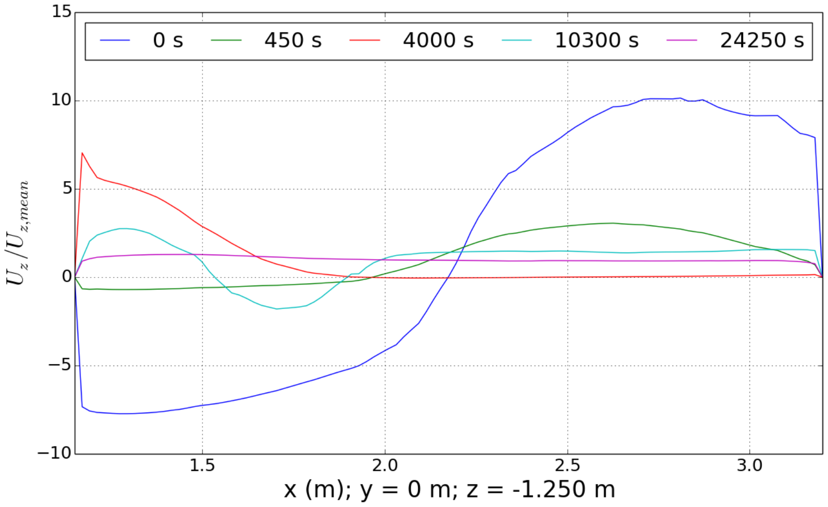

Fig. 4.8: $U_z/U_{z,mean}$ along x coordinate

During steady state the temperature field fluctuates according with the velocity field. Hot jets lead from the core into the large volume of the hot plenum where they mix. This phenomenon can be described as thermal striping [24]. To observe temperatures in large volumes hot plenum that indicate thermal striping or thermal stratification, poles with fixed thermo couples are normally arranged in vertical direction. For CFD such a pole with fixed thermo couples has been recorded during the simulation. Its position and results during steady state can be seen in fig. 4.5, fig. 4.6, fig. 4.7 and fig. 4.8.

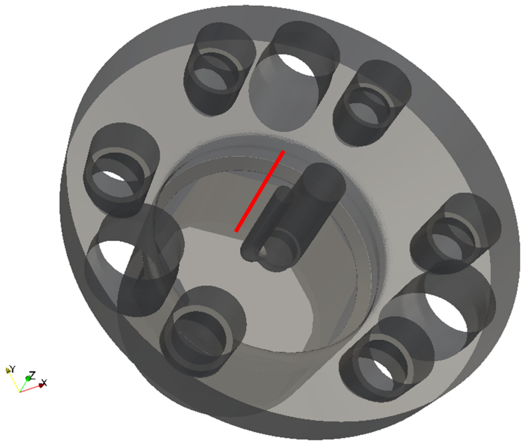

Fig. 4.9: Position of thermocouples (red line)

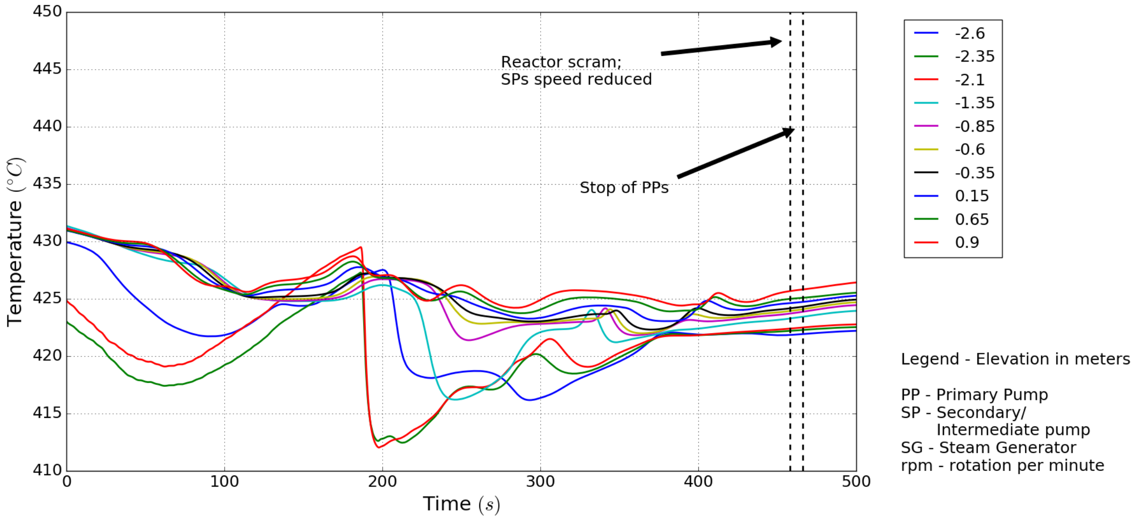

Fig. 4.10: Temperatures along vertical axis ($0s$ to $500s$)

During the transient, the phenomenon of thermal stratification can be observed after shut down of the primary pumps and reactor scram (fig. 4.11).

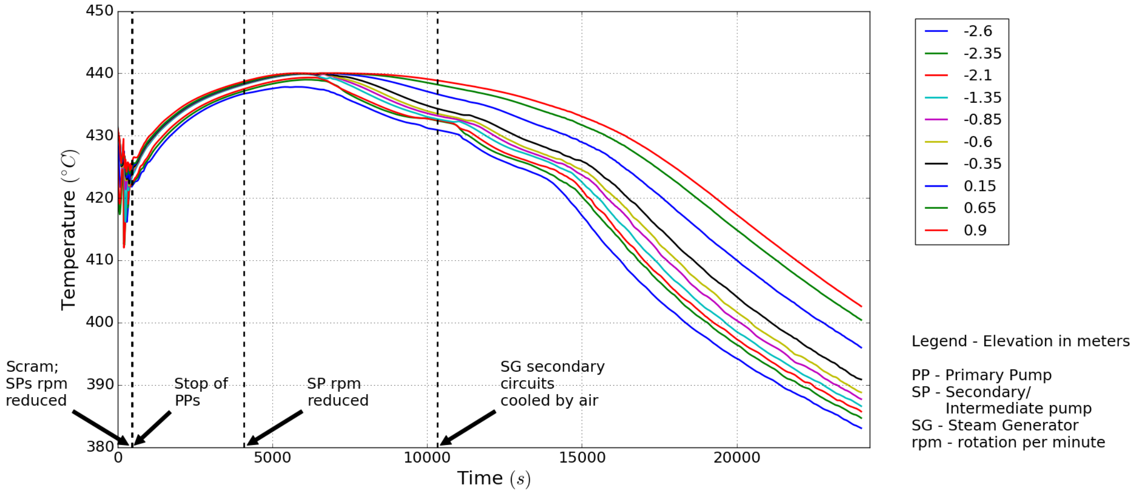

Fig. 4.11: OpenFOAM: Hot plenum - Transient - temperatures along vertical axis

Thermal stratification is well observable, although all boundary walls are assumed adiabatic. The reason why all boundary walls are considered adiabatic is, to capture this phenomenon only because of the size of the fluid volume. During the transient, when the primary pumps are shut down and there is only residual heat coming from the core, temperatures in the upper regions of the hot plenum rise but do not necessarily enter the IHXs. So, even in liquid metal, thermal stratification can be observed. This means, generally speaking, that heat is stored in such large volumes. However, it can also be observed that high temperatures at upper elevations of the hot plenum cannot be removed as quickly as in lower regions without forced flow.

The whole transient is calculated with a standard $k-\epsilon$ turbulence model, which follows a high Reynolds approach. The calculation of the Reynolds numbers is crucial in this case. For that reason, the tree inlet regions as well as the cross section in x,y-plane which contains the previously described line plot are represented in fig. 4.12. The cross section is a plane normal to the z-axis at z-elevation of $-1.25m$. In fig. 4.12 it is named "hot pool".

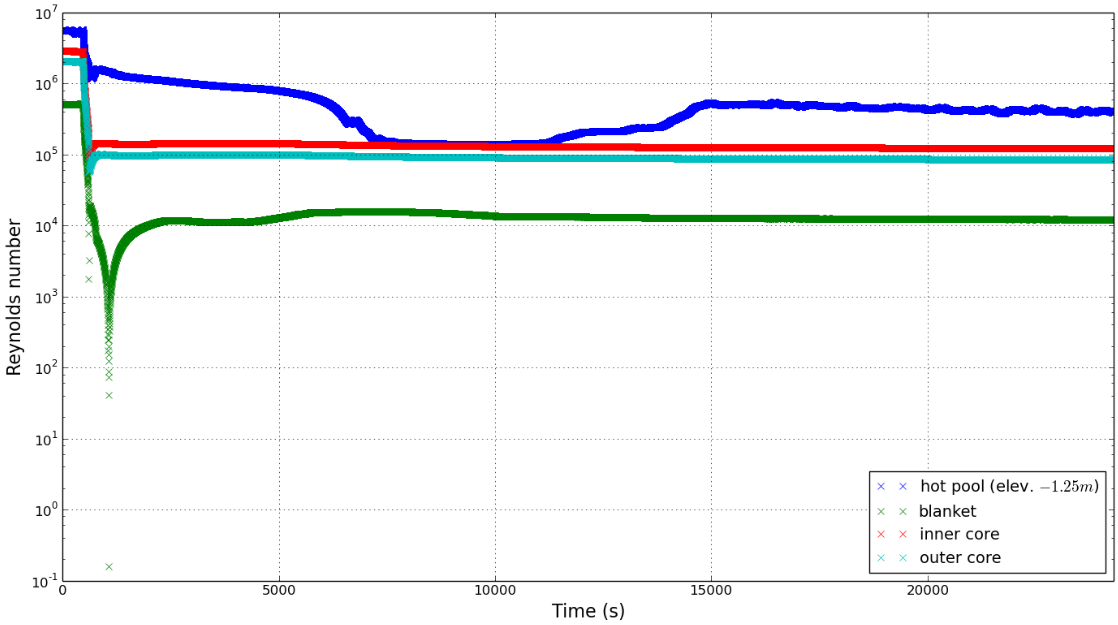

Fig. 4.12: OpenFOAM: Hot plenum - Transient - Reynolds numbers

The Reynolds numbers are directly calculated from derived values (fig. 4.12). For the reason that the blanket inlet region is the sum of several ATHLET STH regions, two spikes can be observed. The curve has not been smoothened. As mass flow (velocity) at that boundary field crosses the zero line at time of flow reversal and dynamic viscosity is small, the Reynolds number comes close to zero. The cross section at $-1.25m$ shows rather high Reynolds numbers so it can be assumed that the $k-\epsilon$ turbulence model can (still) be applied.

As all wall patches of the hot plenum region are considered adiabatic, it can be assumed that the influence of the walls concerning temperature can be neglected. Accordingly, the Prandtl number (eq. (2.17)) close to the wall does not necessarily need to be discussed as intensively as in [53] or [109], but is has to be kept in mind as soon as walls are heated.

In the given transient, the Prandtl number changes according to the given boundary conditions at the inlets (mass flow/velocity and temperature). It is observable that the Prandtl number increases slightly with beginning of the steam generators' dry out and consequently rise of temperature at the inlet to the CFD region. As the pumps are at this time still at full operation, this is an indicator of a drop in the thermal diffusivity

α. As $\alpha = \lambda/(\rho c_p)$ this means that the influence on density and thermal conductivity by temperature is higher here, than on viscosity. Inside the CFD region, the Prandtl number increases by less than 1%. Even after the pump trip, when the boundary inlets' Prandtl numbers drop significantly, the mentioned increase is barely recognizable inside the hot plenum. Until the opening of the steam generator housing, the Prandtl number in the hot plenum changes only about 1% compared to its starting value. After the steam generator housing is opened for residual heat removal, the Prandtl number in the CFD region is increasing about 3% until the end of the transient. With start of the decay heat removal procedure, it can also be observed that mass flows increase slightly again and temperatures at the boundaries further drop. Still, the Prandtl number is over the whole transient very low as it is typical for liquid metal materials as sodium.

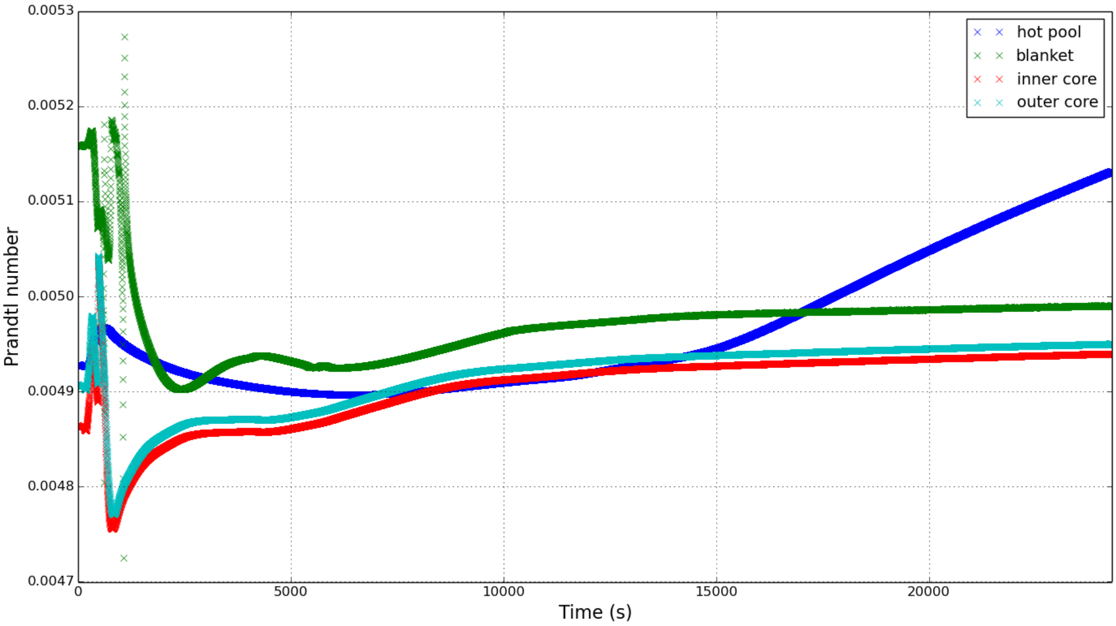

Fig. 4.13: OpenFOAM: Hot pool - Transient - Prandtl numbers

In fig. 4.13, results are surface averaged. The positions are the three inlet regions (surfaces): inner core, outer core and blanket. At an elevation of $-1.25m$ (see cross section given by plane and hot plenum geometry in fig. 4.5), results are averaged over the horizontal cross section. If fig. 4.13 and fig. 4.11 are compared, on can observe, the Prandtl number can be used as an indicator for thermal stratification. Shortly before $15000s$ of the transient, temperatures along the pole of thermo couples shown in fig. 4.11 start to spread. The Prandtl number increases at the same time. So, even if temperatures are dropping slowly in the hot plenum volume, the Prandtl number increases. Accordingly, the viscous diffusion rate must increase stronger than the thermal diffusion rate starting around $15000s$ of the transient. This is the case, if natural circulation is assumed and therefore momentum diffusivity increases. If the discussed velocity profiles given in fig. 4.5, fig. 4.6, fig. 4.7 and fig. 4.8 are additionally taken into reference, it can be seen that even in natural circulation state, the flow field has strong three-dimensional behavior.

5. STH/CFD coupling approach

The main target of this coupling methodology is the representation of three-dimensional effects which cannot be analyzed by single STH calculations. It is a problem of scales as already described in the beginning. Coupling of two scales induces three kinds of challenges:

1. Individual numerical schemes
2. Space and time treatment/handling of regions in each of the two codes
3. Code architecture with focus on data structures and its exchange

Starting from this point of view, it is clear that simple inclusion of the two solvers may be one possible solution but either very challenging or simply impossible (dependent on the availability of the source of each code). Additionally, it may only be possible for single application solutions, while it may be required for large fields of applications. For that reason, it is more practicable to have two codes available (STH and CFD) and provide a platform that makes exchange of data not only possible but also affordable concerning costs - with which is meant calculation time and infrastructure needed. In our days, codes that perform large calculations are able to be run in parallel processes. This can save time but increases the requirement of more calculation power at once. So, it is suitable to have a communication platform available, that can handle multiprocessing. Here, this last mentioned point is not of high priority but still is kept in mind for further development efforts. In this present work the ATHLET code [80] and the OpenFOAM open source computational fluid dynamics (CFD) toolbox is used. As described in previous chapters, the two codes do not share numerical schemes. Also, space and time handling of calculated regions and code architecture are different. This requires interfaces to exchange data between the two codes. One solution could be to use one of the codes as library of the other code. The approach implies one of the codes to master the calculation. Another solution could be, to create a platform to supervise both codes. This way none of the codes' solvers is forced to behave according to its opponent. The codes can perform calculations as in a single code application, which significantly increases the stability of both codes. Still, further steps to control time step size can be done and the individual codes could even be exchanged by others. Following this idea, the first step to a coupled simulation is to research its behavior in time. Here, also two different kinds of methods can be applied. One is to exchange data after a given (fixed or non-fixed) time step, another is to iterate a (large) group of time steps. Following this idea, the shape and structure of data needs to be decided. As shown in ch. 2.6, the two codes can either share regions or they can be separated. Both approaches are capable of performing coupled results. In an overlapping approach, calculation results by one code are "corrected" by the other one. When regions are separated, the codes communicate through boundary conditions. Second approach restricts the variety of exchange parameters to physical boundary conditions (steady state or transient) but makes research on the impact of artificial produced errors almost obsolete and can be verified quickly.

In case of the present work of coupling ATHLET and OpenFOAM, the size of time steps is not considered. As all boundary conditions for both of the systems are given as time tables, causality and time invariance can be assumed. If sophisticated neutron kinetics would be applied, decay and age of fuel must be taken into account which directly conflicts with the given time invariance assumption. Here, neutron kinetics models are not used but power is simply given as a time table in the core of the nuclear reactor PHENIX [129]. This in mind, as a starting point, iterations over the whole given transient can be carried out. With each iteration, the discrepancy between one iteration and its predecessor is assumed to decrease its value.

5.1 Methodology

The present developed code architecture uses a neutral (`ASCII`) format for data exchange. So it can be edited and modified by the coupling interface and be read by the codes without translation (or transition) efforts. This might be likely if binary format was used. Each code has an interface layer to provide values needed from the other code. In the system code regime, only one dimension is needed (e.g. velocity) and not three dimensions (e.g. velocity vector) like in CFD. In the case of data transferred from the STH regime to the CFD regime, values are connected to surfaces and velocities are oriented orthogonally to the surface. In the case of data transferred from the CFD regime to the STH regime, e.g. velocities orthogonal oriented to the surface are taken into account and averaged over the surface. So the value given back to the system code regime is fitting the required dimension (scale). The transferred values are used as boundary conditions for the transient simulation in each of the codes. In the CFD regime, they are given to surfaces, in STH code the values are given through inlet/outlet boundaries that are one-dimensional (scalar). In the demonstration example of the PHENIX NCT transient, boundary conditions that describe the transient are given to ATHLET (see fig. 1.4). All large volumes that could be described in CFD don't need external boundary conditions but the previously described information from data exchange. Boundary conditions, that describe the PHENIX NCT and are given to the ATHLET model are given in tab. 5.1.

Primary side	**Intermediate/Secondary side**
All boundary conditions given as time tables.	
• Core power • Primary pump speed	• IHX inlet temperature • IHX inlet massflow • IHX outlet pressure
→ Closed circuit model	**→ Open circuit model**

Tab. 5.1: Boundary conditions of the PHENIX NCT [59]

Coupling in space

This gives the opportunity to handle CFD and STH as if in standalone mode. In comparison to this methodology, the domain overlapping method given in ch. 2.6 must be mentioned here, where the two regimes are not fully geometrically separated. In addition, the time step treatment is one of the most challenging parts. The two codes have to be run synchronized in (physical) time as described in chapters (ch. 2.6).
In the present methodology, it is not necessary to synchronize the two codes" time steps. The two codes provide the full solution (transient case) after the end of each simulation run. Still, in the present methodology, the geometrical decomposition must be given, but the two regimes are completely separated. Here, the hot plenum is used as CFD regime.

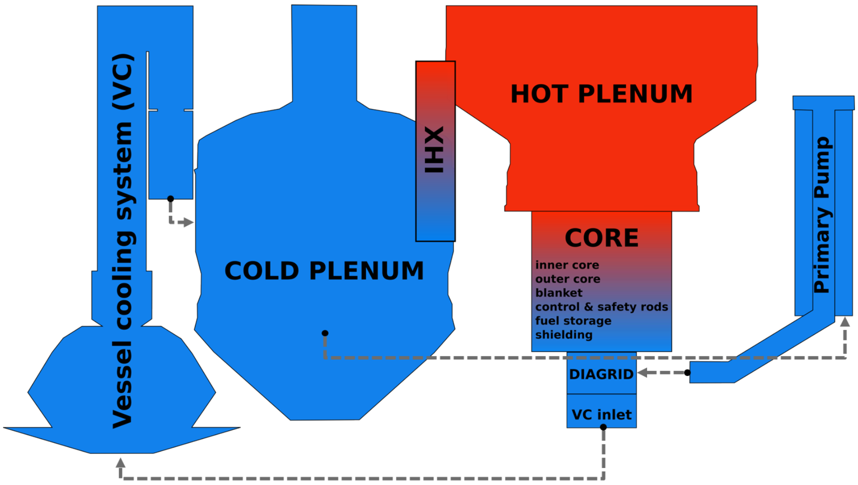

Fig. 5.1: Fluid domains of ATHLET and OpenFOAM in primary circuit

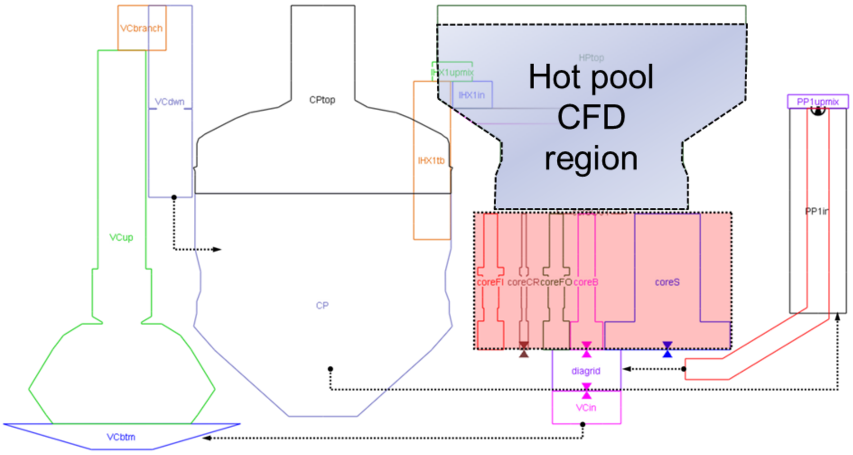

Fig. 5.2: ATHLET representation with 491 CVs

Coupling in time

The coupled simulation starts with one transient simulation of the whole transient case in STH stand-alone. ATHLET must provide all information about the circuit and must therefore be run in a closed circuit configuration. Values needed by CFD for the transient simulation are recorded to csv-files. The CFD regime also simulates the whole transient calculation with boundaries given from the initialization derived from the ATHLET closed circuit run. The derived CFD calculation results from the CFD simulation can be transferred to the ATHLET open circuit system after the end of the CFD simulation. The

ATHLET open-circuit simulation if performed with the conditions (input) from the closed circuit but without the CFD domain. The missing values are given from the CFD simulation's results. After the ATHLET open circuit simulation of the transient case, new boundaries for the CFD regime are derived and transferred to begin the second CFD simulation. This iteration process continues until the delta of residuals (exchanged values) between the actual iteration step and previous iteration step are in specified range.

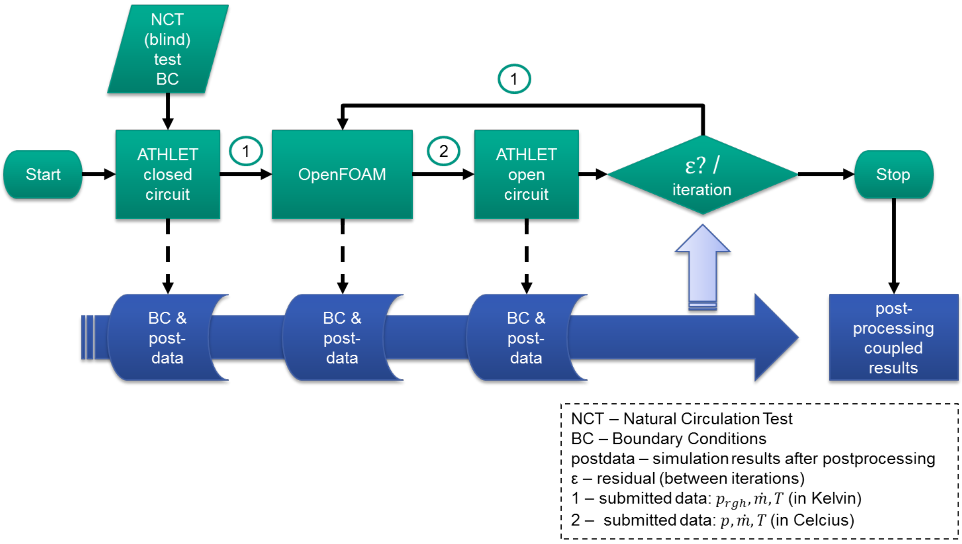

Fig. 5.3: Scheme of iterative methodology for coupling

5.2 Verification

As verification, a very simple and academic example is chosen. It consists of three pipes in horizontal arrangement. All pipes are calculated with the ATHLET code. This allows one to verify the scheme to avoid numerical discrepancies between STH and CFD and to check convergence behavior.

Fig. 5.4: ATHLET/ATHLET coupling: pipes arrangement

The model shown in fig. 5.4 shows one long ATHLET pipe consisting of three thermo fluid objects (TFOs). The middle TFO represents a surrogate OpenFOAM pipe and is calculated with the ATHLET code. All pipes are of equal length ($l_0 = 10.0m$) and equal hydraulic diameter ($d_h = 0.1m$). Each TFO consists of 100 control volumes (CVs; STH mesh) as in principle shown in fig. 5.5.

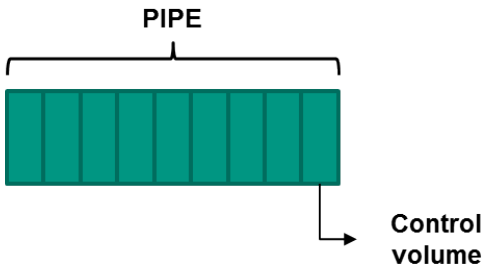

Fig. 5.5: ATHLET/ATHLET coupling: control volume (CV) structure

Boundary conditions

The boundary conditions (BC) are marked in fig. 5.4 with blue arrows. Gravity is taken into account (see black arrow in fig. 5.4). As inlet boundary condition, mass flow and temperature are defined. As outlet boundary condition, pressure is defined.

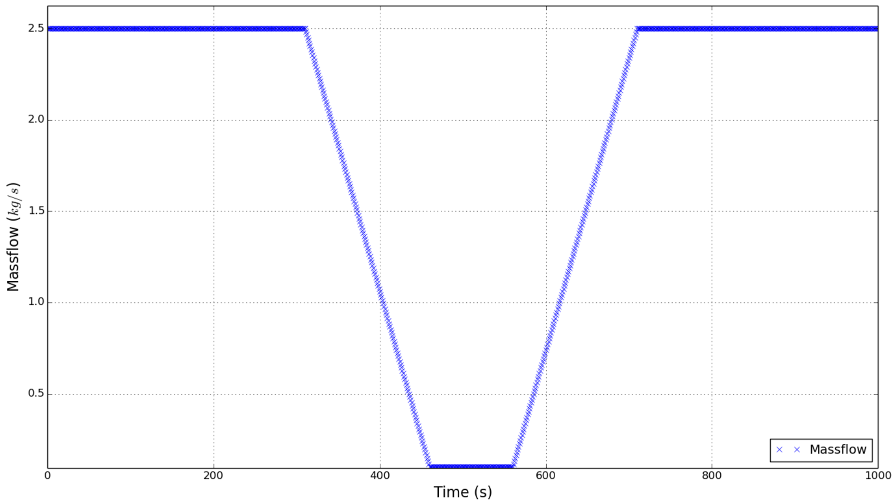

Fig. 5.6: ATHLET/ATHLET coupling: Mass flow boundary condition (academic model, verification)

Temperature at the inlet is constant at 450°C. The inlet temperature is dropping constantly after 100s to $400°C$ and is then increased again to its beginning value. Pressure at the outlet is fixed to $1.5bar$. Pressure is kept constant during the whole transient. The profile of mass flow rate at the inlet boundary is shown in fig. 5.6. Starting point is a mass flow rate of 0.5kg/s. After 300s, mass flow is reduced constantly until a slight flow reversal of -0.1kg/s is initiated. Flow reversal will be kept for 50s and then increased back to the original flow direction and quantity. Concerning mass flows, this setup is more challenging to the coupling interface than the expected dynamical behavior of the PHENIX NCT later on.

Initialization

To show how the coupled solution reacts during iterations (see fig. 5.3), the initialization is modified for the present verification as follows (fig. 5.7).

Fig. 5.7: ATHLET/ATHLET coupling: initialization model (academic model, verification)

The boundary condition at the wall of PIPEOF is modified from adiabatic to a temperature profile (see fig. 5.7 for position and fig. 5.8 for profile). This produces divergent values for PIPEOF as initialization and shall show if the coupled solution is capable of converging to the target solution. This step is crucial for coupling. Otherwise, the coupling interface may add artificial discrepancies to the solution and the coupling interface can not be considered verified.

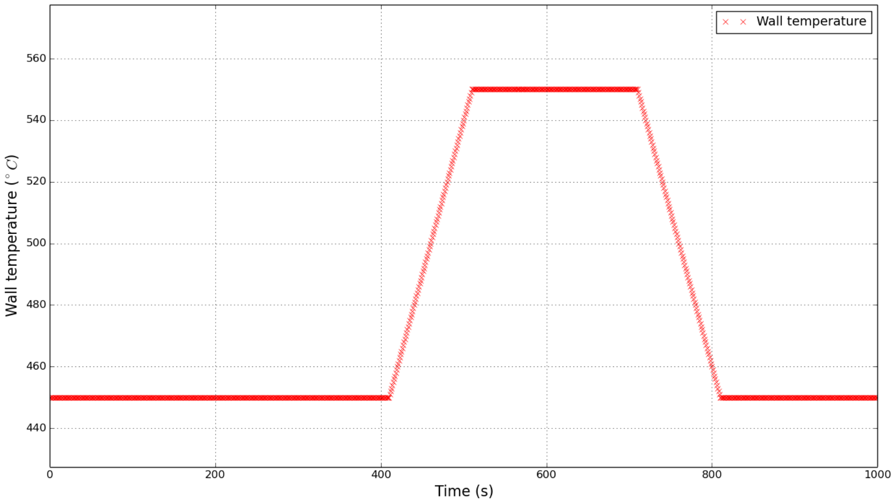

Fig. 5.8: ATHLET/ATHLET coupling: initialization model - temperature profile (academic model, verification)

Information propagation

Information of boundary conditions is provided as shown in fig. 5.9. As inlet condition, mass flow rate and temperature must be provided from the last control volume (CV) of the previous TFO or from boundary conditions. Pressure is provided backwards from the first CV of the following TFO or boundary condition to the last CV of the recent TFO. The numbers in fig. 5.9 are given to keep an overview.

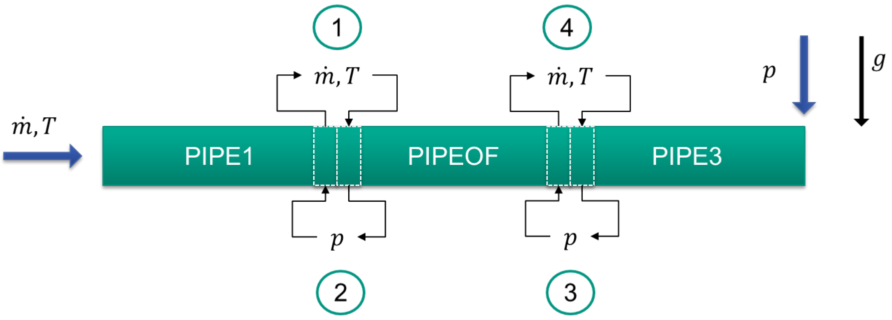

Fig. 5.9: ATHLET/ATHLET coupling: Information propagation at initialization

During iterations, tables are created from every region to provide boundary conditions to the other regime. Normally, this would be ATHLET and OpenFOAM. Here it is only two regimes of ATHLET to test the coupling interface and methodology.

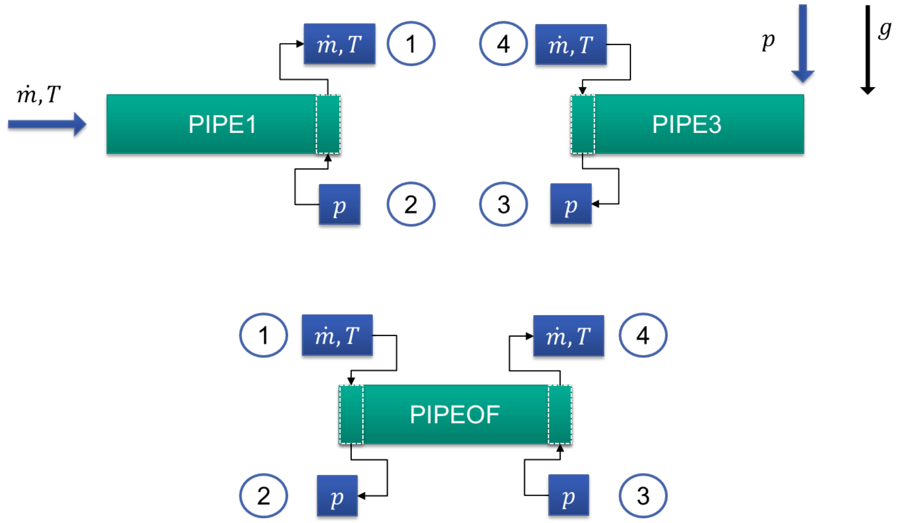

Fig. 5.10: ATHLET/ATHLET coupling: Information propagation during iterations

As shown in fig. 5.9 the boundary conditions in one regime are calculated in the other regime. This avoids possible malfunctions from information propagation to the calculations. It also shows very clearly when programming error may have occurred in the coupling scheme (implementation/methodology). Additionally, convergence behavior can be researched which gives some idea about convergence behavior between STH and CFD later on.

Results

Fig. 5.11 shows 'CV1' (most left CV) of the 'PIPE3' TFO (s.a. fig. 5.10). Mass flow rate and temperature are given as boundary conditions. As it is recorded from the initialization with imprinted high wall temperature in exactly this regime, a different temperature is provided to 'PIPEOF'. Hence target solution only considers adiabatic walls. The two regimes are of the same manner as the target (standalone ATHLET model) solution.

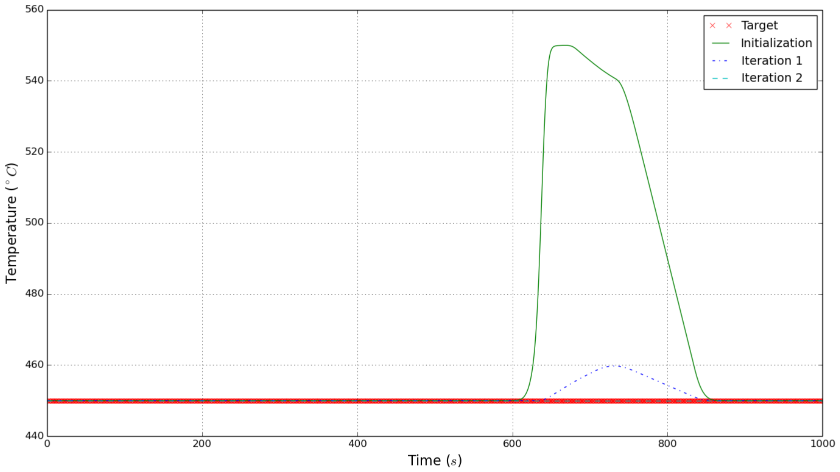

Fig. 5.11: ATHLET/ATHLET coupling: Temperature behavior during coupled run

Similar to the expected and already shown mass flow behavior of the validation test case (see ch. 6) mass flow at the boundary inlet is decreased during the transient calculation significantly (form $2.5 kg/s$ to $0.1 kg/s$). Additionally, the increase of wall temperature in the (pseudo-) CFD pipe is increased in different time scales. So it can be assumed, a coupled simulation may converge within 2 iterations. This is shown in fig. 5.11 where the target represents a full STH solution without additionally imprinted higher temperature at the wall of 'PIPEOF'. Furthermore, it can be assumed, if the initial solution gives different solutions because it is not capable to cover physical effects like thermal stratification, this can be taken in reference by a coupled solution.

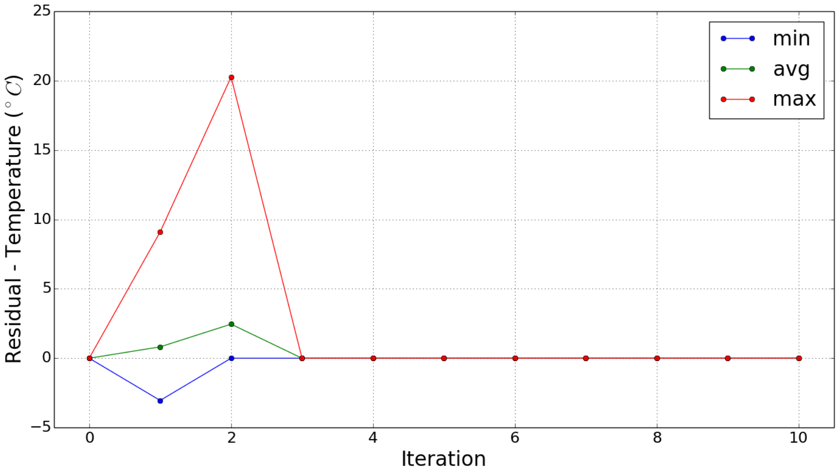

Fig. 5.12: ATHLET/ATHLET coupling: Convergence behavior example (Temperature)

The convergence behavior of this recent coupled simulation can also be seen in fig. 5.12. It should be mentioned here that step zero is the target solution, step 1 is the initialization result and starting from step two open circuit iterations are shown in ascending order. If fig. 5.11 is now reviewed again, one can observe that the coupled solution converges to the target solution after two iterations.

6. Post-test calculations of the PHENIX NCT

The PHENIX natural convection benchmark test (NCT) is calculated with the modified ATHLET code. To calculate heat transfers in the core and in the IHX, the correlation of Mikityuk [95] is used to derive the Nusselt number. Pressure drops are built according to best estimations and adjusted to parameters provided by [59]. In the following subsections, usage of input data as well as simulation results are discussed and compared with data from measurements. First, STH standalone simulations are compared to measurements and discussed. Then, the physical phenomena of thermal stratification and thermal striping are implemented to the hot plenum by CFD and coupled to STH according to the methodology described in ch. 5.

6.1 STH (standalone)

Temperatures

Primary pump inlet temperature

According to the transient test data, the primary pump inlet temperature increases at the same time the IHX intermediate inlet temperature increases, which is caused by the steam generators dry out. ATHLET gives a similar increase of the primary inlet temperature in this stage. During the increase of the temperature, the simulation results show more smooth behavior. The measurements show a more rapid increase of temperature in the beginning. However, after 550s of the transient (fig. 6.1), ATHLET results show higher temperatures. At about 505s the measured temperature at near the primary pump inlet reaches its peak value of about $406°C$ before decreasing rapidly. The core has been shut down at 458s, followed by the stop of the primary pumps at 466s. The temperature measurement can be seen as an indicator of a significant change of flow behavior in the cold plenum, shortly after the execution of shutdown mechanisms. ATHLET results still show the established high temperature. It even increases slightly until 2100s of the transient (see fig. 6.2) before the simulated temperature decreases.

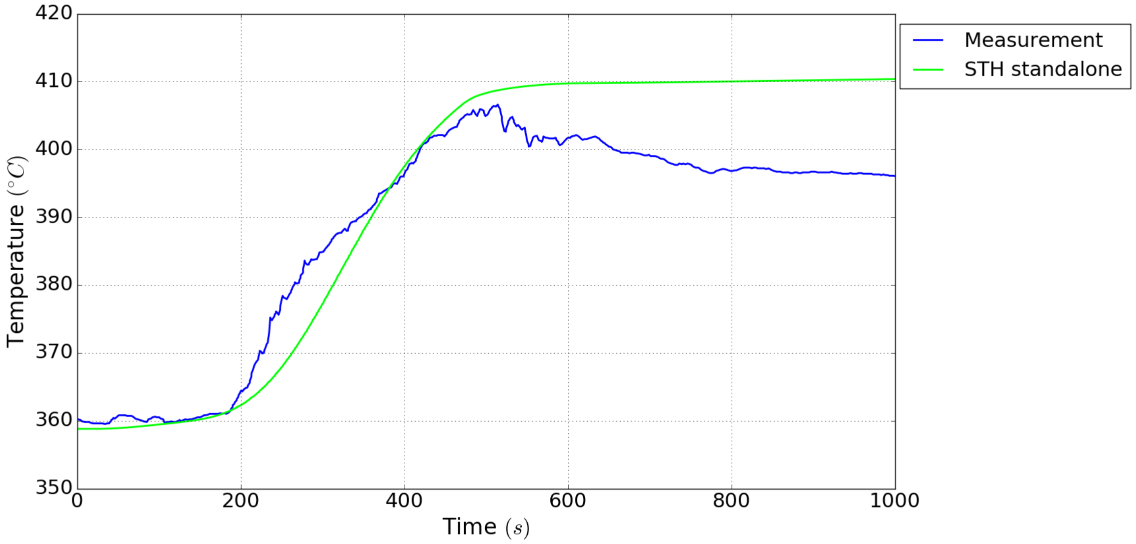

Fig. 6.1: NCT - STH solution: Primary pump inlet temperature (short term)

In ATHLET, CVs are arranged by topology which also describe the positive flow direction. Although the sodium volume is very large, temperature, pressure and mass flow are calculated in one point (center point of CV) at one elevation. In horizontal direction, total mixing is forced by the STH model approach. A three-dimensional, but coarse resolution would be possible. It needs more specific a-priori information about internal flow behavior. That way, flow streams would be modeled as separate pipes with cross-connections. For the presented test case, this information wasn't available which lead to the decision, not to model any flow behavior in horizontal direction. The consequence is total mixing and driven flow along the vertical axis. Hot sodium from the IHX primary outlet directly travels to the pump inlet through a large volume. There is minor energy exchange to the upper region of the cold plenum above the IHX primary outlet. The basic equations that lead to this behavior can be seen in ch. 2.4. It would be possible to assume flow streams during steady state (before start of the transient test case) and model them as pipes with cross-connections. With start of the transient, flow conditions change significantly in reality while ATHLET modeling would still assume flow behavior similar to steady state flow and therefore lead to a wrong simulation results or even conclusions.

The measured primary pump inlet temperature keeps decreasing until about 2100s and then increases slowly again until $10,982$s of the transient (fig. 6.2). STH results keep decreasing after its peak value, and meet the test data again (discrepancy lower than $1K$) at about $11,000$s. The outlet flow of the IHX primary side is driven by natural circulation. Sodium coming from the IHX has a lower density than sodium in the cold plenum. Because the primary pumps are not in operation anymore, the hot sodium travels vertically upwards along the outer shell of the IHX inside the cold plenum. Until the time of about 2100s hot sodium accumulates in the upper region of the cold plenum and cold sodium from the lower region (below the IHX primary side's outlet) travels to the primary pumps. The measured primary pump inlet temperature decreases after $10,982$s caused by air cooling of the steam generator housing, which creates a heat sink there. The air cooling of the steam generator has its start at $10,320$s during the recorded transient. Afterwards both, the measured and calculated primary pump inlet temperature decrease in a similar manner. The STH calculation shows a slight underprediction of the temperature here due to higher cooling of the primary circuit.

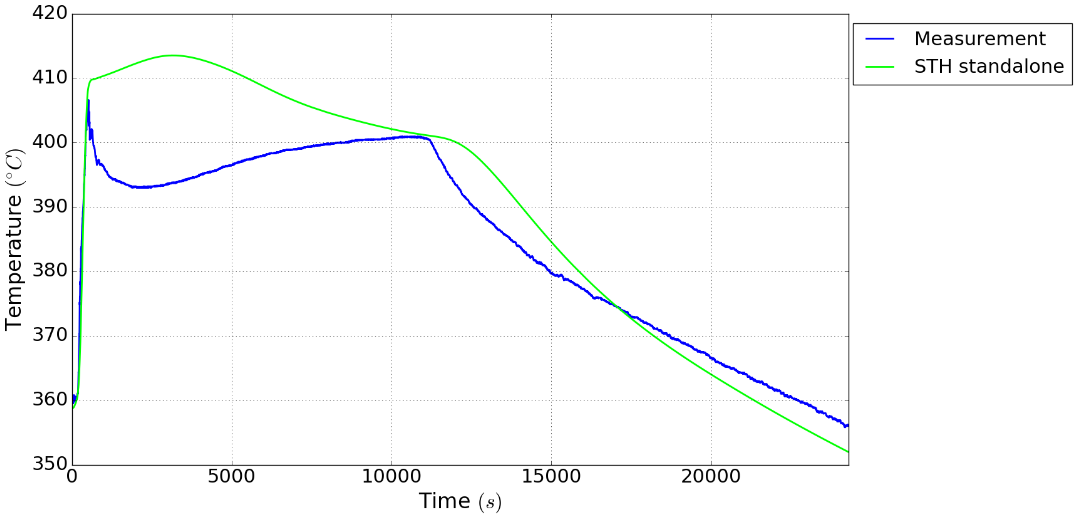

Fig. 6.2: NCT - STH solution: Primary pump inlet temperature (long term)

One reason for the deviation of the STH calculation results from the measured data between 320s and $11,000$s of the recorded transient is the large volume of sodium. Strong thermal stratification as well as thermal striping or complex multidimensional flow directions cannot be represented in the used STH code model. The cold plenum is modeled by a simple branch with the given dimensions of the cold plenum between elevations of inlets (IHX outlet and VC outlet to the cold plenum) and the primary pump inlet regions. More geometrical information can be received by IAEA [59], Sauvage [129] or Tenchine et al. [148]. Thermal stratification cannot be taken into account sufficiently by STH modeling. One reason has been given to be the strong dependency of the energy equation to the continuity equation. The continuity equation is strongly dependent on the topology of the 1D model representation (s.a. 2.4). As a result, the temperature increase is directly transferred to the PP inlet. One can observe an increase of temperature beyond measurements during the STH calculation. Additionally, as there is only one temperature calculated in the control volume, some inertia can be observed that would damp high frequencies of temperature changes. However, strong buoyancy effects that are taking place in the cold plenum, leading to different pump inlet temperatures, cannot be represented because of their strong three dimensional behavior. Reason for that is the velocity field and temperature field which are scalar values in the STH code calculations. Hence, the average velocity is driving flows from one boundary to another. These are the major drivers for the observed discrepancies between STH code calculation and measurements. It should also be mentioned that the position of the thermocouples cannot be represented adequately in the STH code calculations. Mainly only elevations can be approximated through mesh refinement in those places which is of influence to the thermo hydraulic behavior of the STH model for a given transient calculation.

IHX primary side - Temperatures

IHX primary inlet temperature

The measured IHX primary inlet temperature almost keeps unchanged until about 490s of the NCT transient (fig. 6.3). The more than $20°C$ sharp decrease of the measured core outlet temperature right after the reactor scram just leads to about $4°C$ delayed decrease of the measured IHX primary inlet temperature. This is because of large thermal inertia in the hot plenum and as a consequence of this, the very slow transient response speed and strong temperature hysteresis effect. Comparatively, the STH calculated IHX primary inlet temperature displays relative smoother but still similar trend like the calculated core average outlet temperature. It means the STH hot plenum model does not sufficiently slow down or damp the temperature change of coolant from the core outlet. The differences at time 0s originates from the blind test conditions. For the blind test, it was specified a temperature of $432°C$ at the IHX inlet. However, the reference to compare the IHX inlet temperature was taken from a pole of thermocouples which location is not ideally at the (operational) IHX inlet region. The considerably small discrepancy of about $3.2°C$ ($\sim 0.7\%$ deviation) can thus be argued (fig. 6.3) that the blind test condition data was used to adjust the IHX inlet temperature with the given value in [59].

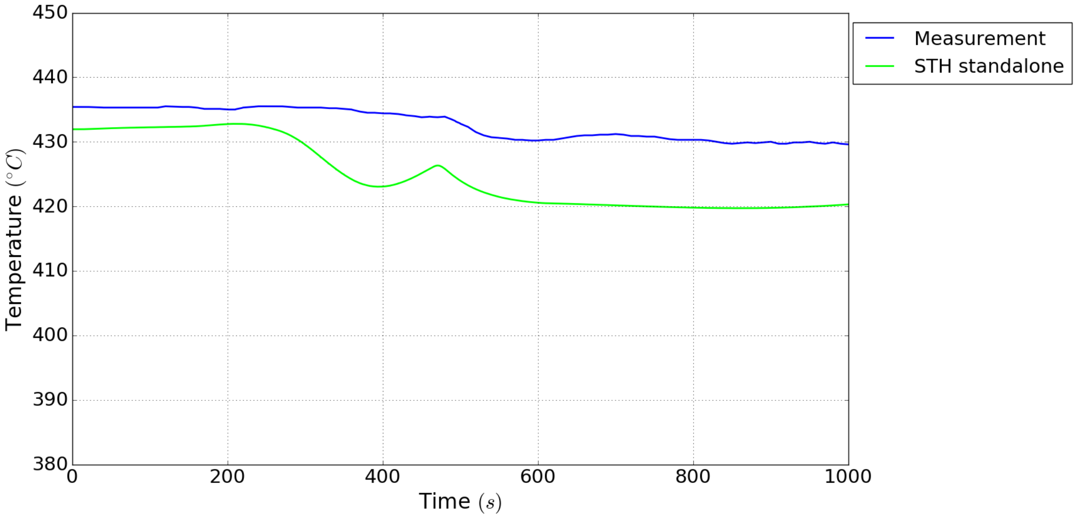

Fig. 6.3: NCT - STH solution: IHX inlet temperature (short term)

During the hot and cold shock of the transient (sudden sharp increase and decrease of the measured temperature during the recorded transient), the large control volume of the hot plenum damps peak values in temperature at the IHX inlet (fig. 6.4). After scram and pump trip, hot sodium leaving the core is only driven by buoyancy forces. As flow velocities are small, hot sodium travels almost vertically to the liquid surface (along the core support structure). Due to thermal stratification, the newly built up temperature field expands into the IHX region. This effect is of strong three dimensional behavior as the hot plenum has different temperature zones in horizontal and vertical dimension. STH codes have only one scalar value so that the mentioned different zones can be seen as averaged. This hypothesis is consistent with results of the given STH solution. For its validation, more measurements could be necessary.

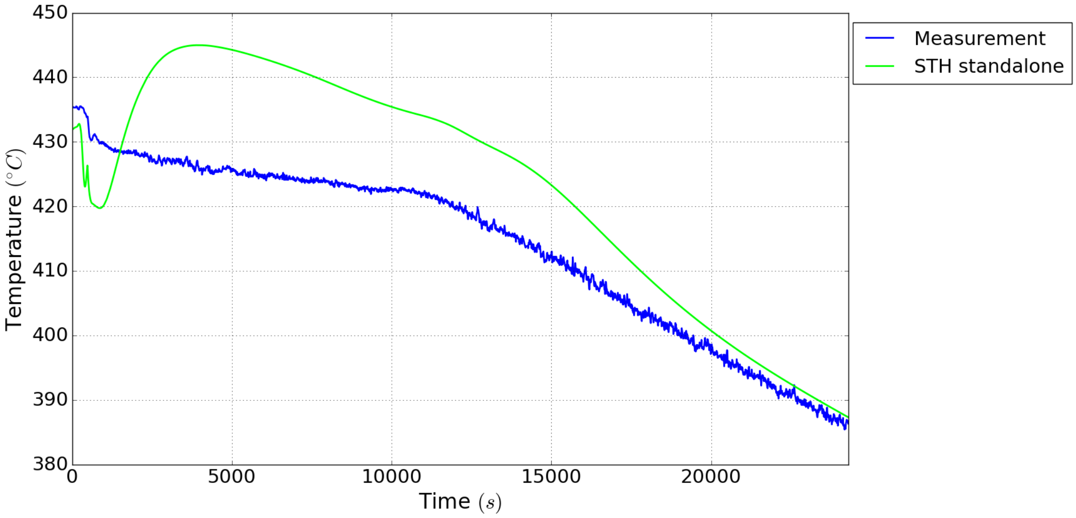

Fig. 6.4: NCT - STH solution: IHX inlet temperature (long term)

IHX primary outlet temperature

At the beginning of the NCT transient, the primary IHX outlet temperature increases as its intermediate inlet temperature increases as described by Tenchine et al. [148] or [147]. The STH simulation with ATHLET gives similar results compared to measurements (see fig. 6.5) during this period of the NCT transient. However, the simulation results show slightly slower increase of the temperature. This may be caused by the large volume modeled also in the cold plenum area in the STH model in ATHLET but also on the position of the thermocouple that recorded the temperature. The thermocouple is not mounted directly in the outlet stream of the IHX outlet but about 35cm away from that position. This may be of influence when looking at the transient results later on.

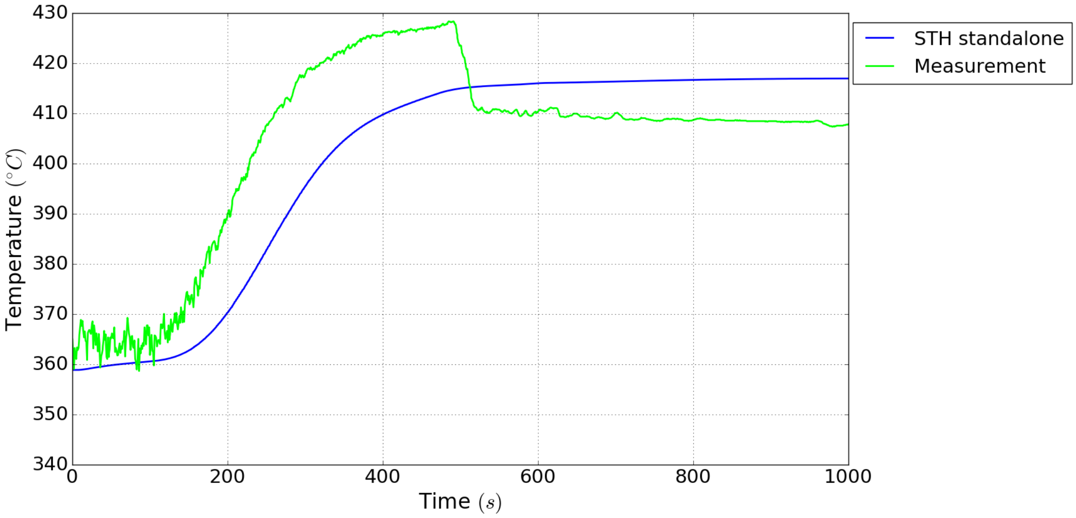

Fig. 6.5: NCT - STH solution: IHX outlet temperature (short term)

The measured temperature decreases steeply at about 550s as a consequence of the sharp decrease of forced circulation mass flow after the shut down of the primary pumps. STH fails to predict this sudden temperature drop (fig. 6.5). Instead, the STH simulation result with ATHLET show a much milder and slower temperature decrease. It has to be pointed out, that the criteria for the shut down of pumps and reactor scram is a temperature difference of 5K in measurements. This criteria is fulfilled at about 490s of the NCT. About 58s after that, the IHX outlet temperature decreases about 19K (fig. 6.5). The temperature different is then twice the stopping criteria and about 10K. STH results show a minimum temperature difference of about 2K during 600s and 700s of the NCT transient. Afterwards, the temperature difference increases again. In STH case, the temperature of rather large volumes given as mixed show more damping to temperature changes than shown in measurements. One reason can be cold sodium that is coming from the cold plenum through the whole circuit to the IHX. As it is a closed circuit without assumed heat losses along flow direction, this is a suitable reason for the discrepancy of about 1.25%.

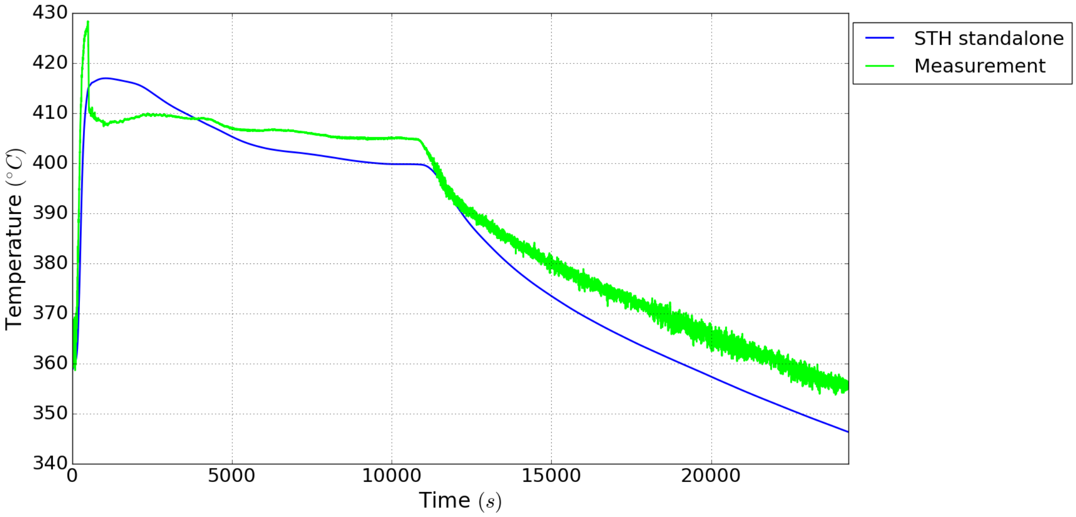

Fig. 6.6: NCT - STH solution: IHX outlet temperature (long term)

Until 5100s the temperature difference calculated by STH gradually increases to 30K while the measured temperature difference is about 17K − 20K after the shut down procedure. Besides three-dimensional effects in the large volumes, that discrepancy is additionally caused by heat losses from the structure to the environment. Those have not been implemented in the ATHLET model because of coupling reasons later on. The goal was here to isolate the effect of a three-dimensional representation of the hot plenum to the transient. Afterwards, both measured and calculated temperature differences from the IHX primary inlet to its outlet change little until about 11,000s (refer to [116] or [59]).

From 11,000s, both measured and calculated temperature differences get larger due to the establishment of a new heat sink (steam generator housing cooled by air). In the final stage of the transient, measured temperature differences become about 32K while the calculated values are about 52.7K. This can be caused by a slightly higher assumed mass flow in the STH model of the intermediate circuit. It had to be implemented that way for numerical stability reasons. The measured signal that had been used as boundary condition has rather strong white noise that is interfering. To summarize the above analysis of the STH results, it can be concluded that the STH code ATHLET fails to capture three dimensional flow characteristics in large sodium plenums during natural circulation. The large sodium mass in the plenums and its large thermal inertia works like a damper to the coolant flowing into the plenums. Also, typical for STH codes, the mesh is very coarse. As consequence, the transient solution can be calculated quickly but has its drawbacks in (compared with CFD) large volumes where calculated values are of scalar dimension (like averaged in CFD). The drastic temperature behavior of coolant leaving the IHX or the core is greatly smoothened and delayed because of the multi-dimensional flow and mixture of cold and hot coolant in different coolant layers when thermally stratified. In dimension of STH, these effects cannot be simulated sufficiently and are responsible for the main deviation between calculation and measurement.

Core outlet temperature

The average temperature at the core outlet region at the start of the NCT is given by IAEA [59] to be 432°C. It is considered a blind test. So no results were provided until the end of the modeling and simulation work. As it is hard to have enough measurement points close to the core outlet (inside the hot plenum) for a considerable large outlet region without influencing flow behavior. A deviation of about 7K can be observed at steady state when compared to provided measurements for the transient (fig. 6.7 and fig. 6.8). At the very beginning of the transient, the measured core outlet temperature almost keeps unchanged under the combined influence of the increased core inlet temperature which approximates the primary pump inlet temperature and the decreasing core thermal power caused by the temperature feedback. Starting at the time of 230s, the measured temperature starts to decrease slightly as the effect of decreasing thermal power gets stronger. The calculated core outlet temperature shows a similar trend compared to the measured value. In the simulation, the temperature decrease starts earlier and varies more quickly. After about 328s, in contrast with the test data, the contribution of the increasing core inlet temperature outstrips that of the decreasing thermal power distinctly, which causes a quick rise of the calculated temperature until the reactor scram (fig. 6.7).

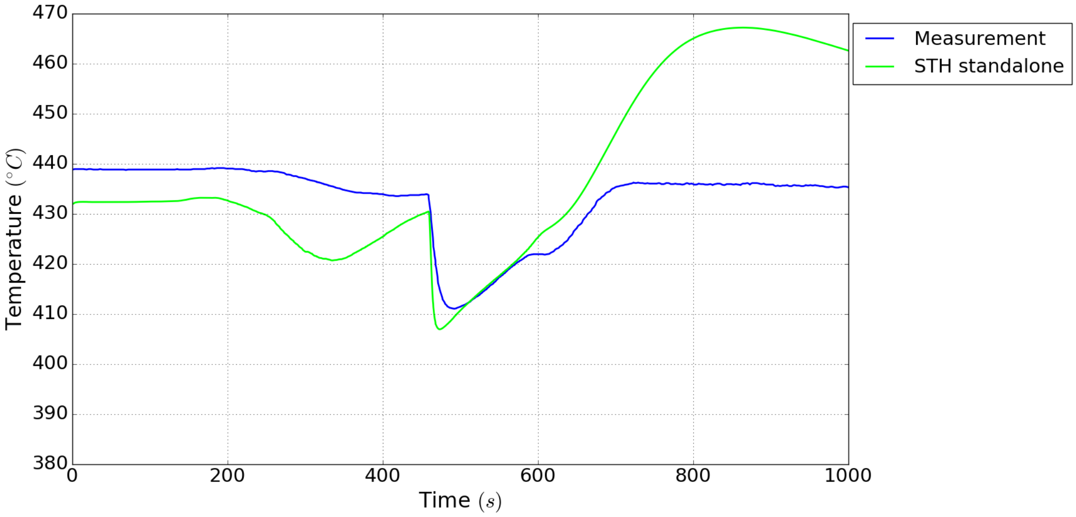

Fig. 6.7: NCT - STH solution: Core average outlet temperature (short term)

This behavior can be seen as a result of the great increase of the primary pump inlet temperature, which reveals that the STH cold plenum model does not appropriately play its ”cooling” effect due to thermal stratification on the coolant flow from the IHX primary outlets. At the transient time of 458s the reactor shuts down, and both the measured and calculated core outlet temperature drop rapidly. As the influence of the temperature feedback on core power disappears after reactor scram, the core inlet temperature turns into the dominant effect, leading to a fast recovery of the core outlet temperature from the sudden drop. This so called recovery of the calculated results happens a little earlier than in measurement data, still caused by the big deviation of the calculated primary pump inlet temperature from the measured values. As the primary pump inlet temperature (very close to the core inlet temperature) decreases slowly, the temperature recovery gradually decreases. For the measured core outlet temperature, as increasing close to 436°C at 726s, it starts to decrease slowly again; while for the calculated result, it firstly keeps a longer and higher increase to 469°C until 942s due to the much higher primary pump inlet

temperature than the test data in the meantime, and then suffers a faster decrease than given in provided test data. It should also be mentioned here, the heating power in the core is given by time tables. That way, higher temperatures of sodium do not influence reactivity in any way in this model.
The knee point of both measured and calculated core outlet temperature caused by the air cooling of the steam generator at 10,320s, happens at approximately 11,000s (fig. 6.8). After the STH calculation basically gives the same tendency of core temperature change as the test data, however larger rate of descend, hence smaller value by the end of the transient. The lower calculated core outlet temperature in the late stage of the transient is possibly due to a larger natural circulation mass flow due to smaller system resistance than in reality. The higher temperature after primary pump trip and reactor scram until the opening of the steam generator housings (air cooling for decay heat removal) can be explained by the three dimensional behavior taking place in the cold plenum. It is observed, due to buoyancy (three dimensional effect) that cannot be displayed with STH, hot sodium is at the top of the cold plenum. Therefore, the primary pump inlets which are connected to the core still supply colder sodium. However, as this thermal energy is not erased, after the onset of decay heat removal, the cold plenum does not cool down as rapidly as calculated by ATHLET and therefore provides the core with hotter sodium during the last stage of the transient [9].

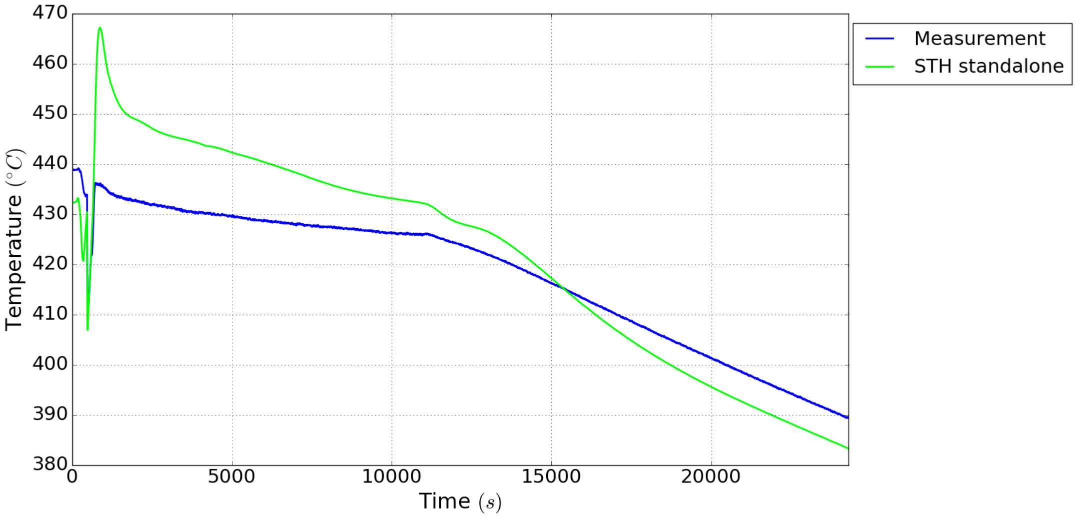

Fig. 6.8: NCT - STH solution: Core average outlet temperature (long term)

It was observed in other experiments, that especially around the pump the influence of structure material (steel) can be of influence. The simulated experiment, the author is referring to was conducted by Zhou et al. [163]. The influence of the structure was significant in the region around the pump. For that reason, the NCT transient simulation with STH was conducted with and without structure material around the pump to get an idea of the influence. The simulation results with structure material around the pump is used further on. To get an idea of the significance, the temperature in the lower core support structure and at the pump outlet was taken from simulation results. For comparison, the difference between simulation results with structure material of the pump against simulation results without structure material of the pump are plotted in fig. 6.9.

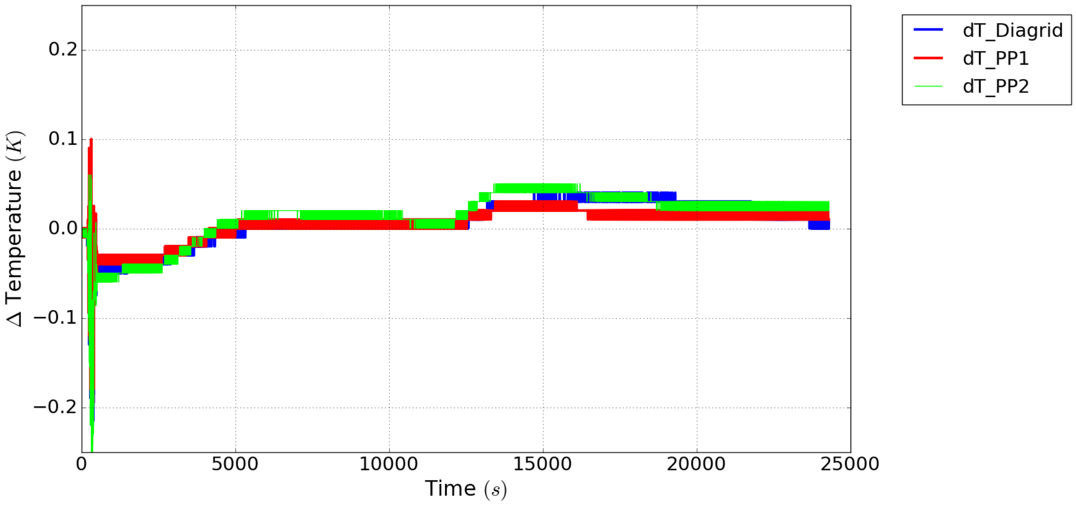

Fig. 6.9: Temperature difference between simulation with pump structure material and without

Fig. 6.9 shows, there is no significant influence by material (steel) to the sodium temperature at the pump outlet. Further the temperature difference between pump inlet and pump outlet was investigated and can be seen in fig. 6.10.

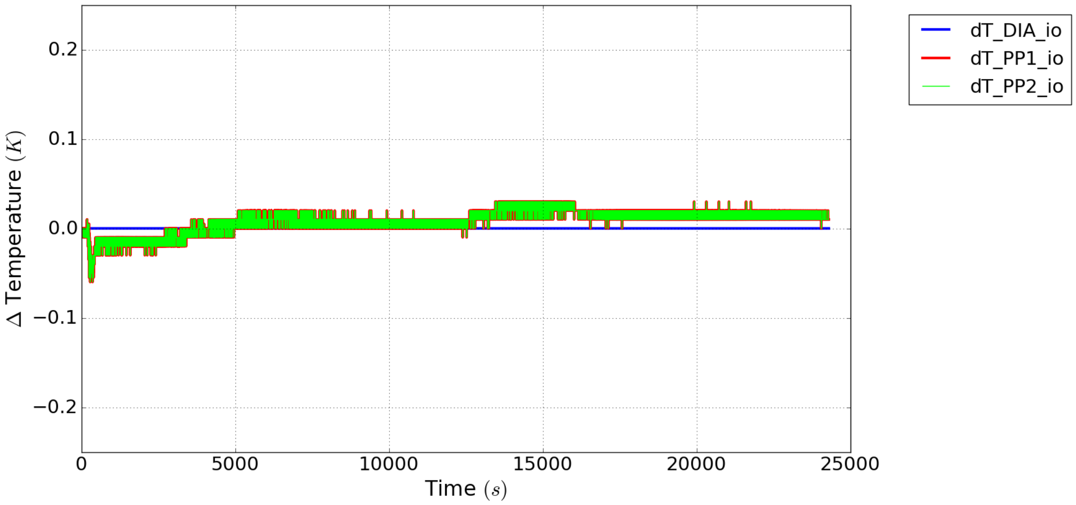

Fig. 6.10: Temperature difference between simulation with pump structure material and without

There was no significant influence from structure material to sodium observable with this method, either. The difference between inlet and outlet temperature of the pump sections was compared. The insignificance of the pump material can be explained by the ratio of sodium and steel in that section. The pumps are plunged within liquid sodium. The mass ratio of the pump's steel to sodium in the plenums surrounding the pumps is about 9.7.

6.2 STH/CFD coupled

As validation of the modified ATHLET code, the primary cooling circuit of the SFR PHENIX reactor is being modelled. The NCT transient scenario [148] from 2009 after the 56^{th} irradiation cycle in the frame of PHENIX End of Life tests is simulated with ATHLET in the presented form shown in ch. 6.1. The following results come from coupled calculations with ATHLET and OpenFOAM simulations. It was shown in ch. 5.2, that less than 5 iterations are necessary to receive converged solutions with the presented coupling methodology. An overview of the coupling process can be seen in fig. 5.3. The hot plenum region is chosen to be represented with CFD.

Temperatures

Primary pump inlet temperature

According to the test data, after the transient starts, the primary pump inlet temperatures increases as the IHX intermediate inlet temperature increases caused by the steam generator dry out. STH standalone gives a similar increase of the primary inlet temperature in this stage, however, after 550s of the transient, STH standalone overpredicts the temperature. At about 505s the measured primary pump inlet temperature reaches its peak value of about $406°C$ and starts to decrease rapidly due to effects taken place in the cold plenum. STH standalone gives a $5°C$ lower temperature compared to the measured temperature peak value of about $407°C$ at about 3250s. The hot plenum compensates the temperature increase due its to large volume with thermal stratification in the region above the IHX inlet regions. Accordingly, the IHX inlet temperatures are colder in the STH/CFD coupled calculation than in STH standalone. The peak temperature is slightly lower in STH/CFD coupled mode than in STH standalone. Still, the increase after the measured peak temperature (fig. 6.11) takes place as the cold plenum still is simulated by STH standalone which represents that region around the IHXs outlets and pumps. It can be seen that effects in the cold plenum cannot be captured by the STH code as the CVs are large and no three-dimensional representation is possible like e.g. in [9].

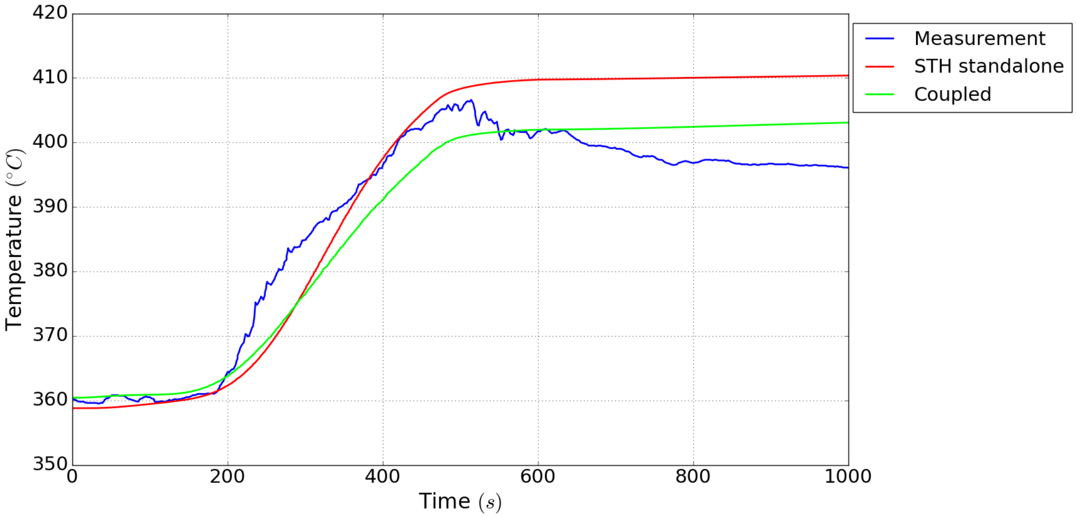

Fig. 6.11: NCT - coupled solution: Primary pump inlet temperature (short term)

On the other hand, the measured primary pump inlet temperature keeps decreasing until about 2100s and then increases slowly again until the time point of about $10,982$s. Meanwhile the STH standalone result keeps decreasing after its peak value, and meets the test data again (discrepancy lower than $1°C$) at about $11,000$s. The measured primary pump inlet temperature decreases after the time point 10, 982s due to air cooling of the redundant steam generator housing which acts as a heat sink here. The air cooling of the steam generator housing has its starting point at 10, 320s during the recorded transient. Afterwards both, the measured and calculated primary pump inlet temperature decrease in a similar manner. The STH/CFD simulation shows a slight over prediction of the temperature here (fig. 6.11 and fig. 6.12, starting after pump trip and scram). Again, this can be explained through a thermally stratified field in the hot and cold plenum (lower temperature in comparison to STH standalone but higher temperature in comparison to measurements). Here the higher elevations slowly decrease in temperature as colder fluid enters the hot plenum through the core outlets at considerable low mass flow rates due to previously tripped primary pumps. The assumption of mixing in the cold plenum can be seen after 10, 982s. There the temperature decrease in measurements is higher as colder sodium from the air-cooled intermediate circuit influences the IHX outlet temperature in the primary circuit to the cold plenum directly. This is due to three dimensional behavior of the large volume of sodium in the cold plenum. STH standalone assumes total mixing with the previously received hot sodium. After 18, 000s of the transient, the measured and calculated temperatures show similar decrease.

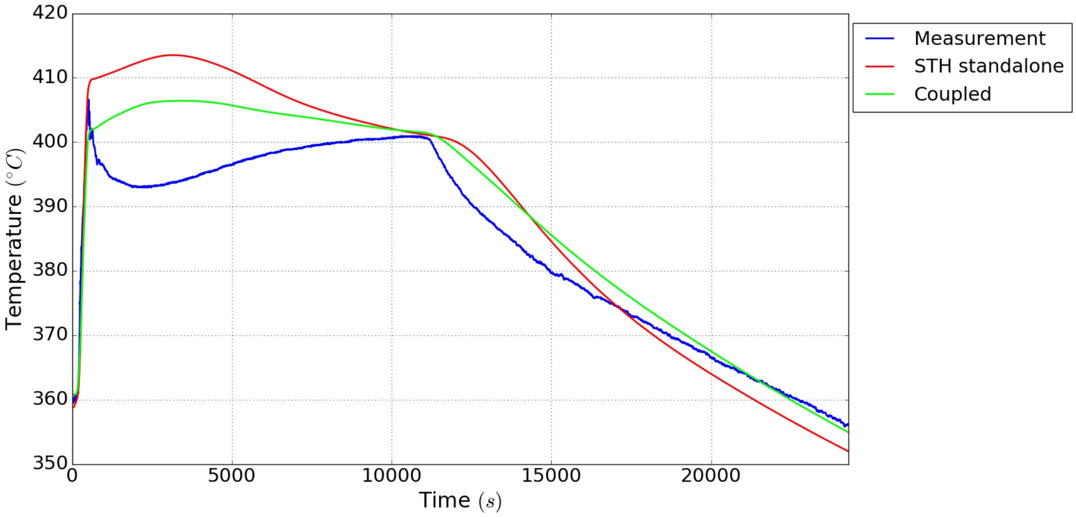

Fig. 6.12: NCT - coupled solution: Primary pump inlet temperature (long term)

As described in ch. 6.1, one reason of the deviation of the STH standalone simulation's results from the measured data at time 320s to 11, 000s of the recorded transient is the large volume of sodium with its strong three-dimensional behavior (see ch. 4.3). Unlike the hot plenum, thermal stratification (fig. 4.11 for hot plenum) as well as other complex multidimensional flow directions (see fig. **??** for hot plenum) cannot be represented with the used STH standalone model. As the present STH/CFD coupled calculation only considers the hot plenum as CFD regime, those effects in the cold plenum are still mispredicted as the cold plenum is still part of the STH standalone regime.

Core outlet temperature

At the very beginning of the transient, the measured core outlet temperature keeps unchanged under the combined influence of the increasing core inlet temperature which approximates the primary pump inlet temperature and the decreasing core thermal power caused by the temperature feedback. Starting at 230s the measured temperature starts to decrease slightly as the effect of decreasing thermal power gets stronger. The calculated core outlet temperature shows a similar trend compared to the measured value. In the calculation, the temperature decrease starts earlier (∼ 180s) and varies faster. After about 328s, different from test data, the contribution of the increasing core inlet temperature outstrips that of the decreasing thermal power distinctly, which causes a raise of the calculated temperature until the reactor scram.

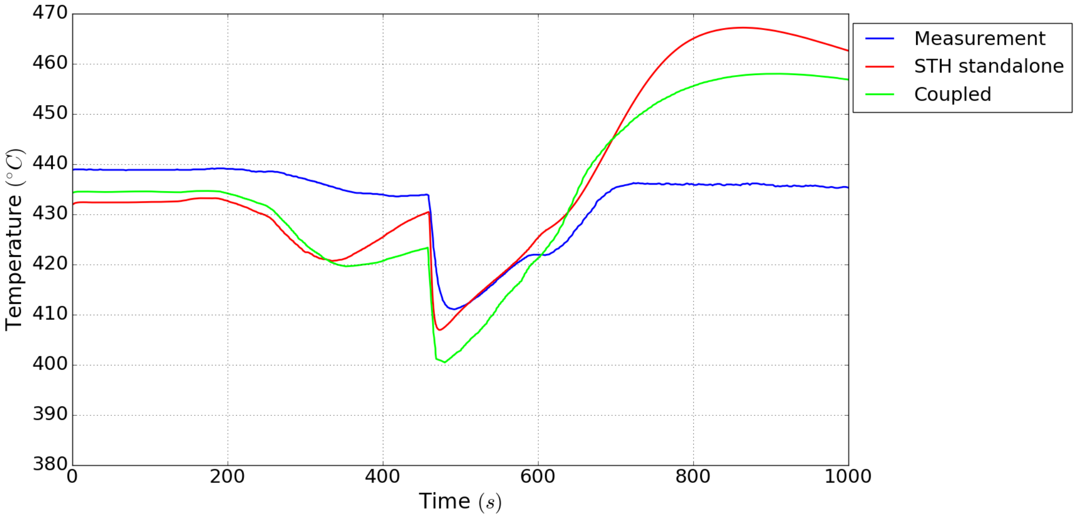

Fig. 6.13: NCT - coupled solution: Core average outlet temperature (short term)

This behavior can be seen as a result of the great increase of the primary pump inlet temperature, which reveals that the STH standalone cold plenum model does not appropriately play its ”cooling” effect due to thermal stratification on the coolant flow from the IHX primary outlet. At the transient time of 458s the reactor shuts down, and both the measured and calculated core outlet temperature drop rapidly. As the influence of the temperature feedback on core power disappears after reactor scram, the core inlet temperature turns into the dominant effect, leading to a fast recovery of the core outlet temperature from the sudden drop. This so called recovery of the calculated results happens slightly earlier in STH standalone than in measured data.

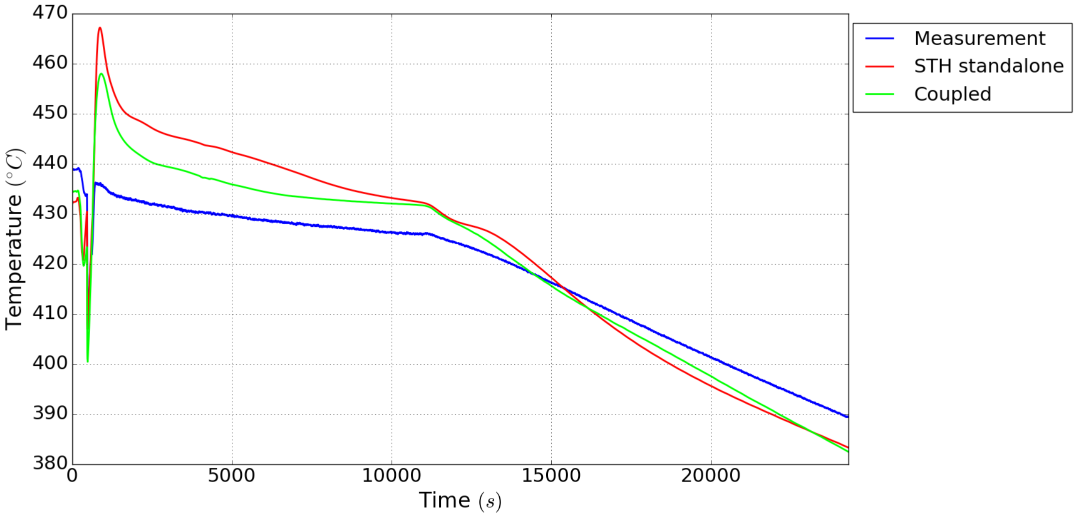

Fig. 6.14: NCT - coupled solution: Core average outlet temperature (long term)

The STH/CFD coupled calculation shows more of that delay. As the primary pump inlet temperature decreases slowly, the temperature recovery gradually slacks off. For the measured core outlet temperature, as increasing close to 436°C by 726s it starts to decrease slowly again; while for the STH/CFD calculated result, it firstly keeps a longer and higher increase until ~ 900s due to the much higher primary pump inlet temperature than the test data in the meantime and high temperatures in high elevations in the hot plenum. Then the STH/CFD calculated temperature shows a stronger decrease. As the mass flows are very low, the influence of buoyancy can be observed in the hot plenum. The STH standalone regime does not. This explains the very high temperature increase at ~ 900s as well as stronger cooling until 15,000s. Then, measured and STH/CFD calculated temperature behave similar while STH standalone over predicts cooling, beginning at 10,320s. Here the hot plenum shows compensating behavior.

IHX primary side - Temperatures

IHX primary inlet temperature

The measured IHX primary inlet temperature almost keeps unchanged until about 490s of the transient. The more than 20°C sharp decrease of the measured core outlet temperature right after the reactor scram just leads to about 4°C delayed decrease of the measured IHX primary inlet temperature. This is due to the large thermal inertia in the hot plenum and as a consequence of this the very slow transient response and strong temperature hysteresis effect. Comparatively, the STH/CFD calculated IHX primary inlet temperature shows good agreement in a short term until ~ 1000s of the recorded transient.

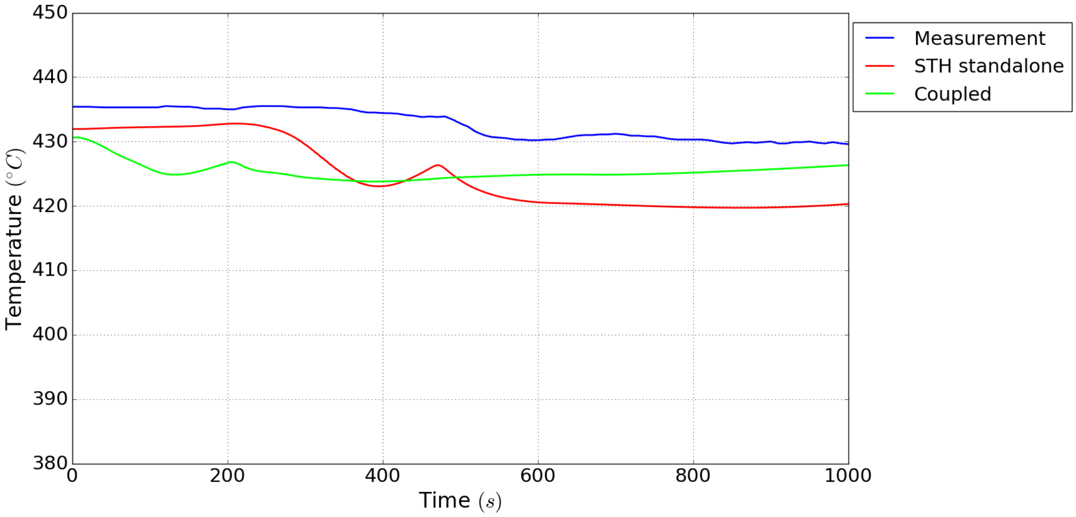

Fig. 6.15: NCT - coupled solution: IHX inlet temperature (short term)

Starting form STH standalone calculation, the STH/CFD coupled calculation shows this damping effect assumed coming from the large sodium volumes. After scram and pump trip, hot sodium leaving the core is only driven by buoyancy forces. As flow velocities are small, hot sodium travels almost vertically to the liquid surface. Due to thermal stratification, the new build up temperature field expands to the IHX inlet region. This effect is of strong three dimensional behavior as the hot plenum has different temperature zones in horizontal and vertical dimension.

However, as the STH standalone code provides boundary conditions to the CFD regime and not all the large volumes are represented with CFD, after 1000s temperatures start to increase and follow the STH standalone calculation. The influence of the hot plenum shows off with the beginning of the steam generator air cooling. Here, the high temperatures in upper regions of the hot plenum take effect and give higher temperatures in the STH/CFD calculation than in STH standalone. As a result, the temperature behavior is more similar to the measured temperature, but with an offset.

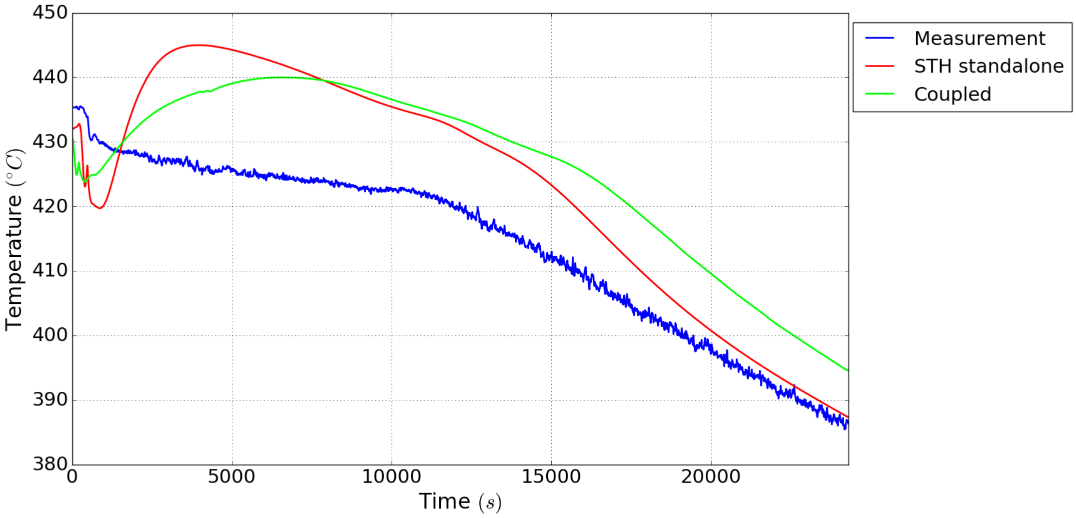

Fig. 6.16: NCT - coupled solution: IHX inlet temperature (long term)

For all coupled results that are represented in the CFD part of the hot plenum, it was chosen, to give averaged quantities. Several reasons came to that conclusion by the author. One is the lack of knowledge of the exact position of the thermo-couple. The second reason are fluctuations in the hot plenum that can easily influence either the measured result and the calculated result. To receive a more robust result, calculation results were averaged and compared to thermo-couple recordings. The third reason, to use averaged quantities is, that it is not in focus to resolve one specific position in such a large volume of sodium, but have a robust and quick calculation in CFD, that not necessarily does resolve small effects, that could occure around the thermo-couple. And as a last reason, it must be mentioned here, the computational power is limited, so it was not possible to have a quick calculation and high resolution. Sufficiently high resolutions need a very clear definition of geometry that wasn't entirely provided. Additionally, the number of cells needed to be kept at a low quantity to keep the computational effort feasible.

IHX primary outlet temperature

The primary IHX outlet temperature first increases and then, due to SG dry out, its intermediate temperature. STH/CFD gives a similar result compared to the measurement for this stage. The measured temperature then descends steeply at about 550s as a consequence of the sharp decrease of forced circulation mass flow after the primary pump trip. STH/CFD fails to predict this sudden temperature drop in its full shape. As the STH standalone calculation uses one volume to cover the regions of IHX outlet, vessel cooling outlet and primary pump inlet, total mixing is assumed at this position. As a result, even at low mass flow as it is after the pump trip, buoyancy effects cannot be represented sufficiently. Hot sodium enters the cold plenum coming from the IHXs. As no forced flow is present, buoyancy takes place immediately.
It should be mentioned here, the thermo couple which is given as a reference is not directly at the IHXs outlet but slightly aside. Through the described buoyancy effects, hot sodium is carried to the top of the cold plenum without having any influence on the thermo couple. As cold sodium is then in the region of the thermo couple, the measured temperature is colder.

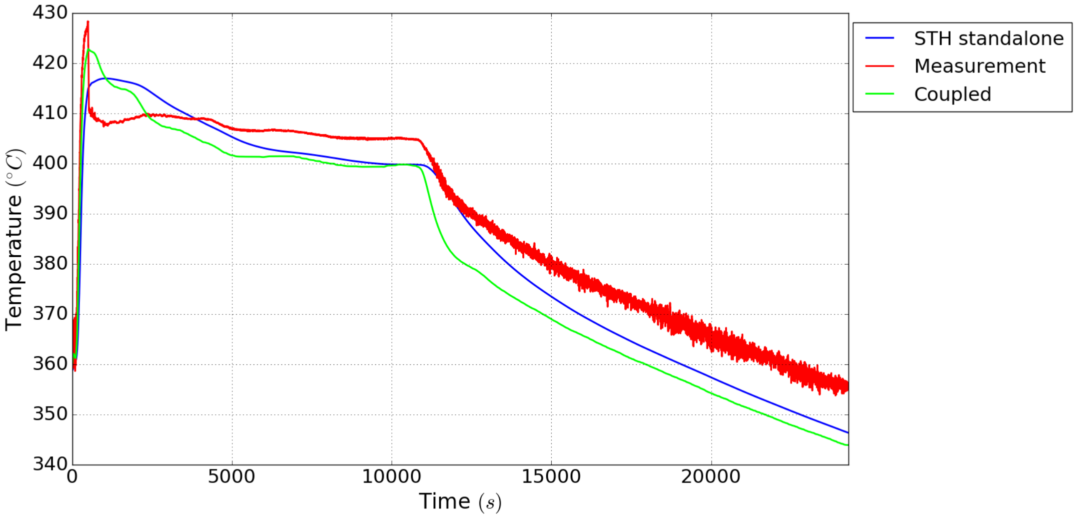

Fig. 6.17: NCT - coupled solution: IHX outlet temperature (long term)

6.3 Summary

STH/CFD coupled calculation clearly shows proof for the lack of the ability to capture effects like thermal stratification or thermal striping in large volumes like the plenums in the PHENIX primary circuit with STH standalone methods. As a result, buoyancy in different magnitudes inside one of those large volumes cannot be captured as well (see Appendix C). The Post-test calculations presented in this chapter also show the need to represent all large volumes in CFD when coupling, as the so-called 'cold shock' [9] coming from the cold plenum, cannot be represented sufficiently with STH standalone. One of the main requirements to the approach was to avoid extensive calculation and as a result long calculation time of a transient scenario. Therefore, STH/CFD coupling, CFD mesh optimization and solver optimization was necessary to be developed as well as the qualification of the STH code for sodium applications. Here, one iteration took approximately 4 days to run, so the considerable long term transient of the PHENIX NCT can be calculated within 2 weeks. As it was one of the goals to have a coupled solution with considerable small computation time, high resolution (LES or high resolution URANS) cannot be expected to be covered. With this approach, it is shown, that STH/CFD coupled calculations can better represent transient scenarios like the PHENIX NCT as more of the effects of high impact taking place in the primary circuit can be resolved.

For this STH/CFD coupling approach, conjugate heat transfer between hot and cold plenum is not being considered. For consistency, the only places with conjugate heat transfer are in the ATHLET model (standalone and coupling). More precise, the heat source with its different contributors (inner core, outer core, etc.) and the primary circuit heat sink, the IHXs where heat is transferred to the intermediate circuit. Deviations can be explained. A direct validation of computational results against measurements does not make sense, as the position of thermocouples are not at places that could be captured by STH calculations. It would require more extensive use of CFD in each place and consequently lead to high computational costs which dissent with the primary targets of this work of coupling [23].

7. Application

As an application of the received coupling methodology and developed models, another transient scenario is being created. Here, it is assumed, that during the transient scenario, the opening of the steam generator housing fails. The question is: “What will happen, if after the reactor scram and pump shut down, none of the following measures to protect the core are functional?” This scenario can also be considered as a protected loss of heat sink (PLOF), which is a design basis accident in our times. The time table of the scenario is given in tab. 7.1.

Time	Action
0 s	Dry out of steam generators in secondary circuit 1 and 3; No change in pumps speed
458 s	Scram; Secondary pumps 1 and 3 rotation speed automatically reduced to 110rpm in 1min
466s	Stop of the three primary pumps on inertia
4080 s	Secondary pumps rotation speed reduced to 100rpm (back-up motors)
24300 s	End of test

Tab. 7.1: Schedule of PHENIX application based on PHENIX NCT [59]

7.1 Boundary conditions

The boundary conditions do look very much the same. Power is given to the coupled model, as well as the secondary side inlet temperature and massflow is given. Still all walls are considered adiabatic, as heat transfer through walls may only lead to blurred results and even maybe false interpretation (see Appendix D).

As boundary conditions are identical for each iteration and none is changed in anyway, this shows that the model itself can be considered as verified.

It has been observed, the secondary inlet temperature is getting almost constant during a short time period before the opening of the steam generator housing. It is caused by an assumed [147] heat loss in the intermediate circuit of about 500kW$_{\mathrm{th}}$. The assumption was taken as idea, to run this application. So in case this decay heat removal procedure would fail during a loss-of-flow (LOF) accident. It can be assumed, that the piping of the intermediate circuit looses power to the environment as perfect isolation of such long pipelines cannot be guaranteed [59]. This means, there is heat transfer from the intermediate circuits to the environment which leads to a reduction in efficiency of the power plant. In case of an accident with loss of heat sink, this can be a significant use as will be shown in this chapter. Another benefit of this heat loss is its passive characteristic.

7.2 STH/CFD coupled solution

Different to the Post-test calculations of the PHENIX NCT presented in ch. 6, the STH standalone and STH/CFD coupled solutions are compared without measurements in this chapter. It should also be mentioned here, that differences to the boundary conditions from the NCT are kept small. The point of interest would be here, if it is possible, to have no additional decay heat removal like in the second half of the NCT. Additionally, two more iterations have been carried out for checks on convergence behavior.

Primary pump inlet temperature

The primary pump inlet temperature shows a slightly different starting temperature in the coupled results like already seen during the NCT scenario. This can be explained through thermal striping that takes place in the hot plenum. A hot jet entering the hot plenum through the core directly aims to the IHX. STH always assumes total mixing (scalar value in each control volume). The increase of temperature during dry out is only of about 60% in coupled solution than in STH standalone. As this sharp increase happens after the primary pumps trip, the hot plenum's capability as a heat storage can be assumed. At about $500s$, the peak temperature is reached at about $423°C$. Then, through natural circulation with a small heat source and small heat sinks, which results only from heat losses of the intermediate piping, temperatures in the whole circuit are starting mix. During the second half of the calculation, it can be observed, the temperature at the primary pump inlet reaches $400°C$ and decreases only very insignificantly. From this point of view, the reactor has reached steady state conditions with decay heat.

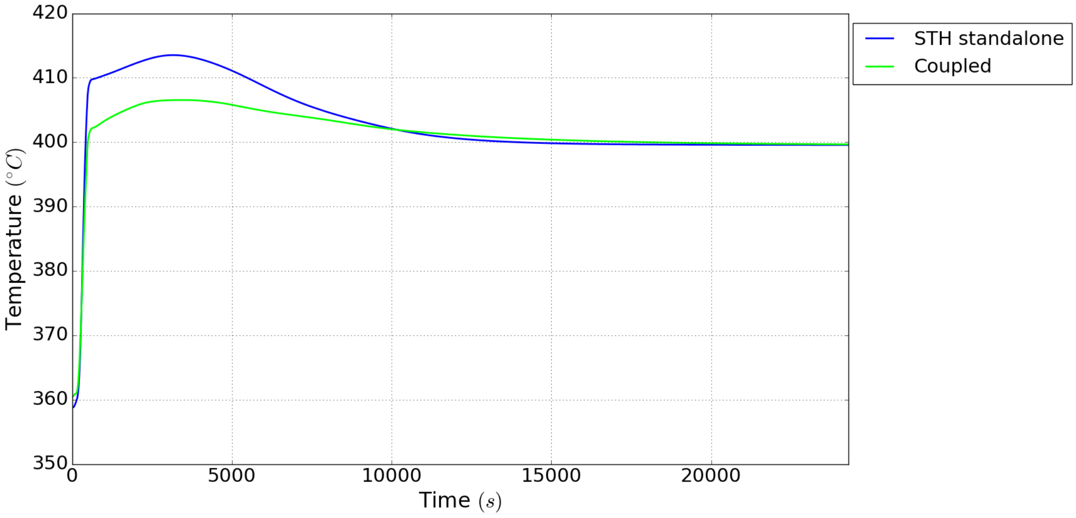

Fig. 7.1: Application - Primary pump inlet temperature

Core outlet temperature

Directly after the core, in the outlet region, another observation can be done. As thermal stratification is assumed during steady state at the start of the NCT transient and this present application, temperatures between STH and coupled STH/CFD calculations are very much different. This can be explained with strong three-dimensional effects like thermal stratification during steady state, and thermal stratification after trip of the primary pumps during the rest of the first half of the NCT transient. However, in this application it is also observable that as soon as total mixing can be assumed and none of the previously mentioned effects is taking place, the STH standalone and the STH/CFD coupled calculations results converge again.

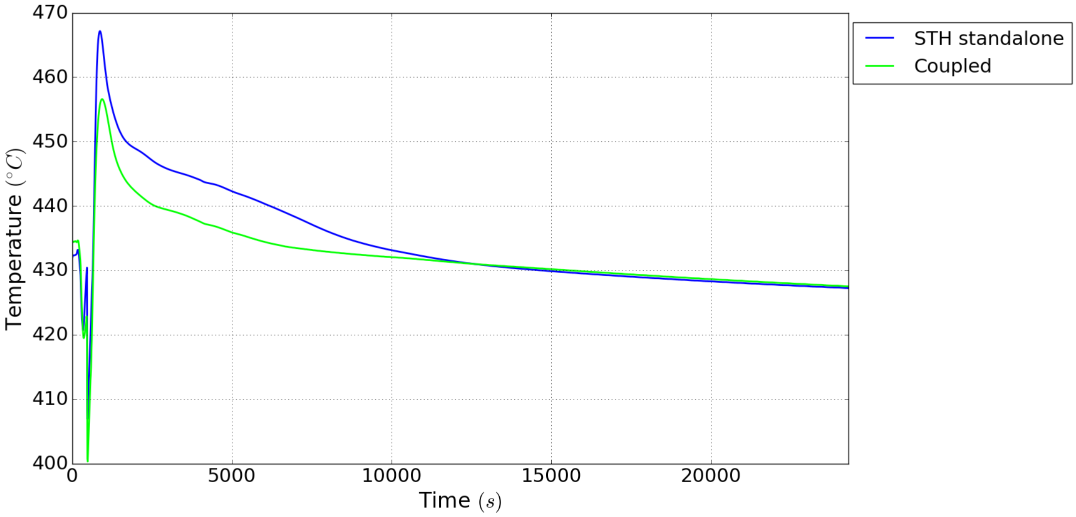

Fig. 7.2: Application - Core average outlet temperature

IHX primary side temperatures

According to the NCT, the behavior during the first half of the transient has improvements through three-dimensional representation of the hot plenum. Significant changes at the IHX primary inlets are damped, so that the sensitivity of the whole system to temperature changes is reduced.

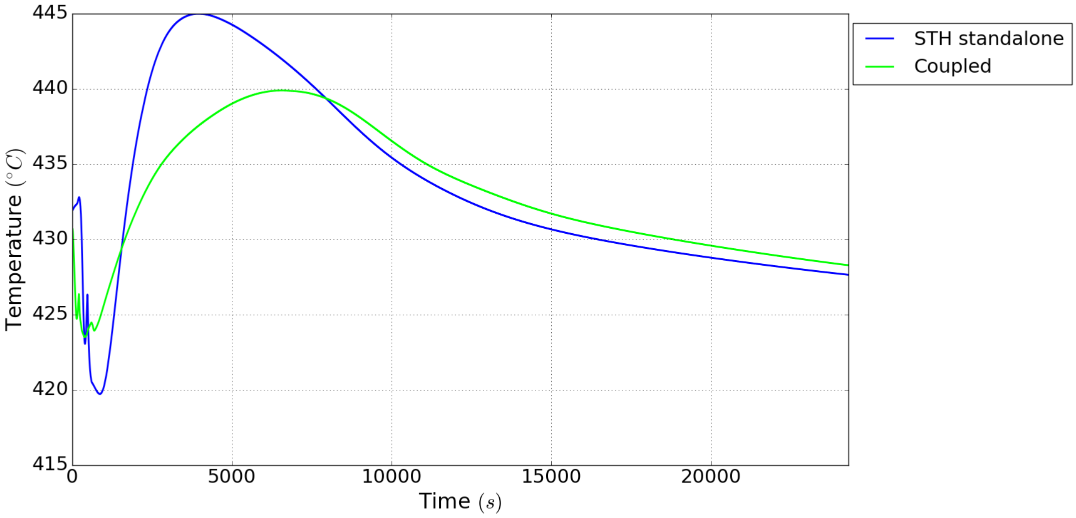

Fig. 7.3: Application - IHX primary side inlet temperature (averaged)

Like in ch. 6, the coupled (STH/CFD) calculation then starts to converge to the STH standalone calculation during the second half of the transient. As the secondary side inlet temperature keeps almost constant after 5000s and natural circulation is driving force as the primary pumps are switched off, the large volume of the hot plenum becomes a similar shape as in a system code when looking at temperature, velocities or pressure. Main velocities are in vertical direction. Thermal stratification comes to an almost steady state during that process and thermal mixing starts - due to very low Prandtl numbers that are significant for liquid metal - which reduces temperature gradients in the hot plenum.

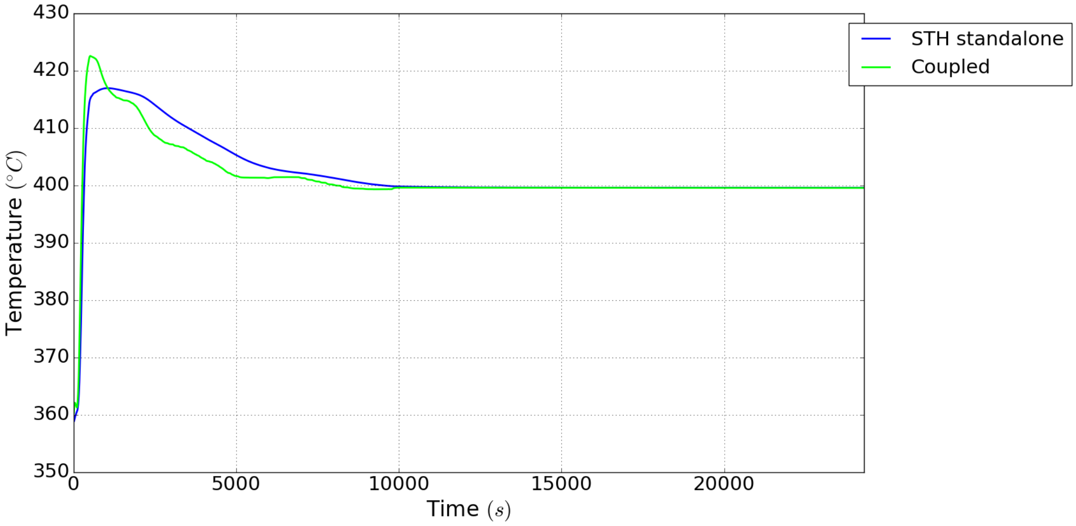

Fig. 7.4: Application - IHX primary side outlet temperature (averaged)

The heat transfer in the IHX still is one of the most impressing parts of this application. So as only small temperature differences between primary and secondary side exist, the IHXs fully transfer heat from the primary circuit to the intermediate circuit, caused by heat losses at the intermediate piping.

7.3 Summary

Inspired by the PHENIX NCT, the case scenario was adapted to a PLOHS[1] and additional loss of flow in the primary circuit. As modification, the decay heat removal process was neglected or considered not operative. The only loss of heat can be observed in the intermediate circuit. Here an assumed heat loss of $\sim$ 500kW provides cooling during all states. It was observed in the PHENIX NCT, shortly before the opening of the steam generator housing, the intermediate circuit does not change temperature any more and can therefore be seen as steady. The calculations give evidence for that as temperatures at the observed positions even shrink.

Indicated by a short time period in the PHENIX NCT, this application was additionally conducted, to show the benefits of coupled simulations but also provide limits for the necessity of STH/CFD coupled calculations. It can be observed even in large volumes, there are states of flow, when CFD does not give much benefit when used in coupled calculations. Dependent on geometry, fluid and boundary conditions, if flow velocities are very small in the PHENIX primary circuit, an almost uniform vertical velocity field is formed between elevations of the core outlet and IHX inlet regions. This can then be observed as similar behavior or even convergence of STH standalone and STH/CFD calculations. STH standalone calculations would be sufficient during a small time period under very specialized conditions. However, the initial state (starting point) at the beginning of this similarity cannot be distinguished by STH standalone but must be provided by STH/CFD coupled

---

[1] *Protected Loss-Of-Heat-Sink* accident scenario

calculations. As it can be considered as a very small possibility to occur, STH/CFD coupled calculations are necessary to provide sufficient representation of major effects taking place in each of the observed components. Even switching off and focusing on a more *lean* approach does not make sense, as STH standalone cannot provide information when STH standalone and STH/CFD coupled solutions differ too much to be treated lean with focus on computational costs.

8. Conclusion and Outlook

8.1 Conclusion

The PHENIX NCT [148] has been performed. Therefore, necessary tools like STH (here ATHLET [80]) and CFD (here OpenFOAM) had to be modified and/or adapted to sodium as working fluid in a thermal hydraulic circuit ([25], [164]).
In a first step, the ATHLET code was modified for sodium applications with a multi fluid approach to extend the capability of ATHLET for liquid metal coolants. Modifications like material properties and heat transfer coefficients have been implemented and released by GRS into following releases of the ATHLET code. Additionally, heat transfer correlations (Nusselt correlations) and pressure drop modifications have been further investigated.
Results of the PHENIX NCT have been generated with ATHLET during a blind test benchmark exercise first. Only little parameters additionally to boundary conditions were known for the calculation. The geometrical representation therefore is limited as well as other thermal-hydraulic parameters (specific mass flow rates, pressures, etc.). For later comparison, measurements were made available. Mainly temperature measurements were taken during the transient test. The comparison with STH standalone results and measurements give some more information about physical effects but cannot be seen fully representative as the positions of thermocouples cannot be resolved with the input model from the blind test. Discrepancies can be found for steady state and therefore in the beginning of the transient. With ongoing transient, physical effects and the position of measurements get more important than initial (steady state) conditions. It can be seen that STH cannot capture three-dimensional behavior in large pools. As an example for a coupling methodology, the hot pool is chosen as coupling regime for a STH/CFD coupled calculation. Here the restrictions have been mainly due to computational efforts and focus on global effects of CFD on the STH results. Local effects in this large and complex geometry are considered to be of minor influence to the received results. STAR-CCM+ is used for geometry development and meshing process. All meshes are unstructured and of polyhedral shape with prism layers near walls. Thermo-physical properties for the CFD calculation are preprocessed and implemented in the input as temperature dependent, polynomial functions.
After the modification of basic tools, the coupling methodology has been developed. A direct validation of the coupling methodology with the PHENIX NCT is not possible as necessary validation data is lacking. Therefore, a verification of the procedure and assessment of the STH standalone calculation is given. This way, the coupling process can be assessed for the PHENIX NCT and results can be compared to measurements with the

restrictions discussed before. The approach of supervised iterative distributed coupling shows the necessity of iterations in coupled solutions if high accuracy is needed. CFD is not considered as a correction object to the STH calculation but as independent part of the general coupled solution to capture physical effects like thermal stratification or thermal striping in large volumes like the hot pool.

Knowledge about behavior at the interfaces in each individual code (STH and CFD) and the verification of its connection - the coupling interface is of high importance to build a level of trust to the coupling methodology. Additionally, it is of crucial importance to know about implicit assumptions of each of the codes. STH for example are only capable of a one-dimensional representation for thermal-hydraulic objects. The idea of STH is the representation of a pipe with pipe specific parameters. With hydraulic diameters and cross-section area, STH can provide thermal-hydraulic objects like subassemblies in a core or even a large volume like the pools in the PHENIX primary circuit. Thermal-hydraulic quantities (temperature, velocity, pressure) are calculated as scalar which directly provides the assumption of flow direction and behavior. However, if pool still is represented as one-dimensional thermal-hydraulic object, three-dimensional effects are missing. Such behavior can be observed when STH results are compared with measurements.

As coupling interface, a python program, has been developed which remote controls both codes independently and exchanges and pre-processes boundary conditions between the codes (filtering, Celcius/Kelvin transfer, etc.). The goal was, to have the possibility to run coupled calculations quickly without time consuming pre- and post-processing during data transmission between the two codes. So, the coupling interface aimed to be a program to manage both of the codes that need to be coupled. It is not considered a simple data exchange interface which would directly lead to a master-slave approach, but can act as a supervisor connecting the codes for coupling. The interface was additionally equipped with graphical post-processing, so coupling iterations can be compared visually and assessed. The coupling methodology is file based. It can still be considered efficient from a computational point of view, as data exchange (file exchange) is only performed after computing one whole transient. If information was exchanged during each time-step this would possibly not be the case. In case of CFD, surface averaged values do not require reconstruction of the distributed mesh when run in parallel. It should also be mentioned here, that data for post-processing and assessment is a lot more than data required for coupling only.

The post-test calculations of the PHENIX NCT (given in ch. 6) show the necessity of STH/CFD coupling in regions of large volumes with (significant) three-dimensional behavior [6], [145]. In the presented transient case scenario, the influence of the hot pool volume shows these effects through thermal striping and thermal stratification that have been captured with CFD. During the transient, it can be seen, flow in the hot pool cannot be considered uniformly. Here, results between STH standalone and STH/CFD coupled calculation differ most. The CFD representation of the hot pool also shows the build-up of thermal stratification right after the pump trip. Residual heat is then lead to the top of the volume vertically and “stored” there until reaching the elevation of the IHX inlet annulus regions. After the start of residual heat removal, it can be observed, this heat is gradually removed in vertical direction. Additionally, the large volume in CFD shows a damping effect to the global solution, where thermal inertia is much stronger than estimated with STH standalone. Shortly before the start of residual heat removal, the flow field can be observed to be close to uniform shape when looking at velocity distributions. It can also be seen, that here, the CFD/STH coupled calculation shows similar behavior as the STH standalone. This behavior can be explained with the fact, that the average velocities in each cell of observed places in the CFD region are close to the average value when looking at horizontal cross-sections. The three-dimensional effects are then comparatively small.

As application, the transient was modified. It was assumed the heat loss in piping of the intermediate circuit ($\sim 500kW_{th}$) is sufficient to reach a steady state without residual heat removal after scram of the core and trip of the pumps. Indicator for that assumption was a short time span before the start of the residual heat removal during the PHENIX NCT. The major result for the calculation here can be seen during the last half of the transient. Here, the three-dimensional behavior of the hot pool sodium volume shrinks significantly and therefore, as assumed when running PHENIX NCT calculations, the STH/CFD coupled calculations get close to the STH standalone calculations. Additionally, the calculations results yield that even if residual heat removal by opening the steam generator housing would have failed during the PHENIX NCT, the reactor would have stabilized by reaching a steady state.

8.2 Outlook

Further work in this field must be done and can be of significant use. Coupled (STH/CFD) calculations can be seen as time saving, even lean solutions for large thermal hydraulic regimes of transient and strong three-dimensional behavior. With higher computational efforts, CFD calculations can be used with not only RANS but LES methods which support a resolution of the flow regime. This way, thermal oscillations during steady state and a given transient test case could be observed [24].

In case of the PHENIX NCT or ongoing PHENIX calculations it is strongly recommended to investigate all large sodium volumes on their individual three-dimensional behavior. An assessment on the impact of the different large volumes could also be beneficiary.

The coupling interface can be extended to message based information transfer. This is seen as the basis for on-line coupling procedures, so data can be exchanged after any coupling time steps quickly. Additionally, an observer based methodology can be developed to even switch off coupling, when not of high impact to the solution. Further ATHLET code development can be done by further extension of the multi fluid library and two-phase approaches for all fluids.

9. Appendix

A Background

STH/CFD coupling

code architecture	information propagation	time-step management	geometry handling
supervised	sequantial	explicit	overlapping
supervised	sequantial	explicit	distributed
supervised	sequantial	semi-implicit	overlapping
supervised	sequantial	semi-implicit	distributed
supervised	parallel	explicit	overlapping
supervised	parallel	explicit	distributed
supervised	parallel	semi-implicit	overlapping
supervised	parallel	semi-implicit	distributed
master-slave	sequantial	explicit	overlapping
master-slave	sequantial	explicit	distributed
master-slave	sequantial	semi-implicit	overlapping
master-slave	sequantial	semi-implicit	distributed
master-slave	parallel	explicit	overlapping
master-slave	parallel	explicit	distributed
master-slave	parallel	semi-implicit	overlapping
master-slave	parallel	semi-implicit	distributed
supervised	iterative	–	overlapping
supervised	iterative	–	distributed
master-slave	iterative	–	overlapping
master-slave	iterative	–	distributed

Tab. A.1: Overview of assumed possible coupling methodologies

GRS - ATHLET/ANSYS CFX

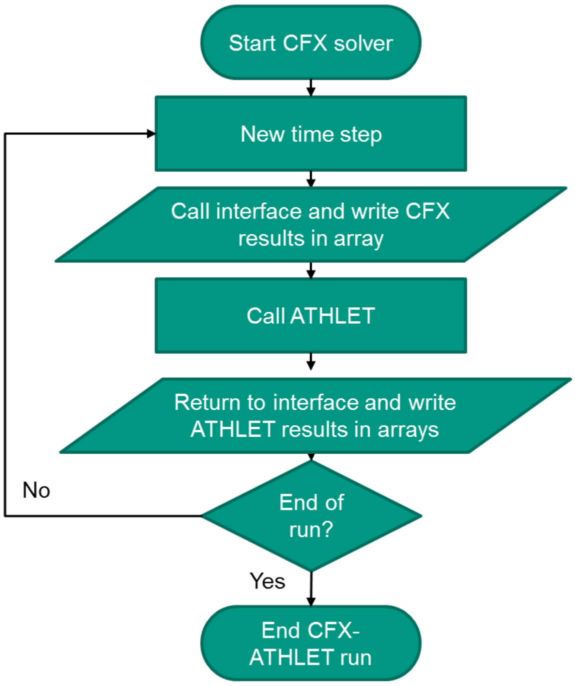

Fig. A.1: ATHLET/ANSYS-CFX: explicit coupling scheme [112]

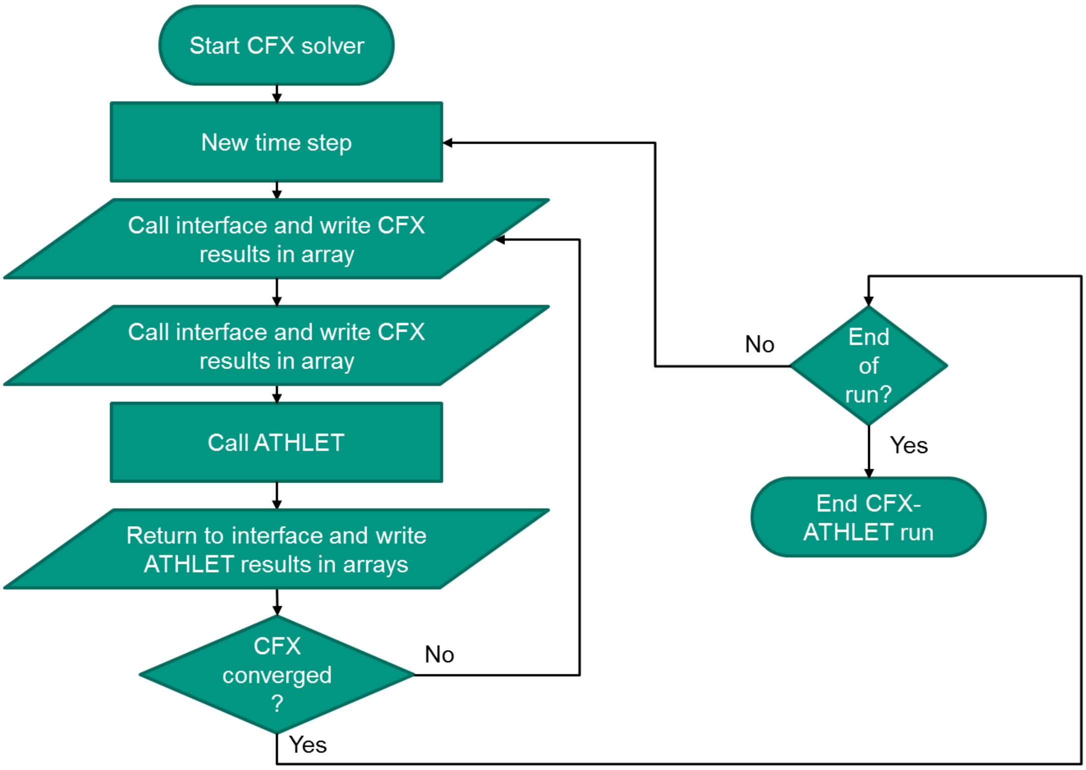

Fig. A.2: ATHLET/ANSYS-CFX: Semi-implicit coupling scheme [112]

B ATHLET code modification

Heat Transfer

Nusselt correlations in tubes

Authors	Temperature, °C	Flow channels	Relative length, L/D	Péclet no., Pe	Nusselt no., Nu	Remarks
			Mercury			
Styrikovich et al. [143],[142]	450 – 500	Steel and low alloy steel tube 16 – 40mm diameter	–	600 – 1800	7 – 14	The work was done in 1939[1]
Mikheev et al. [94],[93]	20 – 180	Machined pipe, carbon steel, 4 – 10mm diameter	30 – 81	300 – 11000	3.5 – 30	–
Kornev [72]	60 – 500	Stainless steel tubing, 19, 28 and 40mm diameter	–	250 – 4500	3 – 25	Tests run with a Hg-Mg amalgam yielded analogous results
English and Barret [40]	–	1.3mm diameter, tube	–	100 – 700	3 – 9	Both local and average heat transfer was measured, and showed marked decrease at low Pe numbers.
Doody and Jounger [35]	–	12.5mm diameter	125	100 – 500	1.5 – 4.5	Addition of sodium raised heat transfer to Nu = 4 – 8
Bailey, Kop, Batshon [84]	–	Steel tube 11mm diameter	–	70 – 2000	1.1 – 6	–
Elzer [84]	–	6 – 8mm diameter	40	900 – 4000	3 – 6	–
Isakoff and Drew [60]	–	38mm diameter steel tube	140	900 – 10000	10 – 37	–
Stromquist [84]	–	9 – 20mm steel tube	60 – 120	100 – 20000	4 – 30	The effect of addition of sodium was not determined
Johnson et al. [66]	–	16mm diameter steel tube	74	200 – 10000	6 – 30	In the region of Pe = 20 to 200 a sharp drop in heat transferred was observed
Gilliland, Musser, Page [92]	–	–	–	500 – 1500	6 – 9	The test was made on heat exchangers without determination of wall temperature.
Trefethen [153]	–	–	–	100 – 2000	5 – 14	–
			Eutectic of lead-bismuth[2]			
Seban [84]	–	16.6mm diameter	72	900 – 2000	7 – 5 – 9	A drop in heat transfer of 30 – 40% was observed with time
Mikheev et al. [94],[48]	–	Common steel tube, 5 – 10mm diameter	30 – 64	1000 – 10000	6 – 20	Experiments with bismuth
Johnson et al. [66]	–	Common steel tube (10mm diameter)	–	30 – 4000	1.5 – 16	–

Authors	Temperature, °C	Flow channels	Relative length, L/D	Péclet no., Pe	Nusselt no., Nu	Remarks
Borishanskii, Kutateladze, Ivashchenko and Shneiderman [12]	–	Of various steels, 9 – 25mm tubing	15 – 100	170 – 11000	5 – 27	Heat fluxes reached $1.3 \cdot 10^6$kcal/m$^2 \cdot$hr. Additions of magnesium did not appreciably affect heat transfer
				70 – 15000	3.5 – 30	–
Untermeyer [84]	–	10mm diameter tube	100	300 – 3000	1.7 – 16	Addition of magnesium raised heat transfer to Nu = 9 – 11
Lubarsky and Kaufman [84]	–	10mm diameter tube	100	800 – 3500	6 – 17	The heat transfer was measured in a flat channel heat exchanger.
Sodium and alloy of sodium-potassium						
Mikheev et al. [94],[93]	–	Copper tube	–	500 – 3000	4.5 – 11	Sodium
		10.3mm diameter steel tube	45	450 – 5000	6 – 19	Sodium-potassium
Novikov et al. [102]	Up to 350	8.6mm diameter copper tube	47	100 – 1400	5 – 11	Sodium; part of the experiments were conducted with nickeled surfaces to change degree of wetting the surfaces
Borishanskii and Kutateladze [12]	Up to 400	Copper, 34 – 35mm diameter	34	90–1800	3 – 9	Sodium
MacDonald and Quitenton [84]	–	16mm diameter tubing	≈ 100	60–2000	2 – 9	Sodium
Lyon [84]	–	Nickel tube	76 – 159	150 – 1600	5 – 15	Heat transfer was measured in 4 heat exchangers of the flat channel type with alloy (48%K + 52%Na) flowing in both passes.
Werner, King and Tidball [84]	–	Steel and nickel tubes	–	100 – 2000	5 – 10 (for steel)	44%Na + 56%K
					9 – 25 (for nickel)	77%Na + 23%K

Tab. B.2: Table of experiments for Nusselt correlations [73]

---

[1] In the years preceding the war, experiments with Hg were conducted by Lozhkin and Kanaev [83],[68]

[2] Best agreement with data of lead-bismuth eutectic is obtained with bismuth[48] and tin.

Nusselt correlations Verification and Validation range plots

Nusselt correlations for plane surfaces

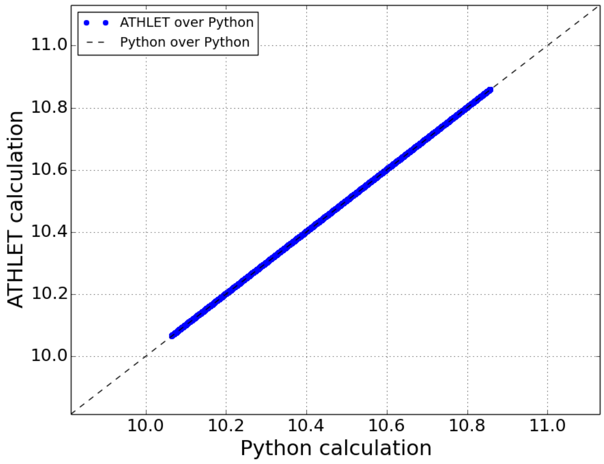

(a) Verification: ATHLET over Python

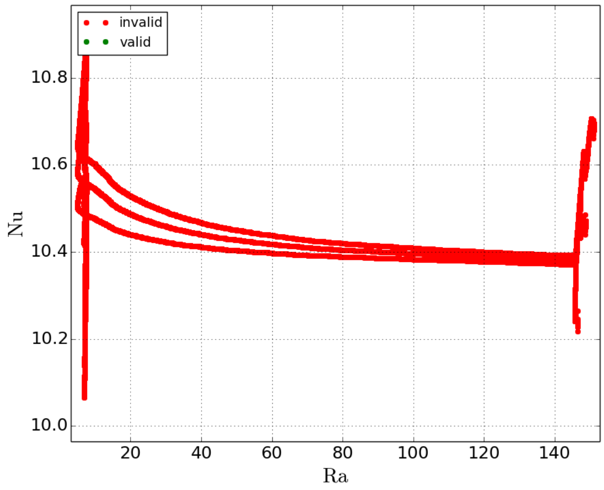

(b) Nusselt numbers in NCT

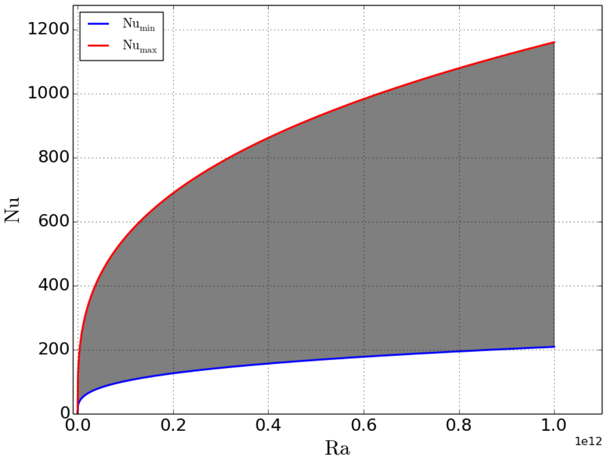

(c) Valid range according to literature

Fig. B.3: Verification and Assessment of eq.3.3 (Churchill and Chu [29])

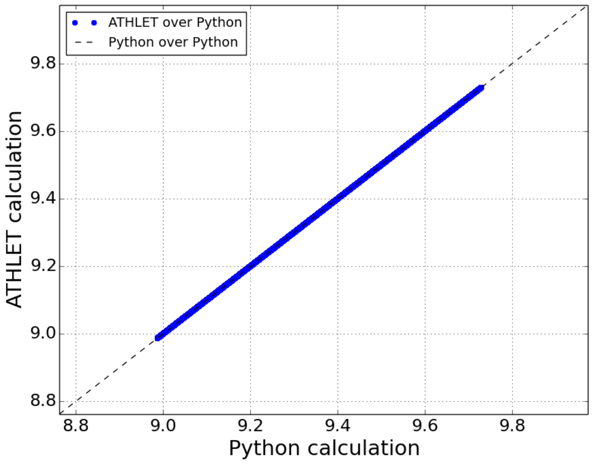

(a) Verification: ATHLET over Python

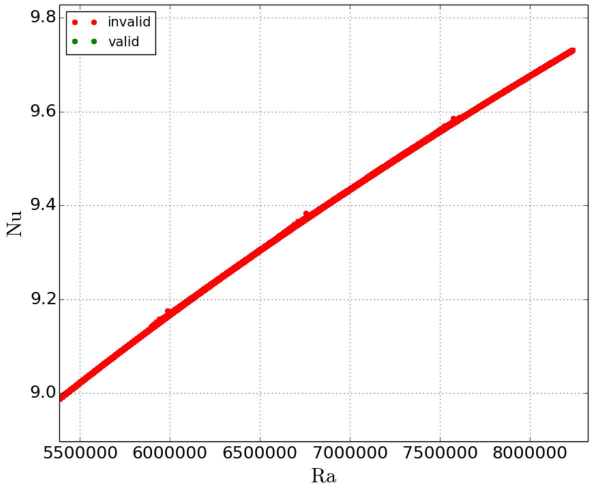

(b) Nusselt numbers in NCT

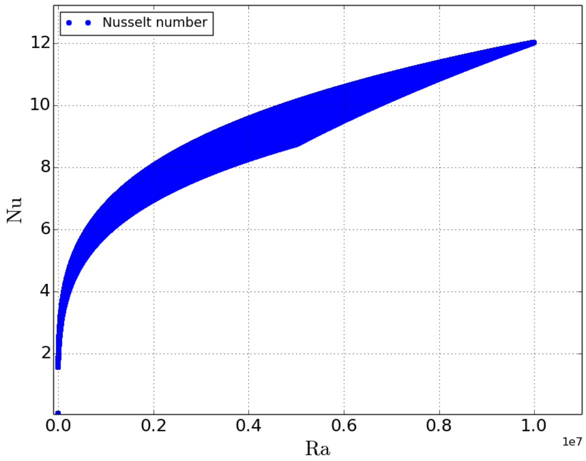

(c) Valid range according to literature

Fig. B.4: Verification and Assessment of eq.3.5 (Gregg and Sparrow [51] & Chang et al. [22])

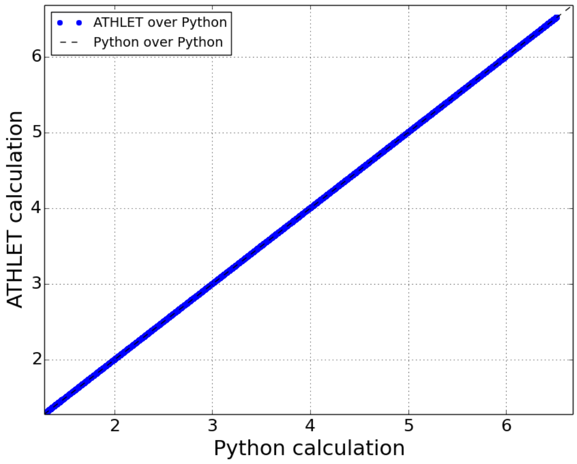

(a) Verification: ATHLET over Python

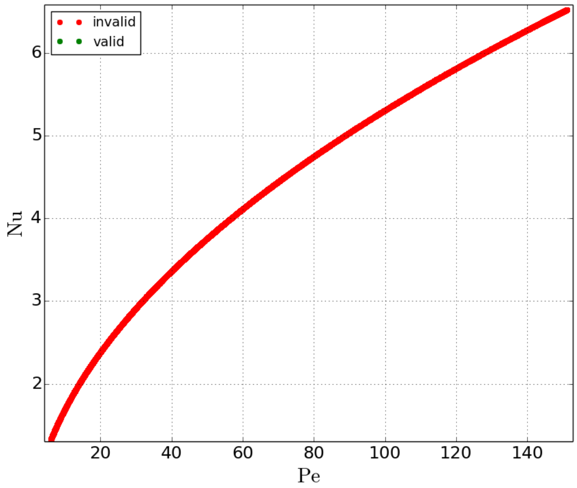

(b) Nusselt numbers in NCT

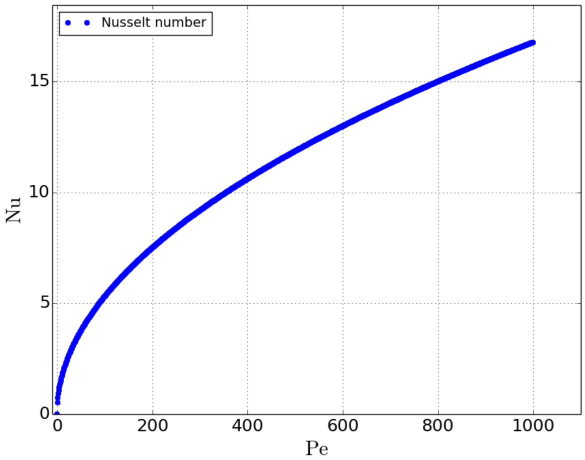

(c) Valid range according to literature

Fig. B.5: Verification and Assessment of eq.3.6 (Holman [55])

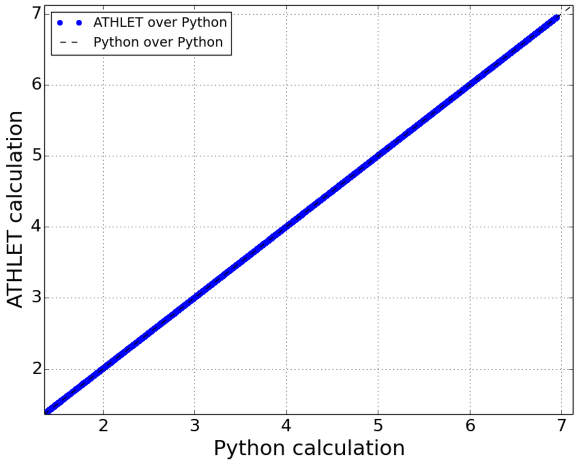

(a) Verification: ATHLET over Python

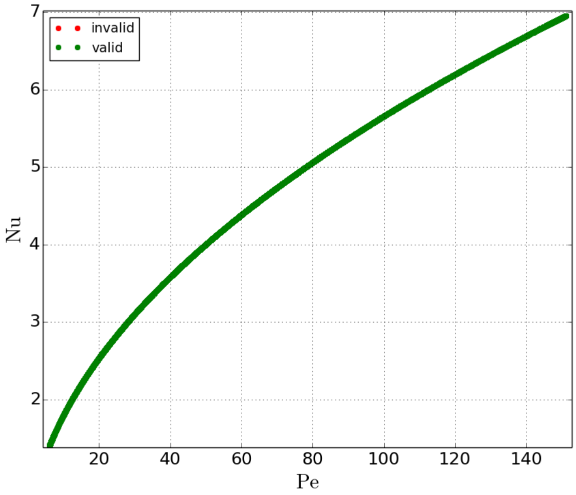

(b) Nusselt numbers in NCT

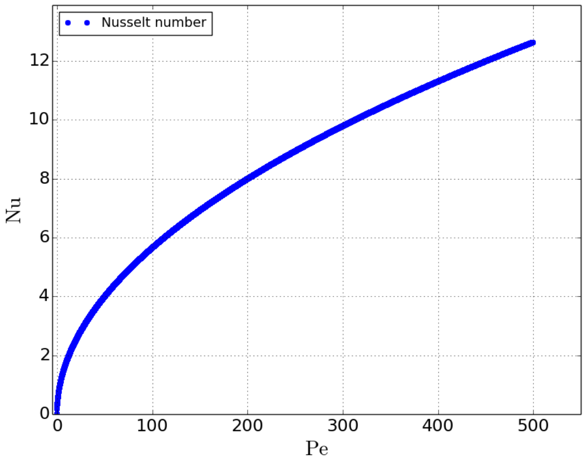

(c) Valid range according to literature

Fig. B.6: Verification and Assessment of eq.3.7 (Çengel et al. [20, p.402])

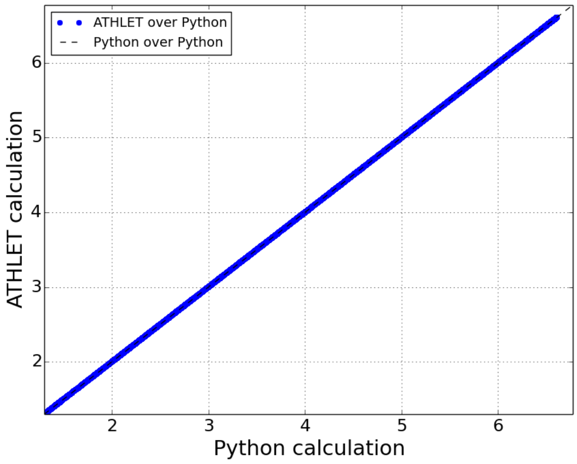

(a) Verification: ATHLET over Python

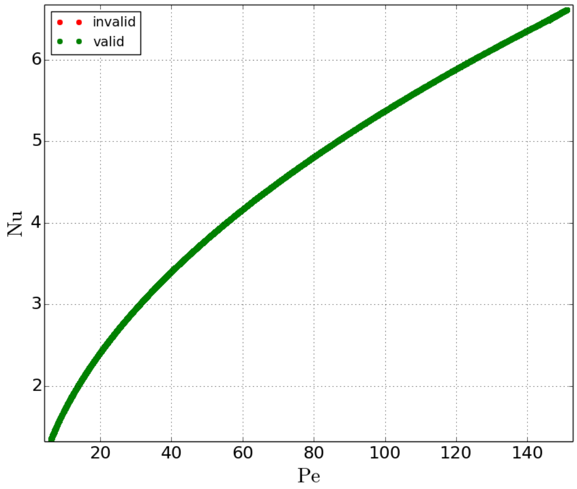

(b) Nusselt numbers in NCT

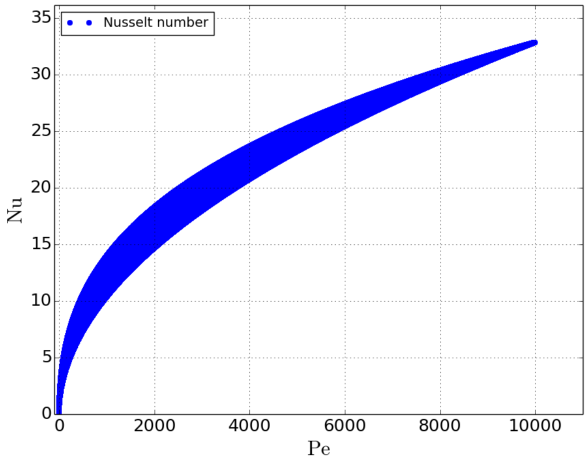

(c) Valid range according to literature

Fig. B.7: Verification and Assessment of eq.3.8 (Churchill and Ozoe [30])

Nusselt correlations for tubes

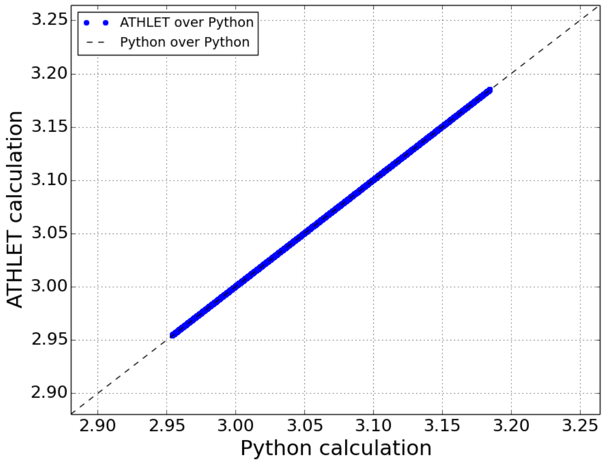

(a) Verification: ATHLET over Python

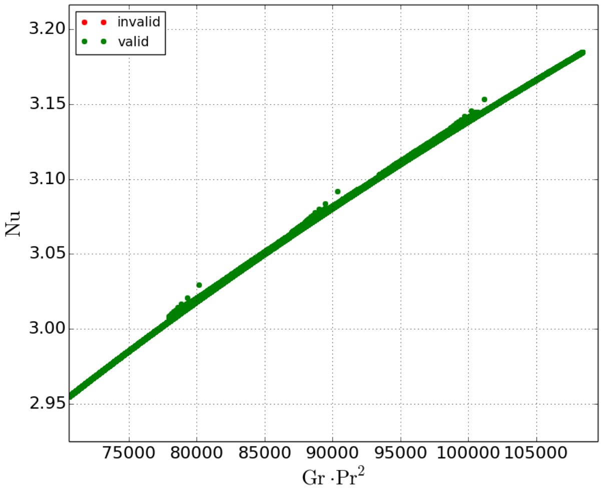

(b) Nusselt numbers in NCT

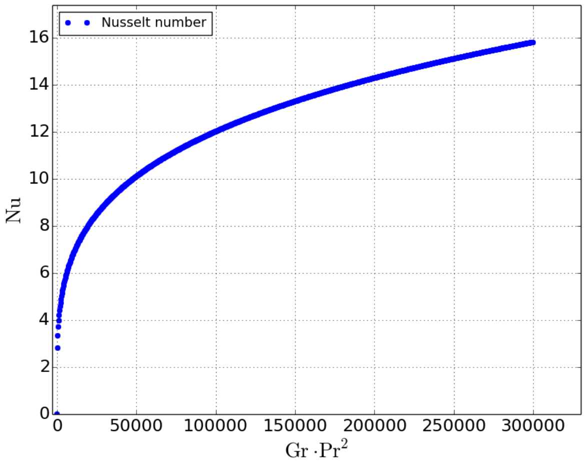

(c) Valid range according to literature

Fig. B.8: Verification and Assessment of eq.3.9 (Jackson [62])

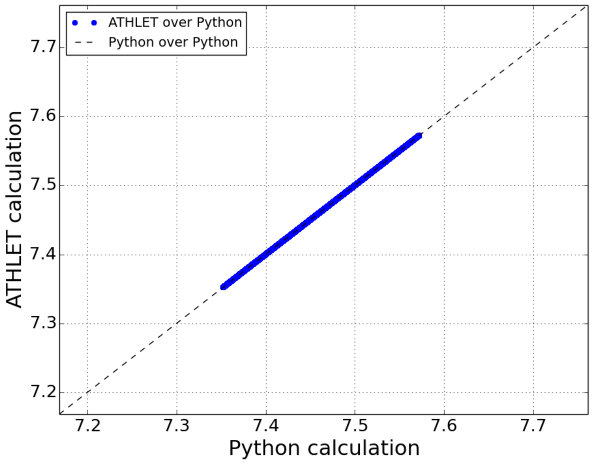

(a) Verification: ATHLET over Python

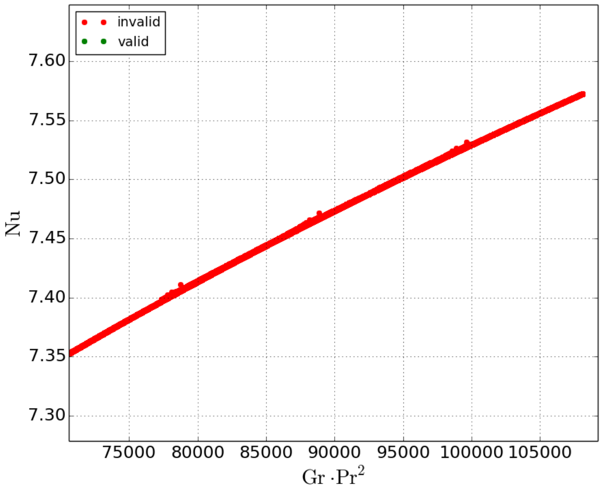

(b) Nusselt numbers in NCT

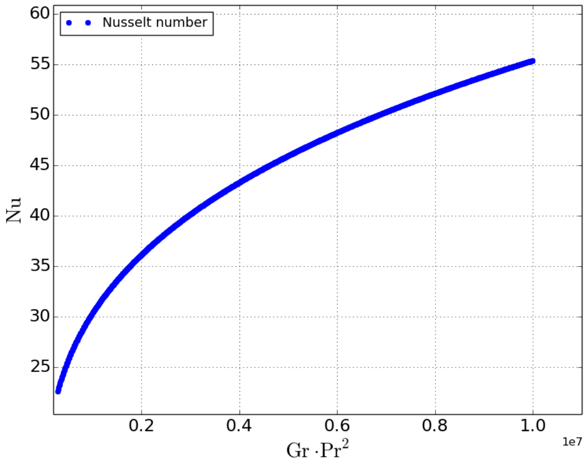

(c) Valid range according to literature

Fig. B.9: Verification and Assessment of eq.3.10 (Jackson [62])

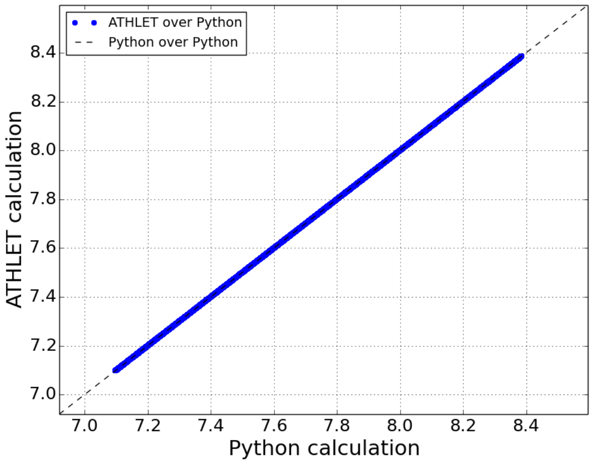

(a) Verification: ATHLET over Python

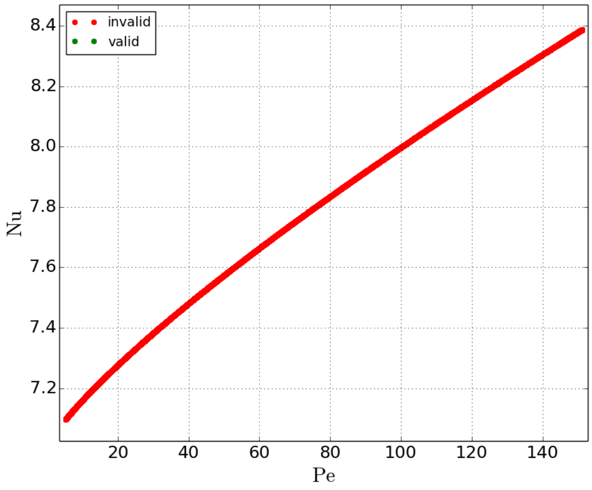

(b) Nusselt numbers in NCT

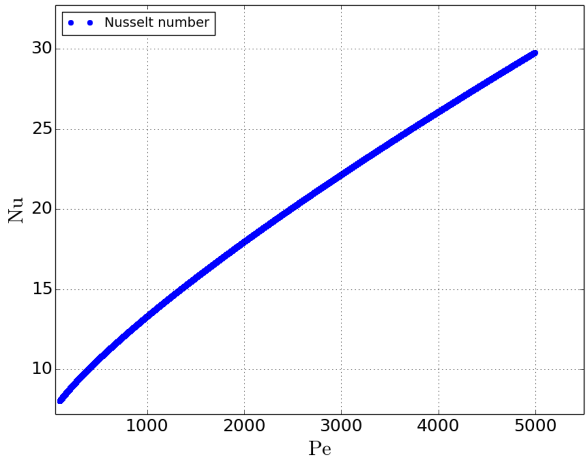

(c) Valid range according to literature

Fig. B.10: Verification and Assessment of eq.3.12 (Lyon [85])

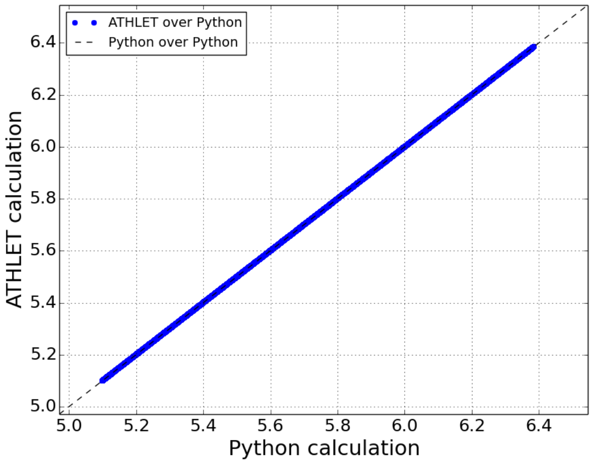

(a) Verification: ATHLET over Python

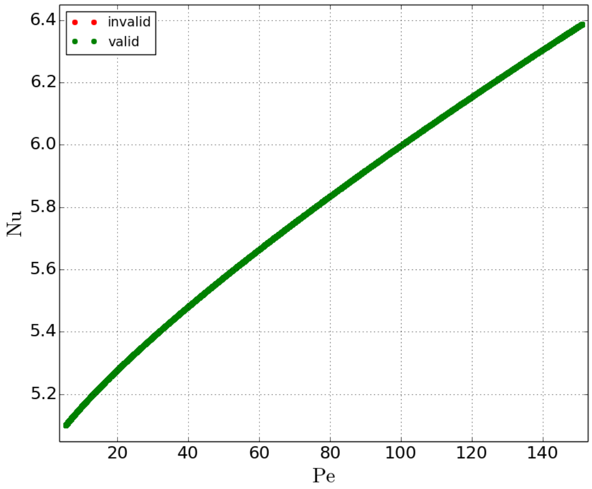

(b) Nusselt numbers in NCT

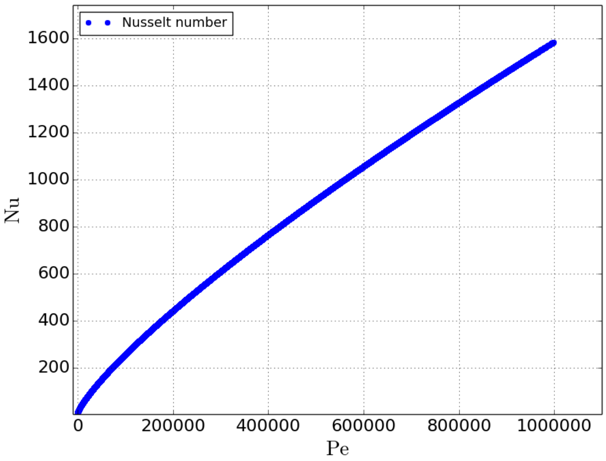

(c) Valid range according to literature

Fig. B.11: Verification and Assessment of eq.3.13 (Seban and Shimazaki [134] & Subbotin et al. [144])

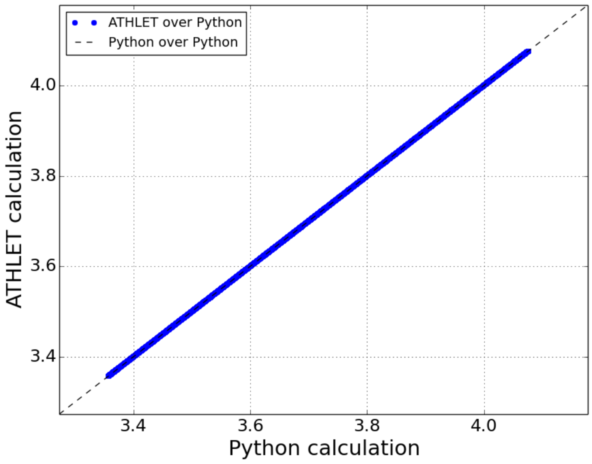

(a) Verification: ATHLET over Python

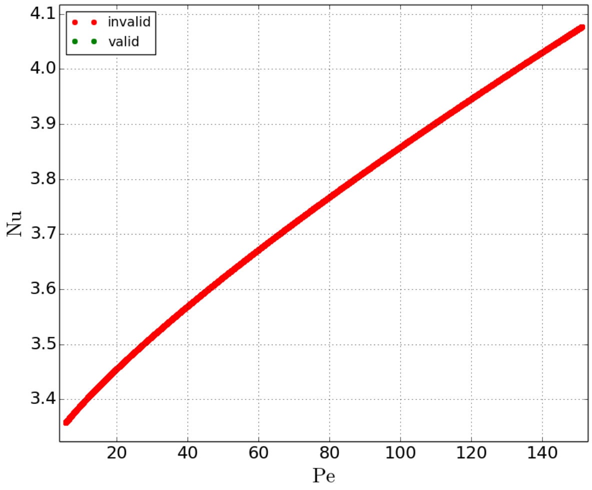

(b) Nusselt numbers in NCT

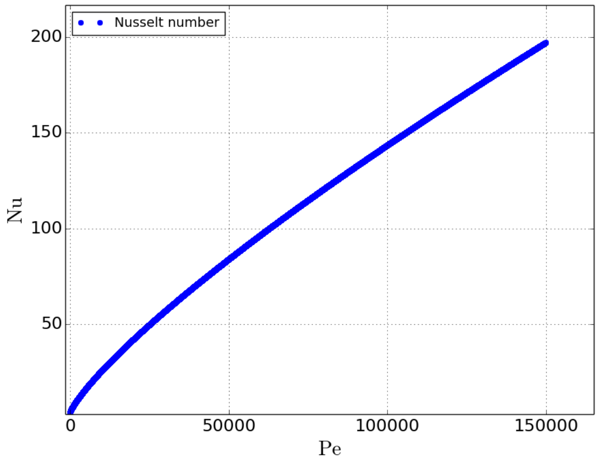

(c) Valid range according to literature

Fig. B.12: Verification and Assessment of eq.3.14 (Kutateladze et al. [73])

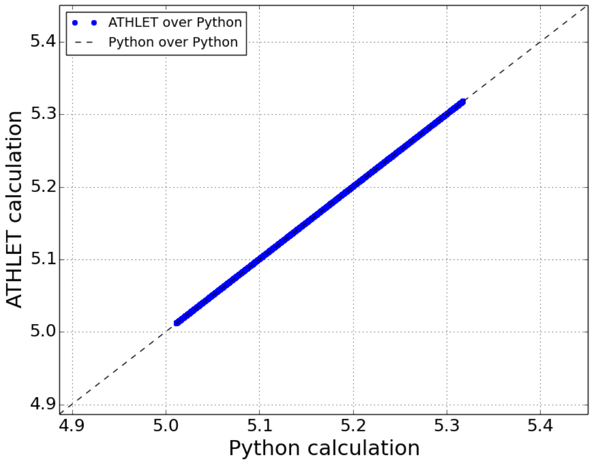

(a) Verification: ATHLET over Python

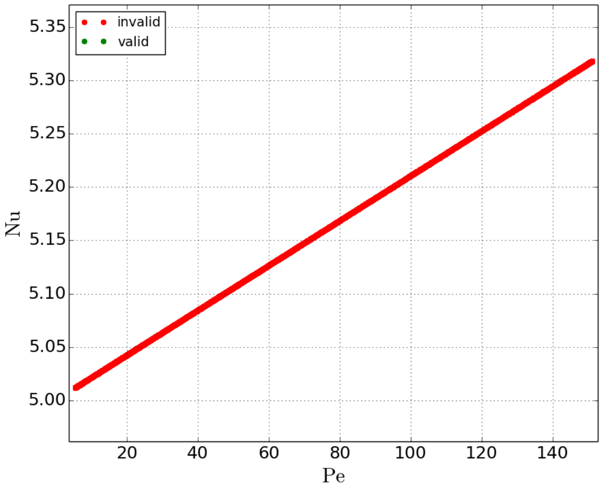

(b) Nusselt numbers in NCT

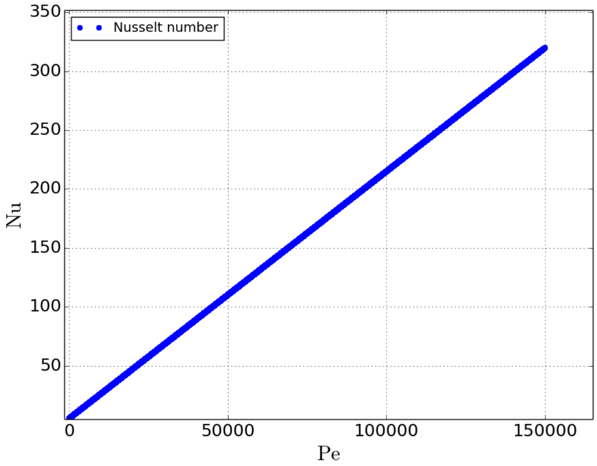

(c) Valid range according to literature

Fig. B.13: Verification and Assessment of eq.3.14 (Kutateladze et al. [73])

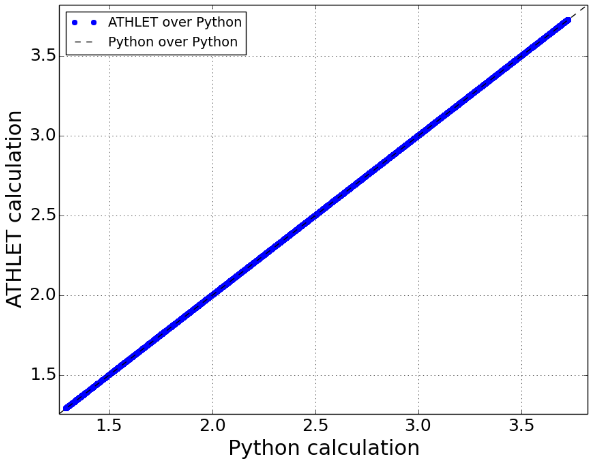

(a) Verification: ATHLET over Python

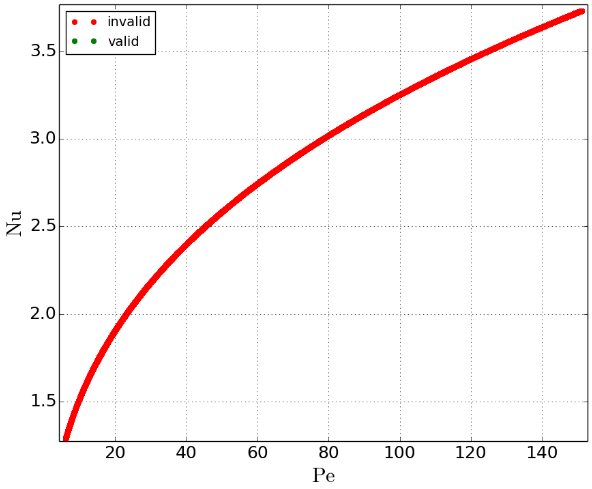

(b) Nusselt numbers in NCT

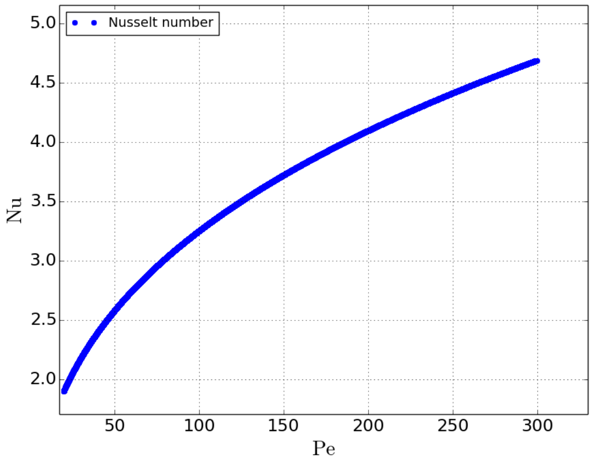

(c) Valid range according to literature

Fig. B.14: Verification and Assessment of eq.3.16 (Kutateladze et al. [73])

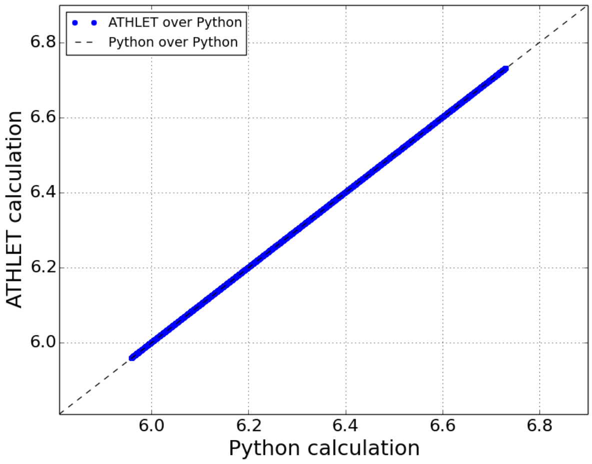

(a) Verification: ATHLET over Python

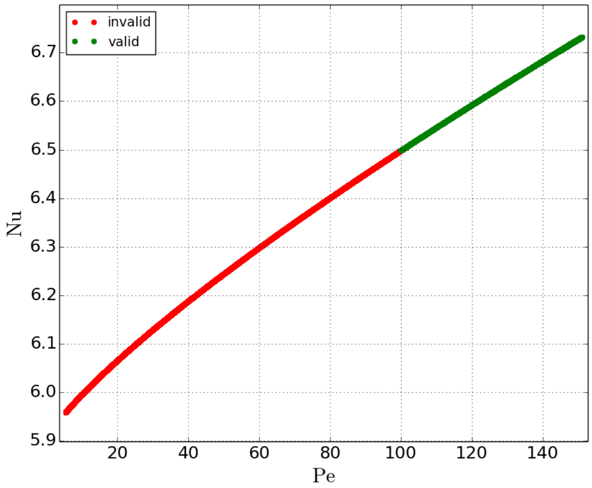

(b) Nusselt numbers in NCT

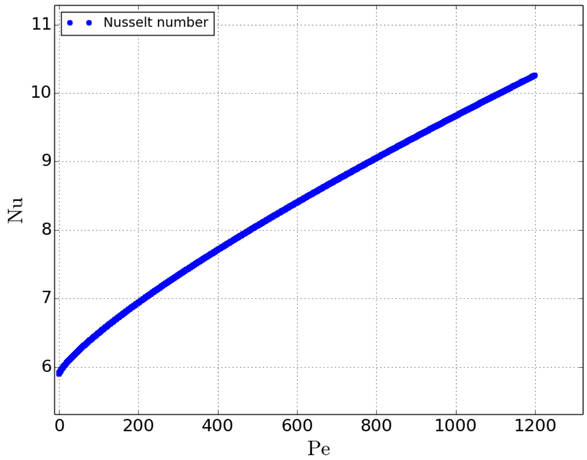

(c) Valid range according to literature

Fig. B.15: Verification and Assessment of eq.3.17 (Kutateladze et al. [73])

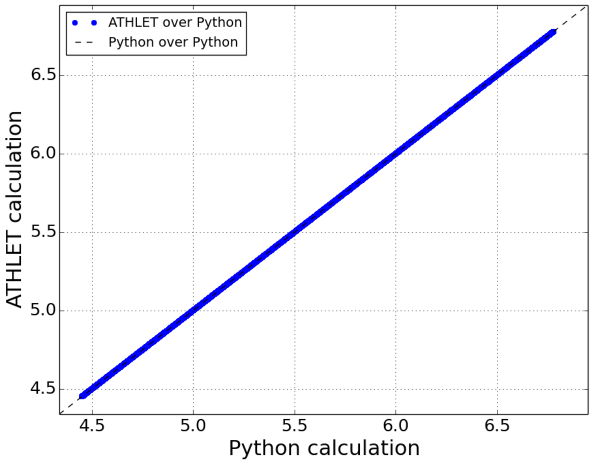

(a) Verification: ATHLET over Python

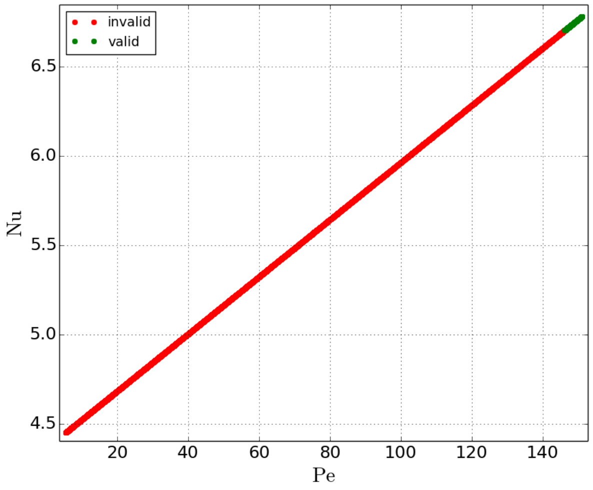

(b) Nusselt numbers in NCT

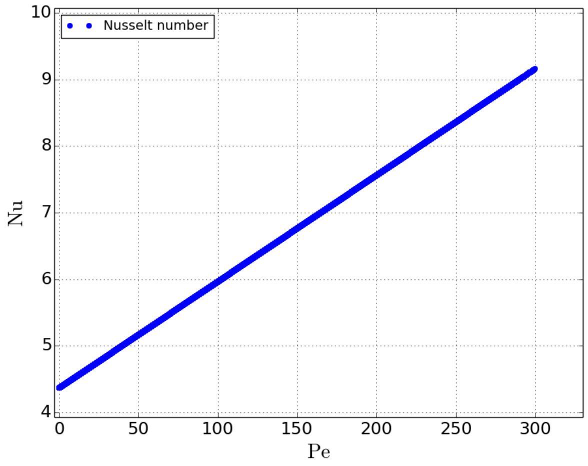

(c) Valid range according to literature

Fig. B.16: Verification and Assessment of eq.3.18 (Borishanskii et al. [13])

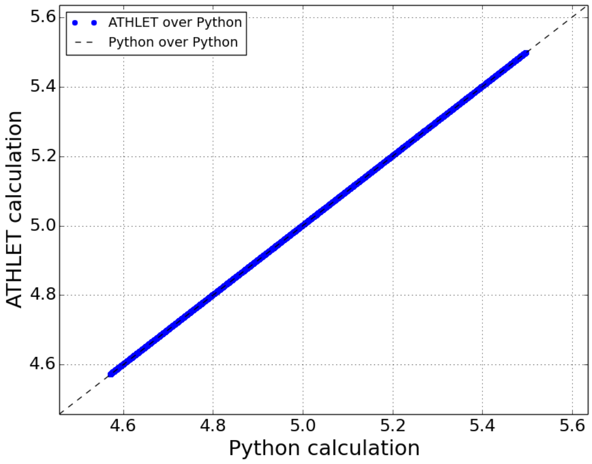

(a) Verification: ATHLET over Python

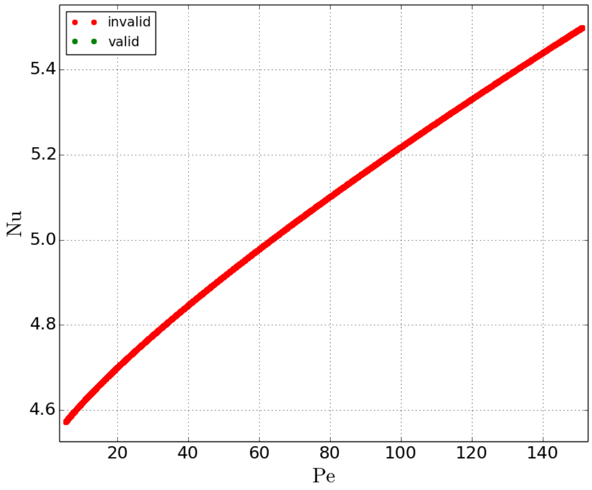

(b) Nusselt numbers in NCT

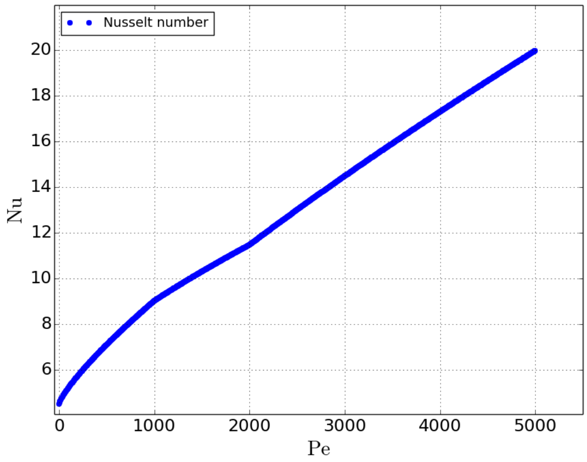

(c) Valid range according to literature

Fig. B.17: Verification and Assessment of eq.3.19 (Cheng and Tak [26])

Nusselt correlations for triangular and square fuel pin arrangements

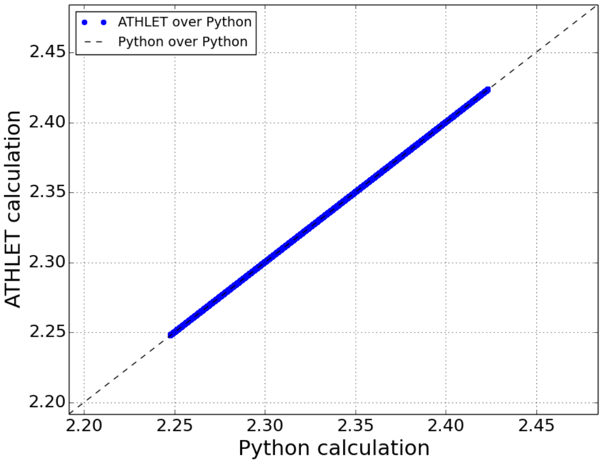

(a) Verification: ATHLET over Python

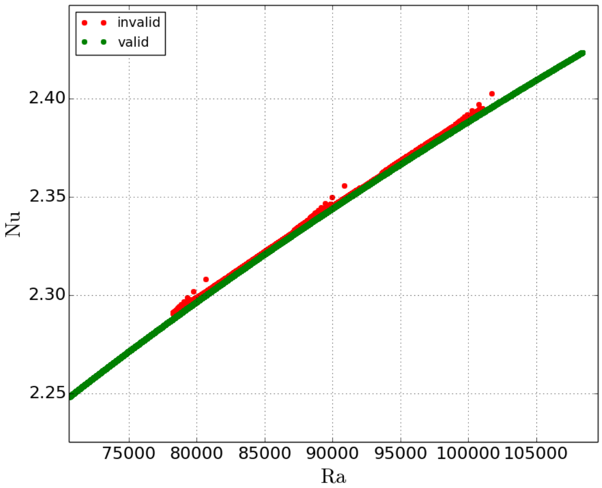

(b) Nusselt numbers in NCT

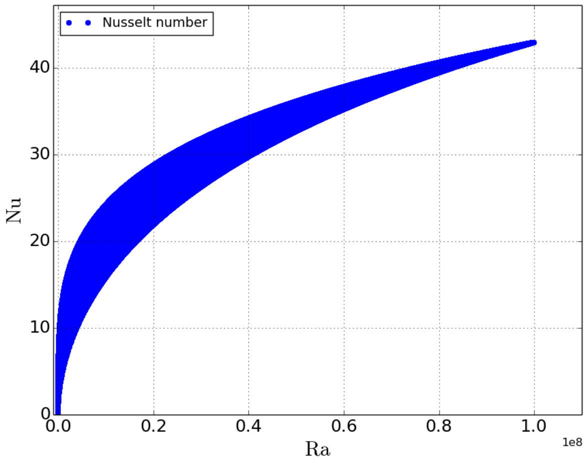

(c) Valid range according to literature

Fig. B.18: Verification and Assessment of eq.3.20 (Eckert [38])

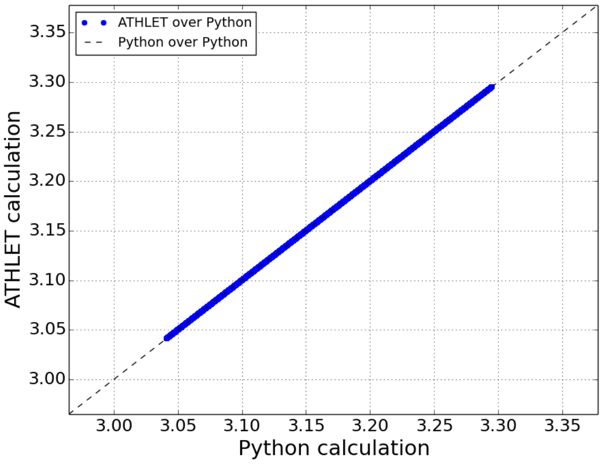

(a) Verification: ATHLET over Python

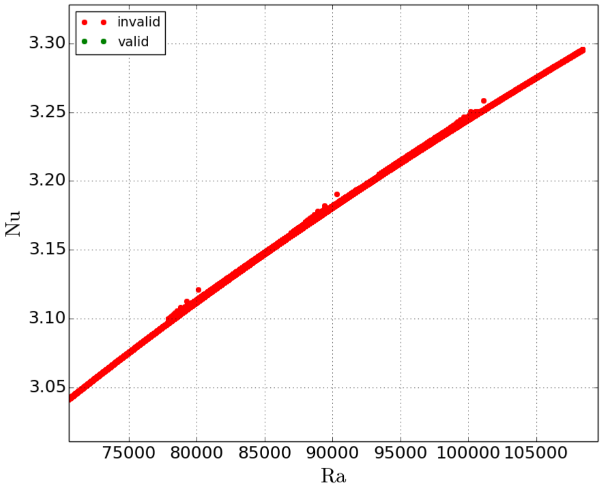

(b) Nusselt numbers in NCT

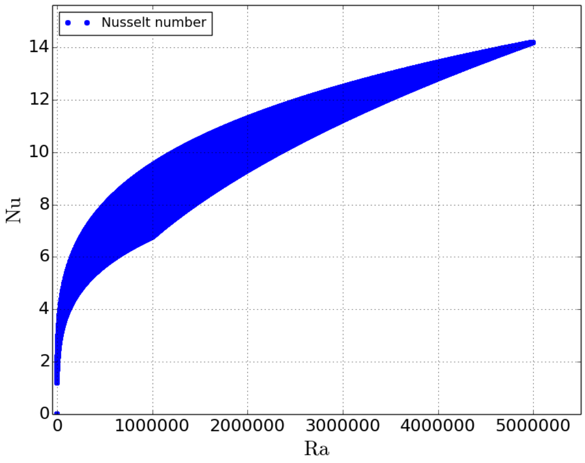

(c) Valid range according to literature

Fig. B.19: Verification and Assessment of eq.3.21 (Chang et al. [22])

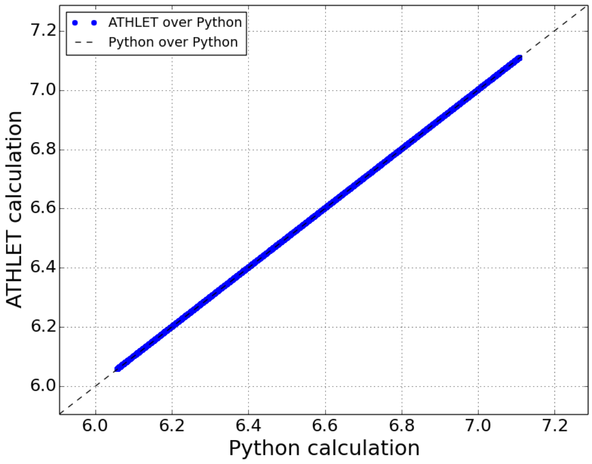

(a) Verification: ATHLET over Python

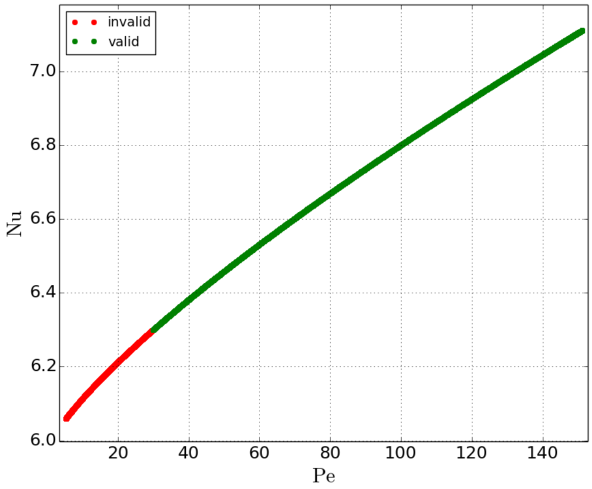

(b) Nusselt numbers in NCT

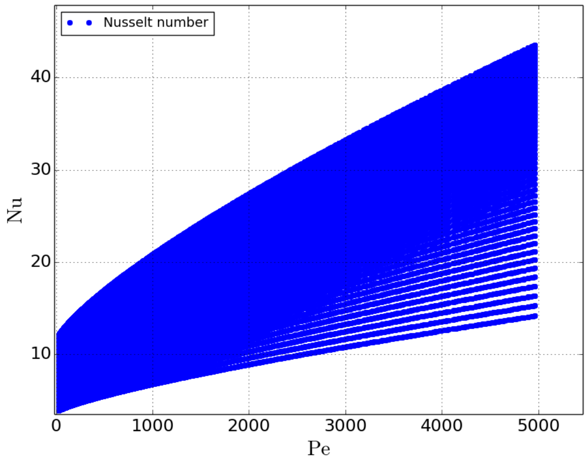

(c) Valid range according to literature

Fig. B.20: Verification and Assessment of eq.3.32 (Mikityuk [95])

Nusselt correlations for square fuel pin arrangements

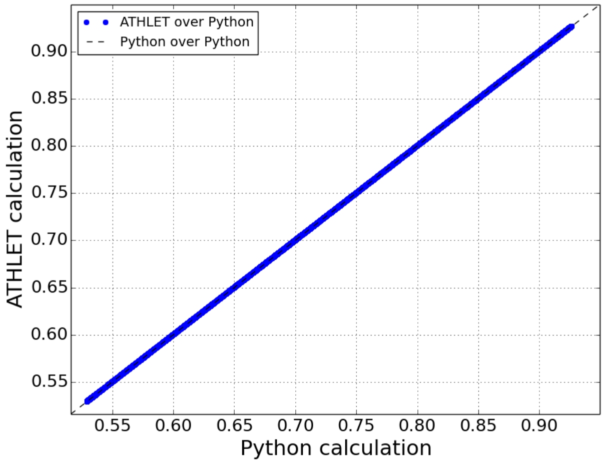

(a) Verification: ATHLET over Python

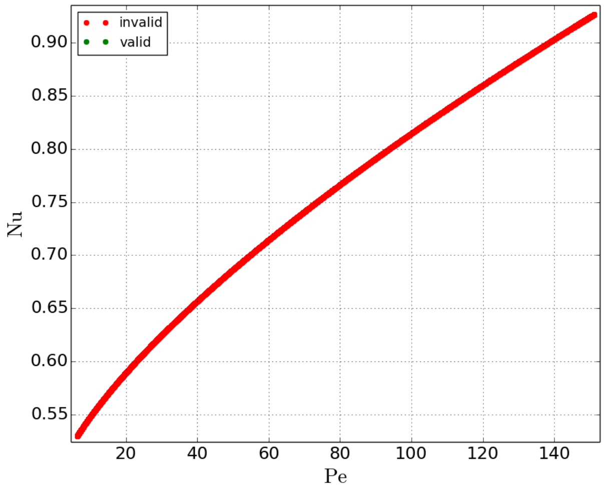

(b) Nusselt numbers in NCT

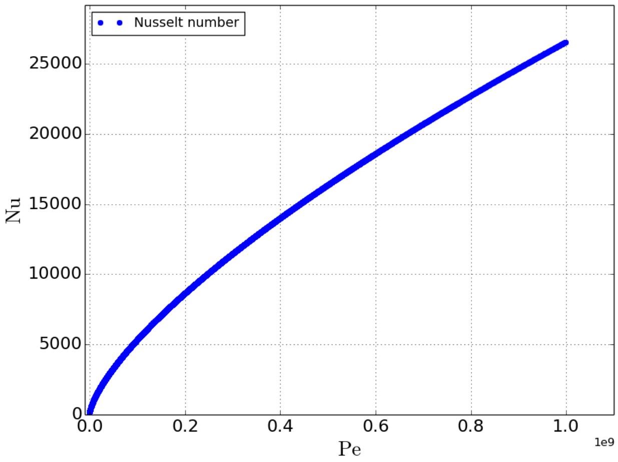

(c) Valid range according to literature

Fig. B.21: Verification and Assessment of eq.3.34 (Ushakov et al. [155])

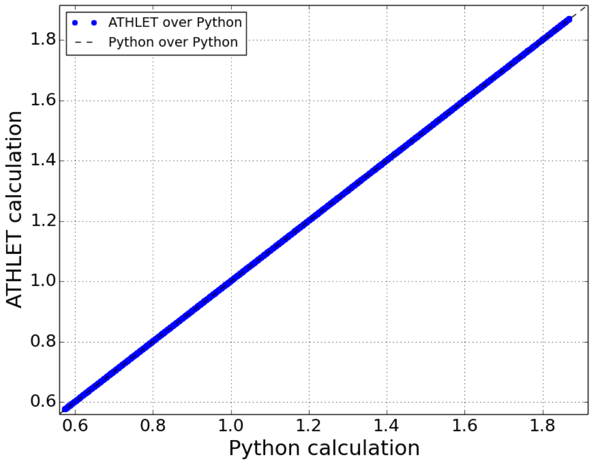

(a) Verification: ATHLET over Python

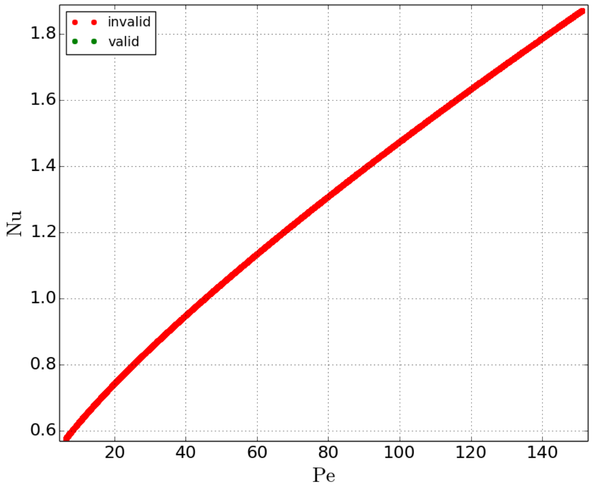

(b) Nusselt numbers in NCT

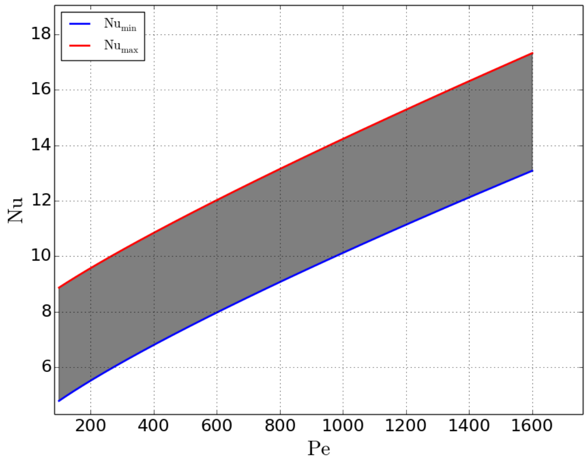

(c) Valid range according to literature

Fig. B.22: Verification and Assessment of eq.3.35 (Mikityuk [95])

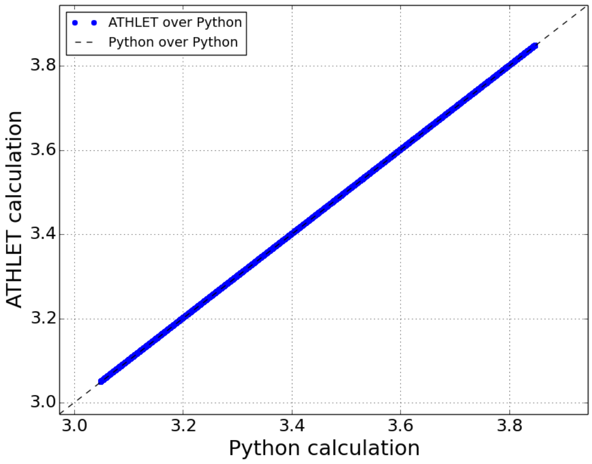

(a) Verification: ATHLET over Python

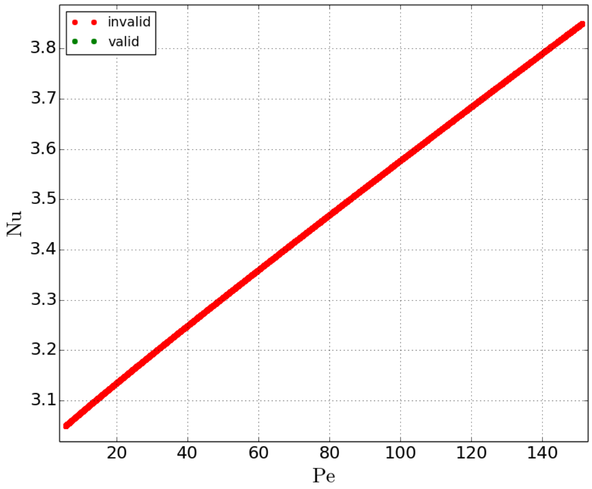

(b) Nusselt numbers in NCT

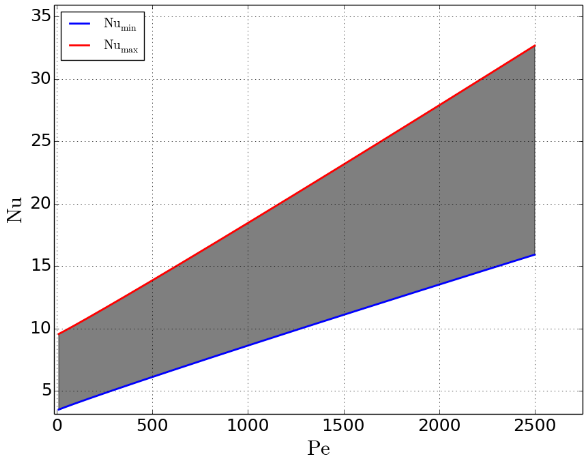

(c) Valid range according to literature

Fig. B.23: Verification and Assessment of eq.3.36 (Zhukov et al. [166])

Nusselt correlations for triangular fuel pin arrangements

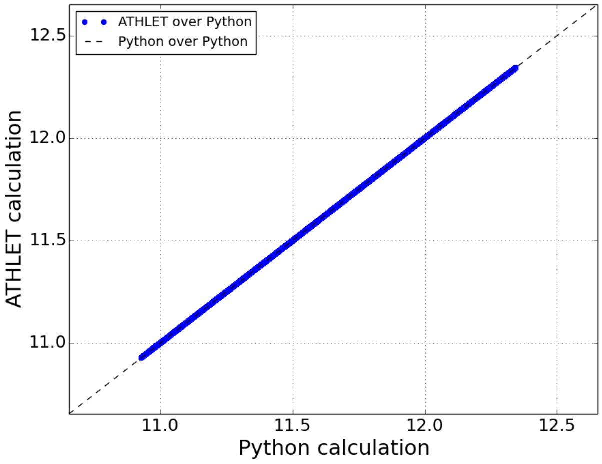

(a) Verification: ATHLET over Python

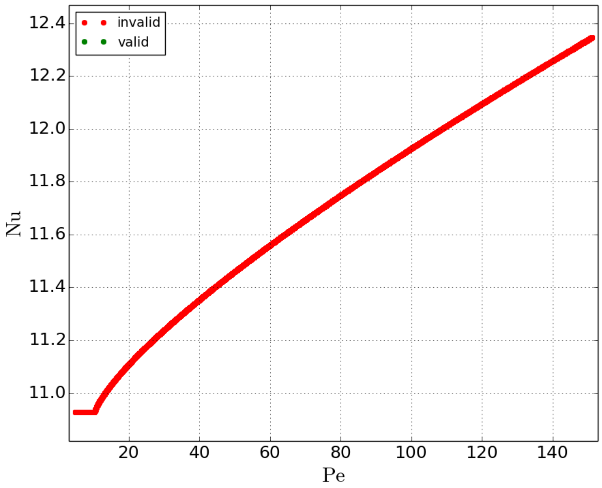

(b) Nusselt numbers in NCT

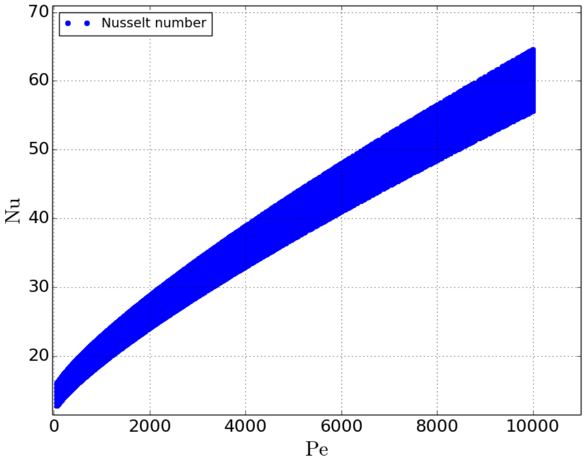

(c) Valid range according to literature

Fig. B.24: Verification and Assessment of eq.3.22 (Dwyer and Tu [37])

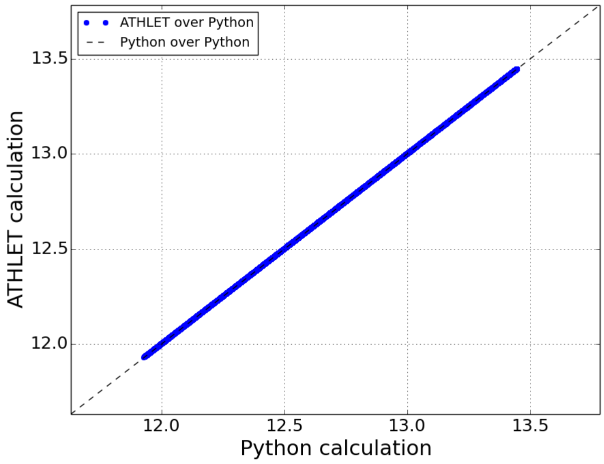

(a) Verification: ATHLET over Python

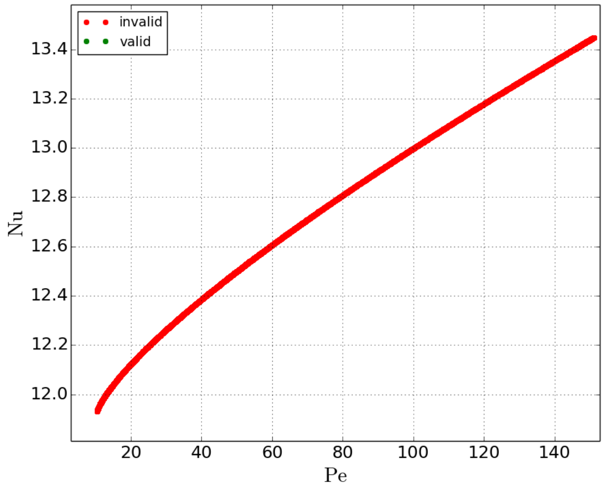

(b) Nusselt numbers in NCT

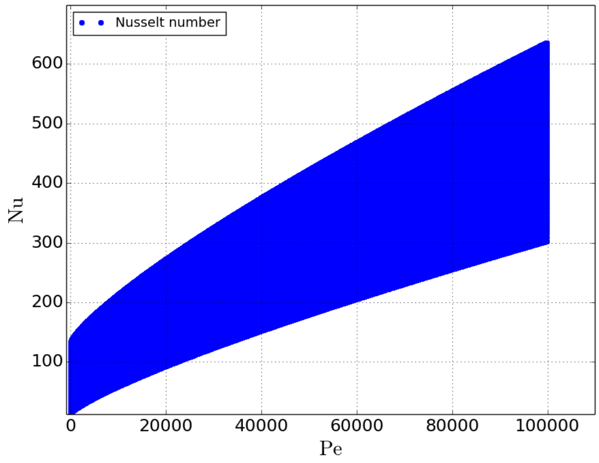

(c) Valid range according to literature

Fig. B.25: Verification and Assessment of eq.3.23 (Friedland and Bonilla [47])

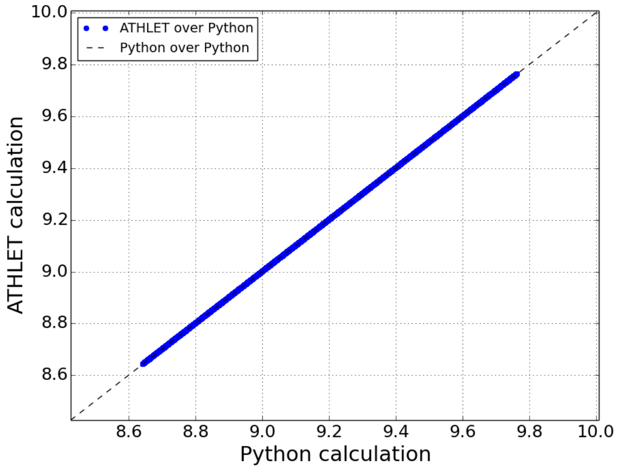

(a) Verification: ATHLET over Python

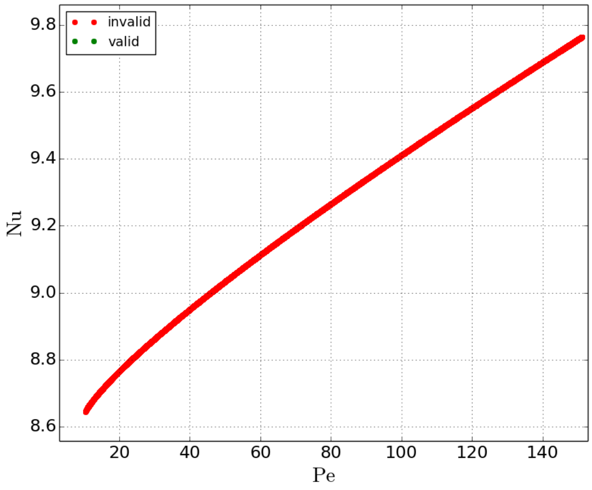

(b) Nusselt numbers in NCT

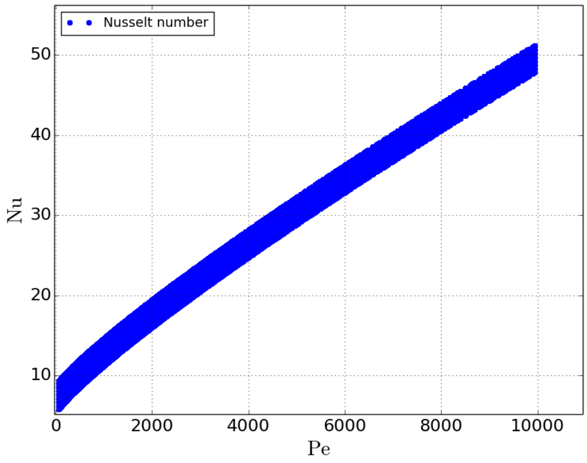

(c) Valid range according to literature

Fig. B.26: Verification and Assessment of eq.3.26 (Maresca and Dwyer [88])

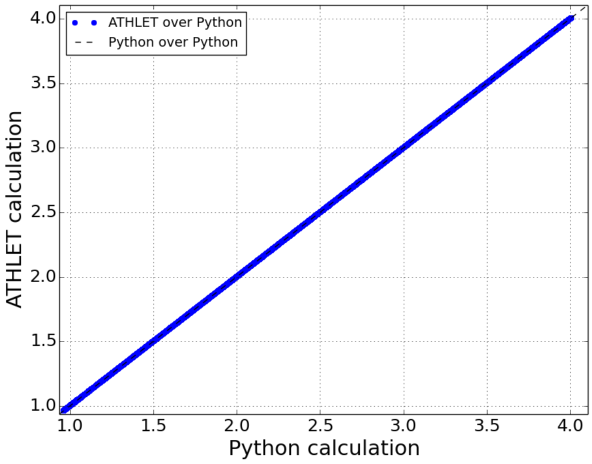

(a) Verification: ATHLET over Python

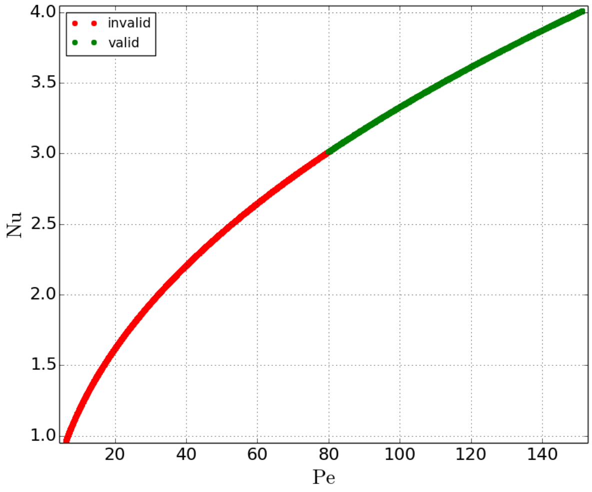

(b) Nusselt numbers in NCT

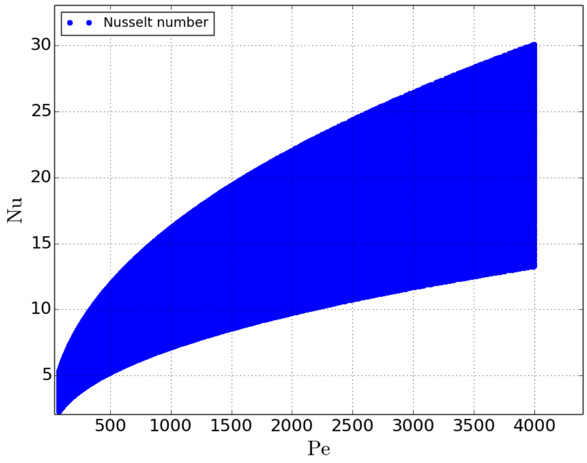

(c) Valid range according to literature

Fig. B.27: Verification and Assessment of eq.3.27 (Subbotin et al. [144])

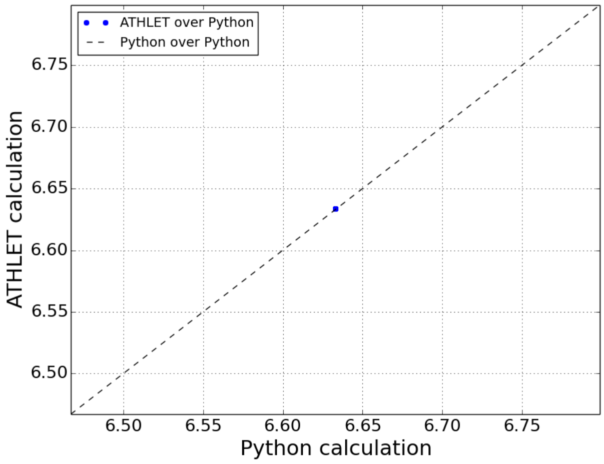

(a) Verification: ATHLET over Python

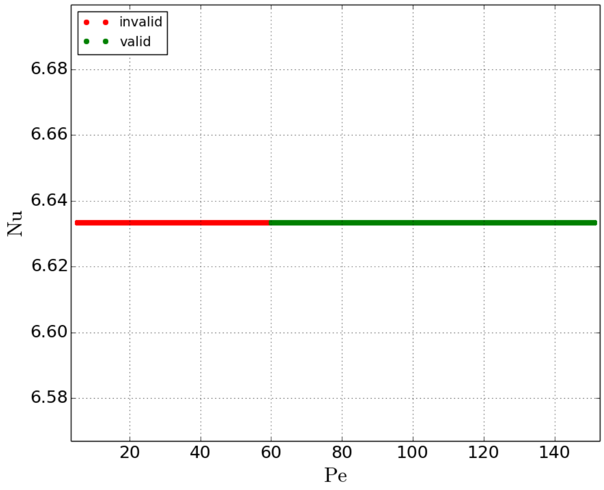

(b) Nusselt numbers in NCT

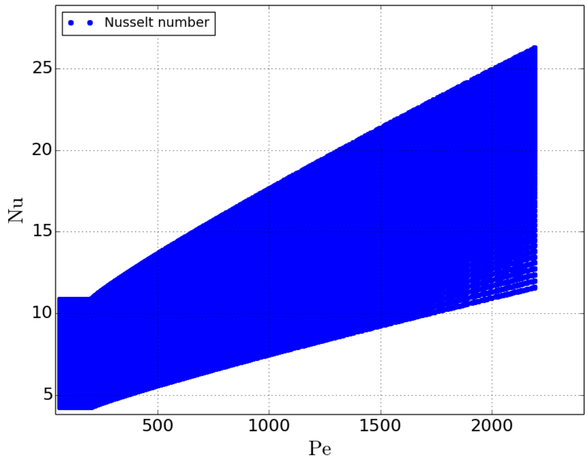

(c) Valid range according to literature

Fig. B.28: Verification and Assessment of eq.3.28 (Borishanskii et al. [14])

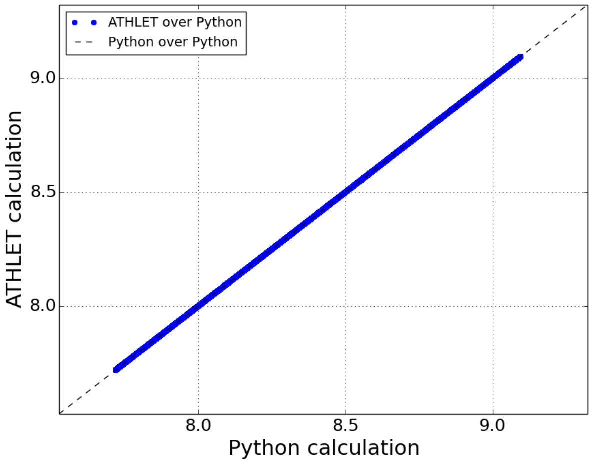

(a) Verification: ATHLET over Python

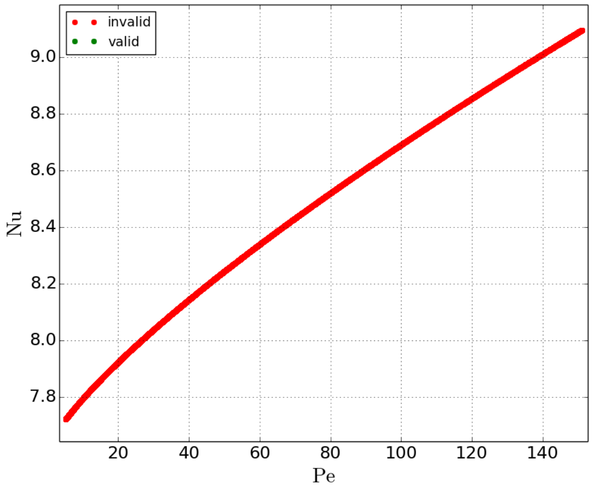

(b) Nusselt numbers in NCT

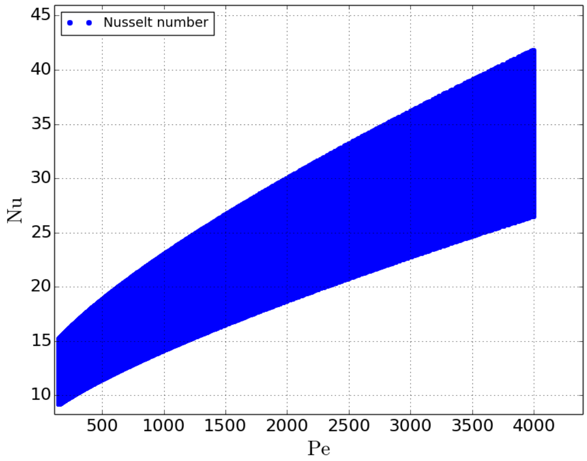

(c) Valid range according to literature

Fig. B.29: Verification and Assessment of eq.3.29 (Gräber and Rieger [49])

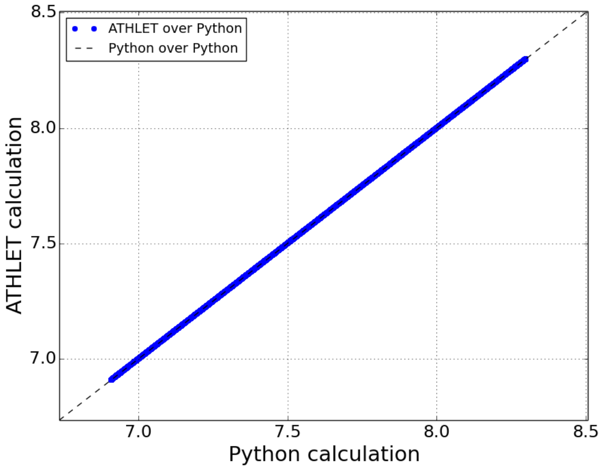

(a) Verification: ATHLET over Python

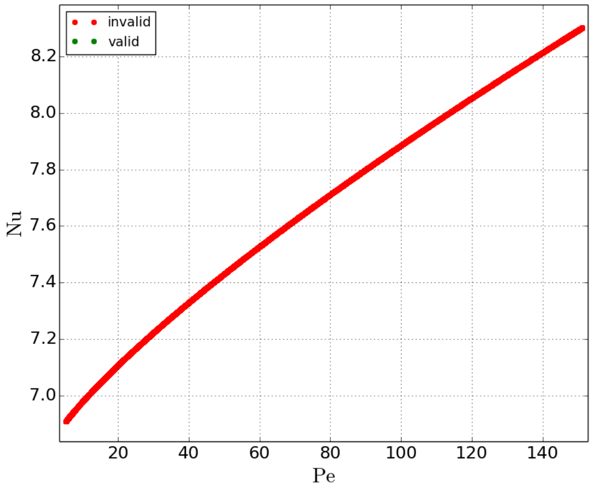

(b) Nusselt numbers in NCT

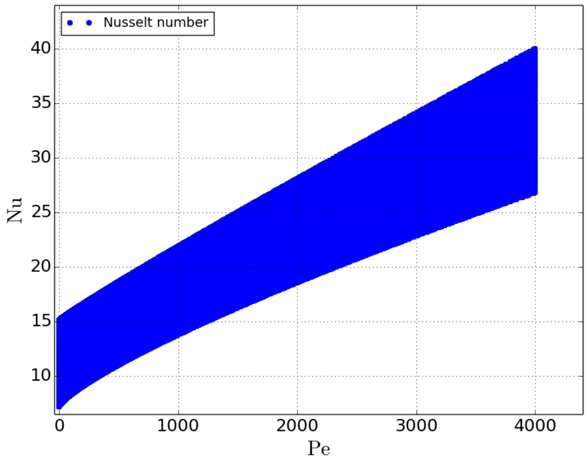

(c) Valid range according to literature

Fig. B.30: Verification and Assessment of eq.3.30 (Ushakov et al. [155])

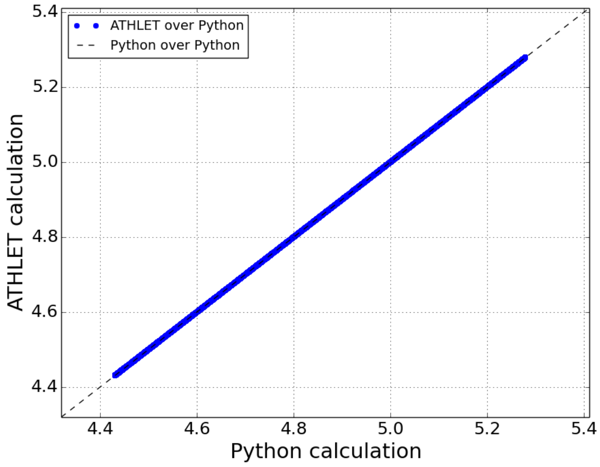

(a) Verification: ATHLET over Python

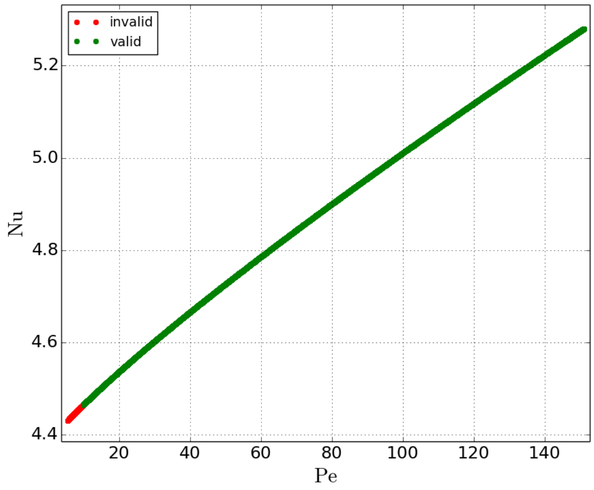

(b) Nusselt numbers in NCT

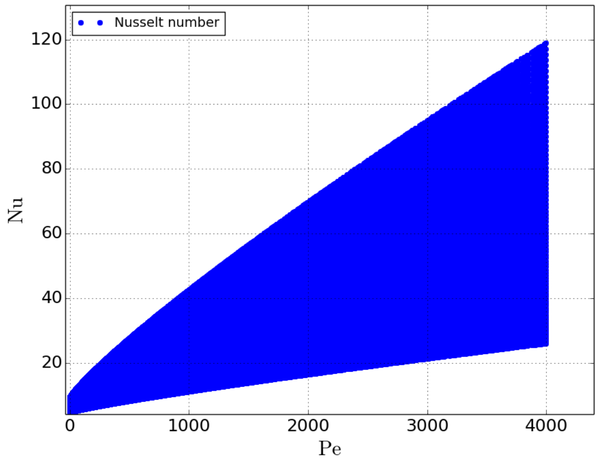

(c) Valid range according to literature

Fig. B.31: Verification and Assessment of eq.3.31 (Kazimi and Carelli [69])

Pressure Drop

Verification

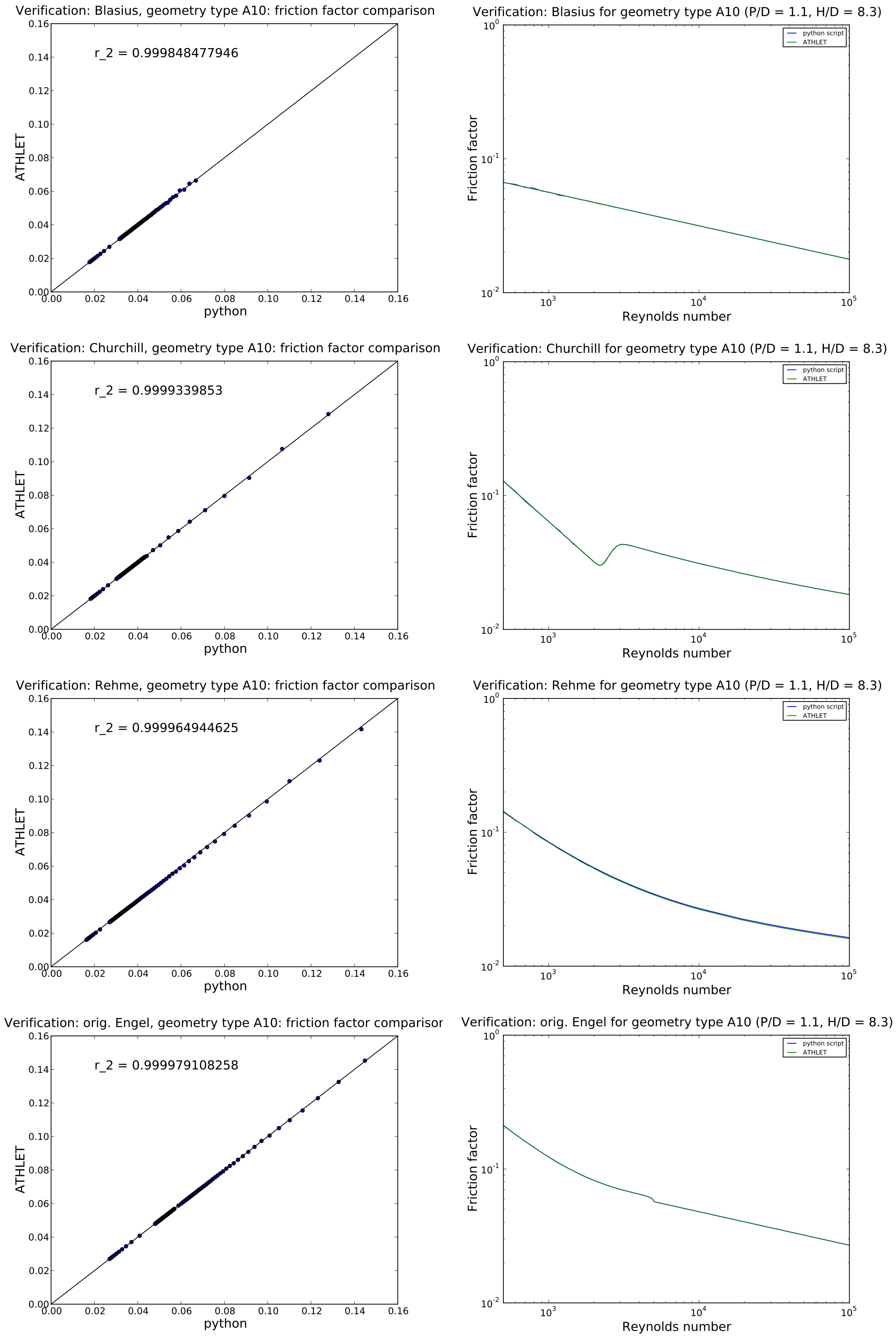

Fig. B.32: Verification: Left side: friction factors, ATHLET over Python for friction model number from 61 to 64 Right side: friction factor in both cases for friction model number from 61 to 64 [15]

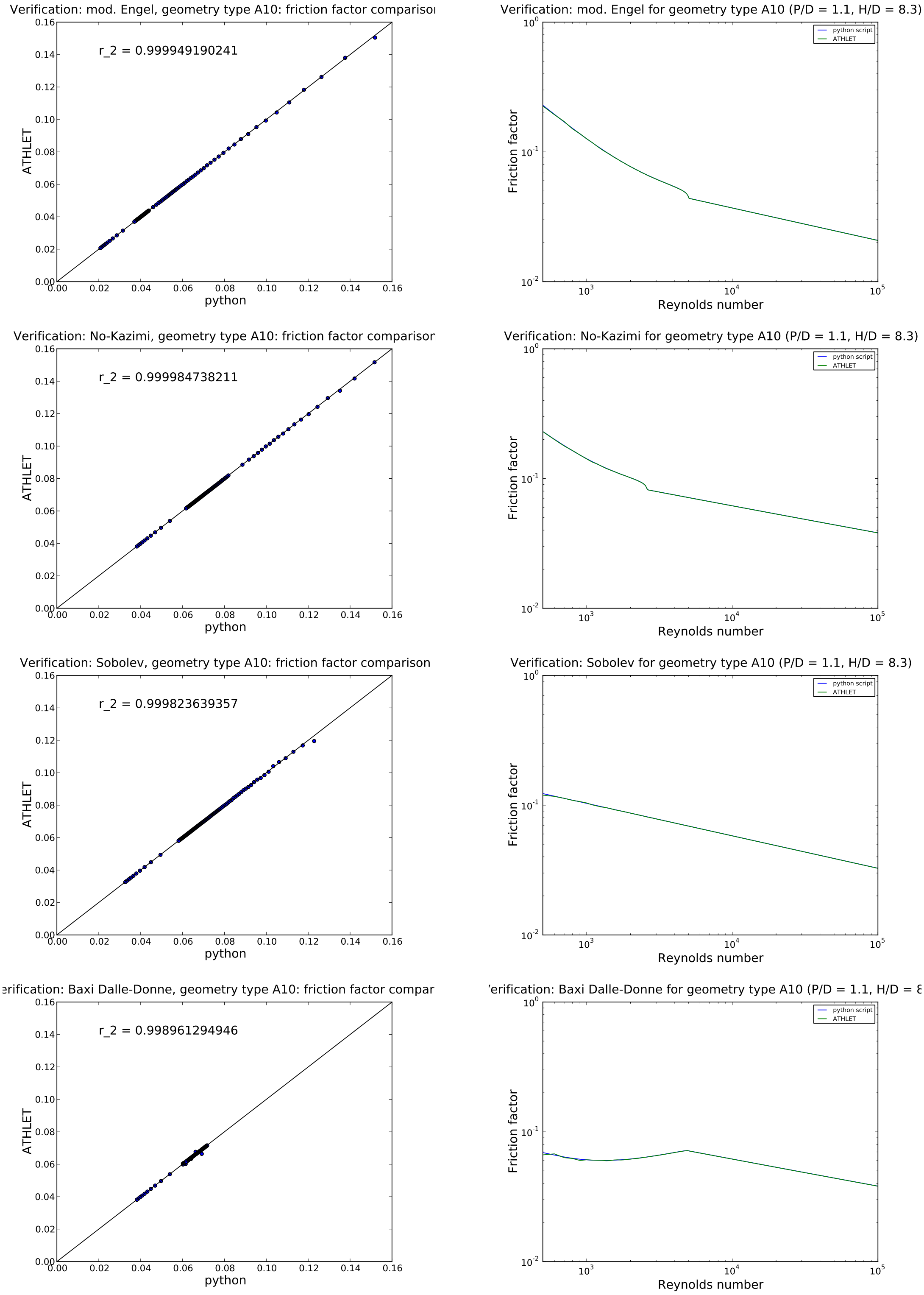

Fig. B.33: Verification: Left side: friction factors, ATHLET over Python for friction model number from 65 to 68 Right side: friction factor in both cases for friction model number from 65 to 68 [15]

Assessment

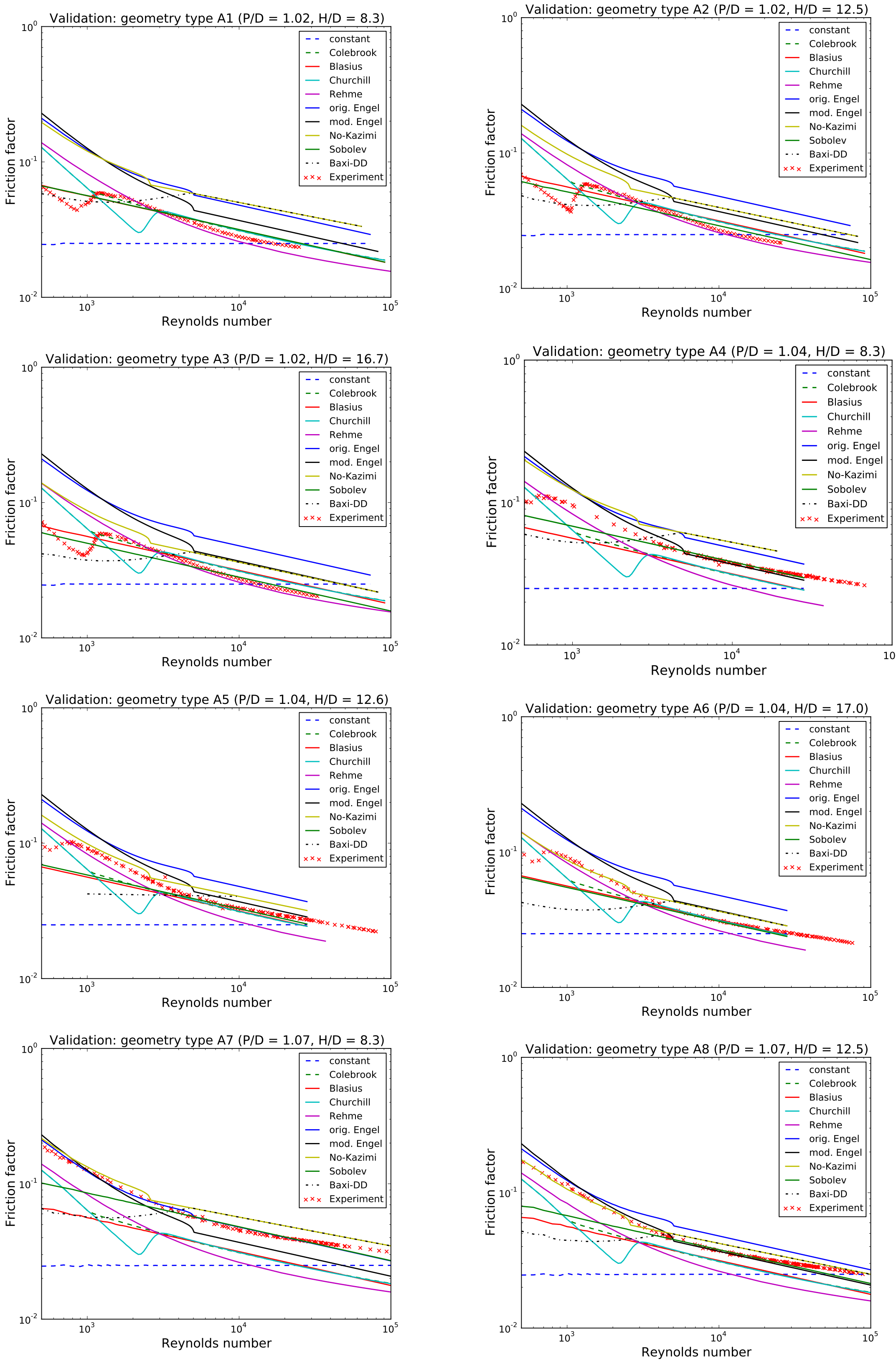

Fig. B.34: Validation: geometry types 1 to 8 [15]

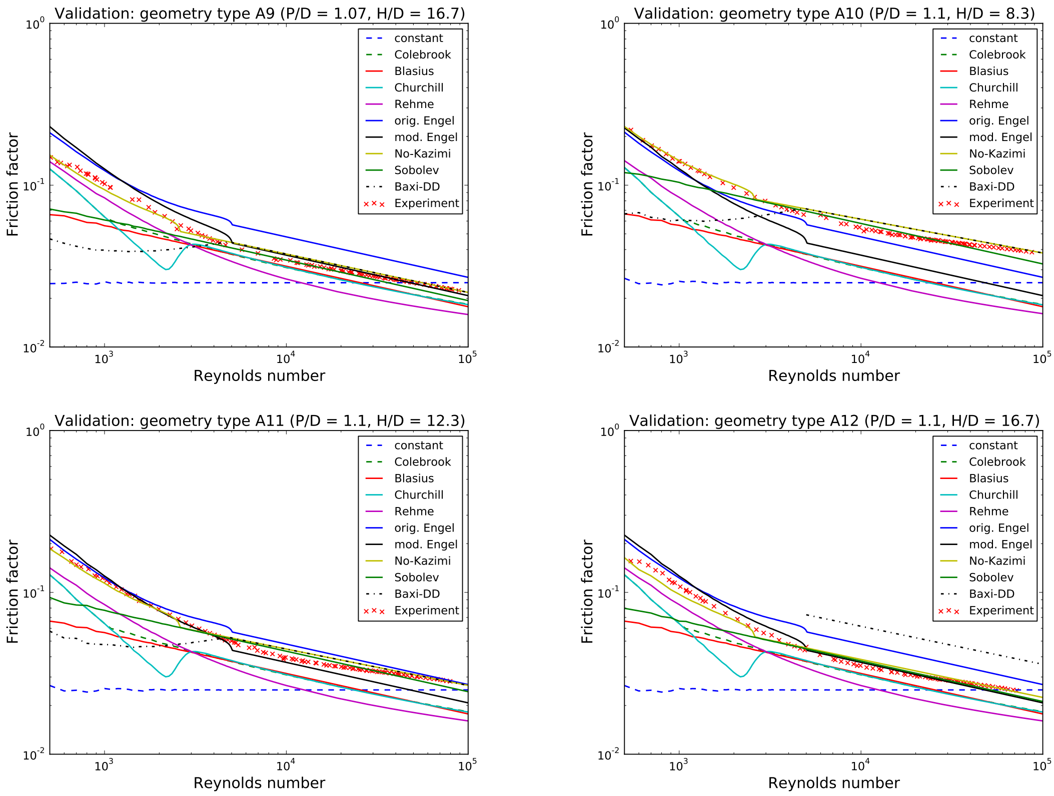

Fig. B.35: Validation: geometry types 9 to 12 [15]

C CFD calculations - OpenFOAM

Boundary conditions

Mass flow

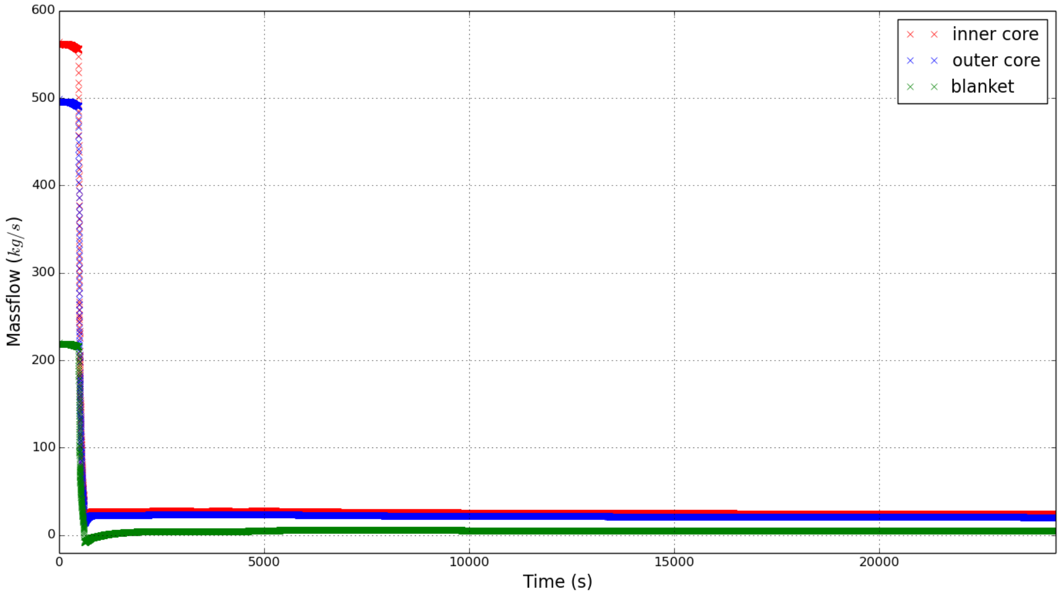

Fig. C.36: OpenFOAM: Hot pool - transient - Boundary conditions - massflow

Temperature

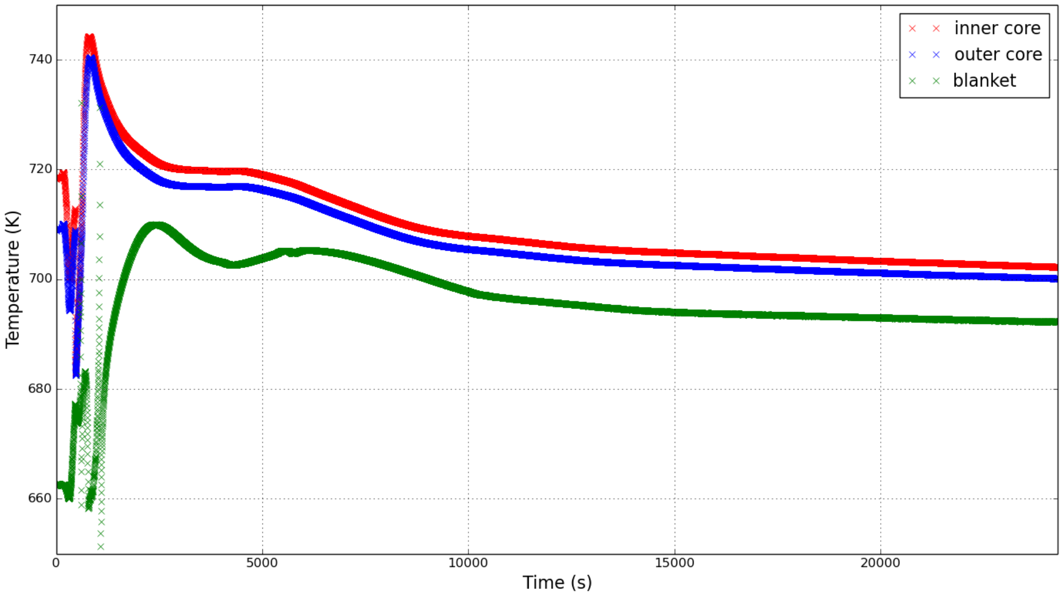

Fig. C.37: OpenFOAM: Hot pool - transient - Boundary conditions - temperatures

Pressure

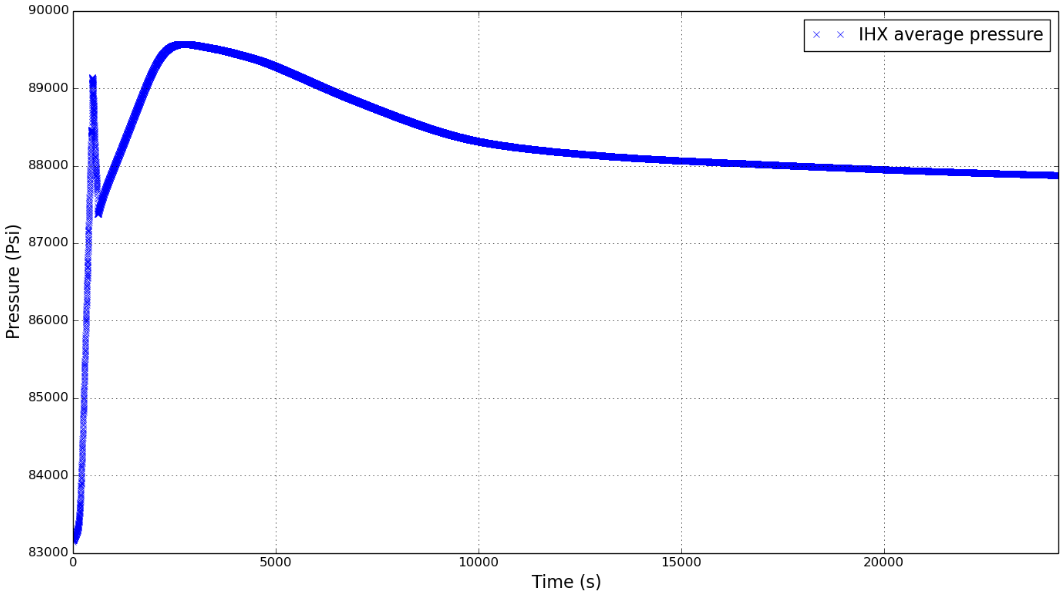

Fig. C.38: OpenFOAM: Hot pool - transient - Boundary conditions - pressure

CFD results

Law of the wall - y^+ results

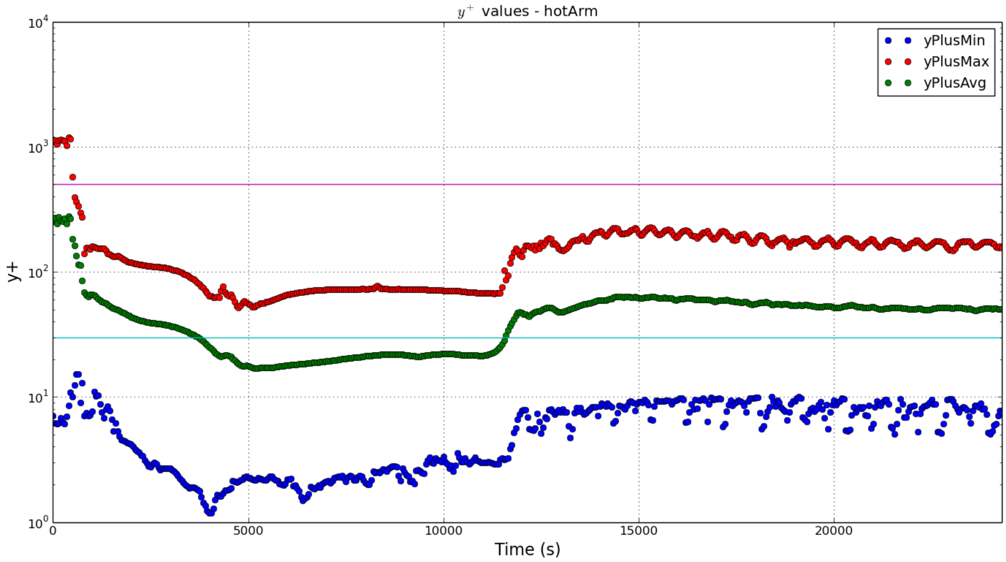

Fig. C.39: y^+ at Hot Arm

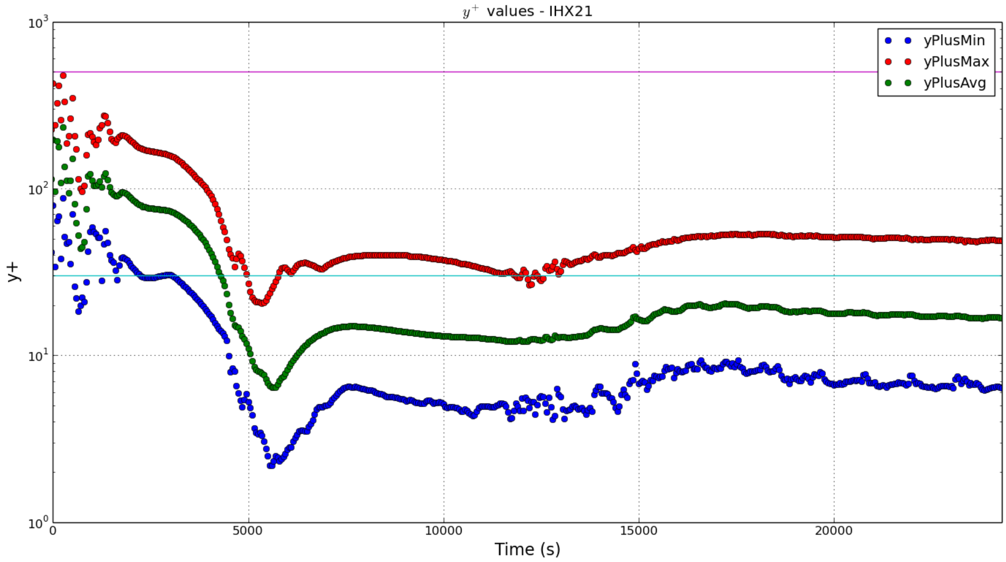

Fig. C.40: y^+ at Hot Arm

Velocity over line

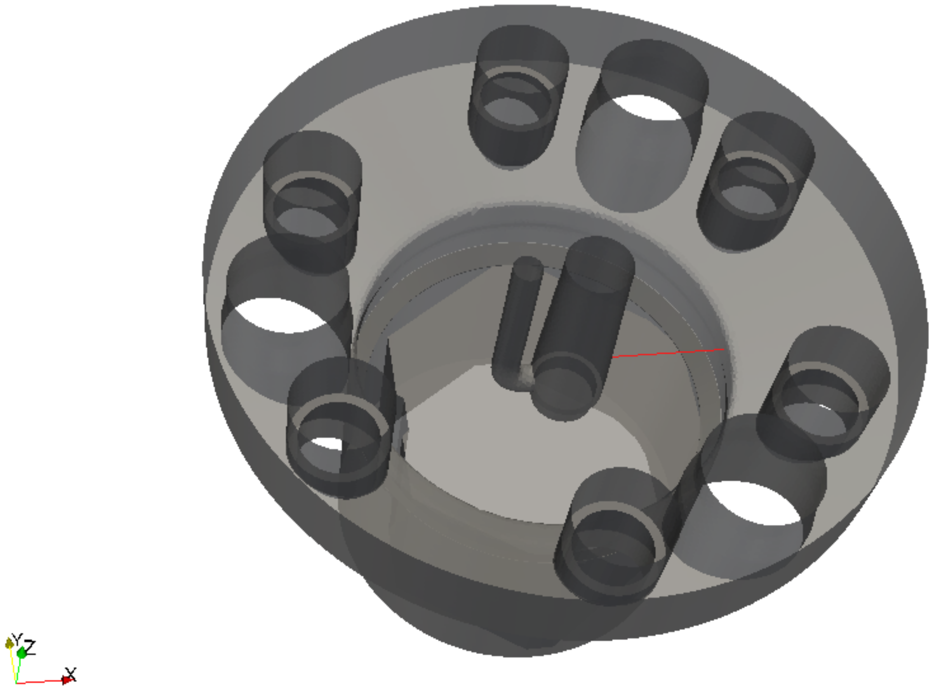

Fig. C.41: OpenFOAM: Hot pool - transient - Plot over line - geometrical position of line

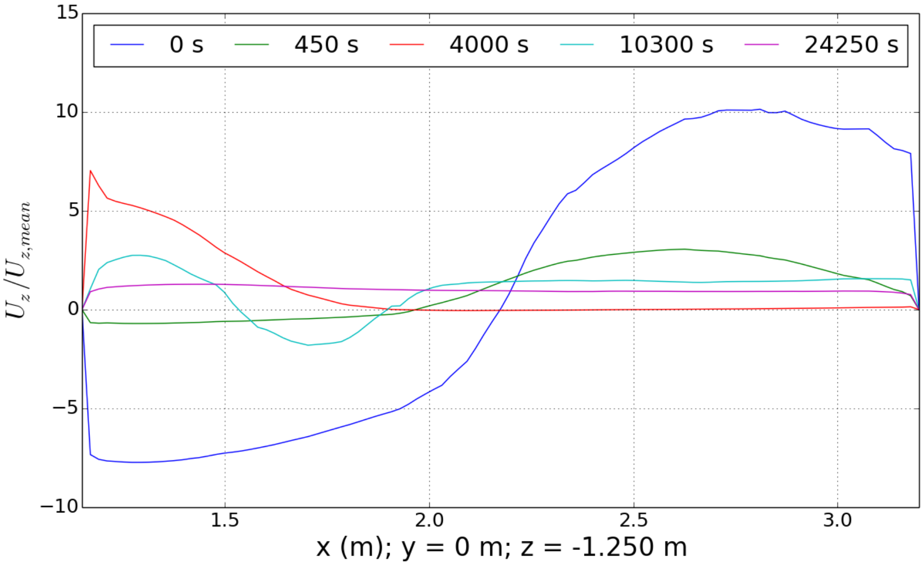

Fig. C.42: OpenFOAM: Hot pool - transient - Plot over line - $U_z/U_{z,mean}$

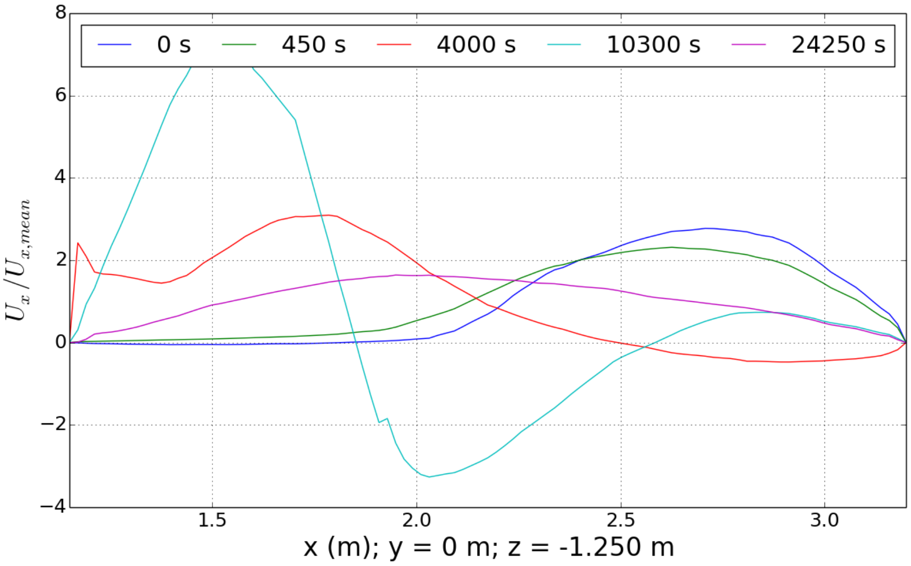

Fig. C.43: OpenFOAM: Hot pool - transient - Plot over line - $U_x/U_{x,mean}$

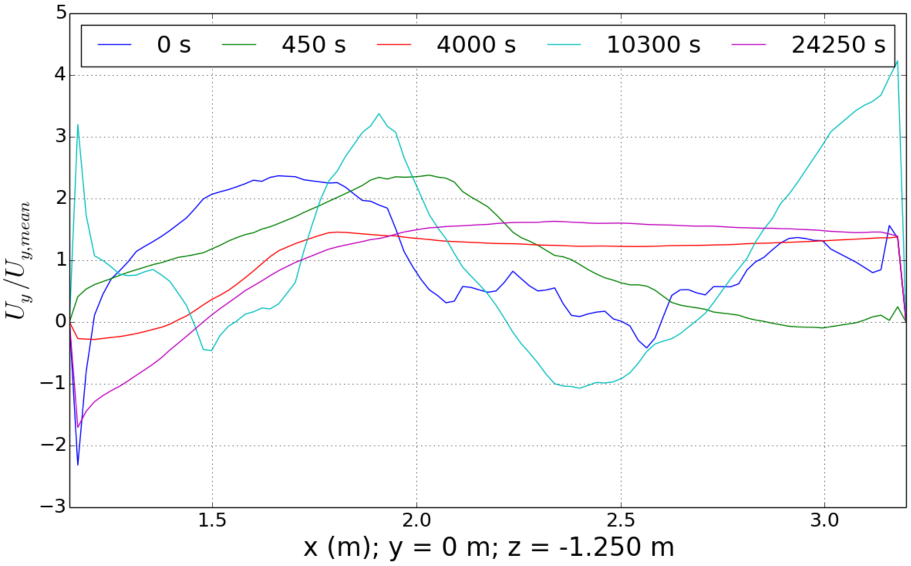

Fig. C.44: OpenFOAM: Hot pool - transient - Plot over line - $U_y/U_{y,mean}$

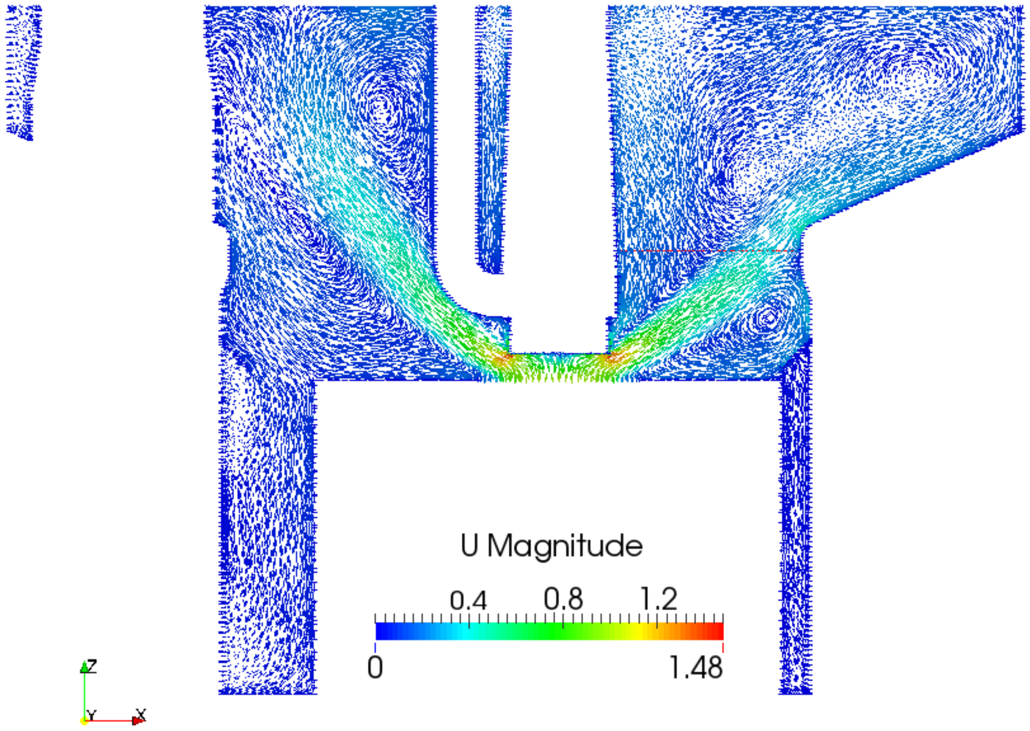

Fig. C.45: OpenFOAM: Hot pool - transient - Slice with glyphs ($0s$) - velocity field

Velocity over line - U_z

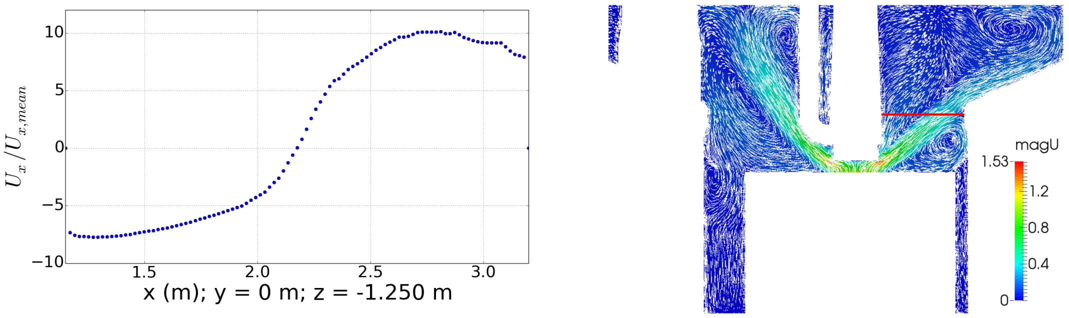

Fig. C.46: Dimensionless vertical velocity U_z at $0s$ (left) taken from red line (right)

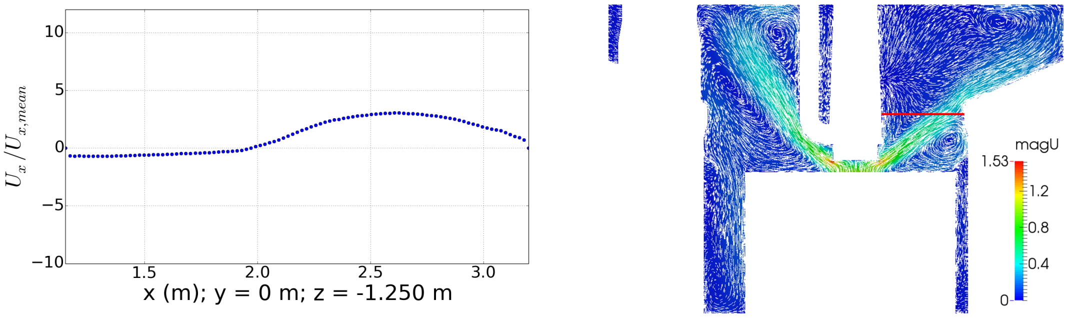

Fig. C.47: Dimensionless vertical velocity U_z at $450s$ (left) taken from red line (right)

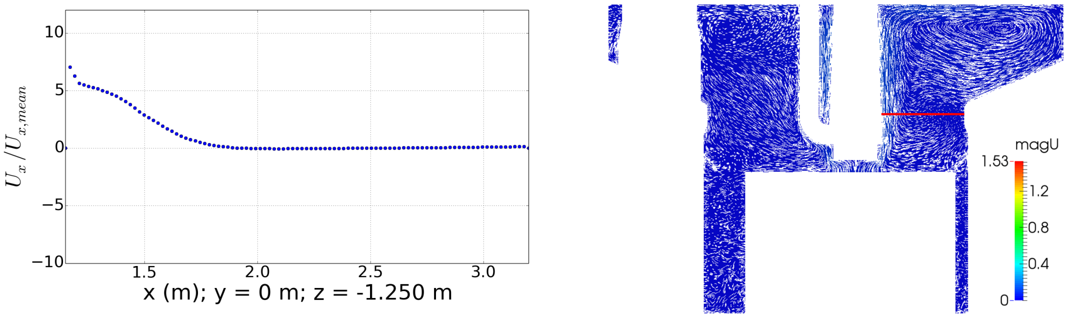

Fig. C.48: Dimensionless vertical velocity U_z at $4000s$ (left) taken from red line (right)

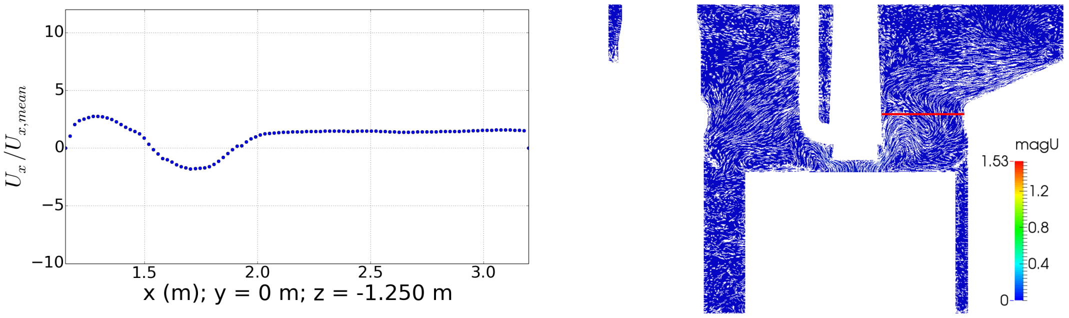

Fig. C.49: Dimensionless vertical velocity U_z at $10300s$ (left) taken from red line (right)

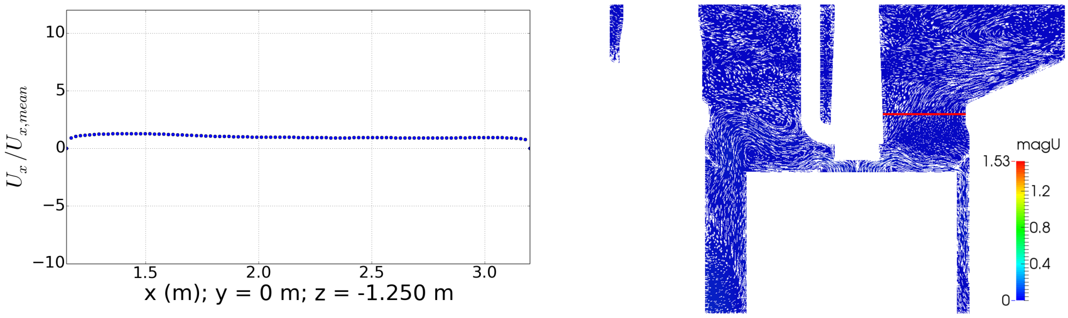

Fig. C.50: Dimensionless vertical velocity U_z at 24250s (left) taken from red line (right)

Temperature

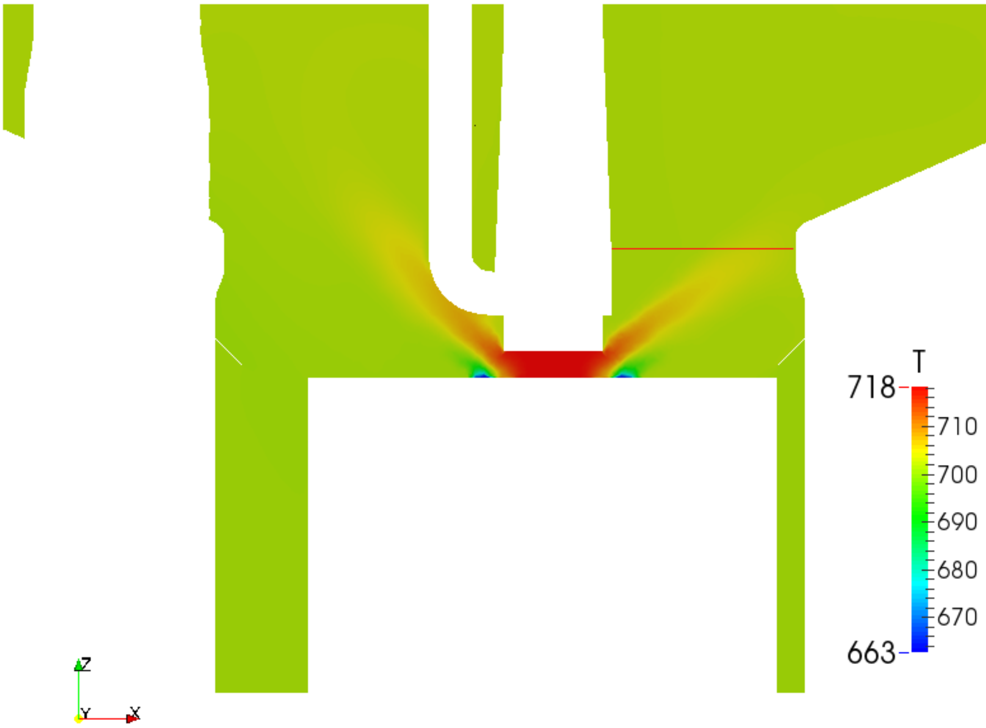

Fig. C.51: OpenFOAM: Hot pool - transient - Temperature field (0s) - velocity field

Fig. C.52: OpenFOAM: Hot pool - transient - Temperature field (0s) - velocity field

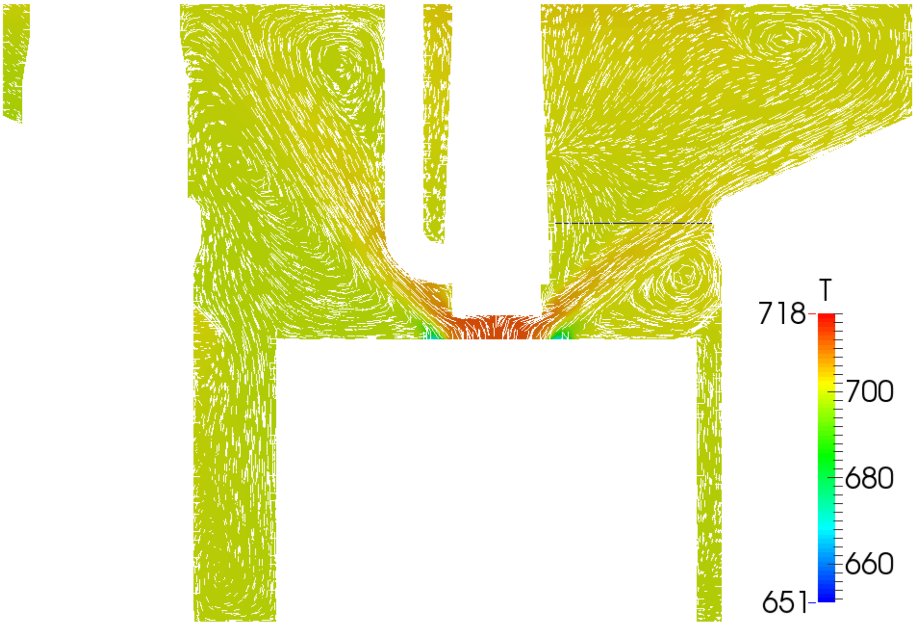

Fig. C.53: OpenFOAM: Hot pool - transient - Temperature field (450s) - velocity field

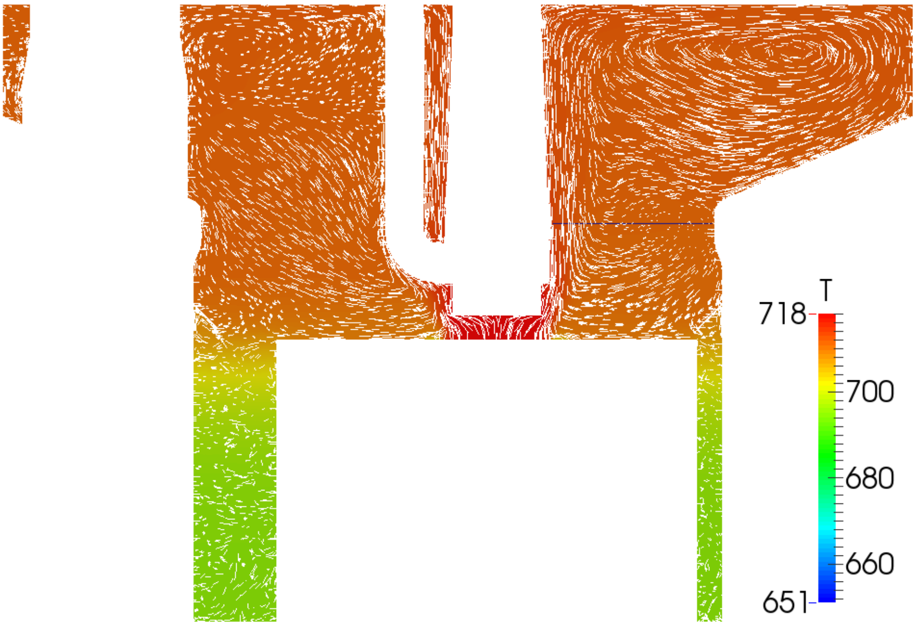

Fig. C.54: OpenFOAM: Hot pool - transient - Temperature field (4000s) - velocity field

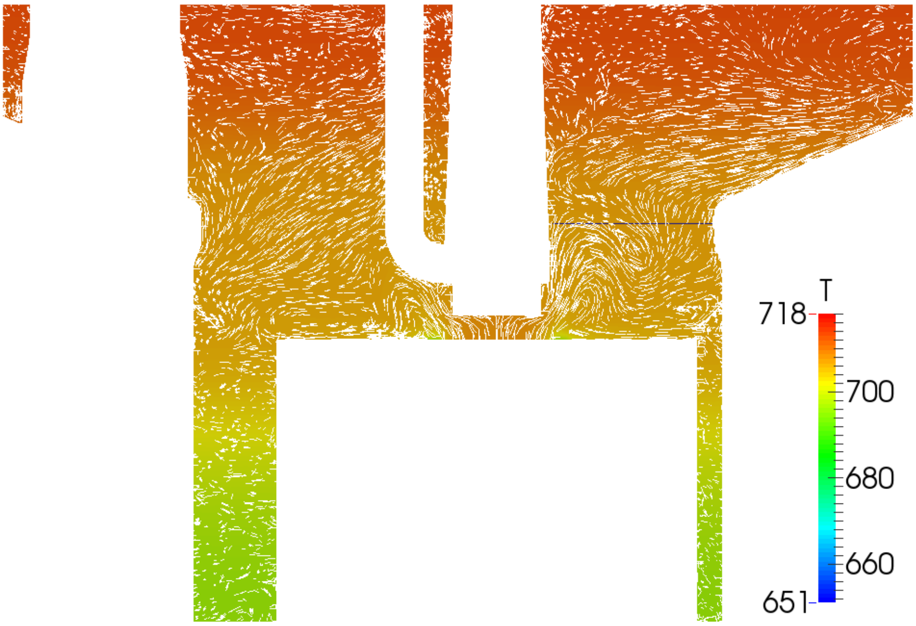

Fig. C.55: OpenFOAM: Hot pool - transient - Temperature field (10300s) - velocity field

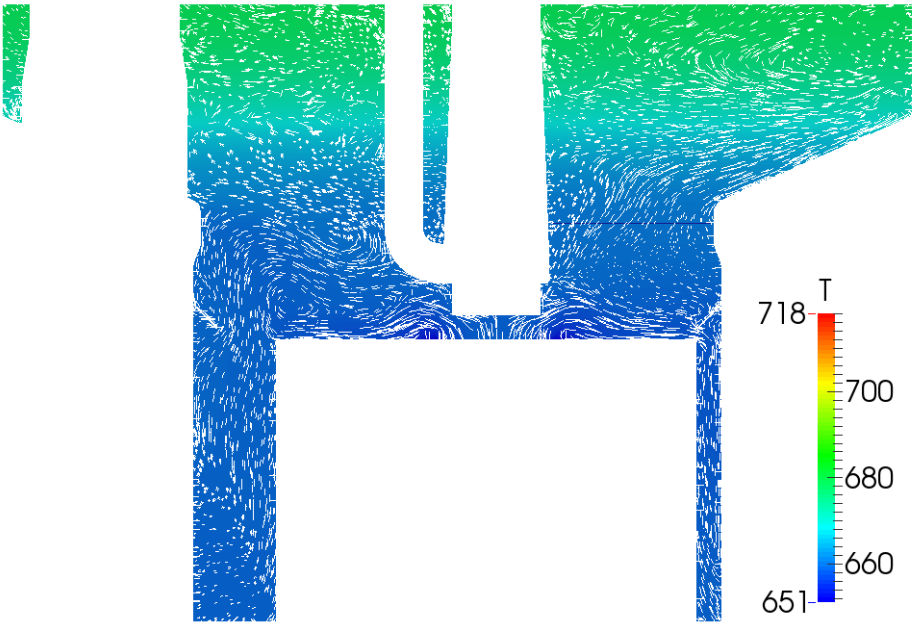

Fig. C.56: OpenFOAM: Hot pool - transient - Temperature field (24250s) - velocity field

Material properties

As functions for material properties in OpenFOAM must be given in explicit form (taylor rows), the polyfit toolbox by `Python` was used to create the polynomial funcitons.

Dynamic viscosity

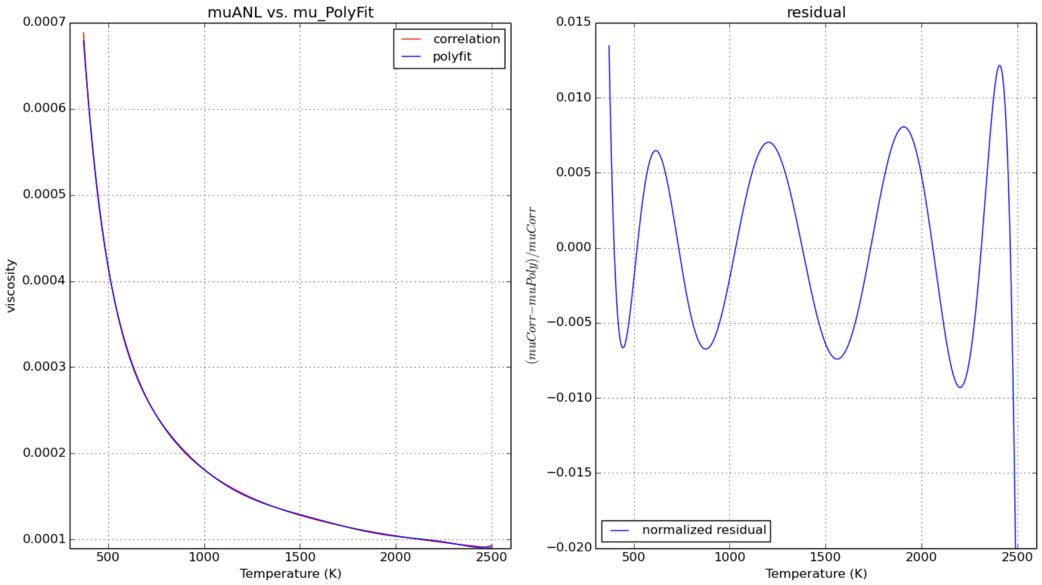

Fig. C.57: Material properties: dynamic viscosity - polyfit

Density

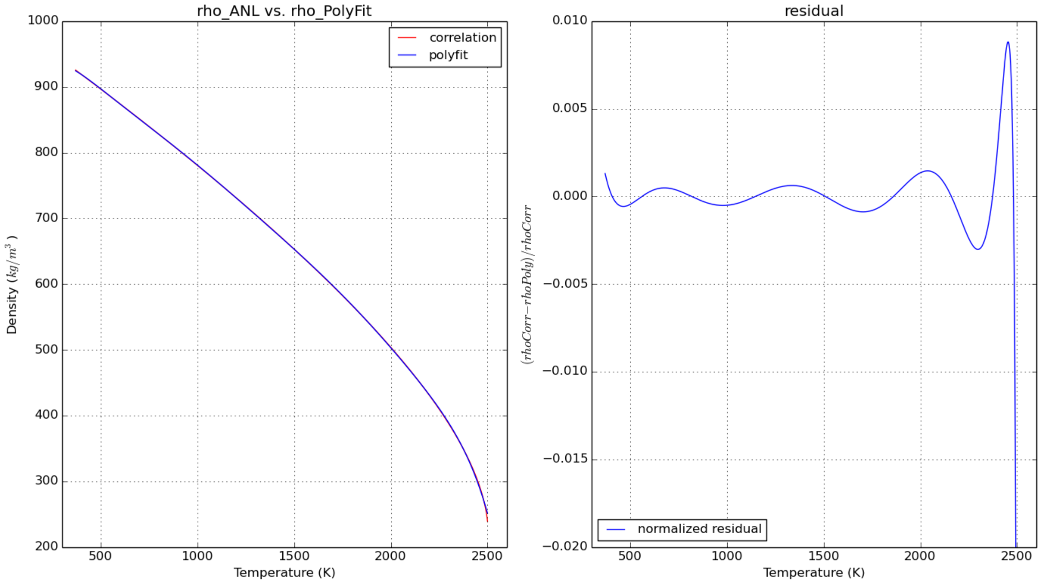

Fig. C.58: Material properties: density - polyfit

Heat capacity

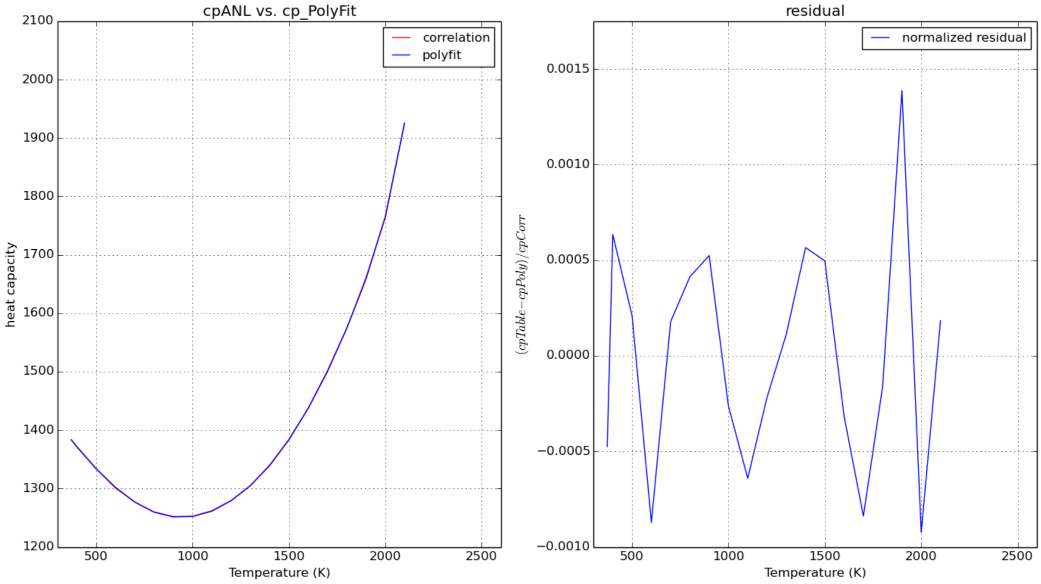

Fig. C.59: Material properties: heat capacity - polyfit

Heat conductivity

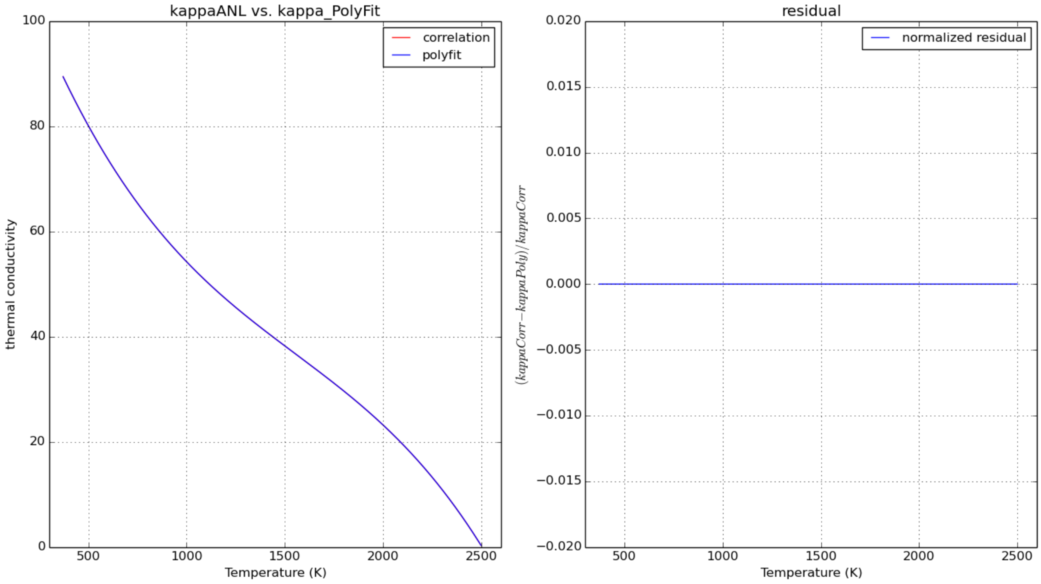

Fig. C.60: Material properties: heat conductivity - polyfit

D PHENIX Application case

Boundary conditions

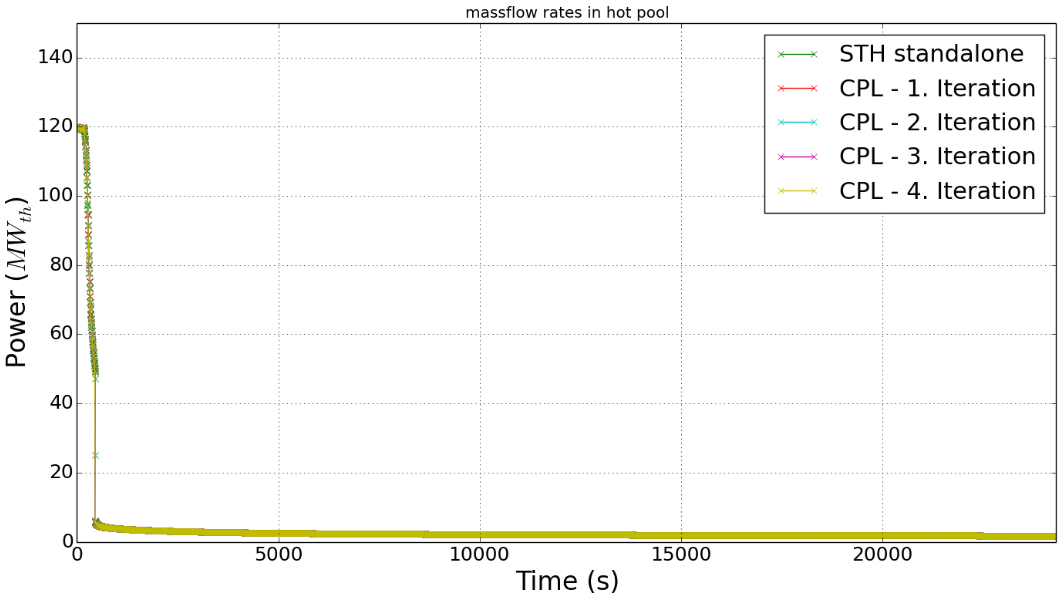

Fig. D.61: Application - boundary conditions: Thermal core power

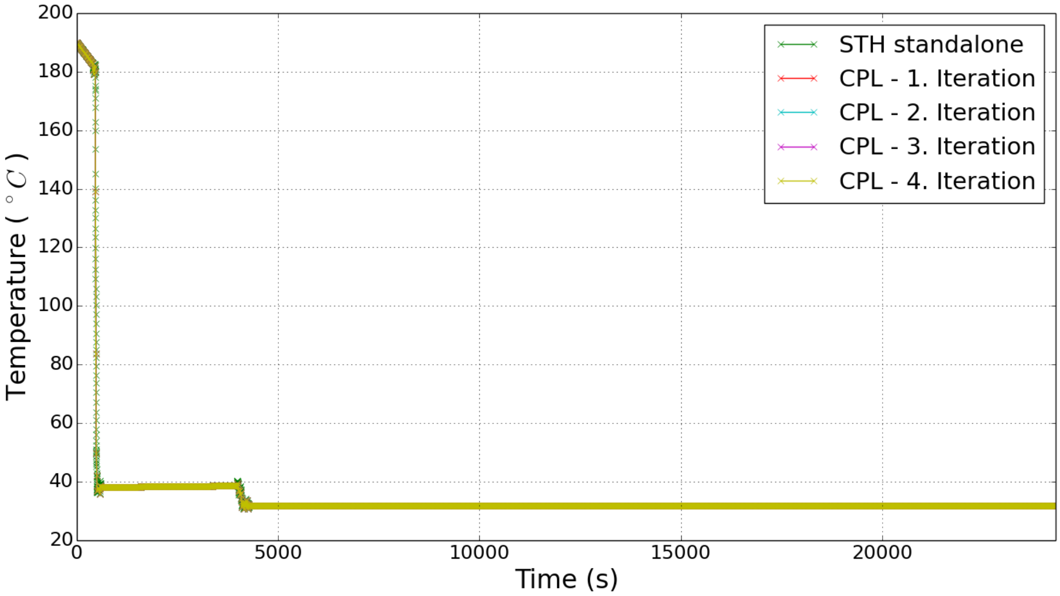

Fig. D.62: Application - boundary conditions: Secondary inlet massflow

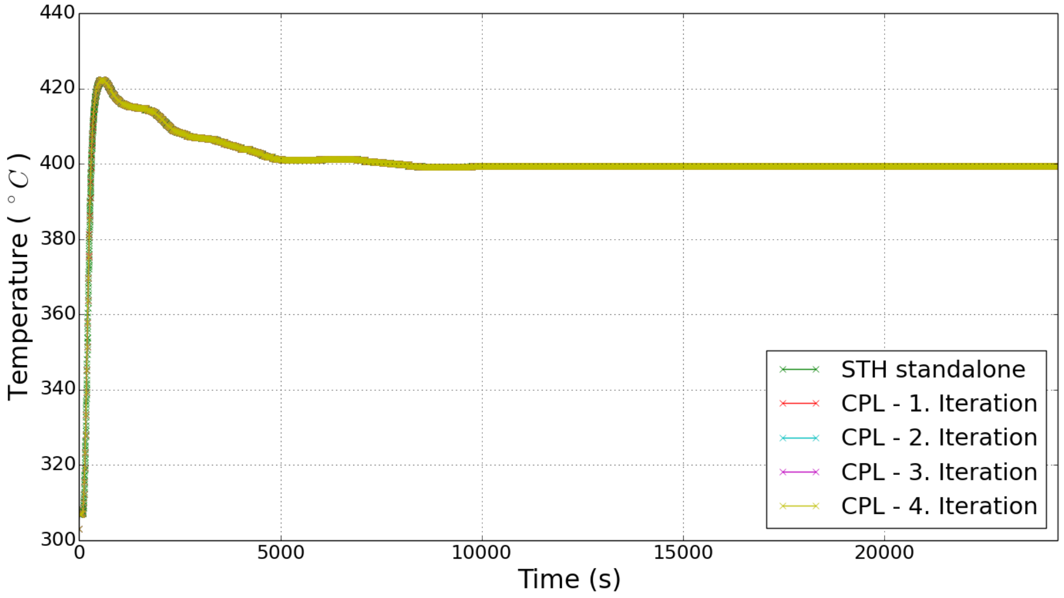

Fig. D.63: Application - boundary conditions: Secondary inlet temperature

Bibliography

[1] M. M. Abu-Khader. Recent advances in nuclear power: A review. *Progress in Nuclear Energy*, 51(2):225 – 235, 2009. ISSN 0149-1970. doi: http://dx.doi.org/10.1016/j.pnucene.2008.05.001. URL `http://www.sciencedirect.com/science/article/pii/S0149197008000851`.

[2] A. Adamantiades and I. Kessides. Nuclear power for sustainable development: Current status and future prospects. *Energy Policy*, 37(12):5149 – 5166, 2009. ISSN 0301-4215. doi: http://dx.doi.org/10.1016/j.enpol.2009.07.052. URL `http://www.sciencedirect.com/science/article/pii/S0301421509005436`.

[3] A. A. Amsden and F. H. Harlow. Transport of turbulence in numerical fluid dynamics. *Journal of Computational Physics*, 3(1):94 – 110, 1968. ISSN 0021-9991. doi: http://dx.doi.org/10.1016/0021-9991(68)90008-9. URL `http://www.sciencedirect.com/science/article/pii/0021999168900089`.

[4] D. L. Aumiller, E. T. Tomlinson, and R. C. Bauer. A coupled relap5-3d/cfd methodology with a proof-of-principle calculation. *Nuclear Engineering and Design*, 205(1–2):83 – 90, 2001. ISSN 0029-5493. doi: http://dx.doi.org/10.1016/S0029-5493(00)00370-8. URL `http://www.sciencedirect.com/science/article/pii/S0029549300003708`.

[5] H. Austregesilo, C. Bals, A. Hora, G. Lerchl, P. Romstedt, P. Schöffel, D. von der Cron, and F. Weyermann. *ATHLET - Models and Methods.* Gesellschaft für Anlagen- und Reaktorsicherheit, athlet mod 2.2 cycle a edition, July 2009.

[6] M. Azarian, M. Astegiano, M. Tenchine, M. Lacroix, and M. Vidard. Sodium thermal-hydraulics in the pool lmfbr primary vessel. *Nuclear Engineering and Design*, 124(3):417 – 430, 1990. ISSN 0029-5493. doi: http://dx.doi.org/10.1016/0029-5493(90)90305-H. URL `http://www.sciencedirect.com/science/article/pii/002954939090305H`.

[7] M. Baba. Fukushima accident: What happened? In *7th International Workshop on Ionizing Radiation Monitoring*, volume 55, pages 17 – 21, 2013. doi: http://dx.doi.org/10.1016/j.radmeas.2013.01.013. URL `http://www.sciencedirect.com/science/article/pii/S1350448713000267`.

[8] G. K. Batchelor. *An Introduction to Fluid Dynamics.* Cambridge University Press, Cambridge, 002 2000. ISBN 9780511800955. doi: http://dx.doi.org/10.1017/CBO9780511800955. URL `https://www.cambridge.org/core/books/an-introduction-to-fluid-dynamics/18AA1576B9C579CE25621E80F9266993`.

[9] R. Bavière, N. Tauveron, and E. Garré. System-cfd simulation of the phenix reactor natural circulation test. In Society [141]. ISBN 978-88-902391-2-0.

[10] R. Bavière, N. Tauveron, F. Perdu, E. Garré, and S. Li. A first system/cfd coupled simulation of a complete nuclear reactor transient using cathare2 and trio_u. preliminary validation on the phenix reactor natural circulation test. *Nuclear Engineering and Design*, 277:124 – 137, 2014. ISSN 0029-5493. doi: http://dx.doi.org/10.1016/j.nucengdes.2014.05.031. URL `http://www.sciencedirect.com/science/article/pii/S0029549314003197`.

[11] D. Bestion. System code models and capabilities. In A. Petruzzi, I. Tóth, and C. Vitanza, editors, *Seminar on the transfer of competence, knowledge and experience gained through CSNI activities in the field of thermal-hydraulics*, pages 81–106, University of Pisa (UNIPI), Italy, May 2008. OECD-NEA / UNIPI.

[12] V. M. Borishanskii and S. S. Kutateladze. Energomashinostroenie. Technical Report 6, Energomashinostroenie, 1957.

[13] V. M. Borishanskii, T. V. Zablotskaya, and N. I. Ivashchenko. Heat transfer by flow of metallic sodium in a tube. *Atomnaya Energiya*, 16(6):524 – 526, July 25 1963.

[14] V. M. Borishanskii, M. A. Gotovskii, and E. V. Firsova. Heat transfer to liquid metals in longitudinally wetted bundles of rods. *Atomnaya Energiya*, 26:549 – 552, 1969.

[15] M. Borsenberger. Analysis of pressure drop in liquid sodium cooled wire-wrapped fuel subassemblies with athlet code. Diplomarbeit, Karlsruhe Institute of Technology, September 2013.

[16] J. Boussinesq. *Essai sur la théorie des eaux courantes.* Imprimerie Nationale, Paris, 1877.

[17] G. Brumfiel. Nuclear proliferation special: We have the technology. *Nature*, 432 (7016):432–437, November 2004. ISSN 0028-0836. URL `http://dx.doi.org/10.1038/432432a`.

[18] E. Bubelis and M. Schikorr. Review and proposal for best fit of wire-wrapped fuel bundle friction factor and pressure drop predictions using various existing correlations. *Nuclear Engineering and Design*, 238(12):3299–3320, December 2008. ISSN 0029-5493. doi: 10.1016/j.nucengdes.2008.06.024. URL `http://www.sciencedirect.com/science/article/pii/S0029549308003762`.

[19] D. Butler. Energy: Nuclear power's new dawn. *Nature*, 429(6989):238–240, May 2004. ISSN 0028-0836. URL `http://dx.doi.org/10.1038/429238a`.

[20] Y. A. Çengel, J. M. Cimbala, and R. H. Turner. *Fundamentals of thermal-fluid sciences.* McGraw-Hill, New York, 4. ed. edition, 2012. ISBN 978-0-07-338020-9.

[21] B. Chanaron, C. Ahnert, N. Crouzet, V. Sanchez, N. Kolev, O. Marchand, S. Kliem, and A. Papukchiev. Advanced multi-physics simulation for reactor safety in the framework of the {NURESAFE} project. *Annals of Nuclear Energy*, 84:166–177, 2015. ISSN 0306-4549. doi: http://dx.doi.org/10.1016/j.anucene.2014.12.013. URL `http://www.sciencedirect.com/science/article/pii/S0306454914006616`.

[22] K. S. Chang, R. G. Akins, L. Burris Jr., and S. G. Bankoff. *Free convection of a low prandtl number fluid in contact with a uniformly heated vertical plate.* Argonne National Laboratory, January 1964. URL `http://hdl.handle.net/2027/mdp.39015078502492`.

[23] C. Chauliac, J. M. Aragonés, D. Bestion, D. G. Cacuci, N. Crouzet, F. P. Weiss, and M. A. Zimmermann. Nuresim – a european simulation platform for nuclear reactor safety: Multi-scale and multi-physics calculations, sensitivity and uncertainty analysis. *Nuclear Engineering and Design*, 241(9):3416 – 3426, 2011. ISSN 0029-5493. doi: http://dx.doi.org/10.1016/j.nucengdes.2010.09.040. URL `http://www.sciencedirect.com/science/article/pii/S0029549311001713`.

[24] P. Chellapandi, S. C. Chetal, and B. Raj. Thermal striping limits for components of sodium cooled fast spectrum reactors. *Nuclear Engineering and Design*, 239(12):2754 – 2765, 2009. ISSN 0029-5493. doi: http://dx.doi.org/10.1016/j.nucengdes.2009.08.014. URL `http://www.sciencedirect.com/science/article/pii/S002954930900404X`.

[25] H. Y. Chen and X. Cheng. The athlet-mf code and its application to heavy liquid metal cooled systems. Technical Report 7165, Forschungszentrum Karlsruhe, Karlsruhe, 2005.

[26] X. Cheng and N. Tak. Investigation on turbulent heat transfer to lead–bismuth eutectic flows in circular tubes for nuclear applications. *Nuclear Engineering and Design*, 236(4):385 – 393, 2006. ISSN 0029-5493. doi: http://dx.doi.org/10.1016/j.nucengdes.2005.09.006. URL `http://www.sciencedirect.com/science/article/pii/S0029549305003584`.

[27] X. Cheng, A. Batta, G. Bandini, F. Roelofs, K. Van Tichelen, A. Gerschenfeld, H. M. Prasser, A. Papukchiev, U. Hampel, and W. M. Ma. European activities on crosscutting thermal-hydraulic phenomena for innovative nuclear systems. *Nuclear Engineering and Design*, 290:1 – 12, 2014. ISSN 0029-5493. doi: http://dx.doi.org/10.1016/j.nucengdes.2014.11.007. URL `http://www.sciencedirect.com/science/article/pii/S0029549314005834`.

[28] S. W. Churchill. Friction factor equation spans all fluid-flow regimes. *Chemical Engineering Journal*, pages 91 – 92, 1977.

[29] S. W. Churchill and H. H. S. Chu. Correlating equations for laminar and turbulent free convection from a vertical plate. *International Journal of Heat and Mass Transfer*, 18:1323 – 1329, 1975.

[30] S. W. Churchill and H. Ozoe. Correlations for laminar forced convection with uniform heating in flow over a plate and in developing and fully developed flow in a tube. *Journal of Heat Transfer*, 95:78–84, 1973.

[31] S. W. Churchill and R. Usagi. A general expression for the correlation of rates of transfer and other phenomena. *AIChE Journal*, 18(6):1121 – 1128, November 1972. American Institute of Chemical Engineers (AIChE).

[32] C. F. Colebrook and C. M. White. Experiments with fluid friction in roughened pipes. *Proceedings of the Royal Society of London A: Mathematical, Physical and Engineering Sciences*, 161(906):367–381, 1937. ISSN 0080-4630. doi: 10.1098/rspa.1937.0150. URL `http://rspa.royalsocietypublishing.org/content/161/906/367`.

[33] U.S. DOE Nuclear Energy Research Advisory Committee and the Generation IV International Forum. A technology roadmap for generation iv nuclear energy systems. Technical report, U.S. DOE Nuclear Energy Research Advisory Committee and the Generation IV International Forum, December 2002.

[34] F. D'Auria and G. M. Galassi. Scaling in nuclear reactor system thermal-hydraulics. *Nuclear Engineering and Design*, 240(10):3267 – 3293, 2010. ISSN 0029-5493. doi: http://dx.doi.org/10.1016/j.nucengdes.2010.06.010. URL `http://www.sciencedirect.com/science/article/pii/S0029549310004280`.

[35] T.C. Doody and T.C. Jounger. Chemical engineering progress symposium series. *AIChE Journal*, 5:33, 1953.

[36] F. Durst. *Fluid mechanics : an introduction to the theory of fluid flows*. Springer, Berlin, 2008. ISBN 978-3-540-71342-5; 3-540-71342-5.

[37] O. E. Dwyer and P. S. Tu. Analytical study of heat transfer rates for parallel flow of liquid metals through tube bundles. part i. *Chem. Eng. Progr.*, 56(30), December 1961. URL `http://www.osti.gov/scitech/biblio/4056144`.

[38] E. R. G. Eckert. *Introduction to the Transfer of Heat and Mass*. McGraw-Hill Book Company, 1950.

[39] F. C. Engel, R. Markley, and A. Bishop. Laminar, transition and turbulent parallel flow pressure drop across wire-wrap-spaced rod bundles. *Nuclear science and engineering*, 69:290–296, 1979.

[40] D. English and T. Barret. Heat-transfer properties of mercury. In Institution of Mechanical Engineers (Great Britain); American Society of Mechanical Engineers, editor, *Proceedings of the General Discussion on Heat Transfer*, volume 13, page 496. London: Institution of Mechanical Engineers, September 1951.

[41] T. H. Fanning, J. W. Thomas, and Nuclear Engineering Division. Advances in coupled safety modeling using systems analysis and high-fidelity methods. Technical Report ANL-GENIV-134 TRN: US1004384, Argonne National Laboratory (ANL), May 2010. URL `http://www.osti.gov/scitech/servlets/purl/982349`.

[42] T. H. Fanning, J. E. Cahalan, F. E. Dunn, J. P. Herzog, A. M. White, R. A. Wigeland, R. B. Vilim, L. L. Briggs, J. Y. Ku, P. A. Pizzica, K. J. Miles, Kalimullah, T. Sofu, J. M. Kramer, and A. M. Tentner. The sas4a/sassys-1 safety analysis code system. Code Manual ANL/NE-12/4, Nuclear Engineering Division, Argonne National Laboratory (ANL), January 2012. URL `https://wiki.anl.gov/sas/Code_Manual`.

[43] H. Fenech. Chapter 1 - general considerations on thermal design and performance requirements of nuclear reactor cores. In Henri Fenech, editor, *Heat Transfer and Fluid Flow in Nuclear Systems*, pages 1 – 41. Pergamon, 1981. ISBN 978-0-08-027181-1. doi: http://dx.doi.org/10.1016/B978-0-08-027181-1.50006-X. URL `http://www.sciencedirect.com/science/article/pii/B978008027181150006X`.

[44] J. H. Ferziger and M. Perić. *Computational methods for fluid dynamics*. Springer, Berlin, 3 edition, 2002. ISBN 3-540-42074-6. URL `http://swbplus.bsz-bw.de/bsz095826459cov.htm;http://www.ulb.tu-darmstadt.de/tocs/100561322.pdf`. kart. : DM 99.90.

[45] J. K. Fink and L. Leibowitz. Thermodynamic and transport properties of sodium liquid and vapor. Technical Report ANL/RE-95/2, Argonne National Laboratory (ANL), January 1995.

[46] O. J. Foust. *Sodium - NaK Engineering Handbook*. Gordon and Breach, Science Publishers, Inc., 1970.

[47] Aaron J. Friedland and Charles F. Bonilla. Analytical study of heat transfer rates for parallel flow of liquid metals through tube bundles: Ii. *AIChE Journal*, 7(1): 107–112, 1961. ISSN 1547-5905. doi: 10.1002/aic.690070125. URL `http://dx.doi.org/10.1002/aic.690070125`.

[48] L. I. Gel'man. Teploenergetika 3. Technical Report 3, Teploenergetika, 1958. p.47.

[49] V. H. Gräber and M. Rieger. Experimentelle untersuchung des wärmeübergangs an flüssigmetall (nak) in parallel durchströmten rohrbündeln bei konstanter und exponentieller wärmeflussdichteverteilung. *Atomkernenergie (ATKE)*, 19:23–40, 1972.

[50] S. Grape, S. J. Svärd, C. Hellesen, P. Jansson, and M. Åberg Lindell. New perspectives on nuclear power–generation {IV} nuclear energy systems to strengthen nuclear non–proliferation and support nuclear disarmament. *Energy Policy*, 73:815–819, 2014. ISSN 0301-4215. doi: http://dx.doi.org/10.1016/j.enpol.2014.06.026. URL `http://www.sciencedirect.com/science/article/pii/S030142151400398X`.

[51] E. M. Gregg and J. Sparrow. Laminar free convection from a vertikal plate with uniform surface heat flux. *Trans ASME*, 78, 1956.

[52] G. Grötzbach. *Direkte numerische Simulation turbulenter Geschwindigkeits-, Druck-, und Temperaturfelder bei Kanalströmungen*. PhD thesis, Karlsruhe, Univ., Fak. für Maschinenbau, 1977. Auch als: KFK-Bericht / Gesellschaft für Kernforschung ; 2426 Karlsruhe, Univ., Diss., 1977.

[53] G. Grötzbach. Challenges in low-prandtl number heat transfer simulation and modelling. *Nuclear Engineering and Design*, 264(0):41 – 55, 2013. ISSN 0029-5493. doi: http://dx.doi.org/10.1016/j.nucengdes.2012.09.039. URL `http://www.sciencedirect.com/science/article/pii/S0029549313000952`. SI:NURETH-14.

[54] C. Hirsch. *Numerical Computation of Internal and External Flows: The Fundamentals of Computational Fluid Dynamics*, volume 1. Butterworth-Heinemann, 2007.

[55] J. P. Holman. *Heat transfer*. McGraw-Hill, New York, 5 edition, 1981. ISBN 0-07-029618-9.

[56] K. Huber and J. W. Thomas. Coupled calculations of SAS4A/SASSYS-1 and STAR-CCM+ for the SHRT-45R test in EBR-II. In American Nuclear Society, editor, *16th International Meeting on Nuclear Reactor Thermal Hydraulics (NURETH-16)*, 2015. ISBN: 978-0-89448-722-4.

[57] IAEA. Status of liquid metal cooled fast reactor technology. Technical report, International Atomic Energy Agency (IAEA), April 1999. URL `http://www-pub.iaea.org/books/IAEABooks/5374/Status-of-Liquid-Metal-Cooled-Fast-Reactor-Technology`.

[58] *Use and Development of Coupled Computer Codes for the Analysis of Accidents at Nuclear Power Plants*, number IAEA-TECDOC-1539, November 2003. IAEA. URL `http://www-pub.iaea.org/MTCD/publications/PDF/te_1539_web.pdf`.

[59] IAEA. Benchmark analyses on the natural circulation test performed during the phenix end-of-life experiments. IAEA TECDOC SERIES IAEA-TECDOC-1703, IAEA, 2013.

[60] S. E. Isakoff and T. B. Drew. General discussion of heat transfer. *Inst. Mech. Eng. and ASME*, page 405, 1951.

[61] R. I. Issa. Solution of the implicitly discretised fluid flow equations by operator-splitting. *Journal of Computational Physics*, 62(1):40 – 65, 1986. ISSN 0021-9991. doi: http://dx.doi.org/10.1016/0021-9991(86)90099-9. URL `http://www.sciencedirect.com/science/article/pii/0021999186900999`.

[62] J. D. Jackson. Turbulent mixed convection heat transfer to liquid sodium. *Int. J. Heat & Fluid Flow*, 1983.

[63] W. Jaeger, J. Perez Manes, U. Imke, J. J. Escalante, and V. Sanchez Espinoza. Validation and comparison of two-phase flow modeling capabilities of cfd, sub channel and system codes by means of post-test calculations of {BFBT} transient tests. *Nuclear Engineering and Design*, 263(0):313 – 326, 2013. ISSN 0029-5493. doi: http://dx.doi.org/10.1016/j.nucengdes.2013.06.002. URL `http://www.sciencedirect.com/science/article/pii/S0029549313002926`.

[64] H. Jasak. *Error analysis and estimation for the Finite Volume method with applications to fluid flows.* PhD thesis, Imperial College, University of London, 1996.

[65] M. Jeltsov, K. Kööp, P. Kudinov, and W. Villanueva. Development of a domain overlapping coupling methodology for sth/cfd analysis of heavy liquid metal thermal-hydraulics. In Society [141]. Pisa, Italy.

[66] H. A. Johnson, J. P. Hartnett, and W. J. Clabaugh. Heat transfer to molten lead-bismuth eutectic in turbulent pipe flow. *Transactions of the American Society of Mechanical Engineers (Trans. ASME)*, 75:1191 – 1198, 1953.

[67] S. Kakaç, editor. *Handbook of single-phase convective heat transfer.* A Wiley-Interscience publication. Wiley, New York, 1987. ISBN 0-471-81702-3. URL `http://www.gbv.de/dms/ilmenau/toc/025544713.PDF`.

[68] A. A. Kanaev. Sovetskoe kolotyrbostroenie 2. *Sovetskoe Kolotyrbostroenie 2*, 2, 1953.

[69] M. S. Kazimi and M. D. Carelli. Clinch river breeder reactor plant heat transfer correlation for analysis of crbrp assemblies. Topical report, Westinghouse, 1976.

[70] J. E. Kelly. Generation IV international forum: A decade of progress through international cooperation. *Progress in Nuclear Energy*, 77:240 – 246, November 2014. ISSN 0149-1970. doi: http://dx.doi.org/10.1016/j.pnucene.2014.02.010. URL `http://www.sciencedirect.com/science/article/pii/S0149197014000419`.

[71] A. N. Kolmogorov. The local structure of turbulence in incompressible viscous fluid for very large reynolds numbers. *Proceedings of the Royal Society of London A: Mathematical, Physical and Engineering Sciences*, 434(1890):9–13, 1991. ISSN 0962-8444. doi: 10.1098/rspa.1991.0075. URL `http://rspa.royalsocietypublishing.org/content/434/1890/9`.

[72] M. I. Kornev. Teploenergetika. *Teploenergetika*, 4:44, 1955.

[73] S. S. Kutateladze, V. M. Borishanskii, and I. I. Novikov. Heat transfer in liquid metals. *The Soviet Journal of Atomic Energy*, 4(5):555–571, 1958. doi: 10.1007/BF01497931. URL `http://dx.doi.org/10.1007/BF01497931`.

[74] B. E. Launder and B. I. Sharma. Application of the energy-dissipation model of turbulence to the calculation of flow near a spinning disc. *Letters in Heat and Mass Transfer*, 1(2):131 – 137, 1974. ISSN 0094-4548. doi: http://dx.doi.org/10.1016/0094-4548(74)90150-7. URL `http://www.sciencedirect.com/science/article/pii/0094454874901507`.

[75] B. E. Launder and D. B. Spalding. The numerical computation of turbulent flows. *Computer Methods in Applied Mechanics and Engineering*, 3(2):269 – 289, 1974. ISSN 0045-7825. doi: http://dx.doi.org/10.1016/0045-7825(74)90029-2. URL `http://www.sciencedirect.com/science/article/pii/0045782574900292`.

[76] E. Laurien and H. Oertel. *Numerische Strömungsmechanik : Grundgleichungen und Modelle - Lösungsmethoden - Qualität und Genauigkeit*. SpringerLink : Bücher. Springer Vieweg, Wiesbaden, 5. edition, 2013. ISBN 978-3-658-03145-9. URL `http://dx.doi.org/10.1007/978-3-658-03145-9`.

[77] J. C. Lefèvre, C. H. Mitchell, and G. Hubert. European fast reactor design. *Nuclear Engineering and Design*, 162(2–3):133 – 143, 1996. ISSN 0029-5493. doi: http://dx.doi.org/10.1016/0029-5493(95)01141-2. URL `http://www.sciencedirect.com/science/article/pii/0029549395011412`.

[78] G. Lerchl and H. Austregesilo. *ATHLET mod 2.1 cycle A - User's Manual*. Gesellschaft für Anlagen- und Reaktorsicherheit, grs-p-1 / vol. 1, rev. 4 edition, July 2006.

[79] G. Lerchl and H. Deitenbeck. *ATHLET Mod 2.2 Cycle A - Input Data Description*. Gesellschaft für Anlagen- und Reaktorsicherheit, July 2009.

[80] G. Lerchl, H. Austregesilo, P. Schöffel, D. von der Cron, and F. Weyermann. *ATHLET - User's Manual*. Gesellschaft für Anlagen- und Reaktorsicherheit, mod 2.2 cycle a edition, July 2009.

[81] S. Levy. The important role of thermal hydraulics in 50 years of nuclear power applications. *Nuclear Engineering and Design*, 149(1–3):1 – 10, 1994. ISSN 0029-5493. doi: http://dx.doi.org/10.1016/0029-5493(94)90269-0. URL `http://www.sciencedirect.com/science/article/pii/0029549394902690`.

[82] G. Locatelli, M. Mancini, and N. Todeschini. Generation {IV} nuclear reactors: Current status and future prospects. *Energy Policy*, 61(0):1503 – 1520, 2013. ISSN 0301-4215. doi: http://dx.doi.org/10.1016/j.enpol.2013.06.101. URL `http://www.sciencedirect.com/science/article/pii/S0301421513006083`.

[83] A. N. Lozhkin and A. A. Kanaev. Binary installations [in russian]. *MAShGIZ*, 1946.

[84] B. Lubarsky and S. J. Kaufman. Review of experimental investigation of liquid metal heat transfer. Technical Report 1270, National Advisory Committee for Aeronautics. Lewis Flight Propulsion Lab., March 1 1956. URL `http://digital.library.unt.edu/ark:/67531/metadc57490/`.

[85] R. N. Lyon. *Heat Transfer at High Heat Fluxes in Confined Spaces*. PhD thesis, University of Michigan, Ann Arbor, 1949.

[86] R. N. Lyon. Liquid metal heat transfer coefficients. *Chemical Engineering Progress*, 47:75–79, 1951.

[87] J. Mahaffy, B. Chung, F. Dubois, F. Ducros, E. Graffard, M. Heitsch, M. Henriksson, E. Komen, F. Moretti, T. Morii, P. Mühlbauer, U. Rohde, M. Scheuerer, B. L. Smith, C. Song, T. Watanabe, and G. Zigh. Best practice guidelines for the use of cfd in nuclear reactor safety applications. Technical report, OECD, 2007.

[88] M. W. Maresca and O. E. Dwyer. Heat transfer of mercury flowing in-line through a bundle of circular rods. *Transactions of the ASME series C. Journal of Heat Transfer*, 86:180 – 186, 1964.

[89] T. Maric, J. Höpken, and K. Mooney. *The OpenFOAM technology primer*. Sourceflux, [s.l.], 1. publ. edition, 2014. ISBN 978-3-00-046757-8.

[90] R Markley and F Engel. LMFBR blanket assembly heat transfer and hydraulic test data evaluation. In *Meeting of Thermodynamics of FBR Fuel Subassemblies under Nominal and Non-Nominal Operating Conditions*, pages 229–253, 1978.

[91] K. Marten, S. Yonekawa, and H. Hoffmann. Experiments and correlations of pressure loss coefficients for hexagonal arranged rod bundles (P/D $>$ 1.02) with helical wire spacers in laminar and turbulent flows. Forschungsbericht KFK4038, Kernforschungszentrum Karlsruhe, Institut für Reaktobauelemente, 1987.

[92] R. C. Martinelli. Heat transfer in molten metals. *Transactions of the ASME*, 69:947 – 959, 1947.

[93] M. A. Mikheev. *Heat Transfer Principles [in Russian]*. Gosenergoizdat, 1956.

[94] M. A. Mikheev, V. A. Baum, K. D. Voskresenskii, and O. S. Fedinskii. Coll: Reactor building and reactor theory [in russian]. Technical report, Izv. AN SSSR, 1955. p. 139.

[95] K. Mikityuk. Heat transfer to liquid metal: Review of data and correlations for tube bundles. *Nuclear Engineering and Design*, 239(4):680 – 687, 2009. ISSN 0029-5493. doi: http://dx.doi.org/10.1016/j.nucengdes.2008.12.014. URL `http://www.sciencedirect.com/science/article/pii/S0029549308006316`.

[96] P. Moin and K. Mahesh. Direct numerical simulation: A tool in turbulence research. *Annual review of fluid mechanics*, 30:539–578, 1998. ISSN 0066-4189. doi: 10.1146/annurev.fluid.30.1.539.

[97] S. Moriya, N. Tanaka, N. Katano, and A. Wada. Effects of Reynolds number and Richardson number on thermal stratification in hot plenum. *Nuclear Engineering and Design*, 99(0):441 – 451, 1987. ISSN 0029-5493. doi: http://dx.doi.org/10.1016/0029-5493(87)90140-3. URL `http://www.sciencedirect.com/science/article/pii/0029549387901403`.

[98] B. R. Munson, D. F. Young, T. H. Okiishi, and W. W. Huebsch. *Fundamentals of fluid mechanics 6th edition*. Wiley, New York, 6. edition, 2010. ISBN 978-0-470-39881-4. URL `http://swbplus.bsz-bw.de/bsz308527593cov.htm`.

[99] P. A. Nikrityuk. *Computational thermo-fluid dynamics : in materials science and engineering*. Wiley-VCH, Weinheim, 2011. ISBN 978-3-527-33101-7. URL `http://swbplus.bsz-bw.de/bsz349771367cov.htm`.

[100] H.C. No and M.S. Kazimi. An investigation of the physical and numerical foundations of two-fluid representation of sodium boiling with applications to lmfbr experiments. Technical report, Cambridge, Mass. : Massachusetts Institute of Technology, Energy Laboratory, 1983. URL `http://hdl.handle.net/1721.1/60581`.

[101] E. H. Novendstern. Turbulent flow pressure drop model for fuel rod assemblies utilizing a helical wire-wrap spacer system. *Nuclear Engineering and Design*, 22: 19–27, 1972.

[102] I. I. Novikov, A. N. Solovyev, E. M. Khabakhpasheva, V. A. Gruzdev, A. I. Pridantsev, and M. Y. Vasenina. Heat transfer and thermophysical properties of molten alkali metals. *The Soviet Journal of Atomic Energy*, 1(4):545–560, 1956. ISSN 0038-531x. doi: 10.1007/BF01479856. URL `http://dx.doi.org/10.1007/BF01479856`.

[103] H. Oertel jr. *Prandtl - Führer durch die Strömungslehre : Grundlagen und Phänomene*. SpringerLink : Bücher. Springer Vieweg, Wiesbaden, 13. edition, 2012. ISBN 978-383-48231-5-1. doi: http://dx.doi.org/10.1007/978-3-8348-2315-1.

[104] Division of Risk Assessment and Special Projects. *TRACE V5.0 USER'S MANUAL - Volume 1: Input Specification*. Office of Nuclear Regulatory Research U. S. Nuclear Regulatory Commission, Washington, DC 20555-0001, v5.0 edition, 2015. URL `http://pbadupws.nrc.gov/docs/ML1200/ML120060239.pdf`.

[105] Division of Risk Assessment and Special Projects. *TRACE V5.0 USER'S MANUAL - Volume 2: Modeling Guidelines*. Office of Nuclear Regulatory Research U. S. Nuclear Regulatory Commission, Washington, DC 20555-0001, v5.0 edition, 2015. URL `http://pbadupws.nrc.gov/docs/ML0717/ML071720510.pdf`.

[106] Division of Risk Assessment and Special Projects. *TRACE V5.0 THEORY MANUAL - Field Equations, Solution Methods and Physical Models*. Office of Nuclear Regulatory Research U. S. Nuclear Regulatory Commission, Washington, DC 20555-0001, v5.0 edition, 2015. URL `http://pbadupws.nrc.gov/docs/ML0710/ML071000097.pdf`.

[107] A. Omoto. The accident at tepco's fukushima-daiichi nuclear power station: What went wrong and what lessons are universal? *Nuclear Instruments and Methods in Physics Research Section A: Accelerators, Spectrometers, Detectors and Associated Equipment*, 731(0):3 – 7, 2013. ISSN 0168-9002. doi: http://dx.doi.org/10.1016/j.nima.2013.04.017. URL `http://www.sciencedirect.com/science/article/pii/S0168900213004129`.

[108] *OpenFOAM v2.3.0 Documentation*. OpenFOAM Foundation, February 2015. URL `http://www.openfoam.org/archive/2.3.0/docs/`.

[109] I. Otic, G. Grötzbach, and M. Woerner. Analysis and modelling of the temperature variance equation in turbulent natural convection for low-prandtl-number fluids. *Journal of Fluid Mechanics*, 525:237–261, 2 2005. ISSN 1469-7645. doi: 10.1017/S0022112004002733. URL `http://journals.cambridge.org/article_S0022112004002733`.

[110] A. Papukchiev. Weiterentwicklung und Validierung von CFX für alternative Reaktorkonzepte. Technical Report GRS-A-3622, Gesellschaft für Anlagen- und Reaktorsicherheit, Forschungszentrum, 85748 Garching b. München, August 2011. URL `http://www.grs.de/sites/default/files/pdf/GRS-A-3622.pdf`.

[111] A. Papukchiev and G. Lerchl. Extension of the simulation capabilities of the 1D system code ATHLET by coupling with the 3D software package ANSYS CFX. In *Proceedings of the 13th international topical meeting on nuclear reactor thermal hydraulics (NURETH-13)*, volume 43 of *4*. American Nuclear Society, October 2009. Japan.

[112] A. Papukchiev and G. Lerchl. Development and implementation of different schemes for the coupling of the system code athlet with the 3d cfd program ansys cfx. In Y. Hassan, X. Cheng, and X. Liu, editors, *Proceedings of the 8th International Topical Meeting on Nuclear Thermal-Hydraulics, Operation and Safety (NUTHOS-8)*, volume 249, August 2010. ISBN: 978-0-89448-722-4.

[113] S. V. Patankar. *Numerical heat transfer and fluid flow*. Series in computational and physical processes in mechanics and thermal sciences. Hemisphere Publ. Corp., New York, 1980. ISBN 0-89116-522-3; 978-0-89116-522-4.

[114] A. Petruzzi and F. D'Auria. Thermal-hydraulic system codes in nulcear reactor safety and qualification procedures. *Science and Technology of Nuclear Installations*, 2008.

[115] W. Pfrang and D. Struwe. Assessment of correlations for heat transfer to the coolant for heavy liquid metal cooled core designs. Technical Report 7352, Karlsruhe : Forschungszentrum Karlsruhe, Karlsruhe, 2007. URL `http://bibliothek.fzk.de/zb/berichte/FZKA7352.pdf`.

[116] D. Pialla, D. Tenchine, P. Gauthé, and A. Vasile. Natural convection test in phenix reactor and associated cathare calculation. In *The 14th International Topical Meeting on Nuclear Reactor Thermalhydraulics (NURETH-14)*. American Nuclear Society, September 2011.

[117] U. Piomelli. Large-eddy simulation: achievements and challenges. *Progress in Aerospace Sciences*, 35(4):335 – 362, 1999. ISSN 0376-0421. doi: http://dx.doi.org/10.1016/S0376-0421(98)00014-1. URL `http://www.sciencedirect.com/science/article/pii/S0376042198000141`.

[118] R. H. Pletcher, J. C. Tannehill, and D. A. Anderson. *Computational fluid mechanics and heat transfer*. Series in computational and physical processes in mechanics and thermal sciences. CRC Press, 3. edition, 2013. ISBN 978-1-59169-037-5.

[119] S. B. Pope. *Turbulent flows*. Cambridge University Press, Cambridge, 1. publ., 9. print. edition, 2011. ISBN 978-0-521-59886-6.

[120] V. H. Ransom, J. A. Trapp, R. J. Wagner, P. D. Bayless, V. T. Berta, K. E. Carlson, C. B. Davis, J. E. Fisher, C. D. Fletcher, E. C. Johnsen, G. W. Johnsen, H. H. Kuo, N. S. Larson, M. A. Lintner, G. L. Mesina, C. S. Miller, G. A. Mortensen, P. E. Murray, C. E. Nielson, R. B. Nielson, S. Paik, R. A. Riemke, A. S L. Shieh, R. R. Schultz, R. W. Shumway, C. E. Slater, S. M. Sloan, J. E. Tolli, and W. L. Weaver. *ATHENA Code Manual, Volume I: Code Structure, System Models and Solution Methods*. Idaho National Laboratory, Idaho Falls, Idaho 83415, ineel-ext-98-00834, volume i, revision 2.3 edition, 2005. URL `http://www4vip.inl.gov/relap5/r5manuals/ver_2_4/vol1_v2_4.pdf`.

[121] M. Rappaz, M. Bellet, and M. Deville. *Numerical modeling in materials science and engineering*, volume 32 of *Springer Series in Computational Mathematics*. Springer-Verlag, Berlin, 1 edition, 2003. ISBN 978-3-540-42676-9. doi: http://dx.doi.org/10.1007/978-3-642-11821-0. URL `http://swbplus.bsz-bw.de/bsz102106843inh.htm`.

[122] K. Rehme. Pressure drop performance of rod bundles in hexagonal arrangements. *International Journal of Heat and Mass Transfer*, 15(12):2499 – 2517, 1972. ISSN 0017-9310. doi: http://dx.doi.org/10.1016/0017-9310(72)90143-3. URL `http://www.sciencedirect.com/science/article/pii/0017931072901433`.

[123] L. F. Richardson. *Weather prediction by numerical process*. Cambridge University Press, 2007.

[124] W. M. Rohsenow, J. P. Harnett, and Y. I. Cho. *Handbook of heat transfer*. McGraw-Hill, New York [u.a.], 1973. ISBN 0-07-053576-0.

[125] J. H. Rust. A parametric analysis of lyon's integral equation for liquid-metal heat transfer coefficients. *Nuclear Engineering and Design*, 16, 1971.

[126] P. Sagaut. *Large eddy simulation for incompressible flows : an introduction*. Scientific computation. Springer, Berlin, 3. edition, 2006. ISBN 3-540-26344-6; 978-3-540-26344-9. URL `http://deposit.ddb.de/cgi-bin/dokserv?id=2647693&prov=M&dok_var=1&dok_ext=htm`.

[127] P. Saha, N. Aksan, J. Andersen, J. Yan, J. P. Simoneau, L. Leung, F. Bertrand, K. Aoto, and H. Kamide. Issues and future direction of thermal-hydraulics research and development in nuclear power reactors. *Nuclear Engineering and Design*, 264:3 – 23, 2013. ISSN 0029-5493. doi: http://dx.doi.org/10.1016/j.nucengdes.2012.07.023. URL `http://www.sciencedirect.com/science/article/pii/S0029549313000988`.

[128] Y. Sakamoto, J.-C. Garnier, J. Rouault, C. Grandy, T. Fanning, R. Hill, Y. Chikazawa, and S. Kotake. Selection of sodium coolant for fast reactors in the us, france and japan. *Nuclear Engineering and Design*, 254(0):194 – 217, 2013. ISSN 0029-5493. doi: http://dx.doi.org/10.1016/j.nucengdes.2012.09.009. URL `http://www.sciencedirect.com/science/article/pii/S0029549312004906`.

[129] J.-F. Sauvage. *Phenix - 30 Years Of History: The Heart Of A Reactor*. Electricite de France (EDF), 2004.

[130] H. Schade and E. Kunz, editors. *Strömungslehre*. De-Gruyter-Lehrbuch. De Gruyter, Berlin, 3. edition, 2007. ISBN 978-3-11-020680-7. URL `http://www.reference-global.com/isbn/978-3-11-018972-8`.

[131] F. G. Schmitt. About boussinesq's turbulent viscosity hypothesis: historical remarks and a direct evaluation of its validity. *Comptes Rendus Mécanique*, 335(9–10):617 – 627, 2007. ISSN 1631-0721. doi: http://dx.doi.org/10.1016/j.crme.2007.08.004. URL `http://www.sciencedirect.com/science/article/pii/S1631072107001386`.

[132] P. Schreiber. Implementation of heat transfer correlations of liquid sodium in athlet. Bachelor thesis, Karlsruhe Institute of Technology, Institut für Fusionstechnologie und Reaktortechnik (IFRT), Kaiserstr. 12, Octobre 2013.

[133] R. R. Schultz, W. L. Weaver, A. M. Ougouag, and W. A. Wieselquist. Validating and verifying a new thermal-hydraulic analysis tool. In *10th International Conference on Nuclear Engineering*, pages 749 – 756. American Society of Mechanical Engineers, 2002.

[134] R. A. Seban and T. T. Shimazaki. Heat transfer to a fluid flowing turbulent in a smooth pipe with walls at constant temperature. *Transactions of the ASME*, 73:803 – 809, May 1951.

[135] J. P. Serpantie, J. P. Debaene, B. Purslow, H. W. Hammers, and M. Cinotti. *Progress in LMFBR design*. American Association for Structural Mechanics in Reactor Technology, United States, 1989.

[136] N. Sheriff and N. W. Davies. Liquid metal natural convection from plane surfaces: A review including recent sodium measurements. *International Journal of Heat and Fluid Flow*, 1, 1979.

[137] H. E. Siekmann. *Strömungslehre : Grundlagen*. Springer-Lehrbuch. Springer, Berlin, 2000. ISBN 3-540-66851-9. URL `http://swbplus.bsz-bw.de/bsz087583089inh.htm`.

[138] E. Skupinski, J. Tortel, and L. Vautrey. Determination des coefficients de convection d'un alliage sodium-potassium dans un tube circulaire. *International Journal of Heat and Mass Transfer*, 8(6):937 – 951, 1965. ISSN 0017-9310. doi: http://dx.doi.org/10.1016/0017-9310(65)90077-3. URL `http://www.sciencedirect.com/science/article/pii/0017931065900773`.

[139] C. A. Sleicher, A. S. Awad, and R. H. Notter. Temperature and eddy diffusivity profiles in nak. *International Journal of Heat and Mass Transfer*, 16(8):1565 – 1575, 1973. ISSN 0017-9310. doi: http://dx.doi.org/10.1016/0017-9310(73)90184-1. URL `http://www.sciencedirect.com/science/article/pii/0017931073901841`.

[140] V. Sobolev. Fuel rod and assembly proposal for xt-ads pre-design. In *Coordination meeting of WP1 & WP2 of DM1 IP EUROTRANS*, Bologna, 8. – 9. February 2006.

[141] American Nuclear Society, editor. *15th International topical Meeting on Nuclear Reactor Thermal Hydraulics (NURETH-15)*, May 2013. ISBN 978-88-902391-2-0.

[142] M. A. Styrikovich and I. E. Semenovker. Heat exchange at very low prandtl numbers. *Journal of Technical Physics (USSR)*, X(16):1324 – 1330, 1940.

[143] M. A. Styrikovich, I. E. Semenovker, and A. R. Sorin. Sovetskoe kolotyrbostroenie. *Sovetskoe Kolotyrbostroenie*, 9(9):316, 1940. p.316.

[144] V. I. Subbotin, A. K. Papovyants, P. L. Kirillov, and N. N. Ivanovskii. A study of heat transfer to molten sodium in tubes. *Atomnaya Energiya*, 13, 1962.

[145] D. Tenchine. Some thermal hydraulic challenges in sodium cooled fast reactors. *Nuclear Engineering and Design*, 240(5):1195 – 1217, 2010. ISSN 0029-5493. doi: http://dx.doi.org/10.1016/j.nucengdes.2010.01.006. URL `http://www.sciencedirect.com/science/article/pii/S0029549310000300`.

[146] D. Tenchine, R. Bavière, P. Bazin, F. Ducros, G. Geffraye, D. Kadri, F. Perdu, D. Pialla, B. Rameau, and N. Tauveron. Status of {CATHARE} code for sodium cooled fast reactors. *Nuclear Engineering and Design*, 245(0):140 – 152, 2012. ISSN 0029-5493. doi: http://dx.doi.org/10.1016/j.nucengdes.2012.01.019. URL `http://www.sciencedirect.com/science/article/pii/S0029549312000520`.

[147] D. Tenchine, D. Pialla, P. Gauthé, and A. Vasile. Natural convection test in phenix reactor and associated {CATHARE} calculation. *Nuclear Engineering and Design*, 253(0):23 – 31, 2012. ISSN 0029-5493. doi: http://dx.doi.org/10.1016/j.nucengdes.2012.08.001. URL `http://www.sciencedirect.com/science/article/pii/S0029549312004244`.

[148] D. Tenchine, D. Pialla, T. H. Fanning, J. W. Thomas, P. Chellapandi, Y. Shvetsov, L. Maas, H.-Y. Jeong, K. Mikityuk, A. Chenu, H. Mochizuki, and S. Monti. International benchmark on the natural convection test in phenix reactor. *Nuclear Engineering and Design*, 258(0):189 – 198, 2013. ISSN 0029-5493. doi: http://dx.doi.org/10.1016/j.nucengdes.2013.02.010. URL `http://www.sciencedirect.com/science/article/pii/S0029549313000599`.

[149] The RELAP5-3D © Code Development Team. *RELAP5-3D © Code Manual Volume I: Code Structure, System Models and Solution Methods.* Idaho National Laboratory, revision 2.4 edition, June 2005. URL `http://www4vip.inl.gov/relap5/r5manuals.htm`.

[150] J. W. Thomas, T. H. Fanning, R. Vilim, and L. L. Briggs. Validation of the integration of cfd and sas4a/sassys-1: Analysis of ebr-ii shutdown heat removal test 17. In *Proceedings of the 2012 International Congress on Advances in Nuclear Power Plants - ICAPP '12*, volume 44, pages 692 – 700, 24. – 28. June 2012.

[151] W. Tischler. Natrium Stoffwerte. Report ITB 76.128, ITB, 1976.

[152] N. E. Todreas and M. Kazimi. *Nuclear Systems I: Thermal Hydraulic Fundamentals*, volume 1. CRC Press, December 1989.

[153] L. M. Trefethen. Liquid metal heat transfer in circular tubes and annuli. general discussion on heat transfer. *Inst. Mech. Engng and ASME*, pages 436 – 438, 1951.

[154] Department of Economic United Nations and Population Division Social Affairs. World population prospects: The 2015 revision, key findings and advance tables. Technical Report ESA/P/WP.241, United Nations, September 2015. URL `http://esa.un.org/unpd/wpp/Publications/Files/Key_Findings_WPP_2015.pdf`.

[155] P. A. Ushakov, A. V. Zhukov, and N. M. Matyukhin. Heat transfer to liquid metals in regular arrays of fuel elements. *High Temperature*, 15:868 – 873, March 1977. URL `http://www.osti.gov/scitech/servlets/purl/7030158`. translated from Teplofizika Vysokikh Temperatur.

[156] E. R. Van Driest. On turbulent flow near a wall. *Journal of the Aeronautical Sciences (Institute of the Aeronautical Sciences)*, 23(11), 2012.

[157] T. von Kármán. Mechanical similitude and turbulence. Technical Report 611, National Advisory Commitee for Aeronautics, 1931.

[158] W. L. Weaver, E. T. Tomlinson, and D. L. Aumiller. A generic semi-implicit coupling methodology for use in relap5-3d©. *Nuclear Engineering and Design*, 211(1):13 – 26, 2002. ISSN 0029-5493. doi: http://dx.doi.org/10.1016/S0029-5493(01)00422-8. URL `http://www.sciencedirect.com/science/article/pii/S0029549301004228`.

[159] J. R. Welty, C. E. Wicks, R. E. Wilson, and G. L. Rorrer. *Fundamentals of momentum, heat and mass transfer.* Wiley, Hoboken, New Jersey, 5. edition, 2008. ISBN 0-470-12868-2; 978-0-470-12868-8. URL `http://swbplus.bsz-bw.de/bsz277449391cov.htm;http://www.gbv.de/dms/ilmenau/toc/543357767.PDF`. Previous ed.: 2001.

[160] D. C. Wilcox. *Turbulence modeling for CFD*, volume 2. DCW industries La Canada, CA, 1998.

[161] K. Wolfert. Scaling of thermal-hydraulic phenomena and system code assessment. *Proceedings of the THICKET-2008*, 2008. URL `http://www.iaea.org/inis/collection/NCLCollectionStore/_Public/42/101/42101980.pdf`. seminar on the transfer of competence, knowledge and experience gained through CSNI activities in the field of thermal-hydraulics.

[162] Y. Zhiyin. Large-eddy simulation: Past, present and the future. *Chinese Journal of Aeronautics*, 28(1):11 – 24, 2015. ISSN 1000-9361. doi: http://dx.doi.org/10.1016/j.cja.2014.12.007. URL `http://www.sciencedirect.com/science/article/pii/S1000936114002064`.

[163] C. Zhou, Y. Yang, and X. Cheng. Feasibility analysis of the modified {ATHLET} code for supercritical water cooled systems. *Nuclear Engineering and Design*, 250(0):600 – 612, 2012. ISSN 0029-5493. doi: http://dx.doi.org/10.1016/j.

nucengdes.2012.06.021. URL `http://www.sciencedirect.com/science/article/pii/S0029549312003408`.

[164] C. Zhou, K. Huber, and X. Cheng. Validation of the modified {ATHLET} code with the natural convection test of the {PHENIX} reactor. *Annals of Nuclear Energy*, 59(0):31 – 46, 2013. ISSN 0306-4549. doi: http://dx.doi.org/10.1016/j.anucene.2013.03.035. URL `http://www.sciencedirect.com/science/article/pii/S0306454913001655`.

[165] A. V. Zhukov, A. P. Sorokin, V. P. Smirnov, and M. V. Papandin. Heat transfer in lead-cooled fast reactor (LCFR). *Proceedings of the international topical meeting on advanced reactors safety*, 1:66–69, 1994.

[166] A. V. Zhukov, Y. A. Kuzina, A. P. Sorokin, V. N. Leonov, V. P. Smirnov, and A. G. Sila-Novitskii. An experimental study of heat transfer in the core of a brest-od-300 reactor with lead cooling on models. *Thermal Engineering (English translation of Teploenergetika)*, 49(3):175 – 184, 2002. URL `http://www.scopus.com/inward/record.url?eid=2-s2.0-61649085926&partnerID=40&md5=de0873176a39a09c60eeddf931f99028`.